Design, Synthesis and Characterization of Nanomaterials for Efficient Solar Energy Conversion

Thesis submitted to

University of Calicut

for the award of the degree of

Doctor of Philosophy in Chemistry
under the Faculty of Sciences

by

Ambily Jacob K.

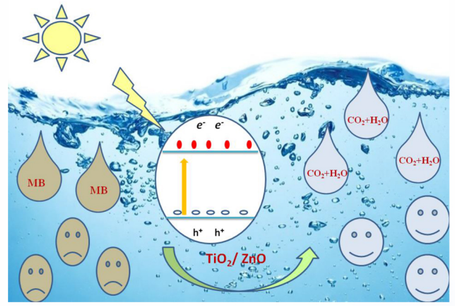

Post Graduate & Research Department of Chemistry
Christ College (Autonomous)
Irinjalakuda, Thrissur, Kerala - 680125
June 2022

Ambily Jacob K.

Design, Synthesis and Characterization of Nanomaterials for Efficient Solar Energy Conversion

PhD Thesis
2022

Design, Synthesis and Characterization of Nanomaterials for Efficient Solar Energy Conversion

Thesis submitted to

University of Calicut

in partial fulfillment of the requirements for the award of the degree of

Doctor of Philosophy
in
Chemistry
under the Faculty of Sciences

by

Ambily Jacob K.

Under the guidance of

Dr. V.T. Joy
Associate Professor and H.O.D.
Department of Chemistry
Christ College (Autonomous)
Irinjalakuda, Thrissur, Kerala – 680125

June 2022

DEPARTMENT OF CHEMISTRY
CHRIST COLLEGE (AUTONOMOUS)
IRINJALAKUDA - KERALA 680125

Date: 11/11/2022

Certificate

This is to certify that the corrections recommended by both the adjudicators have been incorporated in the thesis titled "**DESIGN, SYNTHESIS AND CHARACTERIZATION OF NANOMATERIALS FOR EFFICIENT SOLAR ENERGY CONVERSION**", submitted by Ms Ambily Jacob K. and that the contents in the thesis and soft copy are one and the same.

Dr. V. T. Joy

(Supervising Guide)
Associate Professor and Head
Department of Chemistry
Christ College (Autonomous), Irinjalakuda

Certificate

This is to certify that the thesis entitled "**DESIGN, SYNTHESIS AND CHARACTERIZATION OF NANOMATERIALS FOR EFFICIENT SOLAR ENERGY CONVERSION**" is an authentic record of the research work carried out by **Ambily Jacob K.** under my guidance for the award of the degree of Doctor of Philosophy in Chemistry under the faculty of Sciences, University of Calicut, Kerala and the same has not been submitted elsewhere for any Degree or Diploma.

Calicut University
. 6. 2022

Dr. V.T. Joy
(Supervising Teacher)
Associate Professor and Head
Department of Chemistry
Christ College (Autonomous), Irinjalakuda

Declaration

I hereby declare that the thesis entitled **"DESIGN, SYNTHESIS AND CHARACTERIZATION OF NANOMATERIALS FOR EFFICIENT SOLAR ENERGY CONVERSION"** is the bonafide report of the original work carried out by me under the supervision of Dr. V.T. Joy, Associate Professor, Department of Chemistry, Christ College (Autonomous), Irinjalakuda for the award of the degree of Doctor of Philosophy in Chemistry Under the Faculty of Sciences, University of Calicut, Kerala. The contents of this thesis have not been submitted to any other Institute or University for the award of any Degree or Diploma.

Christ College, Irijalakuda
. 6. 2022

Ambily Jacob. K.

Acknowledgement

I would like to thank God almighty.

I sincerely thank my supervisor Dr. V.T. Joy for his continuous support, constructive criticism, encouragement and insightful guidance during the course of my doctoral studies.

I express my sincere thanks to Dr. Jolly Andrew, Principal Christ College, Irinjalakuda, for allowing me to do research in Christ College, Irinjalakuda and use the facilities in the institution.

I am extremely grateful to Late Rev. Fr. Jose Thekkan C.M.I, Former Principal, Christ College, Irinjalakuda, for allowing me to do research in Christ College, sincere support and help extended to me during my research work.

I wish to acknowledge all faculty members of Department of Chemistry, Christ College, Irinjalakuda for their kind co-operation.

I value the sincere support rendered by Dr. Moly P.P., Mrs. Elsa P.J., Mrs. Jeena C.B. and Ms Daiphy Davis, who helped me directly or indirectly during the tenure of my work.

I would like to thank all members of the research group of Christ College, Irinjalakuda for their cooperation and for maintaining a very competitive yet friendly environment.

I express my sincere thanks to Dr. Sr. Gisalla George, Principal, Mercy College, Palakkad.
I wish to acknowledge former principal Dr. Sr. Alice Thomas, Dr. Sr. Lilly P.V. at this juncture.

I extend my thanks to all faculty members of Department of Chemistry, Mercy College, Palakkad for their help and support during the course of my work.

I wish to extend my thanks to STIC, Kochi, CSIF, Calicut University and St. Thomas College, Thrissur for the instrumental facilities made available to me for analysis.

I express my deepest gratitude to my sisters Dr. Anjaly Jacob K. and Mrs. Arathy Jacob K. and my friends Mrs. Anu kuruvila, Mrs. Melda Francis, Dr. Anas S., Dr. Mahesh K.V., Dr. Prashanth and Dr. Linsha for their help throughout my study.

I deeply thank my parents for their unconditional love and support, without which I would not have been able to succeed in this endeavour. I remember with gratitude my appapan, mema and relatives who were always a source of strength and support. I would like to take this opportunity to thank amma and daddy. Last but not least I thank my husband and my son for their incredible understanding, support and patience during the most difficult phase of my Ph.D.

Ambily Jacob K.

Dedicated to my parents. . . . .

Contents

List of figures

Preface

Semiconducting metal oxide such as TiO_2 and ZnO have attracted worldwide attention due to peculiar physical and chemical properties such as photoactivity, stability, non toxicity, environmentally friendly nature and low cost. TiO_2 have been used in many technological applications such as heterogeneous catalysis, photocatalysis, gas sensor devices and dye-sensitized solar cells. However there are some limitations such as high bandgap and fast recombination of photogenerated electrons and holes and these factors limits its photoactivity. It is necessary to modify these properties for photocatalysis under sunlight. Transition metal and non-metal doping can shorten the bandgap and reduce the recombination rate.

Chapter 1 describes the current energy resources, global challenges of energy availability, the significance of solar energy harvesting by photocatalysis, general principle of mechanism of heterogeneous catalysis and importance of waste water treatment. Crystalline structure, properties and applications of TiO_2 and ZnO, different methods used for the synthesis of metal oxides and objective of the present work are also included in chapter.

Chapter 2 deals with basic principles of various instrumental methods used for the characterization of TiO_2 and ZnO samples.

Chapter 3 discusses the synthesis of anatase-rutile mixed phase TiO_2 from a convenient precursor, potassium titanyl oxide oxalate. TiO_2 were also prepared by doping with 1 mol % Co, Ni, Mn, Cu and C. Thermal stability, structure, morphology, composition and properties of TiO_2 were determined by various techniques like TG-DTG, XRD, FT-Raman, FT-IR, HRTEM, FESEM, BET surface area and UV-DRS. On refluxing potassium titanium oxide oxalate a white precipitate was obtained and this white precipitate was found to be titanium oxalate complex from the XRD pattern. Formation of the complex was further supported by FT-IR spectra. The calcination of the sample at 450 ºC was found to give a mixed phase of anatase rutile TiO_2 consisting of 70% anatase and 30 % rutile, from the XRD results. The SEM and TEM techniques were used to determine the morphologies of the prepared samples. The EDS spectra were used to determine the amount of dopants in the doped TiO_2 samples. Photocatalytic performance of the samples were studied using

photocatalytic degradation of methylene blue under visible LED light irradiation. All doped TiO_2 samples showed higher photocatalytic activity than undoped TiO_2.

Chapter 4 deals with synthesis of anatase TiO_2 nanomaterials using titanium isopropoxide, doping of TiO_2 sample with cobalt ion doping and study of its photocatalytic activity under sunlight irradiation. The prepared samples were characterized by various techniques like TG-DTG, XRD, FT-IR, HRTEM, FESEM-EDS, XPS and UV-DRS. Synthesized TiO_2 and Co-doped TiO_2 nanomaterials were used as a photocatalyst for the degradation of methylene blue.

Chapter 5 gives the preparation of ZnO through various methods like simple precipitation, sol-gel method, reflux technique using convenient precursors. Their structure, morphology and properties were determined by various techniques like TG-DTG, XRD, FT-IR, HRTEM, FESEM, BET surface area and UV-DRS. Spherical nanoparticles were obtained by precipitation and sol-gel methods. The ZnO nano rods were prepared by the thermo-hydrolysis of zinc nitrate using HMTA via low temperature reflux route. Photocatalytic activities of the samples were studied using photocatalytic degradation of methylene blue under visible LED light irradiation. The ZnO prepared from zinc nitrate and citric acid route show better photocatalytic activity than ZnO prepared form zinc nitrate and HMTA.

The conclusion of the thesis are given in **Chapter 6**.

Chapter 7 gives the recommendations for future work.

Key words: Nanomaterials, TiO_2, mixed phase anatase rutile TiO_2, ZnO, doped TiO_2, Photocatalysis.

Chapter 1

Introduction to semiconductor photocatalysis

Contents

1.1 Sustainable energy and environment

Sustainable energy is the energy derived from clean, renewable sources of energy without endangering the energy needs of future generations and without affecting the climate. These energy sources renew themselves, rather than sources like fossil fuels that can be depleted. According to World Energy Council report, the world energy demand in 2020 grew 50–80% higher than that in 1990.[1] Figure 1.1 shows the yearly energy demand and development. Such increasing demand could place significant damage on world environmental health. Researchers are actively working to develop eco-friendly alternative technologies for sustainable energy production and pollutant destruction in all areas of daily life. Semiconductor photocatalysis is a widely used technique for pollutant degradation and energy production. The appropriate position of the valence and conduction bands makes the semiconductors suitable materials for the absorption of light.

1.2 Energy harvesting and human progress

World is becoming a global village. Energy is one of the basic needs for technological advancements and economic developments of human society. With world population increasing to 9 billion people by 2050, the demand for energy will also double by this time. The economic growth, energy security and environment protection are the fundamental aspects of the national energy policy

of every country. The industrialisation consumes 75% of the world's energy supply. The rest of the energy used for enhancing lifestyle.

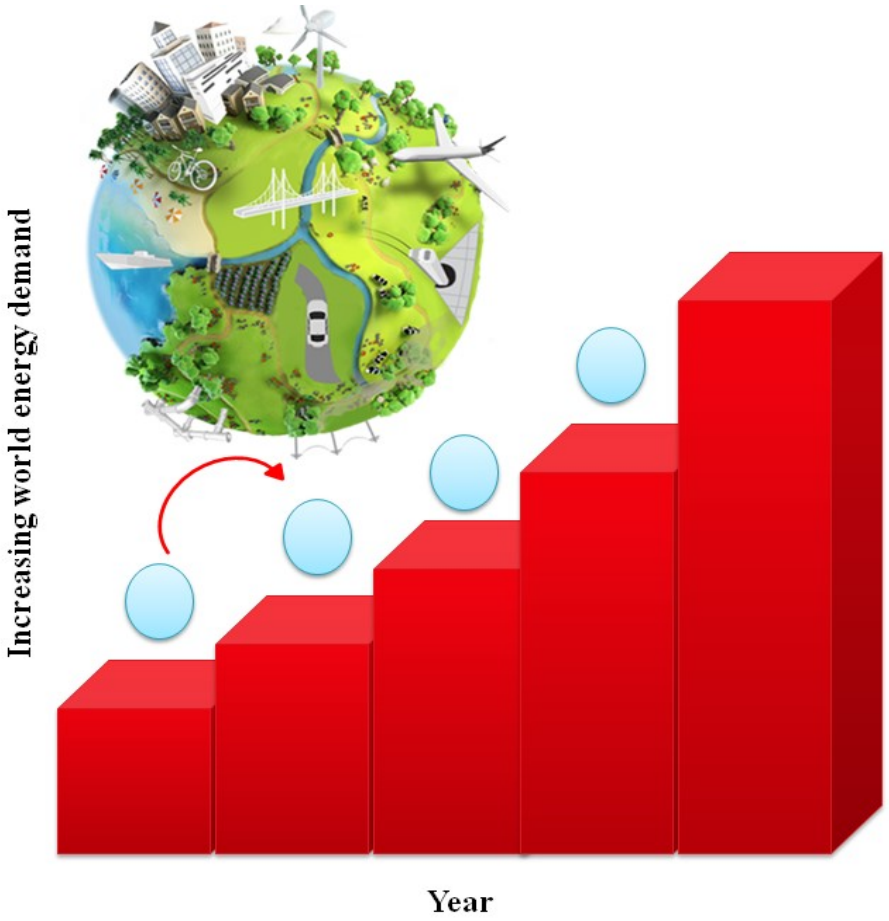

Fig. 1.1 Energy demand and development

Fossil fuels currently supply about 80% of the energy demand. At current rate of usage, fossil fuel will run out during this century. Fossil fuels take thousands of years to form naturally and cannot be replaced as fast as they are being consumed. The gases produced by the combustion of fossil fuels cause enhanced greenhouse effect and global warming. The serious consequences of these hazards are drastic climate changes like extreme weather, sea level rise leading to flooding and erosion of coastal and low lying areas, etc. Nuclear power is capable of providing large scale power generation. But it has safety and waste management issues. Also the amount of uranium present in the Earth's crust is limited. Alternative clean energy resources are needed for sustainable development.

1.2.1 Types of energy resources

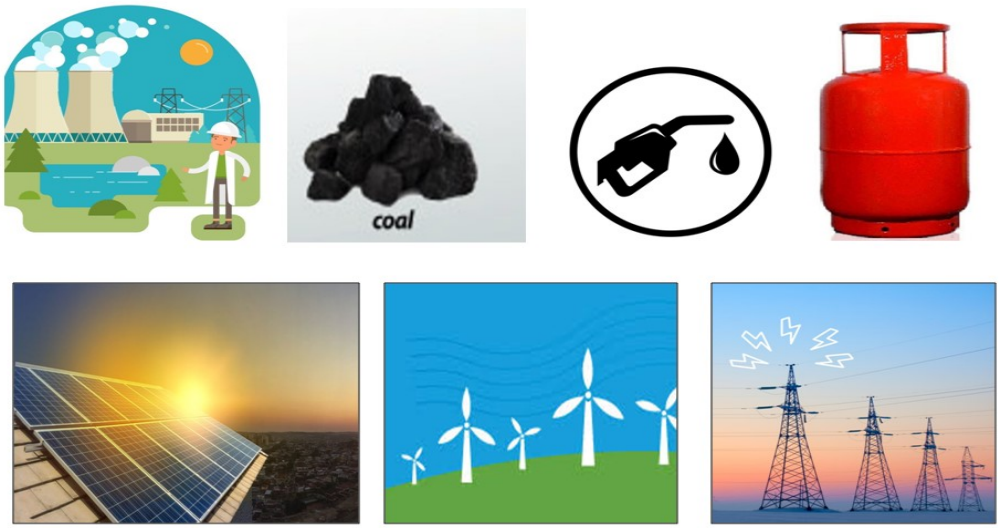

Fig.1.2 Different types of energy resources

Sources of energy are divided into two major categories, renewable and non-renewable energy resources (Figure 1.2). Non-renewable resources are those that cannot be replenished in a short period. Renewable energy resources are replenished naturally. Resorting to renewable resources could protect us from the negative effect of climate changes and increasing energy price and supply.

1.2.2 Non-renewable energy resources and its limitations

Non-renewable resources are mainly coal, natural gas and oil and nuclear energy. First three of these are collectively called fossil fuels and they are derived from biomass of dead plants and animals decomposed under high pressure and temperature, millions of years ago. Fuels from non-renewable resources are the primary source of energy in the world due to their affordable cost and availability. Advantages of non-renewable energy resources are that they are high energy sources, easy to use and can be conveniently moved across the world. Apart from these advantages, they have disadvantages also. The massive consumption of fossil fuel has a negative impact on the environment. Intergovernmental Panel on Climate Change observed that the global temperature is increasing since 20th century due to the increased consumption of fossil fuels. Carbon dioxide emitted

while burning of fossil fuel can trap heat in the earth atmosphere. Moreover processing methods like extraction, transportation, processing and combustion of fossil fuel causes health issues. Also the cost of this energy is continuously rising. Nuclear energy provides about 6% of total energy. Highly radioactive product formed in the nuclear power reactor and their disposal has negative impact on human health and environment. Also nuclear reactors are prone to accidents, for example the Fukushima nuclear disaster where a severe tsunami that followed a massive earthquake severely damaged the cooling systems of nuclear reactor leading to explosion and severe exposure to nuclear radiation.

1.2.3 Need for renewable energy resources and its challenges

Renewable energy resources are the most efficient and effective solutions for sustainable development. There are five major renewable energy resources such as solar, wind, biomass, geothermal, etc. They are sustainable, eco-friendly and available locally in abundance. The sun and wind will not be exhausted in the near future. Many countries have agreed to lower the amount of CO_2 and greenhouse gas emissions through the Kyoto Protocol and the Paris Agreement. However, the amount of CO_2 keeps on rising in the atmosphere and the Earth is heating up at an alarming rate. Before industrial revolution the level of CO_2 in the atmosphere was about 280 ppm. Currently this level has increased to about 420 ppm. Scientists warn that if this warming due to increased greenhouse effect continues unattended, it could bring major environmental catastrophe to much of the world, including record-breaking droughts, staggering sea-level rise and floods, and widespread species loss.

Depending on renewable energy resources can help us to mitigate climate change. They do not emit any carbon dioxide when they generate energy. Wind, hydroelectric and solar energies are carbon-free energy sources. Biomass and biofuels are considered as the chemical energy stored inside the plants by photosynthesis. Biomass and biofuels produce carbon dioxide when they are burned. The carbon dioxide returns to atmosphere are balanced in above process.[2] Hence, the biomass and biofuels are carbon-neutral resources. Nuclear power does not produce CO_2 and air pollution. Nuclear energy generates heat through fission, not combustion and it is also considered a carbon-free energy resource.

Today, the renewable energy sources contribute only around 22% to energy production.[3] Extracting the renewable energy, conversion, transportation and utilization without loss are the major challenges today. Opportunities of renewable energy resources are shown in Figure1.3.

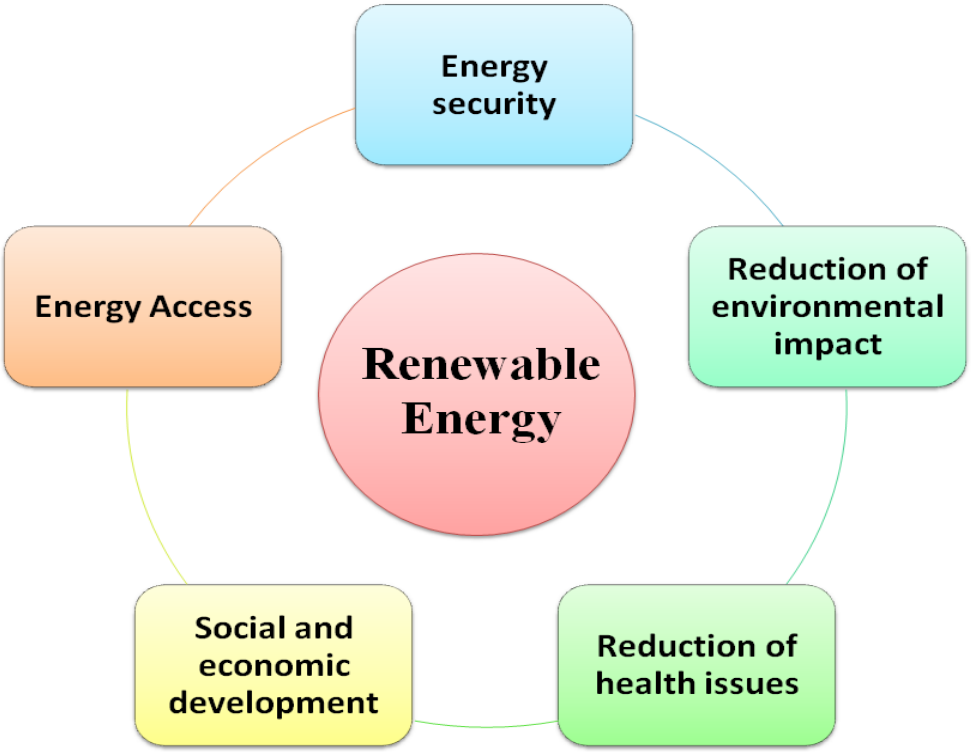

Fig.1.3 Opportunities of renewable energy resources

1.3 Solar energy harvesting by photocatalysis

Among the renewable energy resources, solar energy is the most plentiful energy source for the earth and available locally. Solar energy is utilised for widespread applications such as lighting, heating, cooling, cooking, space technology, communication electronics etc.[4,5] Technology for solar energy harvesting was started from seventh century B.C.[6] They used magnifying glass for making fire. In 1876 William Grylls Adams and Richard Evans Day found that selenium produces electricity during the exposure to sunlight. Development of materials and new approaches for the direct utilization of solar energy with improved efficiency is necessary for the future generations.

Semiconducting materials can be used for solar energy harvesting in environmental and energy systems. Solar energy has potential for photovoltaic, photodegradation of waste water and water splitting for hydrogen fuel production using nanostructured semiconductors.[7] In this manner solar cells and photocatalysis applications are very important for the future. Various metal oxides such as TiO_2, ZnO, CeO_2, MnO_2 and Bi_2O_3 have been studied for photocatalysis and photovoltaics applications. Among them TiO_2 and ZnO are most attractive due to their good chemical stability, high photocatalytic activity, non-toxicity and long term photostability.

1.3.1 Silicon solar cells

Photovoltaic technology using silicon was developed at Bell Laboratory in 1954. This was the first solar cell capable of converting solar energy into electricity with 4% efficiency. The silicon solar cells are known as first generation solar cells. It consists of more than 90% of commercial solar cell production. It has broad spectral absorption range (Except blue and violet). The theoretical efficiency for single junction silicon solar cells is 33%. Si wafers (thickness ~ 200 μm) are used for fabricating crystalline silicon solar cells. But the minimum cost for silicon 125 mm diameter wafers is about US $ 1 per square inch.[8] To address the high production costs of silicon solar cells, a change from silicon solar cells to metal oxide based solar cell is necessary.

1.3.2 Metal oxides semiconductor solar cells

Metal oxide semiconductor solar cells are low cost alternative to first generation solar cells. Thin film solid state solar cells, dye-sensitised solar cells (DSSC) and hybrid solar cells have been considered as a promising candidate for next generation solar cells. They can be produced very easily on demand and are quite stable. Variety of metal oxides are used for the synthesis of solar cells. Among them, the most studied metal oxide is TiO_2. It is the best successful anode owing to its chemical stability and suitable band alignment. Its unique electronic structure allows the separation of excited charge carriers during the absorption of light, whose energy greater than or equal to the energy bandgap. ZnO is a promising alternative to TiO_2 due to its larger bandgap. Solar cells can be

classified as shown in Figure 1.4. DSSC, Hybrid solar cells and thin film solid state solar cells consist of semiconductor metal oxide especially TiO_2 and ZnO.

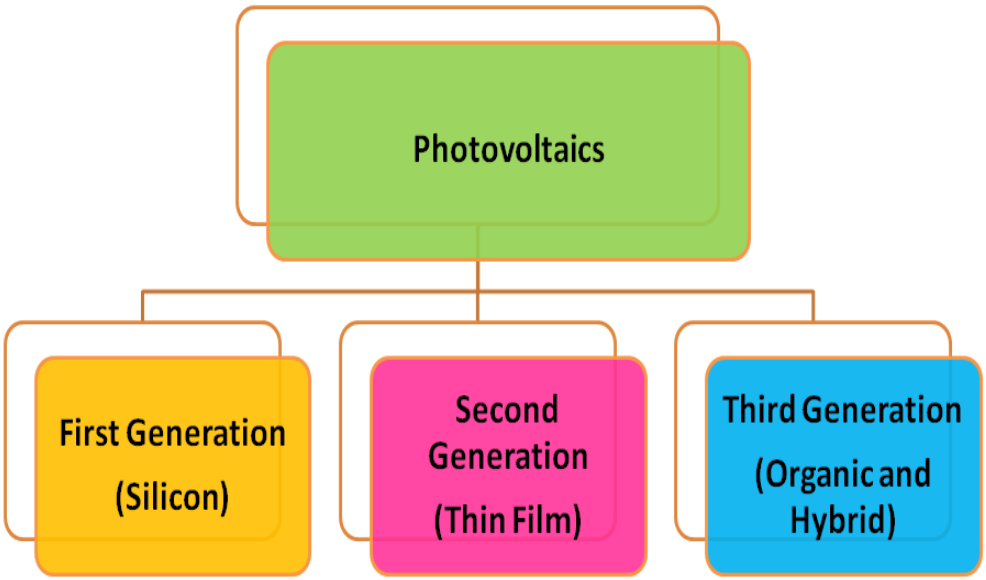

Fig.1.4 Generations of solar cells

1.4 Working principle of solar cells

The working principle of solar cells are based on photoelectric effect. In photovoltaic effect, a potential difference is generated at the junction in response to absorption of sunlight. Classical P-N junction solar cells consist of a p-doped semiconductor and n-doped semiconductor. They are arranged in contact to form a junction. Charge carriers are generated due to the absorption of photons and the bandgap of semiconductor should match with the energy of light.

Dye sensitized solar cells are third generation solar cell that converts visible light into electricity. The DSSCs were invented in 1991 by Professor Michael Graetzel and Dr Brian O'Regan and is often referred to as the Graetzel cell. The dye-sensitised solar cells consist of thin layer of metal oxide deposited over a transparent conducting glass plate. Common conducting glass plates are fluorine doped tin oxide (FTO) or indium tin oxide (ITO). Figure 1.5 represents the schematic representation of DSSC. Dye molecules get adsorbed on the semiconductor metal oxide surface. When the sunlight strikes on the surface of the dye-sensitised solar cells, the dye molecules absorb light and undergo excitation

from HMO to an unoccupied MO. Subsequently electron is injected into the conduction band of TiO_2. Metal oxide layer acts as an anode. The platinum film prepared on the transparent conducting glass substrate, acts as a counter electrode. The counter electrode completes the internal electrical circuit by injecting electrons into the electrolyte. Original state of dye is regenerated by interaction with the electrolyte. The electrolyte (organic solvent containing I^-/I_3^- redox couple) is filled over the conducting sheets. These two plates are joined and sealed together.

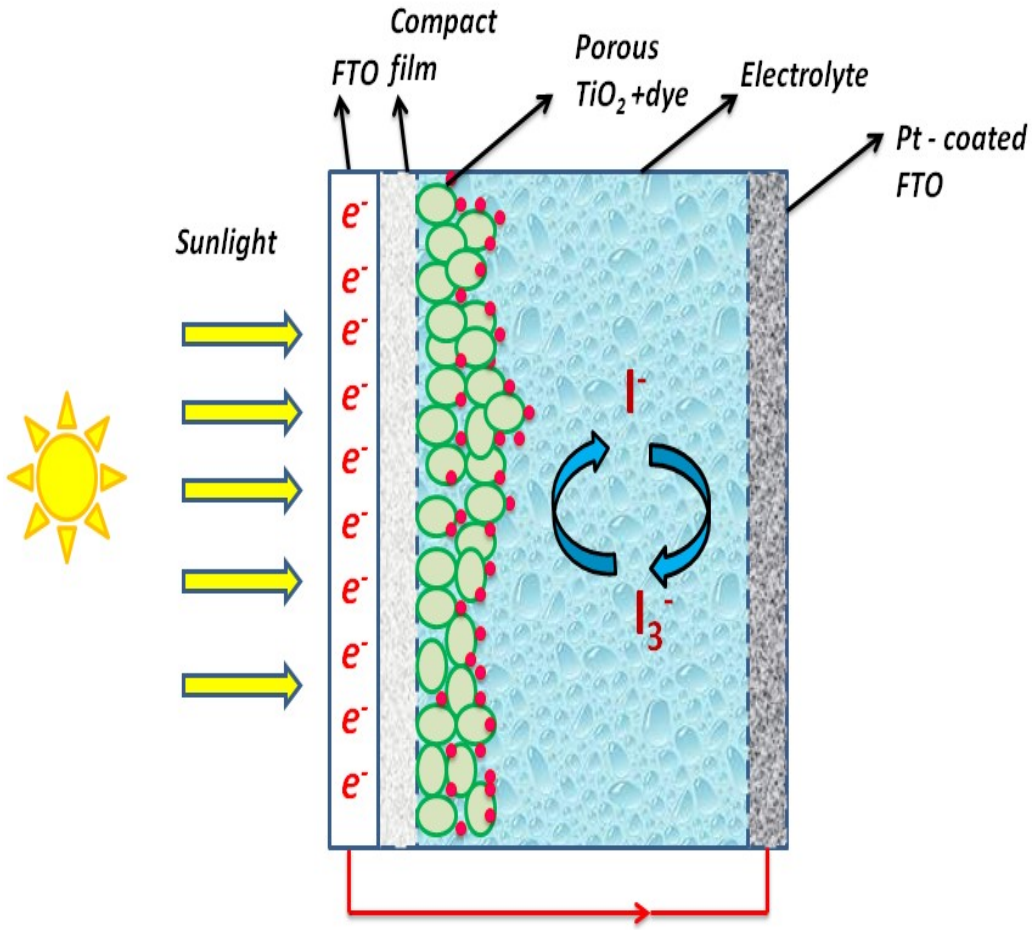

Fig.1.5 Schematic representation of Dye sensitized solar cell

1.5 Water pollution and degradation of pollutants /waste water treatment

Human activity is connected with extraction, manufacture, distribution, use and finally disposal of materials. This process has vital role to the overall prosperity of our civilization. However, human activities are unavoidably

connected with environmental pollution especially water pollution because of consumption and industrialisation and hence fresh water is becoming a limited resource. About 70% of the earth surface is covered by water. Among them 97% of the water is in the ocean and unfit for human consumption. Only 1% is available as fresh water. Most of the industrial wastes are released to river, lakes and sea. Water resources are becoming increasingly scarce and polluted. Contaminants such as pesticides, surfactants, dyes, organic pollutants etc. produced by industries are increasing day by day and are harmful to both the environment and human beings. Several pollutants are soluble in water. They have been detected in surface water and ground water also. India is one of the world's biggest textile manufacturing nation. Majority of the dyes used in textile industries are organic compounds. The discharge of wastewater to the water bodies will causes several environmental problems such as: 1) Reduced dissolved oxygen 2) increase in the growth of microorganism and aquatic plants, leading into eutrophication 3) release of large amount of toxic material.

1.5.1 Different methods for water treatment

The recycling and reuse of wastewater effluents are important to reduce the demand for water. The different physical and chemical processes used for waste water treatment are adsorption, chemical treatment, biological treatment, ion exchange, reverse osmosis, coagulation, flocculation and membrane based separations, etc., as shown in the Figure 1.6.

1.5.1.1 Physical methods

Physical methods are non-destructive operations to remove insoluble particles and soluble contaminants. Simple equipments are used for physical methods. No chemicals are used in these processes. These methods are inadequate for removing non-degradable compounds such as phenols, surfactants and heavy metals. In contrast with conventional techniques, adsorption is well-established technique for removal of pollutants, as it is efficient, easy to implement and cost-effective. Adsorption could remove pollutant molecules without generating sludge. Main disadvantage is weak selectivity and needs post-treatment. Other physical methods like coagulation-flocculation process based on the addition of aluminium sulphate and ferric sulphate etc. are also used. But the presence of residual aluminium and

iron can cause health issues like Alzheimer's disease and significant problems for ecosystems.

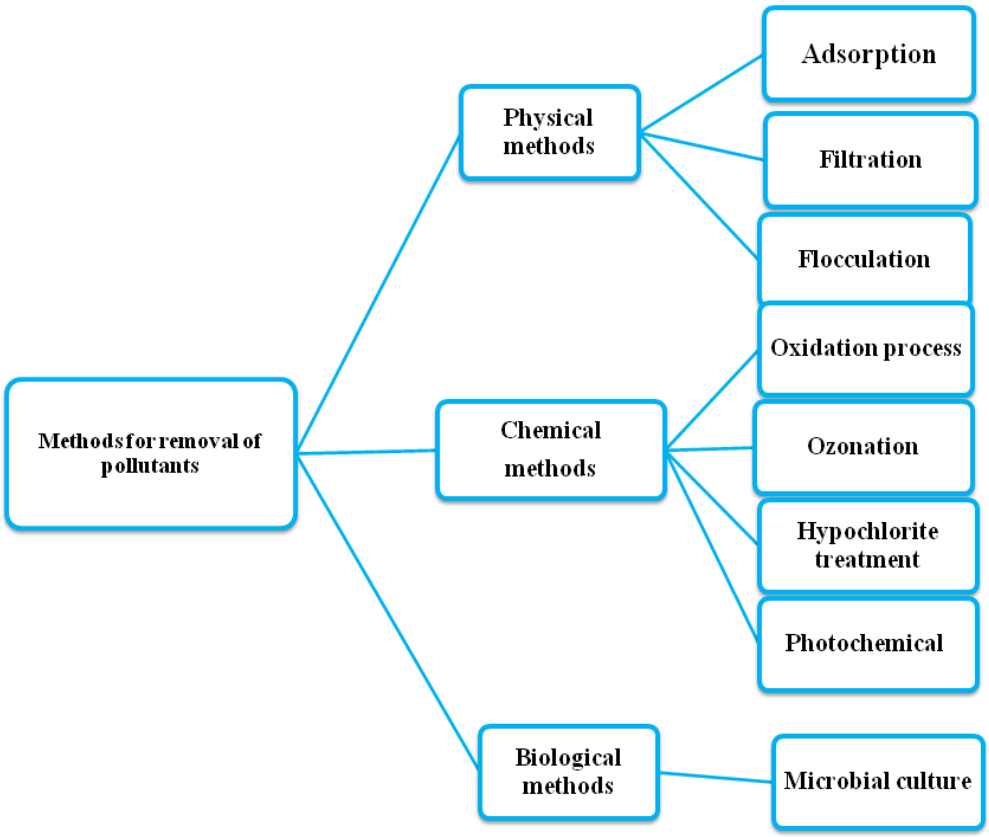

Fig.1.6 Different methods for the removal of pollutants.

1.5.1.2 Biological methods

In Biological methods microorganism break down the organic matter such as soap, human waste, oil and food. Biological methods are environmentally friendly, inexpensive and effective. However, biological approaches are time consuming. They are sensitive to the toxicity of pollutants.

1.5.1.3 Chemical methods

Chemical methods includes precipitation, neutralization, coagulation, oxidation and reduction etc. Chlorine, ozone are the oxidizing agents commonly used for waste water treatment. Chlorination is the safest and most reliable method. When bleaching powder is dissolved in water, the chlorine gas is release and hydrolyzes to form hypochlorous acid and hydrochloric acid. This

process is used to kill microorganisms like bacteria and viruses in water. Ozone is a powerful oxidant used in waste water treatment. Since ozone is an unstable molecule, it should be produced at the point of application for waste water treatment.

Heterogeneous photocatalysis is a promising advanced oxidation process for water purification. This method has been found to be safe, cost effective, environmentally friendly and reusable. It has the potential to fully oxidize organic pollutants and destroy microorganisms. The development of new innovative methods such as membrane separation is expanding the possibilities in future.

1.5.1.4 Semiconductor nanoparticles in photocatalysis

Semiconductor nanoparticles participate in either direct or indirect manner in a photocatalysis process. The bandgap excitation leads to charge separation in semiconductor particles. The substrates retained on the semiconductor are reduced or oxidized by the photogenerated electrons and holes. In addition, the charge exchange between two assimilated particles may also happen as a result of the photocatalytic response by the semiconductor nanocluster.[9] This procedure, called photosensitization, is also broadly utilized in photochemistry.

The origin of various size-dependent properties of nanoparticles originating from a spatial confinement of the photogenerated charge carriers (excitons) in ultra-small semiconductor nanoparticles (quantum dots) have been focus on many studies. Unique optical, magnetic, electrical, catalytic, sensing and other properties emerge from the molecules at nanoscale.[10] Highly active catalysts are generated from inert metal or metal oxides when size of the materials reduce to nano level. Nanoparticles have very high surface to volume ratio due to the fact that the large fraction of atom or molecule is exposed on the surface of the materials compared to bulk materials.[11] Lower coordination and unsatisfied bonds make the surface atom less stabilized than bulk atoms and make them highly reactive in surface energy. These sites called active sites tries to reduce its surface energy by binding with foreign atoms and molecules.

1.5.1.5 Waste water treatment using semiconductor photocatalysis.

Semiconductor photocatalysis for waste water treatment is attractive for both industries and environmental sector since it would be relatively cheap and simple to implement. The minimum energy required for photoactivation of semiconductor depends upon its bandgap energy. The examples for semiconductors used as photocatalysts include Si, Fe_2O_3, WO_3, SnO_2, CeO_2, Bi_2O_3, TiO_2, ZnO, CdS, ZnS, GaAs. Among them, TiO_2 and ZnO are promising one due to low cost, non-toxicity and stability. However, turning of semiconductor photoactivity to visible radiation of sunlight is the most challenging task. Eventhough the bandgap of CdS and ZnS are in the visible region, there are only few reports of using them as photocatalysts.

1.6 Principles of heterogeneous photocatalysis and photoactivation of semiconductor

Catalysts are divided into two categories homogenous or heterogeneous. Homogeneous catalysts have higher activity and selectivity. Heterogeneous catalysts can be separated easily and recycled. The photocatalysts are materials that alter the rate of a chemical reaction on exposure to light. Compared to conventional catalysis methods, which lower the transition state energy, visible-light photocatalysis usually transfer electron or energy to generate reactive intermediates. The heterogeneous photocatalysis can be classified into four major processes: 1) light harvesting, 2) charge excitation, 3) charge separation and transfer and 4) surface electrocatalytic reactions. The light harvesting process mainly depends upon the structure and surface morphology of photocatalysts.

Heterogeneous photocatalysis can be divided into two main categories: first category is the sensitised photoreaction, in which the catalyst is induced into a photo-excited state followed by transfer of an electron to an adsorbed molecule. Second category is the catalysed photoreaction which is defined as initially photo-excited adsorbed molecule such as a dye molecule reacts with the molecule adsorbed on catalytic surface. In both cases the reduction or oxidation of a target compounds occur resulting in the conversion of the reactants into the desired products.

Photocatalyst may influence rate of chemical reaction either by transferring the energy or charge carrier. UV and Visible regions are much concern to photochemist. UV region can be again subdivided into three UV-A (320-380 nm), UV-B (280 -320 nm) and UV-C (below 280 nm). Photocatalysis using TiO_2, ZnO etc. usually employs low energy UV-A light. The n-type photocatalytic semiconductor materials are mainly used in various fields such as energy production, environmental depollution and chemical synthesis. TiO_2 and ZnO have been most intensively investigated photocatalysts for the environmental pollutants degradation studies. The semiconductor is irradiated with photon, whose energy equal or exceeds semiconductor band gap energy. On irradiation, electrons are excited from valence band to the conduction band within femtosecond timescale resulting the generation of charge carriers. These charge carriers have the ability to promote oxidation and reduction photochemical reactions on semiconductor surface. Electrons in the conduction band can reduce oxygen adsorbed on the catalytic surface site into superoxide anions and form hydroxyl radicals.[12] The hydroxyl radicals have the potential to initiate photoreduction reaction.[13] Several reactive oxygen species like $O_2^{\bullet-}$, $OH^{\bullet}$, $HO_2\bullet$ and H_2O_2 are oxidising agents in photocatalysis. Equations for the formation of oxygen species are given below.

$$TiO_2 + hv \longrightarrow e + h^+ \quad (1)$$

$$h^+ + H_2O \longrightarrow H^+ + OH^{\bullet} \quad (2)$$

$$e + O_2 \longrightarrow O_2^{-\bullet} \quad (3)$$

$$O_2^{-\bullet} + H^+ \longrightarrow HOO^{\bullet} \quad (4)$$

Hydroxyl radical may also be formed by the oxidation of hydroxyl group by interaction with positive holes.[14,15] Presence of hydroxyl radicals have been confirmed by electron paramagnetic resonance. Hydroxyl radical is a very powerful oxidant and is capable of oxidizing organic compounds with one or many double bonds. Hydroxyl radical has higher oxidising power due to its high reduction potential (+2.8) than other oxidising species such as hydroperoxyl/superoxide radical. The electron-hole recombination is competing

process with charge transfer reactions. Recombination can occur either in the semiconductor bulk or at the surface resulting in the release of heat.

Redox potentials of semiconductor plays a vital role in photocatalysis. The charge transfer process depends upon the redox potential of the adsorbed species and the position of valence and conduction band edges. For the reduction of adsorbed oxidant, the conduction band of semiconductor must be more negative than reduction potential. For the oxidation of the adsorbed species, the valence band of the semiconductor must be more positive than its reduction potential of adsorbed species.

1.7 Advanced oxidation processes

The photocatalysis using semiconductor as catalyst are widely investigated for advanced oxidation process (AOP). AOP involves in-situ generation of highly reactive species for the complete decomposition of dye in the waste water. The advanced oxidation technology using semiconductors especially TiO_2 are promising technology and can remove even low level of organic pollutants. It has several advantages over conventional oxidation processes such as complete mineralization of the pollutants, use of the near-UV or solar light, low cost and operation at near room temperature.[16] Major applications of TiO_2 photocatalyst are water purification, CO_2 conversion, self cleaning glass, surface sterilization etc.

1.8 TiO_2 as photocatalyst

TiO_2 is the most popular and widely used semiconductor photocatalyst because of its diverse applications.[17] Fujishima and Honda discovered water splitting using an n-type rutile TiO_2 photoanode in a PEC cell in 1972.[18] Since then intense research has been carried out to understand the effect of the nature of TiO_2 semiconductor photocatalysts on charge separation and transfer.[19,20] TiO_2 is more attractive and an ideal photocatalyst due to several factors such as its high refractive index, ultraviolet absorption, chemical stability, corrosion resistance, low cost, water insolubility, hydrophilicity, cheap availability, environmentally friendly nature and nontoxicity etc.[21] TiO_2 can be prepared in the pure form very easily. TiO_2 can be supported on various substrates such as glass, fibres, stainless

steel, inorganic material, sand and activated carbon.[22] TiO_2 has become most popular photocatalyst for water purification (green detoxification of environmental pollutants), degradation of organic pollutants, energy production, CO_2 conversion, air pollution, self cleaning glass, dye sensitised solar cells, sensor and surface sterilization tool, etc.[23-25] The most attractive property of TiO_2 is photocatalysis to harvest the incident light for wide range of applications shown in the Figure 1.7. The TiO_2 has been used for photooxidation, photoreduction and photo degradation of organic and inorganic compounds.

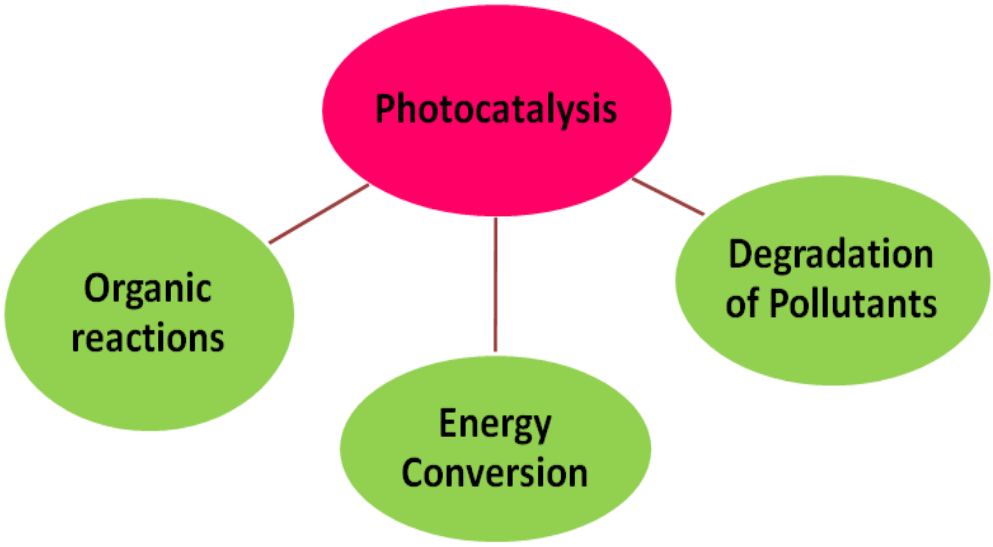

Fig. 1.7 Main applications of photocatalysis

The main drawback of TiO_2 is its large bandgap restricting its application only within the UV region having the wavelength lower than 387 nm. Band gap energy for rutile is 3 eV (410 nm) and for anatase it is 3.2 eV (380 nm).[26] So its photoactivation can be done only under UV radiation. Sunlight consist of 5% UV radiation (300-400 nm), 43% Visible light (400-800 nm) and 52% IR radiation (800-2500 nm).[27] A larger part of sunlight cannot be absorbed by TiO_2.

The TiO_2 has high recombination rate of electron and hole pair. Majority of the excited charge carriers recombine before reaching the catalytic surface and dissipating the absorbed energy as heat. The bandgap energy, recombination rate of charge carriers and the surface charge transfer are the main factors which affect the photocatalytic activity. The defects and imperfections can act as recombination centres.[28]

1.8.1 Crystalline structure and properties of TiO_2

Crystallinity of TiO_2 has the vital role in the charge transportation of excited charge carriers through the crystal lattice. TiO_2 has three crystalline phases in nature anatase, rutile and brookite.[29] Anatase and rutile exist in tetragonal crystalline structure and brookite exists in orthorhombic crystalline structure.[30] Figure 1.8 represents anatase and rutile phases of TiO_2 and crystal structure.

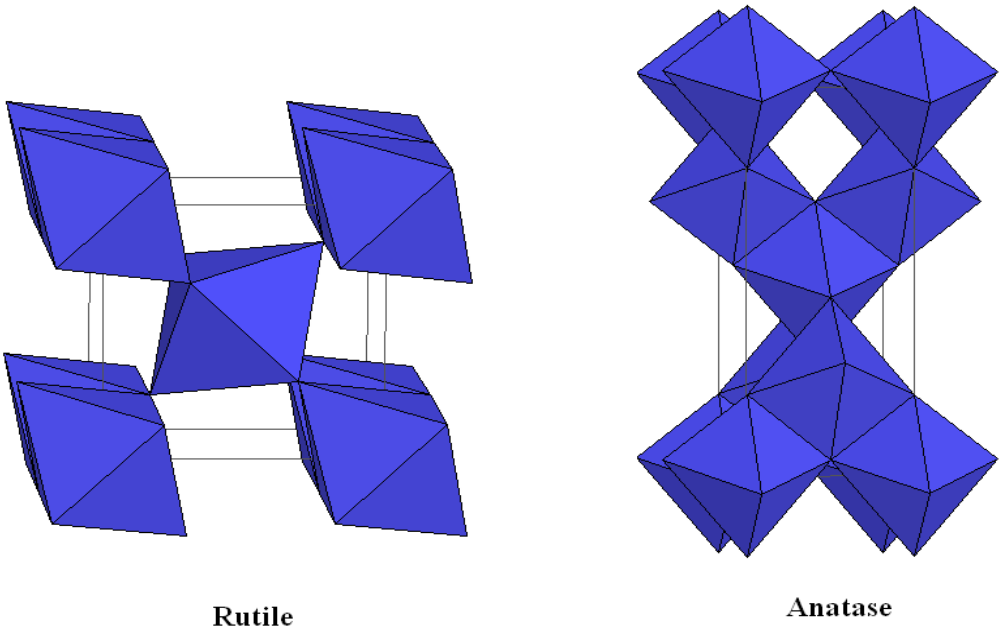

Fig.1.8 Unit cell and crystal structure of rutile and anatase phase of TiO_2 (Adopted from http://ruby.colorado.edu/~smyth/min/tio2.html)

Different crystalline structures have different physical properties. Rutile phase is the most stable phase of TiO_2. Anatase and brookite are metastable state and converted to rutile under high temperature.[31] The brookite is least common and rarely used commercially. It is difficult to synthesis and seldom studied for photocatalysis. Properties of anatase and rutile phases are listed in the Table 1.1. Anatase and rutile structure have many similarities but they are differ in variety of ways. These crystalline structures consist of $[TiO_6]^{2-}$ octahedra. Each Ti^{4+} ions are surrounded by irregular octahedron of six oxide ions in these three crystalline phases. Oxide ions are grouped into two. Four oxide ions are closer to Ti^{4+} ions and other two oxygen atoms are relatively away from Ti^{4+} ions. These distances are 1.92 A˚ and 2.01 A˚ in rutile. In anatase, these distances are 1.9 A˚ and 1.95 A˚ respectively. Each oxide ions are linked to three Ti^{4+} ions. The octahedra

of anatase is more distorted than rutile. The transformation from anatase to rutile is a thermodynamically stable process. There is no unique temperature for these phase transformation and occurs in the temperature range 600-800 ˚C.

In anatase, TiO_2 octahedra are connected by their vertices where as in rutile, octahedra are connected through edges. In the rutile structure, each octahedron is connected with 10 neighbours, with two sharing edge oxygen pairs and eight sharing corner oxygen atoms. For the anatase, every octahedron is in contact with only eight neighbours (four sharing an edge and four sharing a corner). Hence rutile structure is more densely packed. Three-dimensional TiO_2 network is formed from a mixture of corner-sharing and edge-sharing octahedral units.

Table 1.1 Properties of anatase and rutile phase of TiO_2

Properties	Anatase	Rutile
Crystal structure	Tetragonal	Tetragonal
Atoms per Unit cell	4	2
Density (g/cm^3)	3.83	4.24
Lattice parameters (nm)	a =0.3785, c =0.9514	a = 0.4594, c = 0.2958
Band gap (eV)	3.2	3.0
Refractive index	2.54,	2.79
Hardness (moh)	5-6	6-7

Since photoactivity of nanoparticles is sensitive to the particle size and shape, it is essential to control nanoparticle size and shape.[32] A variety of nanostructures such as nanoparticle, nanorods, nanotube, nanofiber, nanoflower are reported for TiO_2.[33] The TiO_2 nanocrystals have several advantages over bulk materials such as high surface-to-volume ratio, increased number of delocalized carriers on the surface, improved charge transport and efficient separation of photo-generated hole and electrons. Anatase exhibits lower rate of recombination due to greater rate of hole trapping.[34]

Anatase shows higher photocatalytic activity than rutile due to higher degree of hydroxylation, differences of the Fermi level and lower charge carrier recombination.[35] Anatase nanoparticles provide more surface area for light harvesting.[36]

There are two different types of band gap exist in semiconductors, direct band gap and indirect band gap. In direct band gap semiconductor, an electron can move from the highest-energy state in the valence band to the lowest energy state in the conduction band without a change in momentum. According to Density of states (DOS) considerations and density functional theory (DFT) calculations, anatase has an indirect band gap whereas rutile and brookite have direct band gap transitions.[37] Thus anatase photocatalyst has longer lifetimes of photogenerated charge carriers to participate in surface reaction.[38] But the bandgap of anatase is higher than the rutile. The larger band gap of anatase than rutile reduces the amount of light that it can absorb. However, the higher bandgap raises the valence band maximum to higher energy levels. This increases the oxidation power of anatase by facilitating the electron transfer to adsorbed molecule.[39] It is necessary to develop most efficient photocatalyst in visible light viable for industrial scale applications. There are various strategies applied to extend the photoactivity to visible region and these includes coupling with low bandgap semiconductors, sensitization with dyes, doping with metal or non-metals, or deposition of noble metal into semiconductor.[40]

Best photocatalyst have the ability to create electron-hole pairs and reduces the recombination of charge carriers generating free radicals capable of undergoing secondary reactions. Degussa P25 contain approximately 78% anatase phase, 14% rutile and 8% of an amorphous phase of TiO_2 and is more active than pure crystalline phases of TiO_2.[41] The Degussa P25 is composed of mixed phase anatase-rutile nanoparticles with an average diameter of 21 nm, surface area of approximately 50 m^2/g and an anatase to rutile composition of around 4:1. Degussa P25 is accepted as benchmark for photocatalysis studies. But the rapid recombination of photo induced charge carriers and need for ultraviolet excitation are the major disadvantages of TiO_2.[40] The TiO_2 has been used as a photocatalyst for the water splitting.

1.8.2 Band structure and effect of dopants in the optical properties of TiO_2

The limitations of semiconductors can be modified by heterostructuring, which is a composite system in which two or more materials with different energy landscapes are integrated. The mixed phase anatase/rutile titania can improve the

charge separation of electron and hole pair through interfacial electron transfer at the phase boundary. Different mechanisms have been proposed to explain the photoactivity of mixed phase. One view is that rutile can act as the electron sink due to its lower CB edge compared with anatase. Other view is that low-energy trap sites in the anatase phase capture excited electrons from the rutile phase.[42] Scanlon et al. have reported a study on the band alignment of anatase and rutile mixed phase TiO_2 photocatalysts supporting the flow of electrons from the conduction band of the rutile phase to the lower energy conduction band of anatase phase, while the holes moving in the opposite direction.[5] The synergistic effect occurs since the interface of these two distinct phases in the mixed phase of TiO_2 are in direct contact.

The composition and optical properties of TiO_2 can be modified by metal or non-metal doping. The transition metal doping into semiconductor have been of great interest to the researchers. The dopant may replace the Ti^{+4} ions in the lattice or may be present in the interstitial site. Doping introduce localized states in the bandgap and can shift the absorption region of TiO_2 from UV to visible region.[43] Doping introduces the energy states close to either valence band or conduction band edges. This results in electrons or holes occupying energy states shown in the Figure 1.9. The p-type semiconductor introduces vacant states, or holes, close to the upper edge of the valence band and promoting easier transition of electrons. So the holes are the carriers in p-type semiconductors. The n-type semiconductors introduce electron states close to its conduction band where the carriers are electrons.

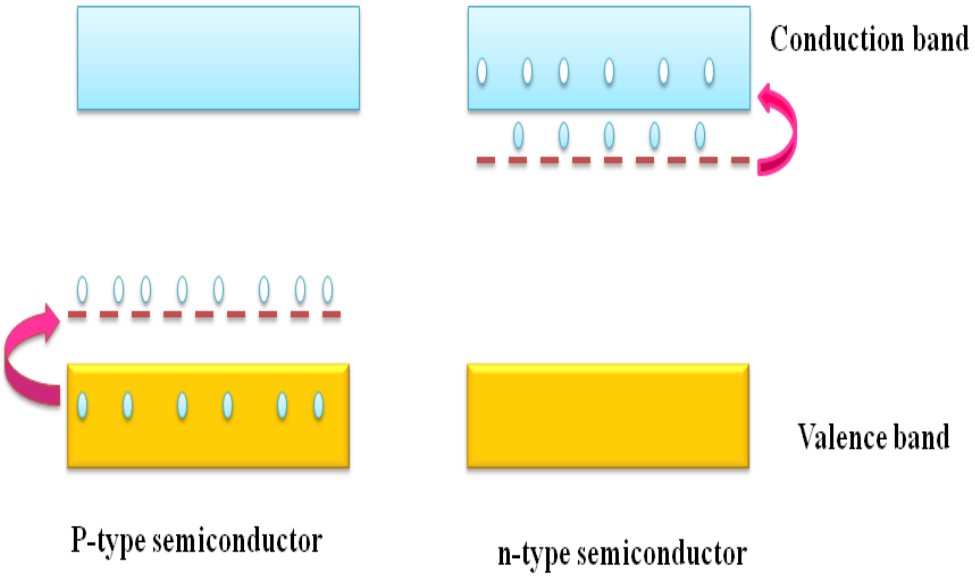

Fig. 1.9 p-type and n-type semiconductor

Photogenerated electrons on the surface of the semiconductor react with electron acceptors (represented by A) in reduction reactions and holes with electron donors (represented by D) in oxidation reactions, adsorbed on the surface. Hence photocatalytic activity is improved. These processes are represented in the Figure 1.10.

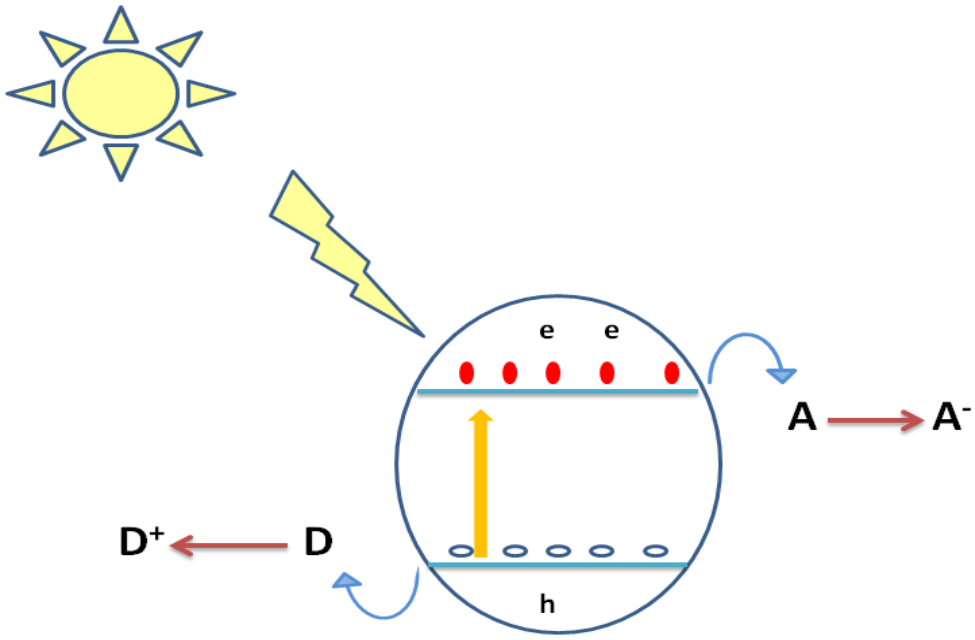

Fig. 1.10 Photoexcitation and transfer of electron and holes and surface transfer of charge carriers in semiconductor.

1.9 ZnO

The nano ZnO structures are attractive due to their multifunctional applications in photocatalysis, solar cells, piezophototronics, piezotronics, sensors, energy storage devices etc.[44-47] It is n-type semiconductor having the bandgap energy of 3.35 eV.[48,49] Hence ZnO is a important alternative for TiO_2 in photocatalysis.

ZnO has three different phases: wurtzite, zinc blende and rock salt. Usually ZnO crystals exist in the rocksalt and wurtzite phases. The wurtzite phase is most stable under ordinary conditions. It has been reported that the zinc blende phase of ZnO is metastable. The crystal structure of wurtzite and zinc blend are shown in the Figure 1.11. The Zn and O atoms are represented by orange and blue spheres, respectively. The atomic arrangement of zinc blende structure is similar to the wurtzite structure. [50] In the hexagonal wurtzite structure, each anion is surrounded by four cations at the corners of a tetrahedron, and vice versa with lattice parameters a = 0.3296 and c = 0.520 65 nm.[50]

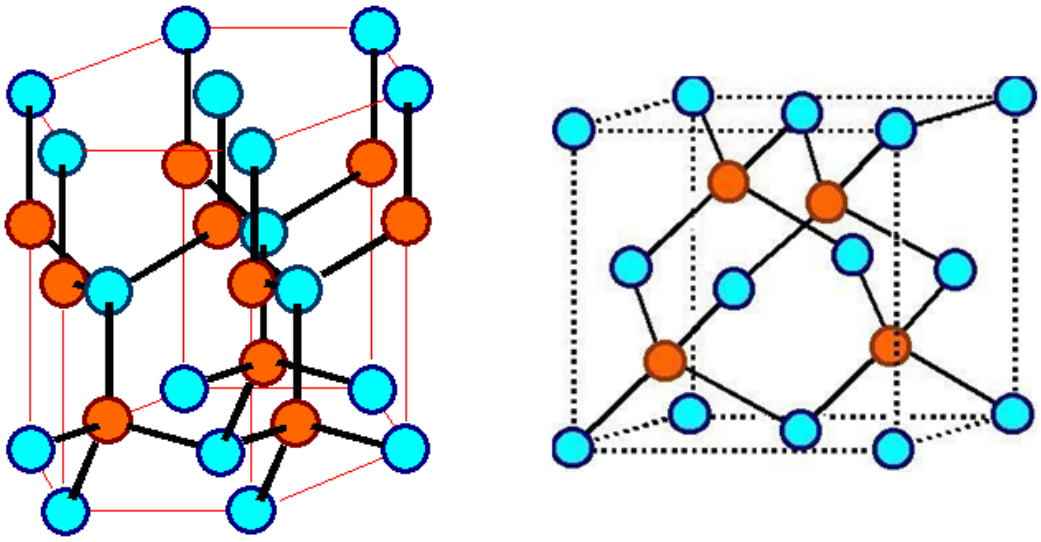

Fig.1.11 A schematic representation of ZnO crystal structures: a) wurtzite and b) zincblende(Adaptedfromhttps://www.tf.unikiel.de/matwis/amat/semitech_en/kap_2/illustr/i2_1_2.html)

ZnO has been proven to be the richest in the verity of morphologies such as sphere, tubes, rods etc.[51] Different methodologies have been reported for the synthesis of ZnO nanostructures and these methodologies are focused on controlling the shape, size and phase composition.[52] A single step process without unwanted impurities is feasible for the cost-effective, large scale preparation of ZnO nanoparticles.[53] Final particle shape depend upon the two important mechanisms (a) (mono)- crystal growth habit and dissolution/recrystallization phenomena or (b) nanoparticles oriented aggregation.[54,55] Only few works have been done to investigate morphological effect on the photocatalysis.[56,57]. Photodegradation mechanism of ZnO has been found to be similar to that of TiO_2.

1.10 Different methods for the preparation of semiconducting metal oxides

There are several synthetic processes being used to produce metal oxide nano structures including sol-gel, hydrothermal, solvothermal, chemical vapour deposition (CVD), thermal decomposition, precipitation method, etc.[58]

1.10.1 Sol gel method

The sol-gel method is a versatile process for synthesizing metal oxides. In this method, usually an inorganic metal salt or metal organic compounds such as metal alkoxides are used as precursors. When the precursor reacts with water, both hydrolysis and condensation occur by nucleophilic substitution reaction followed by removal of either alcohol or water and a colloidal suspension or a sol is gradually formed by the polymerization reaction. Sol gradually transforms to gel. The gel on drying and sintering yields nanomaterials.

Sol-gel process have been used to fabricate thin film coatings, ultra fine or spherical shaped powders, microporous inorganic membranes and extremely porous aerogel materials through sol-gel process.[59] Figure 1.12 shows the overview of sol-gel method and its applications. This method has several advantages such as homogeneity of the product with high purity. It is very simple, fast and cheap method. Low processing temperature is the main advantages of this method. Sol-gel method has some limitations; the chemicals used for the process

are very expensive. Also during drying, there is a lot of volume shrinkage and cracking.[60]

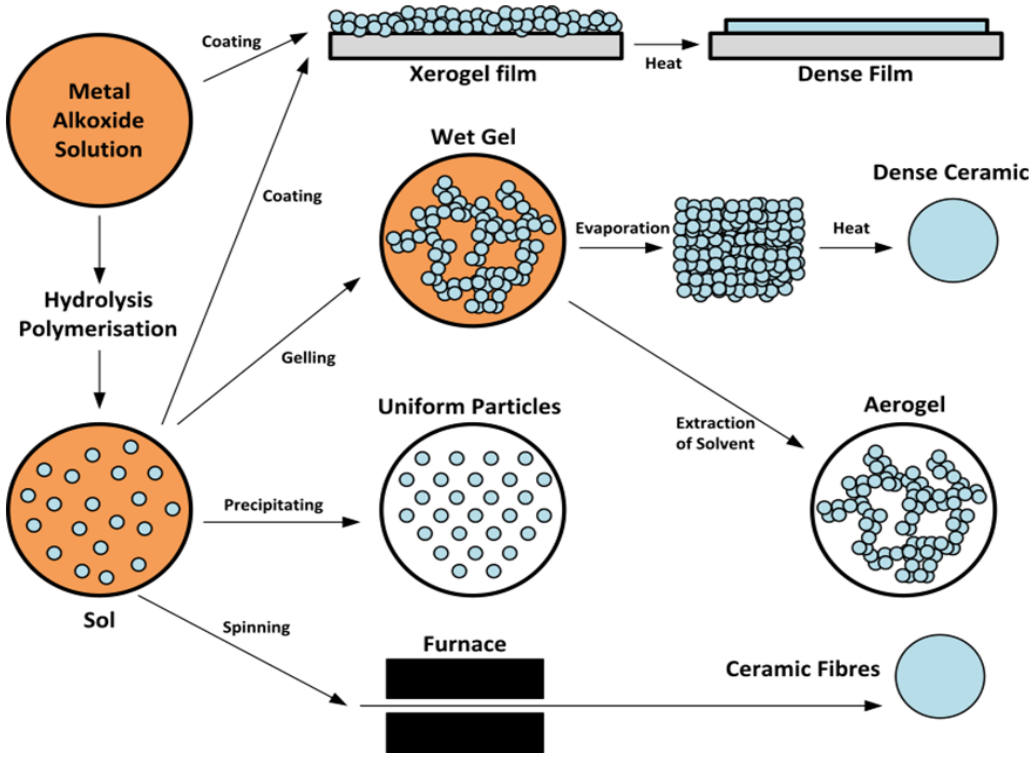

Fig.1.12 A schematic representation of ZnO crystal structures: (adapted fromhttps://en.wikipedia.org/wiki/Sol%E2%80%93gel_process#/media/File:SolGelTechnologyStages.svg)

1.10.2 Hydrothermal method

The hydrothermal synthesis is widely used for the preparation of nanostructural materials. An aqueous mixture of precursors is heated in an autoclave. The synergistic effect of temperature and pressure provides a one-step process to synthesis highly crystalline material without annealing.

This method has been used to prepare nanoparticle with homogeneity, high purity, crystal symmetry and unique properties. The solubility of the precursor can be increased due to high temperature and pressure. Intermediate, metastable state or specific phase may be easily formed. This method has some limitation; it needs expensive autoclaves and safety measures during the reaction process.

1.10.3 Solvothermal method

The solvothermal method is similar to hydrothermal method and in this method aqueous and non-aqueous solvent mixtures can be used. The temperature and pressure can be higher than hydrothermal method. This method also has been used for the synthesis of wide variety of nanoparticles with controlled size distribution and shape.

1.10.4 Chemical vapour deposition (CVD)

Chemical vapour deposition (CVD) is widely applied for depositing high-purity, high-performance thin solid film and coatings on a heated substrate through chemical reaction of gas phase precursors.[61] This method does not require high-vacuum working environments. It makes this method a popular technology for electronics, optoelectronics and biomedical application. This method can be used for different variety of coating materials based on metals, alloys and ceramics. The coating with very low porosity levels can be achieved.

Higher temperature requirement is the main limitation of this method and it is difficult to scale up. The CVD method is rather complicated and any change of reaction conditions may influence the final morphology. Solvents such as methanol, ethanol, hexane, dichloromethane and isopropanol are used for this method.

1.10.5 Thermal decomposition

Thermal decomposition process is defined as a chemical process in which metal precursor is heated above its decomposition temperature.[62] Usually metal alkoxides are used as precursors for the synthesis of metal oxides. Pure and doped metal nanomaterials can be easily synthesized by this method and the properties of nanomaterial depend upon the concentration of the precursor. The major drawbacks of this method are high cost and low yield. The morphology of the synthesized nanomaterials is very difficult to control using this method.

1.11 Objectives of the present work

- The synthesis of TiO_2 and ZnO nanopowders having different morphology by reflux method, simple precipitation method and sol-gel method, using simple precursors.
- Characterisation of metal oxides using different analytical techniques like TG, XRD, TEM, FESEM-EDS, FTIR, BET surface area, UV-Visible spectroscopy etc.
- Doping of TiO_2 and ZnO with various transition metals and non-metals for the efficient visible light photocatalysis.
- Systematic study of effect of doping on the phase composition of anatase and rutile mixed phase TiO_2.
- To measure the photocatalytic activity of ZnO and TiO_2 nanopowders by studying the degradation of methylene blue dye under sunlight/white light LED irradiation.

1.12 Overview of the thesis

Chapter 1 gives an overview of semiconductors, different methods of synthesis and their applications. Individual chapters cover the experimental methods, results and discussions. Chapter 2 describes various instrumental techniques used for the characterization of nanomaterials. In chapter 3, synthesis of mixed phase anatase and rutile TiO_2 and doped TiO_2 and photocatalytic activity of the samples under visible LED light irradiation are given. In chapter 4, preparation of anatase TiO_2 and 1 mol % Co-doped TiO_2 and their photocatalytic application are given. In chapter 5, preparation of ZnO via different methods and comparison of their photoactivity with TiO_2 under visible LED light irradiation are discussed. Chapter 6 describes summary and conclusion of the present studies. The recommendations for future work are given in chapter 7.

References

1. Omer, A. M. (2008). Energy, environment and sustainable development. *Renewable and sustainable energy reviews*, *12*(9), 2265-2300.

2. Hanaki, K., & Portugal-Pereira, J. (2018). The effect of biofuel production on greenhouse gas emission reductions. *Biofuels and sustainability* ,53-71. Springer, Tokyo.

3. Owusu, P. A., & Asumadu-Sarkodie, S. (2016). A review of renewable energy sources, sustainability issues and climate change mitigation. *Cogent Engineering*, *3*(1), 1167990.

4. Scanlon, D. O., Dunnill, C. W., Buckeridge, J., Shevlin, S. A., Logsdail, A. J., Woodley, S. M., & Watson, G. W. (2013). Band alignment of rutile and anatase TiO_2. *Nature materials*, *12*(9), 798-801.

5. Yadav, R. K., Lee, J. O., Kumar, A., Park, N. J., Yadav, D., Kim, J. Y., & Baeg, J. O. (2018). Highly Improved Solar Energy Harvesting for Fuel Production from CO_2 by a Newly Designed Graphene Film Photocatalyst. *Scientific reports*, *8*(1), 1-10.

6. Taguchi, M., Suzuki, A., Ueoka, N., & Oku, T. (2019). Effects of poly(methyl methacrylate) addition to perovskite photovoltaic devices. *AIP Conference Proceedings*, *2067*.

7. Anas, S., Mahesh, K. V., Ambily, K. J., Chandran, M. R., Uma, K., Warrier, K. G. K., & Ananthakumar, S. (2012). New insights on physico-chemical transformations of ZnO: From clustered multipods to single crystalline nanoplates. *Materials Chemistry and Physics*, *134*(1), 435-442.

8. https://www.semi.org/en/macroeconomics-450mm-wafers.

9. Tripathi, G., Srivastava, D. K., Singh, J., & Mishra, V. (2020). Advancement and modification in photoreactor used for degradation processes. In *Nano-Materials as Photocatalysts for Degradation of Environmental Pollutants* 305-321. Elsevier.

10. Mahajan, J., & Jeevanandam, P. (2018). Synthesis of TiO_2@ α-Fe_2O_3 core–shell heteronanostructures by thermal decomposition approach and their application towards sunlight-driven photodegradation of rhodamine B. *New Journal of Chemistry*, *42*(4), 2616-2626.

11. Maji, S. K., & Jana, A. (2017). Two-dimensional nanohybrid (RGS@ AuNPs) as an effective catalyst for the reduction of 4-nitrophenol and photo-degradation of methylene blue dye. *New Journal of Chemistry*, *41*(9), 3326-3332.

12. Ahmed, S., Rasul, M. G., Martens, W. N., Brown, R., & Hashib, M. A. (2010). Heterogeneous photocatalytic degradation of phenols in wastewater: a review on current status and developments. Desalination, 261(1-2), 3-18.

13. Lu, G., Linsebigler, A., & Yates Jr, J. T. (1995). Photooxidation of CH_3Cl on TiO_2 (110): a mechanism not involving H_2O. *The Journal of Physical Chemistry*, *99*(19), 7626-7631.

14. Ohuchi, T., Miyatake, T., Hitomi, Y., & Tanaka, T. (2007). Liquid phase photooxidation of alcohol over niobium oxide without solvents. *Catalysis today*, *120*(2), 233-239.

15. Imoberdorf, G. E., Irazoqui, H. A., Cassano, A. E., & Alfano, O. M. (2005). Photocatalytic degradation of tetrachloroethylene in gas phase on TiO_2 films: A kinetic study. *Industrial & engineering chemistry research*, *44*(16), 6075-6085.

16. Yu, J., Zhang, L., Cheng, B., & Su, Y. (2007). Hydrothermal preparation and photocatalytic activity of hierarchically sponge-like macro-/mesoporous titania. *The Journal of Physical Chemistry C*, *111*(28), 10582-10589.

17. Yu, J., Qi, L., & Jaroniec, M. (2010). Hydrogen production by photocatalytic water splitting over Pt/TiO_2 nanosheets with exposed (001) facets. *The Journal of Physical Chemistry C*, *114*(30), 13118-13125.

18. Akira Fujishima; Tata N. Rao; Donald A. Tryk (2000). Titanium dioxide photocatalysis. *Journal of Photochemistry and Photobiology C: Photochemistry Reviews,* 1(1), 1–21.

19. Li, A., Wang, Z., Yin, H., Wang, S., Yan, P., Huang, B., & Li, C. (2016). Understanding the anatase–rutile phase junction in charge separation and transfer in a TiO_2 electrode for photoelectrochemical water splitting. *Chemical science*, *7*(9), 6076-6082.

20. Tseng, L. T., Luo, X., Bao, N., Ding, J., Li, S., & Yi, J. (2016). Structures and properties of transition-metal-doped TiO_2 nanorods. *Materials Letters*, *170*, 142-146.

21. Xu, D., Li, J., Yu, Y., & Li, J. (2012). From titanates to TiO_2 nanostructures: controllable synthesis, growth mechanism, and applications. *Science China Chemistry*, *55*(11), 2334-2345.

22. Kumar, S. G., & Devi, L. G. (2011). Review on modified TiO_2 photocatalysis under UV/visible light: selected results and related mechanisms on interfacial charge carrier transfer dynamics. *The Journal of physical chemistry A*, *115*(46), 13211-13241.

23. Yin, S., Zhang, Q., Saito, F., & Sato, T. (2003). Preparation of visible light-activated titania photocatalyst by mechanochemical method. *Chemistry Letters*, *32*(4), 358-359.

24. Yamabi, S., & Imai, H. (2002). Crystal phase control for titanium dioxide films by direct deposition in aqueous solutions. *Chemistry of materials*, *14*(2), 609-614.

25. Chanda, A., Rout, K., Vasundhara, M., Joshi, S. R., & Singh, J. (2018). Structural and magnetic study of undoped and cobalt doped TiO_2 nanoparticles. *RSC advances*, 8(20), 10939-10947.

26. Xie, W., Li, R., & Xu, Q. (2018). Enhanced photocatalytic activity of Se-doped TiO_2 under visible light irradiation. *Scientific reports*, *8*(1), 1-10.

27. Barakat, M. A., Hayes, G., & Shah, S. I. (2005). Effect of cobalt doping on the phase transformation of TiO_2 nanoparticles. *Journal of nanoscience and nanotechnology*, *5*(5), 759-765.

28. Lacerda, A. M. (2015). Modified TiO_2 Photocatalysts for the Degradation of Organic Pollutants and H_2 generation via Solar Energy Conversion (Doctoral dissertation, Queen Mary University of London).

29. Kerrami, A., Mahtout, L., Bensouici, F., Bououdina, M., Rabhi, S., Sakher, E., & Belkacemi, H. (2019). Synergistic effect of Rutile-Anatase Fe-doped TiO_2 as efficient nanocatalyst for the degradation of Azucryl Red. *Materials Research Express*, *6*(8), 0850f5.

30. Smith, A. M., & Nie, S. (2010). Semiconductor nanocrystals: Structure, properties, and band gap engineering. *Accounts of Chemical Research*, *43*(2), 190–200.

31. Hanaor, D. A., & Sorrell, C. C. (2011). Review of the anatase to rutile phase transformation. *Journal of Materials science*, *46*(4), 855-874.

32. Li, Y. F., & Liu, Z. P. (2011). Particle size, shape and activity for photocatalysis on titania anatase nanoparticles in aqueous surroundings. *Journal of the American Chemical Society*, *133*(39), 15743-15752.

33. Reghunath, S., Pinheiro, D., & KR, S. D. (2021). A review of hierarchical nanostructures of TiO_2: Advances and applications. *Applied Surface Science Advances*, *3*, 100063.

34. Hurum, D. C., Agrios, A. G., Gray, K. A., Rajh, T., & Thurnauer, M. C. (2003). Explaining the enhanced photocatalytic activity of Degussa P25 mixed-phase TiO_2 using EPR. *The Journal of Physical Chemistry B*, *107*(19), 4545-4549.

35. Yin, S., Zhang, Q., Saito, F., & Sato, T. (2003). Preparation of visible light-activated titania photocatalyst by mechanochemical method. *Chemistry Letters*, *32*(4), 358-359.

36. Luttrell, T., Halpegamage, S., Tao, J., Kramer, A., Sutter, E., & Batzill, M. (2014). Why is anatase a better photocatalyst than rutile?-Model studies on epitaxial TiO_2 films. *Scientific reports*, *4*(1), 1-8.

37. Zhang, J., Zhou, P., Liu, J., & Yu, J. (2014). New understanding of the difference of photocatalytic activity among anatase, rutile and brookite TiO_2. *Physical Chemistry Chemical Physics*, *16*(38), 20382-20386.

38. Weber, A. S., Grady, A. M., & Koodali, R. T. (2012). Lanthanide modified semiconductor photocatalysts. *Catalysis Science & Technology*, *2*(4), 683-693.

39. Weber, A. S., Grady, A. M., & Koodali, R. T. (2012). Lanthanide modified semiconductor photocatalysts. *Catalysis Science & Technology*, *2*(4), 683-693.

40. Luo, Z., Poyraz, A. S., Kuo, C. H., Miao, R., Meng, Y., Chen, S. Y., Jiang, T., Wenos, C. & Suib, S. L. (2015). Crystalline mixed phase (anatase/rutile) mesoporous titanium dioxides for visible light photocatalytic activity. *Chemistry of Materials*, *27*(1), 6-17.

41. Liu, G., Wang, L., Yang, H. G., Cheng, H. M., & Lu, G. Q. M. (2010). Titania-based photocatalysts—crystal growth, doping and heterostructuring. *Journal of Materials Chemistry*, *20*(5), 831-843.

42. Liu, G., Zhao, Y., Sun, C., Li, F., Lu, G. Q., & Cheng, H. M. (2008). Synergistic effects of B/N doping on the visible-light photocatalytic activity of mesoporous TiO_2. *Angewandte Chemie International Edition*, *47*(24), 4516-4520.

43. Chen, D., Wang, Z., Ren, T., Ding, H., Yao, W., Zong, R., & Zhu, Y. (2014). Influence of defects on the photocatalytic activity of ZnO. *The Journal of Physical Chemistry C*, *118*(28), 15300-15307.

44. Anas, S., Mangalaraja, R. V., Poothayal, M., Shukla, S. K., & Ananthakumar, S. (2007). Direct synthesis of varistor-grade doped nanocrystalline ZnO and its densification through a step-sintering technique. *Acta Materialia*, *55*(17), 5792-5801.

45. Palumbo, M., Lutz, T., Giusca, C. E., Shiozawa, H., Stolojan, V., Cox, D. C., Wilson, R. M., Henley, S. J., & Silva, S. R. P. (2009). From stems (and stars) to roses: shape-controlled synthesis of zinc oxide crystals. *Crystal Growth and Design*, *9*(8), 3432-3437.

46. Öner, M., Norwig, J., Meyer, W. H., & Wegner, G. (1998). Control of ZnO crystallization by a PEO-b-PMAA diblock copolymer. *Chemistry of materials*, *10*(2), 460-463.

47. Mclaren, A., Valdes-Solis, T., Li, G., & Tsang, S. C. (2009). Shape and size effects of ZnO nanocrystals on photocatalytic activity. *Journal of the American Chemical Society*, *131*(35), 12540-12541.

48. Ashrafi, A. B. M. A., & Jagadish, C. (2007). Review of zincblende ZnO: Stability of metastable ZnO phases. *Journal of Applied Physics*, *102*(7), 4.

49. Özgür, Ü., Alivov, Y. I., Liu, C., Teke, A., Reshchikov, M., Doğan, S., Avrutin, V., Cho, S.J., & Morkoç, A. H. (2005). A comprehensive review of ZnO materials and devices. *Journal of applied physics*, *98*(4), 11.

50. Pal, U., & Santiago, P. (2005). Controlling the morphology of ZnO nanostructures in a low-temperature hydrothermal process. *The Journal of Physical Chemistry B*, *109*(32), 15317-15321.

51. Yin, S., & Sato, T. (2005). Mild solution synthesis of zinc oxide films with superhydrophobicity and superhydrophilicity. *Journal of Materials Chemistry*, *15*(43), 4584-4587.

52. Ghorbani, H. R., Mehr, F. P., Pazoki, H., & Rahmani, B. M. (2015). Synthesis of ZnO nanoparticles by precipitation method. *Oriental Journal of Chemistry*, *31*(2), 1219-1221.

53. Oliveira, A. P. A., Hochepied, J. F., Grillon, F., & Berger, M. H. (2003). Controlled precipitation of zinc oxide particles at room temperature. *Chemistry of materials*, *15*(16), 3202-3207.

54. Mishra, Y. K., & Adelung, R. (2018). ZnO tetrapod materials for functional applications. *Materials Today*, *21*(6), 631-651.

55. Gowtham, M., Chandrasekar, S., Mohanraj, K., & Kumar, N. S. (2020). Morphology dependent photocatalytic activity of ZnO nanostructures-A short review. NanoNEXT, 1(1), 30-38.

56. Kajbafvala, A., Ghorbani, H., Paravar, A., Samberg, J. P., Kajbafvala, E., & Sadrnezhaad, S. K. (2012). Effects of morphology on photocatalytic performance of Zinc oxide nanostructures synthesized by rapid microwave irradiation methods. *Superlattices and Microstructures*, *51*(4), 512-522.

57. Wang, Y., He, Y., Lai, Q., & Fan, M. (2014). Review of the progress in preparing nano TiO_2: An important environmental engineering material. *Journal of environmental sciences*, *26*(11), 2139-2177.

58. X. Wang, Preparation , synthesis and application of Sol-gel method University Tutor : Pr . Olivia GIANI Internship Tutor : Mme, (2020).

59. Carter, C. B., & Norton, M. G. (2013). Sols, gels, and organic chemistry. In *Ceramic Materials* (pp 411-422). Springer, New York, NY.

60. Sun, L., Yuan, G., Gao, L., Yang, J., Chhowalla, M., (2021). Chemical vapour deposition. *Nat Rev Methods Primers* **1,** 5.

61. Nikam, A. V., Prasad, B. L. V., & Kulkarni, A. A. (2018). Wet chemical synthesis of metal oxide nanoparticles: a review. *CrystEngComm*, *20*(35), 5091-5107.

Chapter 2

Experimental Techniques

Contents

Abstract

Properties and nature of the materials are very important for their application in materials science. The proper selection of experimental techniques is the crucial steps to identity the material for a research problem. Full image of the material helps the researcher to find out the exact field of its application. This chapter describes the characterization techniques used in the present work. Characterisation techniques can be divided into two main types, spectroscopic and microscopic methods. Vibrational frequencies from IR and Raman spectroscopic methods helps to understand molecular structure and composition. Electron microscopy is the simplest characterization technique for analysing the morphology of solid materials.

2.1 Thermogravimetry (TGA)

Thermogravimetry is a thermal analytical technique in which the mass of the sample is continuously measured against time or temperature when it is heated at a constant linear rate in a specified atmosphere. The thermogram is a plot of mass change against temperature. It provides information about phase transition, thermal decomposition, thermal stability, dehydration, oxidation adsorption and desorption of the material studied.[1] In this work the thermal stability of the prepared samples were analysed by heating the sample from 40 to 730 ˚C at a heating rate of 20 ˚C/min in a thermo gravimetric analyzer (Perkin Elmer STA 6000). Pictorial representation of thermogravimetrical analyser is shown in the Figure 2.1.

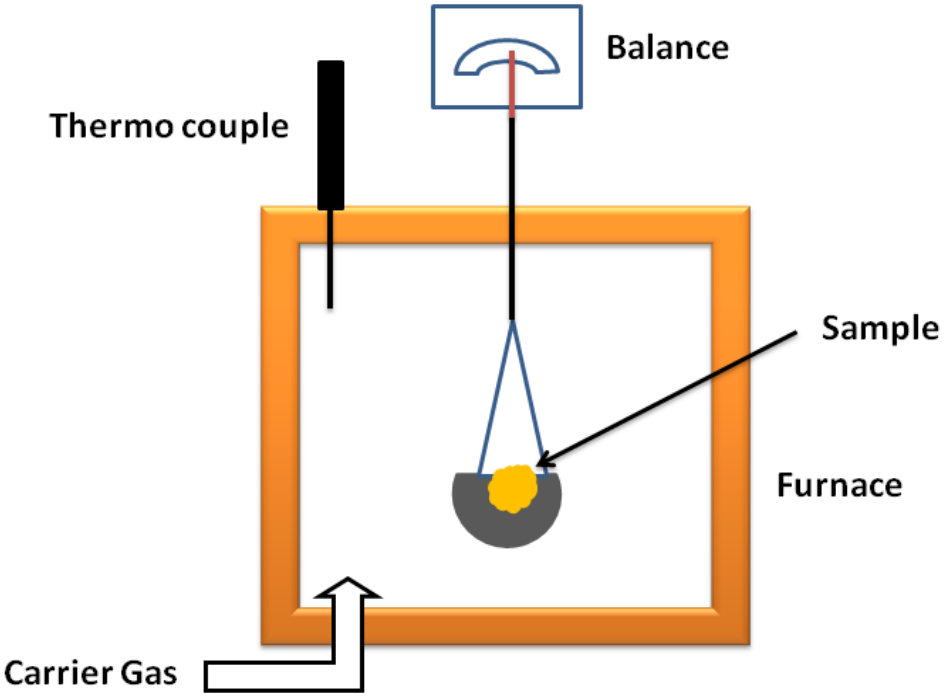

Fig. 2.1 Pictorial representation of Thermogravimetric Analyser

Thermogravimetric analysis was performed in the presence of oxygen or inert gas mixture. The sample is placed in a thermal microbalance during the TG analysis and heated at a predetermined rate. Changes in the mass of the sample that occur in a variety of ways are recorded using microbalance.

Derivative thermogravimetric curve (DTG) enhances the steps in the thermogravimetric curve and the temperatures at which sudden mass change occur are represented by peaks.[2] This is the plot of the rate of mass change with time (dm/dt).

Some instrument also records the temperature difference between the sample and the reference and is known as DTA. Differential thermal analysis (DTA) is based on the difference in temperature between the sample and reference material against time as the sample and reference are heated or cooled at a uniform rate.

2.2 X-ray diffraction (XRD)

X-ray diffraction technique is used for the characterization of crystalline materials. X-ray powder diffraction technique was invented by William Lawrence

Bragg and Willium Hentry Bragg in 1913. The crystalline structure determination at the atomic level was made possible with this invention. The atoms of a crystal are arranged in a regular, ordered manner with uniform spacing. The wavelength of X-rays is approximately equal to the interatomic distance in crystals. Hence crystal planes can diffract X-rays. The atomic planes act on the X-rays in the same manner as a uniformly ruled grating on a beam of light. As the X-ray beam interact with these atoms, a part of the X-ray beam is transmitted, some are absorbed, refracted, scattered and one part is diffracted. Scattering rays from atoms leads to the diffraction effect. Hence the diffracted beam is composed of scattered rays. These diffracted X-rays are then detected and intensity values (y axis) are plotted against the diffraction angle 2θ (x axis). From the θ values the d-spacing is calculated by the Bragg's law given below.[3]

$$\mathbf{n\lambda = 2d \sin\theta} \qquad (5)$$

where λ is the wavelength of the X-ray, θ is the angle of diffraction from the lattice plane, d is the inter planar distance and n is the order. The Bragg's diffraction from various planes of crystalline material is shown in Figure 2.2.

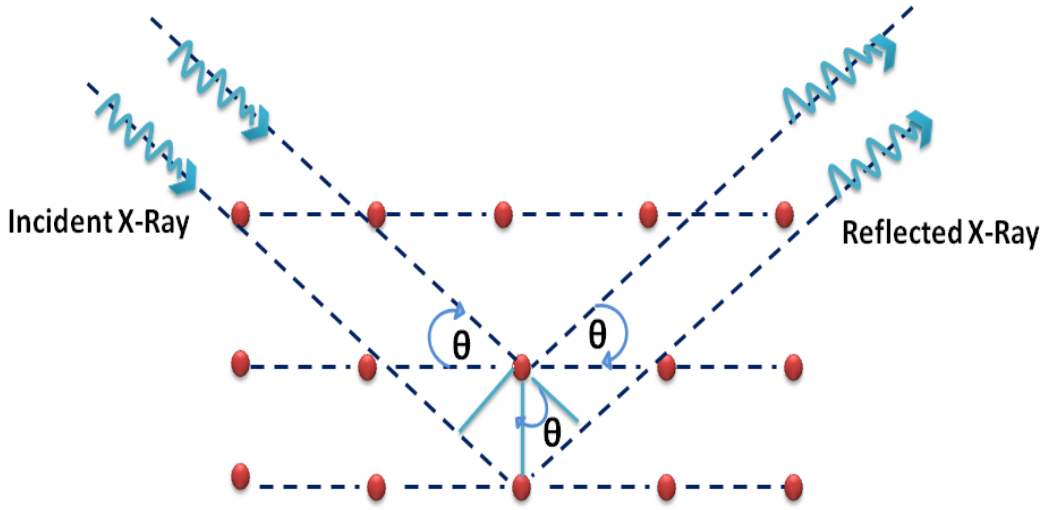

Fig. 2.2 Bragg diffraction of X-rays from a set of crystal planes

The XRD spectrum provides the information of crystalline structures, phases, average grain size and crystallinity. The XRD pattern of a pure material is like a fingerprint of the material. The analysis was carried out using a Bruker X-ray diffractometer with a step size of 0.02˚ (2θ). Cu Kα radiation (λ =1.5406 Å, 40kV, 35 mA) was used as an

X-ray source. Samples were scanned in diffraction angle range of 20-80˚. The spectra were compared with the data from the Joint Committee Powder Diffraction Standards (JCPDS). The position of peaks was used to identify the crystal planes and crystal phases. The XRD also provide the information on unit cell dimensions.

2.3 Raman spectroscopy

Raman spectroscopy is another scattering technique in which a laser source usually in the UV-Visible and near infrared range are used for excitation.[4] It is a powerful characterisation tool for studying the vibrational modes of a molecule.[5] Raman spectroscopy can be performed over a wide range of temperatures and pressures in all three phases (solids, liquids and gases) of matter. The Raman spectroscopy is complimentary to infrared spectroscopy. The physical phenomenon involved in both the techniques is entirely different. Infrared spectroscopy is based on absorption of photons. Raman spectroscopy is based on inelastic scattering of incident monochromatic light from laser through its interaction with molecule.[6]

When a monochromatic radiation having frequency 'ν_0' is incident on a non-absorbing medium, most of the radiation is often transmitted without any change, and some of it is scattered. The scattered radiation split up into three components. When the frequency of incident light is same as that of emitted light, the process is referred to as Rayleigh scattering. A few photons undergo Raman scattering, losing its energy through exciting vibrational modes of the sample and resulting in the energy of the laser photons being shifted up or down than the incident radiation. When the frequency of emitted radiation is higher than the incident radiation, it is called as anti stokes shift ($\nu_0 + \nu_m$). If the frequency of emitted radiation is lower than that of incident radiation, stock Raman shift ($\nu_0 - \nu_m$) occurs.

In quantum interpretation, the scattering results from the incident photon exciting the molecule into a virtual energy state. The molecule subsequently undergos transition to lower energy state by emitting radiation. If the molecule comes back to the original state results in Rayleigh scattering. If the molecules comes to higher energy state it is called Stock Raman scattering and are shown in the Figure 2.3. The stokes lines are more intense and monitored for analysis. The Raman shifts are reported in wavenumbers.

Raman spectroscopy is used to study the phase transitions, chemical bonding and intramolecular bonds etc.[5] Spectra provides a fingerprint to identify the structure of a molecules. The Raman spectra were obtained using Bruker's MultiRam Spectrophotometer using 1064 nm excitation.

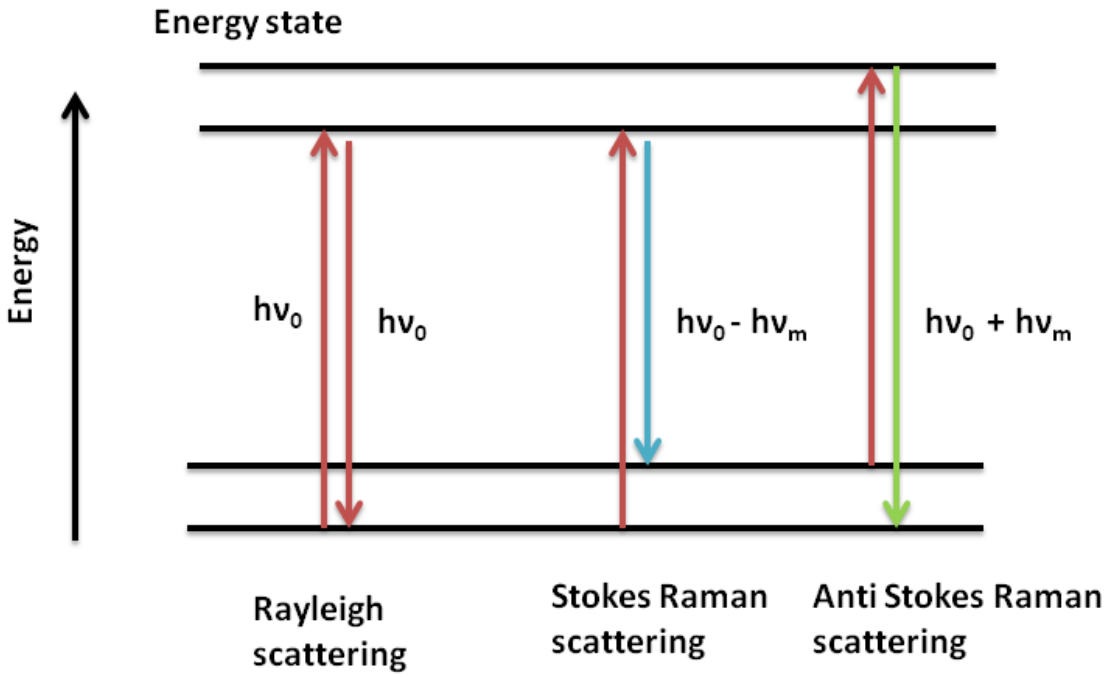

Fig 2.3 Modes of scattering of light in Raman spectra

2.4 Transmission electron microscopy (TEM)

TEM is a microscopic imaging technique in which a beam of electrons are used instead of visible light. It works under the same principle of optical microscopy. The crystalline sample interacts with electron beam by diffraction.[7] When the electrons pass through the material, they are scattered by the electrostatic potential set up by the constituent elements in the specimen. Some of the electrons are absorbed and others are scattered over small angles depending on the composition and structure of the molecule. Scattering of electrons in very distinct direction causes diffraction. The intensity of diffraction depends on how the planes of atoms in a crystal are oriented. It is used for the analysis of structure, size, crystallization, degree of aggregation and morphology. Its resolution power is higher than light microscopes. A few electrons are reflected (backscattered) by the sample and some other electrons can knock electrons from sample which escape as low energy secondary electrons.[8] The

transmitted electrons can be counted by the amount of energy lost in interactions with the sample. An image is formed by the magnification of transmitted electron beam. The path of the electron beam in a transmission electron microscope is shown in the Figure 2.4. X-ray produced by the interaction of the sample is used for determining the elemental composition of the sample.

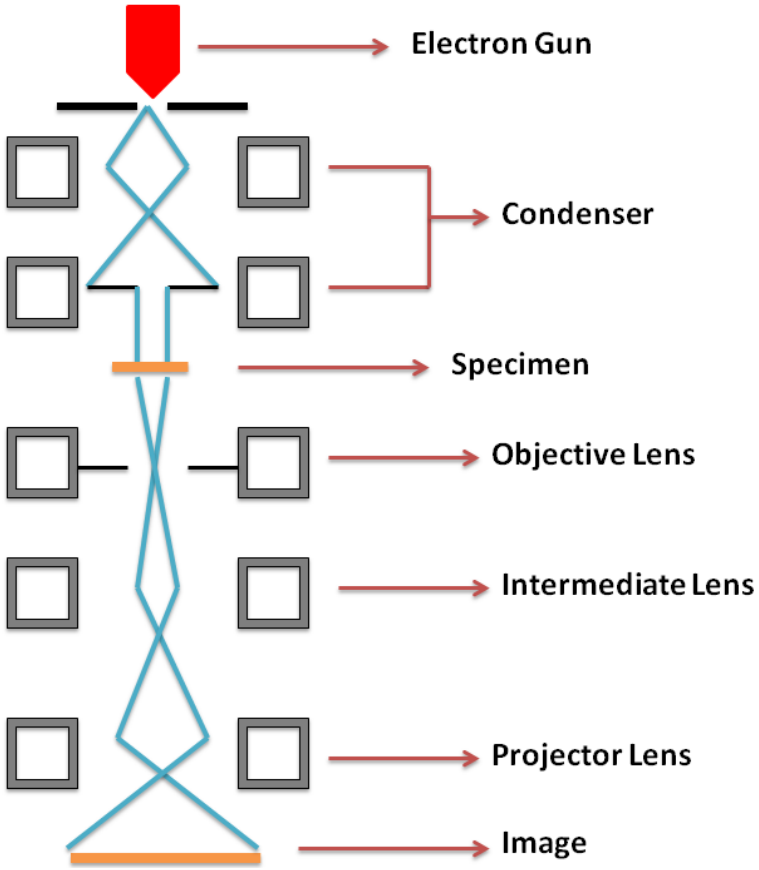

Fig 2.4 Schematic diagram of TEM

High-resolution transmission electron microscopy (HRTEM) is an imaging mode of advanced transmission electron microscopes. It allows direct imaging of the sample's atomic structure. The transmitted electrons interact with the atoms through elastic and inelastic scattering. Electrons undergoing inelastic scattering have a change in energy whereas elastically scattered electrons maintain their initial transmitted energy. Elastically scattered electrons can be useful for the final data interpretation. They leave the sample and move through the lenses of the microscope to form the high-resolution images. Inelastically scattered electrons are not used in this technique. The HRTEM is an efficient tool for studying the properties of

materials on the atomic scale. The TEM images were recorded using High resolution Transmission electron microscope (JEOL/JEM 2100 with voltage of 200kV). The diffraction patterns obtained from a selected area of the specimen is used to determine the lattice parameter and crystal symmetry. This mode of operation is called selected area electron diffraction pattern (SAED).

2.5 Scanning electron microscopy (SEM)

Scanning electron microscope is an electron microscope. It produces sample images by scanning the surface with electron beam in a raster scan pattern and produce secondary electrons, backscattered electrons, and characteristic X-rays.[9] The electron beam is produced by an electron cathode and the columns of electromagnetic lenses.[10] The electron beam finally hits the surface of a sample. Schematic diagram of SEM is shown in the Figure 2.5. Secondary electrons and backscattered electrons are usually used for preparing the SEM images of the samples. The SEM images provides details on the surface topography and morphology. Backscattered electron are used for sample composition. The data are collected over a selected area of the surface of the sample. Approximately 1 cm to 5 microns in width can be imaged in a scanning mode. Its potential for resolution is up to nanometer scale.

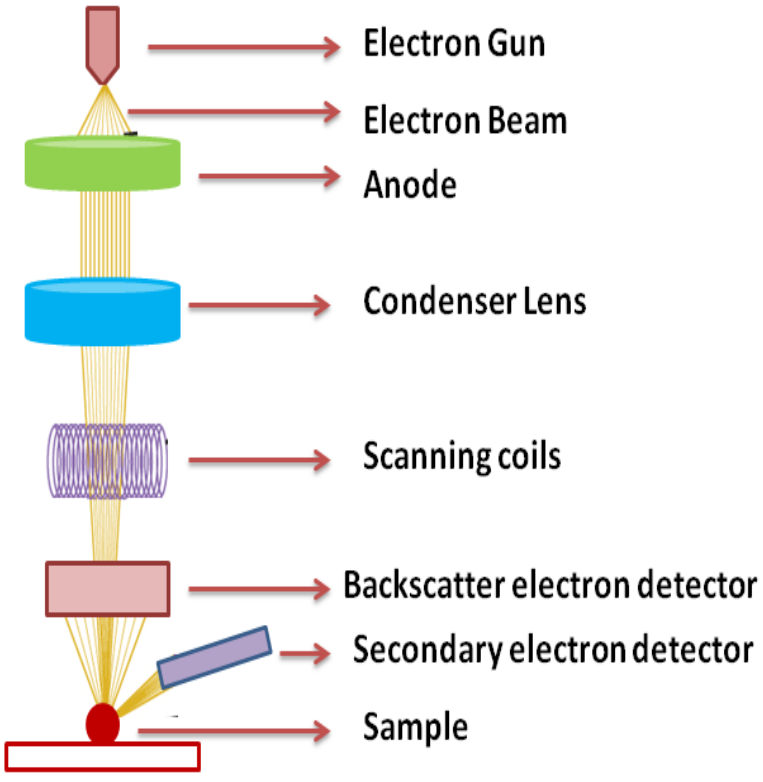

Fig 2.5 Schematic diagram of SEM

The FESEM is an advanced microscope having increased magnification. The Field Emission Scanning Electron Microscope (FESEM) has a much brighter electron source and smaller beam size. It has the ability to observe very fine features at a lower voltage than the conventional SEM. The FESEM images were obtained by using FE-SEM, Zeiss Gemini 300 field emission scanning electron microscopy. The FESEM provides topographical information at magnifications of 10x to 500,000x and produces high-quality, low-voltage, clearer and less electrostatically distorted images with spatial resolution down to1-2 nanometers, which is three to six times better than conventional scanning electron microscopy. The FESEM has the ability to examine smaller-area at electron accelerating voltages compatible with energy dispersive X-ray spectrometry (EDS).

The EDS provides the information about elemental analysis map over a much broader area and chemical composition of materials in few micron spot size. The EDS analysis uses characteristic X-rays generated by the atoms. Basic principle behind EDS spectrum are shown in the Figure 2.6.

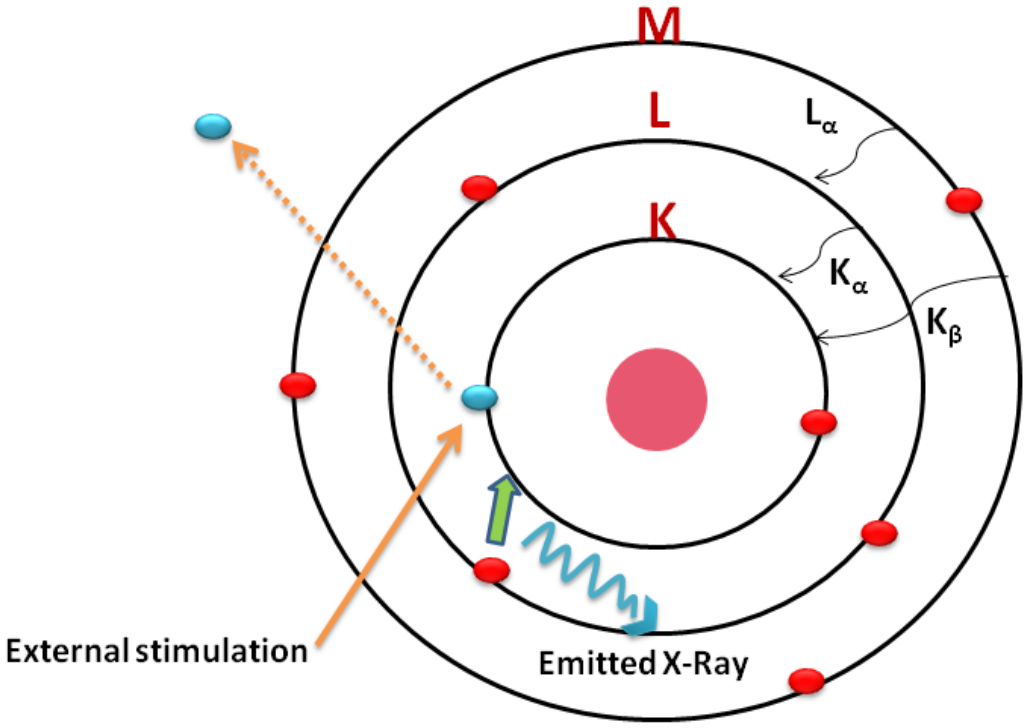

Fig 2.6 Representation of principle behind EDS

Measurement is more efficient for heavier atoms especially for atomic number greater than 30. The main advantages of this technique are high speed data collection, almost all elemental coverage and easy to use. An energy-dispersive detector is used to separate the X-rays of different elements produced by the interaction of electron beam with the sample target. The EDS system software is used to analyze the energy spectrum to determine the presence of specific elements.

2.6 Fourier transform infrared spectroscopy (FT-IR)

Fourier-transform infrared spectroscopy gives the information on the vibrational motions of a molecule which are the characteristic of their functional groups. The sample absorbs IR radiations corresponding to the energy of these vibrations. Most of the molecules having the covalent bond absorb IR radiation. This technique helps for the identification and characterization of organic, inorganic and biological compounds. The molecule must undergo a change in its dipole moment as a function of time to show FT-IR spectrum. The position of the band in the FT-IR spectra helps us to identify the functional group. The intensity of the band is proportional to the concentration of the compound. Hence FT-IR is used for the quantitative estimations. The FT-IR spectra can be used to find out the presence of metal-oxygen bonds in semiconducting materials. In this study FT-IR technique is used for the detection of Ti-O and Zn-O stretching vibrations. The FT-IR spectra were recorded using the Perkin Elmer FT-IR (Model L160000A) spectrophotometer over a range of 4000- 400 cm^{-1}. The measurements were carried out using ATR attachment.

2.7 UV –Visible diffuse reflectance spectra (DRS)

UV-Visible Diffuse Reflectance Spectra is used to study the optical properties of the materials by the interaction of UV-Vis radiation with molecules. The electron is excited from low energy state to a higher electronic state by absorbing UV-Visible radiation from the spectrophotometer. This can be detected in the absorbance spectrum. The qantitative analysis using UV-Visible spectroscopy is based on Beer Lambert's law. The law states that the absorbance of a sample is directly proportional to the concentration of the solution and the path length. When the light radiation interacts with sample, it absorbs a certain amount of light and the remaing amount of energy is transmitted, scattered or reflected. The transmitted light is measured by UV-

Visible spectrophotometer using the photodetector. The UV-Visible spectrum is a graphical representation of the amount of light which the sample absorbs or transmits as a function of the wavelength.

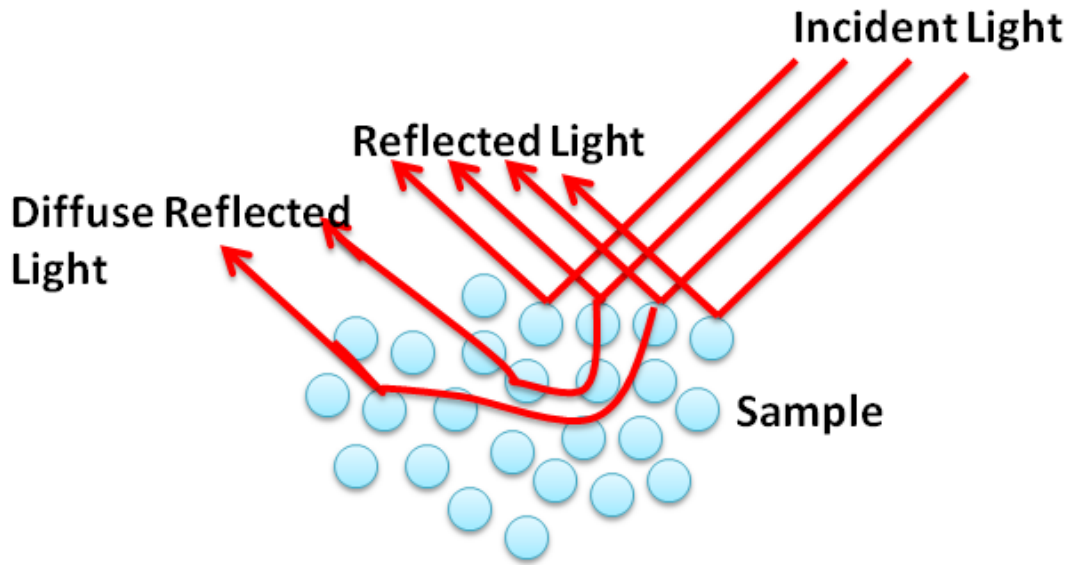

Fig 2.7 Representation of principle behind DRS

The diffuse UV- visible absorption spectra of the prepared samples were recorded on the Perkin Elmer (Lambda 35) spectrophotometer and were scanned in the wavelength range 200-800 nm. The Diffuse reflectance spectra of the sample was recorded on the same instrument equipped with an integrating sphere. $BaSO_4$ disk was used as reference. One part of the incident beam is scattering inside the sample and return to the surface of the sample, which is referred to as diffuse reflection, as shown in the Figure 2.7. Diffuse reflectance spectroscopy is used to find out the absorption edges of the sample. From the band edge the band gap was calculated using the equation $E = hc/\lambda$.

2.8 X-ray photoelectron spectroscopy (XPS)

XPS is a surface-sensitive quantitative spectroscopic technique based on the photoelectric effect (X-ray hitting atom generate photoelectron). It is also known as Electron spectroscopy for chemical analysis (ESCA). In this technique the sample is illuminated with monochromatic X-rays (soft X-ray beam is used as the stimulant). It induces the photoemission of the core level electrons, whose binding energies are characteristic of the present elements. Figure 2.8 represents the principle of XPS.

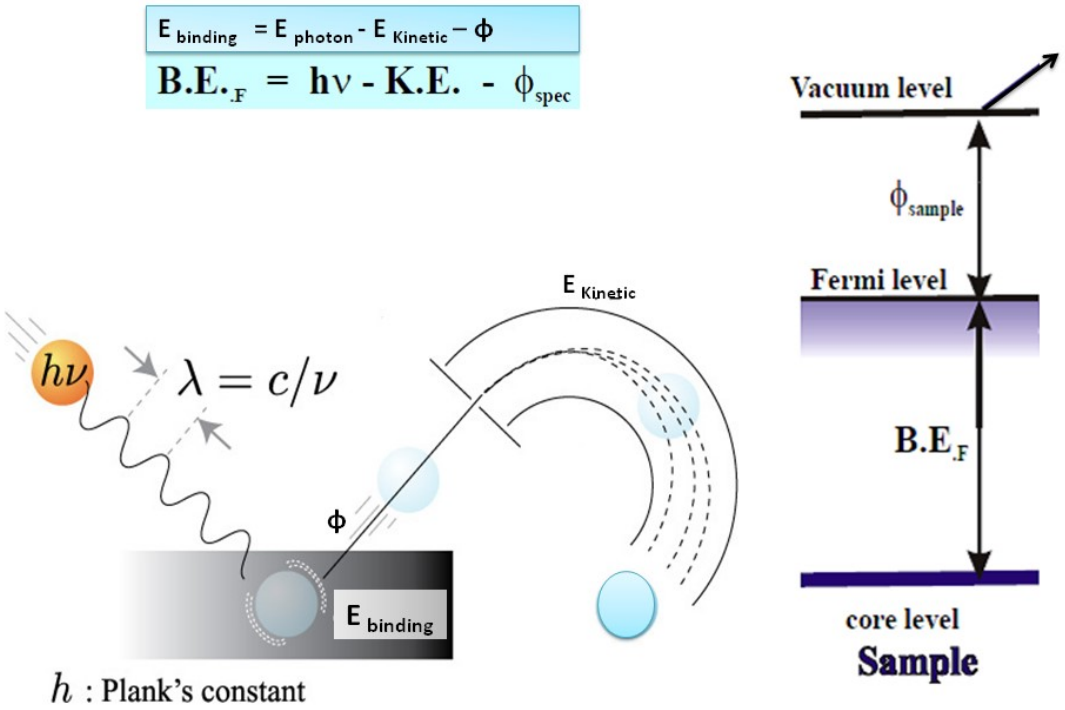

Fig 2.8 Representation of principle behind XPS

Binding energy also represents the chemical state as well as element of atom. The kinetic energy of the emitted electron is recorded in terms of binding energy. The binding energy **($E_{binding}$)** of the emitted electrons is given by

$$E_{binding} = E_{photon} - E_{Kinetic} - \varphi \qquad (6)$$

where $E_{Kinetic}$ is the kinetic energy of the emitted electron, E_{photon} is the energy of the X-ray photons and φ is the work function. The work function is the minimum energy an individual electron required to escape from the surface. The position of the peaks provides information about the oxidation state. The intensity of the peaks gives quantitative information for all elements except hydrogen. It is also used for determining the elemental composition and empirical formula within the material based on photo electric effect. Hydrogen and helium cannot be detected due to the smaller diameter of the orbital. A number of other peaks are also present along with the main binding energy peaks. Secondary peak is required for the correct interpretation of the element. The X-ray photoelectron spectra (XPS) were collected using Kratos Axis Ultra X-ray Photoelectron Spectroscope (UK). The spectra were

deconvoluted using Casa XPS programme (Casa Software Ltd, UK). The background was simulated using the Shirley function. The peaks were fitted using Gaussian software. All binding energies were referenced to C1s (284.8 eV) for calibration of XPS spectra.

2.9 Fluorescence spectroscopy

The energy levels in the semiconductor are investigated using fluorescence spectroscopy. Semiconductor can be excited by a photon having energy greater than band gap energy. In the excited state, the electron will have higher potential energy and come back to the ground state by emitting energy. This can be detected in the fluorescence spectrum. The intensity of emitted light is directly related to the recombination rates. The Fluorescence spectra were measured using Perkin Elmer Fluorescence spectrometer.

2.10 BET surface area measurement

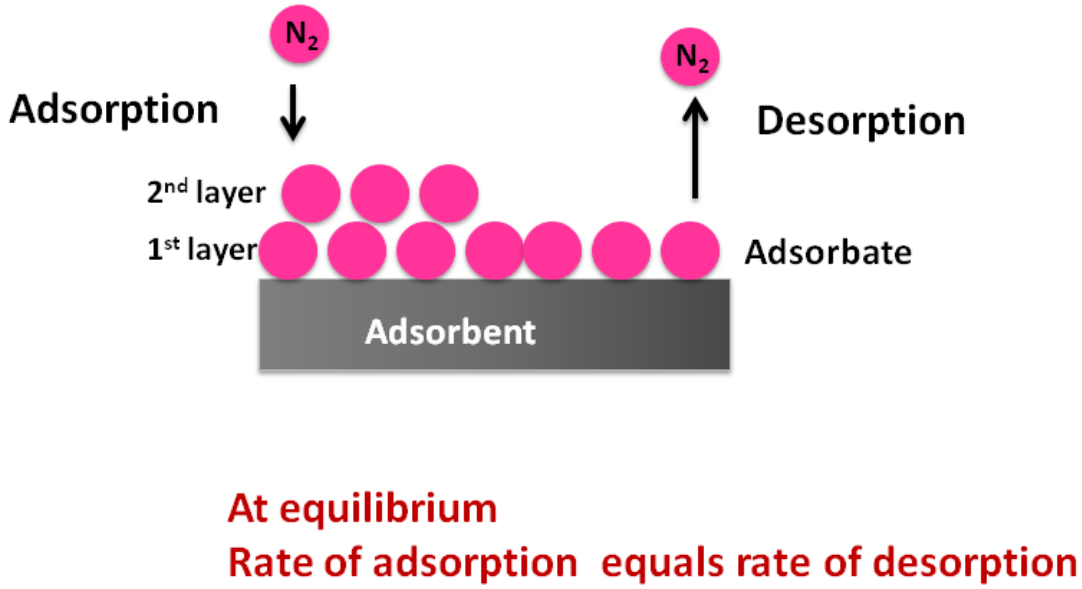

Fig 2.9 Figure Brunauer-Emmett-Teller method for the surface area measurement

The surface area of the prepared samples was calculated by BET method. Surface area determination is very important for heterogeneous catalysis to predict the catalytic activity.[11] The heterogeneous catalytic reaction occurs at the surface. The Brunauer-Emmett-Teller method is used for the determination of the surface area of solid materials.[12] Figure 2.9 is the graphical representation of BET method. This technique

follows the multilayer physical adsorption of gases on solid surfaces using the BET equation 7. Solid surface possesses uniform, localized sites.

$$\mathbf{P/V\ (P_0\text{-}P) = (1/Vm.C) + ((C\text{-}1)/Vm.C)\ P/P_0} \qquad (7)$$

Where V is the volume of gas adsorbed at equilibrium pressure P, V_m is the volume corresponding to the mono layer coverage, P_0 is the standard vapour pressure of the adsorbate at liquid nitrogen temperature, P is the equilibrium pressure of the adsorbate and C is the isothermal constant.

V_m can be determined by plotting P/V (P_0-P) Vs P/P_0. The specific surface area can be calculated from slope of the graph using the relation at liquid nitrogen temperature

$$\mathbf{A = V_M N_0 A_M / M} \qquad (8)$$

where N_0 is the Avogadro number, Am is the molecular cross sectional area of the adsorbate (for nitrogen it is 0.162 nm^2), M is the weight of the adsorbate.

The graphical representation of variation of adsorption with pressure at a given constant temperature is called adsorption isotherm.[13]

The advantage of nitrogen adsorbate is that the area occupied by single adsorbed molecule can be estimated. The total surface area can be calculated from the number of molecules required for forming the monolayer (multiplying the area of one molecule).

In the present study the nitrogen adsorption and desorption isotherms were measured at 77 K (Micromeritics ASAP2010). Before the analysis, the sample was degassed at 150 ˚C for two hours.

References

1. Saadatkhah, N., Carillo Garcia, A., Ackermann, S., Leclerc, P., Latifi, M., Samih, S., Patience, G., S., & Chaouki, J. (2020). Experimental methods in chemical engineering: Thermogravimetric analysis—TGA. *The Canadian Journal of Chemical Engineering*, *98*(1), 34-43.
2. Haines, P. J. (2012). *Thermal methods of analysis: principles, applications and problems*. Springer Science & Business Media.

3. Patel, J. P., & Parsania, P. H. (2018). Characterization, testing, and reinforcing materials of biodegradable composites. In *Biodegradable and biocompatible polymer composites* 55-79. Woodhead Publishing United Kingdom.

4. Rostron, P., Gaber, S., & Gaber, D. (2016). Raman spectroscopy, review. *laser*, *21*, 24.

5. Larkin, P. (2017). *Infrared and Raman spectroscopy: principles and spectral interpretation*. Elsevier.

6. Wei, D., Chen, S., & Liu, Q. (2015). Review of fluorescence suppression techniques in Raman spectroscopy. *Applied Spectroscopy Reviews*, *50*(5), 387-406.

7. Amelinckx, S., Van Dyck, D., Van Landuyt, J., & Van Tendeloo, G. (Eds.). (2008). *Electron microscopy: principles and fundamentals*. John Wiley & Sons.

8. Reimer, L. (2013). *Transmission electron microscopy: physics of image formation and microanalysis* (Vol. 36). Springer.

9. Goldstein, J. I., Newbury, D. E., Michael, J. R., Ritchie, N. W., Scott, J. H. J., & Joy, D. C. (2017). *Scanning electron microscopy and X-ray microanalysis*. Springer.

10. Goldstein, J. (Ed.). (2012). *Practical scanning electron microscopy: electron and ion microprobe analysis*. Springer Science & Business Media.

11. Sheng, T., Jiang, Y. X., Tian, N., Zhou, Z. Y., & Sun, S. G. (2017). Nanocrystal catalysts of high-energy surface and activity. In *Studies in Surface Science and Catalysis* (Vol. 177, pp. 439-475). Elsevier.

12. Brunauer, S., Emmett, P. H., & Teller, E. (1938). Adsorption of Gases in Multimolecular Layers. *Journal of the American Chemical Society, 60(2), 309–319.*

13. Sultan, M., Miyazaki, T., & Koyama, S. (2018). Optimization of adsorption isotherm types for desiccant air-conditioning applications. *Renewable Energy*, *121*, 441-450.

Chapter 3

A simple method for the synthesis of anatase-rutile mixed phase TiO_2 and doped TiO_2 using a convenient precursor and an investigation of photocatalytic activities under visible light

Contents

Abstract

This work reports a novel and simple method for the synthesis of mixed phase TiO_2 (Anatase 70% and Rutile 30%) and Co, Mn, Cu, Ni and C-doped TiO_2. Refluxing aqueous solution of potassium titanyl oxide oxalate lead to direct crystallization of titanium oxalate complex $[Ti_2O_3(H_2O)_2(C_2O_4).3H_2O]$ and this complex on calcination at 450 ˚C for one hour yielded TiO_2 powder. The powder samples were characterized by XRD, Raman spectroscopy, FESEM-EDX, TEM, XPS, FT-IR, UV-Visible spectroscopy and BET techniques. The XRD, TEM and Raman spectra of TiO_2 indicates the coexistence of anatase and rutile phases. The XRD result shows that the primary particle size of anatase crystals is 8.3 nm and that of rutile crystals is 35 nm. From the UV-Visible DRS spectrum, the bandgap of TiO_2 was found to be 3.0 eV. The Co, Mn, Cu, Ni and C-doped TiO_2 (Metal : Ti ratio 1:99) were prepared by adding cobalt nitrate, manganese chloride, copper sulphate, nickel nitrate and ethylene glycol, respectively, to the precursor solution. On Co, Mn, Ni and C-doping, anatase:rutile composition was changed from 70:30 to 84:16, 60: 40, 71:29 and 33:67 respectively. On Cu doping, the TiO_2 obtained was found to consist of only anatase phase. The optical analysis shows the red shift in the doped samples and reduction in the bandgap. The visible light photocatalytic activity of doped TiO_2 samples were found to be better than that of pure TiO_2 due to higher visible light absorption. The highest photocatalytic degradation of methylene blue was obtained with Ni-doped TiO_2 sample.

Chapter 3

3.1 Introduction

Nanoparticles exhibit unique physical, chemical, and biological properties relative to bulk materials due to their large surface area and quantum confinement effect. They have tremendous applications as basic building blocks in the field of nanotechnology for various practical applications. The nanomaterials and their complexes with organic ligands have been widely studied for the degradation of pollutants, catalysis, as antibacterial and antifungal agents, for the extraction of poisonous metal ions, in hydrogen storage etc.[1-7] Various techniques have been reported to prepare nanomaterials in different shapes like nanoflower, nanosquare, nanohexagon, nanowires have been reported by many groups.[8-10]

In recent years, TiO_2 has been explored for diverse applications such as pigments, sensors, photocatalysts, energy storage devices, solar cells etc.[11-16] It is a promising semiconductor material due to its commercial availability, chemical and thermal stability, low cost, non toxicity and ease of handling.[17,18] The TiO_2 belongs to n-type semiconductor. Titania can exist in three crystalline phases, *viz* anatase, rutile and brookite and these phases are having bandgap energy of 3.2 eV (380 nm), 3.0 eV (415 nm) and 3.6 eV (344 nm), respectively.[19] Controlled crystallisation of TiO_2 from solutions is a prerequisite for preparing high quality TiO_2 nanopowder.[20] Rutile phase is difficult to obtain at low temperature and it is usually prepared by calcinations of anatase at higher temperature.[21,22] The high temperature leads to agglomeration and larger particle size.[23,24] Rutile has also higher chemical stability and higher refractive index compared to anatase.[25,26] Zhang and Banfield demonstrated that the rutile is more stable than anatase but the stability reverses when the particle size is less than 14 nm.[27] There are several methods for the preparation of TiO_2. Most of the traditional methods involved corrosive precursors or complicated and expensive equipments. The reflux method is comparatively easy and has potential to fabricate TiO_2 with controlled morphology. It needs simple equipment, environmentally friendly process conditions. This method avoids the use of volatile precursors and release of harmful organic compounds. Commonly used precursors are titanium alkoxides or titanium chloride. But they quickly undergo hydrolysis in air producing HCl gas and titanium hydroxides and may get precipitated in the lungs on inhalation.

Most of the aqueous solution methods so far reported gives only anatase phase TiO_2.[28] There are only a few reports on the synthesis of mixed phase TiO_2 containing both anatase and rutile phases.

Anatase has more photocatalytic activity than rutile and hence most of the previous photocatalytic studies of TiO_2 involved anatase phase. Hence the anatase phase of TiO_2 is mainly used in photocatalytic and photovoltaic devices, and for the degradation of contaminants in water.[29,30] The photoelectrochemical splitting of water by nanocrystalline TiO_2 was first reported by Honda and Fujishima in 1972.[31] This invention paved the way for utilizing the energy of sunlight for generating hydrogen fuel from water splitting and led to an explosion of research activities.[32] The high photocatalytic activity of Degussa Aeroxide® *P25* (80% anatase and 20% rutile) is due to synergistic effect between anatase and rutile phase.[33] The photochemistry of mixed-phase anatase and rutile TiO_2 nanocomposites was studied by Gray, Rajh, and co-workers by using electron paramagnetic resonance (EPR) spectroscopy.[33] They reported that the improved photocatalytic activities of mixed-phase TiO_2 nanocomposites were due to the effective separation of interfacial charge between anatase and rutile, providing high percentage of reactive phase of TiO_2 and inhibiting the electron-hole recombination.[34-37] The transfer of electrons from rutile to a lower energy anatase electron trapping site during the photo excitation in mixed-phase TiO_2 catalysts reduce the recombination rate of anatase. This synergistic effect leads to more efficient electron-hole separation and higher photocatalytic activity. Since sunlight consists of only 5% UV radiation, TiO_2 cannot be used for complete solar energy harvesting.[38,39]

Various methods have been developed to shift the spectral response and the photoactivity of TiO_2 to the visible region such as doping with metal, non-metal and deposition of noble metal.[40,41] Transition metals have partially filled d-orbitals and have been used for doping TiO_2.[42-45] The doping leads to the introduction of new energy levels between valence band and conduction band.[46-49] According to various studies, doping TiO_2 with transition metals like copper or chromium forms new energy level below the conduction band from their partially filled d-orbital. The optical response of the doped TiO_2 can be tuned by varying the metal and amount of ions during doping, which leads to changes in the bandgap.[50,51]

The non-metal dopants also improve the photocatalytic activity in visible region by reducing bandgap energy of TiO_2. On doping with nonmetal elements like C, N and S, new energy level are formed above the valence band.[52] Doping causes a red shift in the bandgap enhancing the visible light harvesting. Carbon has been considered as one of the better dopant among the nonmetal elements. Dong et al. reported the visible light photocatalytic activity of TiO_2 nanomaterials by carbon doping approach.[53] When non-metals are doped into the TiO_2 lattice, oxygen vacancies are often formed. But the photocatalytic efficiency of non-metal-doped titania is still low under visible light.

The photocatalytic performance of TiO_2 is limited by recombination of photo-generated electrons and holes, resulting in a low quantum yield rate. Doping element in TiO_2 may act as trapping sites to prevent charge recombination. Some transition metals, on the other hand, may act as recombination sites. When some transition metals are doped on TiO_2, the band gap energy is reduced, but the photocatalytic activities are not greatly improved. In some cases, the transition metals ions are not incorporated into the TiO_2 crystal lattice and accumulate on the surface, blocking some reaction sites.

Hydrolysis, solvothermal method, hydrothermal method, microemulsion-mediated solvothermal method, solvent mixing and calcination method, sol-gel method and high-temperature calcination method are currently used to prepare mixed-phase TiO_2. He, Jing, et al. reported the synthesis of anatase/rutile mixed phase TiO_2 nanoparticles through sol-gel technique followed by calcinations using $TiCl_4$ as titanium source with enhanced photocatalytic degradation of methylene blue under ultraviolet light illumination.[54] The synthesis of anatase-rutile mixed phase TiO_2 photocatalyst by one-pot redox reactions of $TiCl_3$ in the presence of graphene oxide with variable ratio of anatase to rutile was reported by Xiong et al. and sample with 55% anatase and 45% rutile had the maximum photoactivity.[55] Almashhori et al. synthesized (anatase/rutile) mixed phase TiO_2 nanophotocatalysts via microwave-assisted sol–gel technique.[56] Ishigaki, et al. reported high-temperature heat treatment improved the visible-light photocatalytic activity of anatase-rutile mixed-phase nano-size powder.[57] The high-temperature heat treatment, on the other hand, causes grain formation and a reduction in specific surface area, lowering the photocatalytic activity. It also gives rise to the phase transformation process from anatase to rutile. The preparation of

high-performance TiO_2 photocatalysts with high visible light activity and thermal stability is important for practical applications.

There are only a few reports in the literature, on the preparation of TiO_2 from potassium titanyl oxalate. When potassium titanyl oxalate was used as a precursor, the intermediate titanium oxalate $[Ti_2O_3(H_2O)_2(C_2O_4)\cdot H_2O]$ was formed and it was thermally decomposes to form TiO_2. It may be more favourable to prepare TiO_2 with adjustable crystal phase composition, controllable morphology and high crystallinity.[58] But most of these methods gives anatase phase or rutile phase TiO_2 alone. Hu et al. reported synthesis of rutile/anatase TiO_2 mixed crystal from potassium titanyl oxalate by hydrothermal method.[59] On hydrothermal treatment, titanium oxalate precursor was converted to Ti complex and this complex on calcinations at temperature higher than 450 ˚C yielded TiO_2. However, they used hydrothermal method which require longer reaction times. The present method provides a simple route to prepare mixed phase TiO_2 without using hydrothermal conditions and TiO_2 synthesis was done in open glass vessels and hence is highly useful for the bulk synthesis of TiO_2.

Khlyustova, et al. investigated the effect of the metal ion (Al, Cu, Mo and W) doping on the visible light photocatalytic performance of TiO_2 using Rhodamine B dye.[60] Zhang, Zhiyong, et al. reported the wide range tunability in transition-metal (V, Cr, Mn, Fe, Co, Ni, Cu, Mo, etc.) doped brookite-phase TiO_2 nanorods.[61] Fu, Fan, et al. synthesised Mn-doped and anatase/rutile mixed-phase TiO_2 nanofibers and reported enhanced photocatalytic activity performance.[62] There are a few reports on the preparation of Co, Ni, Mn, and Cu doped anatase/rutile mixed phase TiO_2 nanostructures.

In this work, we report the synthesis of nanocrystalline anatase and rutile mixed phase TiO_2 and Co, Mn, Cu, Ni and C-doped TiO_2 by refluxing aqueous potassium titanyl oxide oxalate solutions followed by calcination at 450 ˚C. The potassium titanium oxide oxalate precursor is noncorrosive, non-volatile, easy to handle and soluble substance in aqueous medium.[63] On doping the phase composition and visible light absorption properties of mixed phase TiO_2 was found to change relative to that of undoped TiO_2. The photocatalytic activity of the pure and doped TiO_2 was studied by monitoring the photodegradation of methylene blue under visible LED light

irradiation. The LEDs have the advantages that they are small in size, have a longer life span than conventional light sources and do not contain environmentally hazardous mercury.[64] These properties of LEDs offer advantages over UV and open new possibilities for the design of various types of photocatalytic reactors. The activities of the samples were compared with TiO_2 under same experimental conditions. The photoactivity of the doped samples were found to be higher than that of TiO_2 and the photoactivity of the doped samples were in the order Ni > Co > Mn > Cu > C.

3.2 Materials and methods

Potassium titanium oxide oxalate dihydrate (Sigma- Aldrich, 98%), Sulphuric acid (Merck, 98%), Cobalt nitrate hexahydrate (Merck, 99%), Manganese chloride tetrahydrate (Merck, 99%), Copper sulfate pentahydrate (Merck, 99%), Nickel nitrate hexahydrate (Merck, 99%) and Ethylene glycol (Merck, 99%) were used as starting material. All standard solutions were prepared by using distilled water. Methylene blue dye (Merck, 90%) was used for the photodegradation study.

3.2.1 Preparation of mixed phase TiO_2 and doped TiO_2

Mixed phase TiO_2 was synthesised by reflux method using potassium titanium oxide oxalate as titanium source. Con. H_2SO_4 (6.25 g) was added to 40 mL of distilled water. Then 5.75 g (16.23 mmol) of potassium titanium oxide oxalate was added to the above solution and dissolved under vigorous stirring. The solution was diluted to 400 mL. The resulting solution was refluxed in a 1000 mL round bottom flask attached to Liebig condenser at 100 ˚C for two hours. A white precipitate was formed directly and was filtered and washed with distilled water many times. The samples were dried in a hot air oven at 100 ˚C. Figure 3.1 shows the experimental method for the preparation of anatase-rutile mixed phase TiO_2 from potassium titanium oxide oxalate.

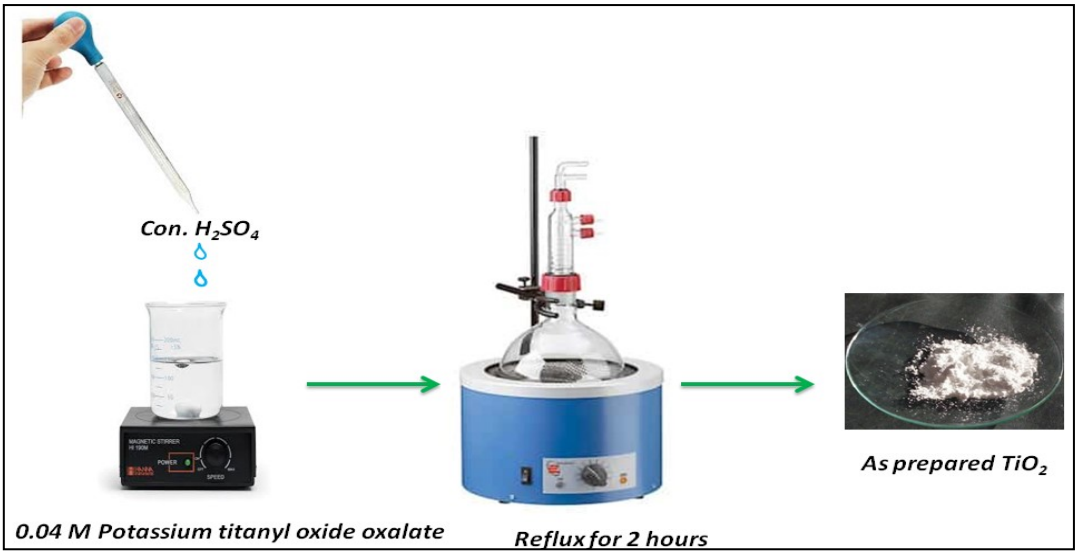

Fig. 3.1 Experimental method for the preparation of anatase-rutile mixed phase TiO_2 from potassium titanium oxide oxalate.

The prepared sample was calcined at 450 ˚C for one hour. Same method was also used for the preparation of 1 mol% Co-doped TiO_2. To the sulphuric acid solution prepared as above, 0.052 g, (0.17 mmol) of cobalt nitrate and 5.75 g (16.23 mmol) of potassium titanyl oxide oxalate was added and refluxed for two hours. Same procedure was repeated for 1 mol% Ni, Mn, Cu and C-doped TiO_2. Schematic diagram for the preparation of mixed phase anatase - rutile TiO_2 is given in the Figure 3.2.

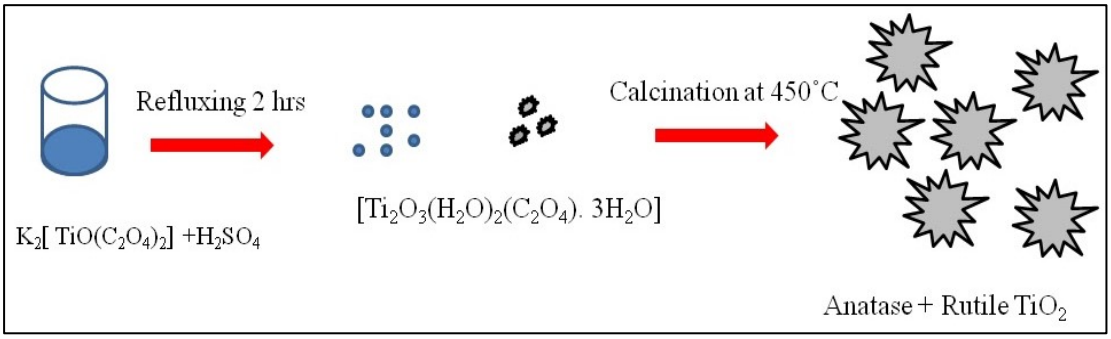

Fig. 3.2 Schematic representation of mixed phase anatase-rutile TiO_2 formation mechanism.

3.2.2 Photocatalytic activity of mixed phase TiO_2 and doped TiO_2 under visible LED light irradiation

The photocatalytic activity of the mixed-phase TiO_2 and 1 mol% doped TiO_2 (Co, Mn, Ni, Cu, C) samples were investigated by analysing the aqueous solutions of

methylene blue (MB) after visible light LED irradiation. The degradation studies were done according to the reported standard procedure.[24] A suspension of 0.05 g of mixed phase TiO_2 or 1 mol% doped TiO_2 was dispersed in 100 mL of 10^{-4} M solution of the dye and was stirred under dark to attain adsorption and desorption equilibrium. After stirring in the dark, the suspensions were centrifuged. The clear solution was used to calculate the initial concentration of MB from the intensity of the peak at 663 nm in the UV-Visible spectrum. For visible LED light photodegradation studies, the solutions were kept in a homemade visible light LED reactor (20 W) for 15 hours. After exposure to visible radiation the concentration of MB was measured from the UV visible spectrum.

3. 3 Results and discussion

3.3.1 Thermogravimetric analysis

The thermogravimetry (TG) and derivative thermogravimetry (DTG) curves of the precipitate obtained by refluxing potassium titanyl oxalate aqueous solution is given in Figure 3.3. There were three stages in the thermo gravimetric analysis. First stage started from room temperature to 150 ˚C which accounted for 7% weight loss of the sample.

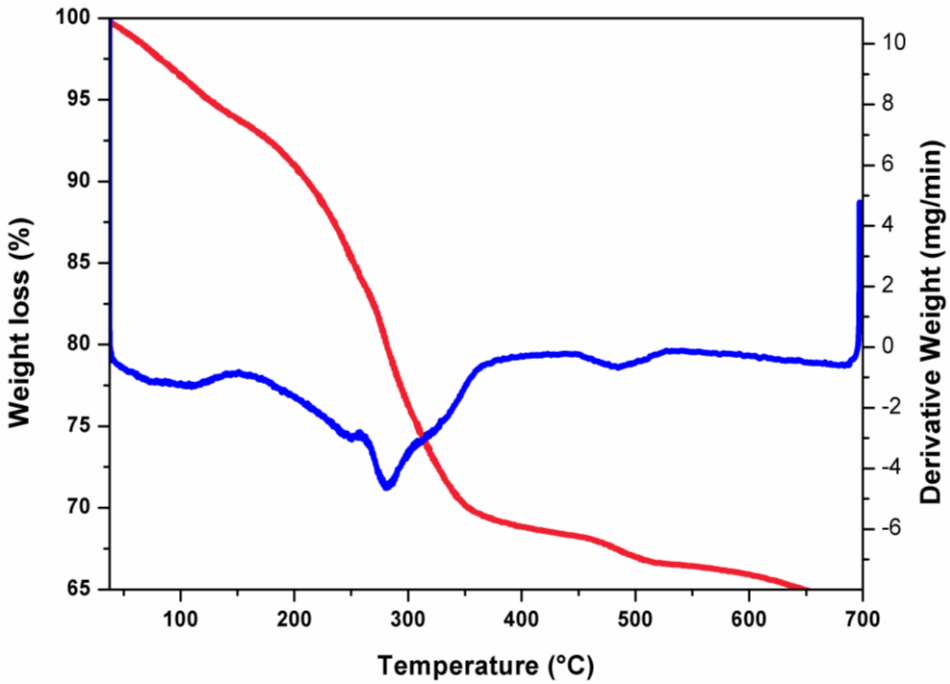

Fig. 3.3 TG-DTG curve of prepared TiO_2 sample.

The endothermic curve appeared in the same temperature region, corresponding to the evaporation of water. In the second stage, there was a drastic drop in weight from 150 to 380 ˚C due to the decomposition of oxalate to TiO_2.[65] Weight loss is approximately 26%. Third stage started from 450 to 550 ˚C showed a weight loss of 2%. The weight loss indicates the loss of chemisorbed water. Further increase of temperature did not produce any considerable change to weight of the sample.

3.3.2 XRD analysis

XRD patterns of the precipitate obtained by refluxing potassium titanyl oxalate aqueous solution is given in the Figure 3.4 (a) and was similar to that of titanium oxalate complex $Ti_2O_3(H_2O)_2(C_2O_4).\ 3H_2O$ [JCPDS card no. 54-0330].[66,67] A low concentration of titanium oxalate precursor yielded titanium oxalate–based complex $[Ti_2O_3(H_2O)_2(C_2O_4)].H_2O$.

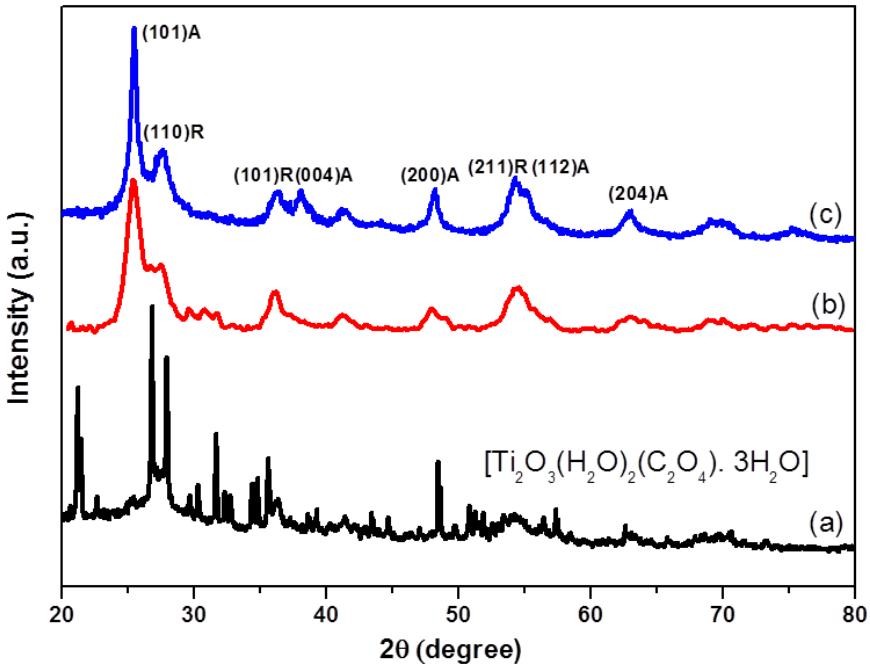

Fig. 3.4 XRD pattern of a) prepared TiO_2 b) TiO_2 calcined at 300 ˚C and c) TiO_2 calcined at 450 ˚C.

Crystalline structure of complex is represented in the Figure 3.5. Four vertices of each TiO_6 octahedron in the $[Ti_2O_3(H_2O)_2(C_2O_4)].H_2O$ crystal are corner shared with the adjacent octahedron and remaining two vertices are attached with the carbon atoms.[65] During the calcination, the Ti-O bond in the titanium oxalate is broken and oxalate is decomposes to carbon monoxide, carbon dioxide and water molecule are

also eliminated. The residual titanium oxalate complex is decomposed to form mixed phase anatase and rutile TiO_2.

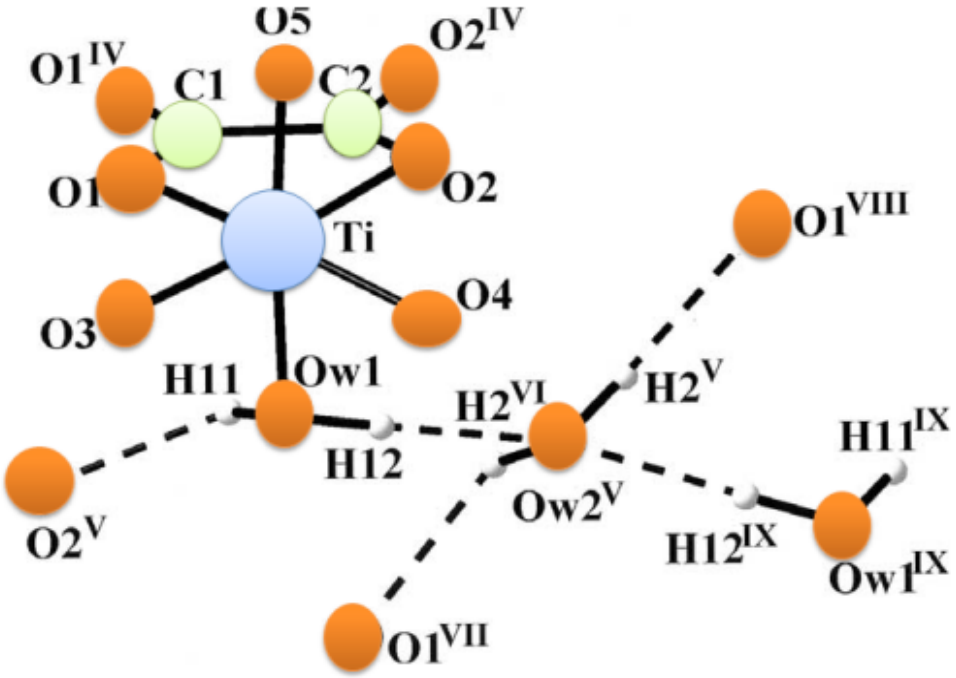

Fig. 3. 5 Crystal structure of $[Ti_2O_3(H_2O)_2(C_2O_4)].H_2O$, Hydrogen bond are represented by dotted line.[65]

After calcination of the precipitate at 300 ˚C and 450 ˚C respectively, the XRD patterns obtained are given in Figure 3.4 (b-c). After calcinations at temperature above 300 ˚C, the peaks corresponding to titanium oxalate complex disappeared. The XRD patterns obtained at 300 and 450 ˚C showed the peaks corresponding to both anatase and rutile phase. This data also supported the TG-DTG results, which showed the maximum weight loss at 281 ˚C corresponding to the decomposition of titanium oxalate complex. Since peaks corresponding to oxalate phase was very weak in the XRD spectra of TiO_2 calcined at 300 ˚C for one hour, we may conclude that the appreciable conversion of oxalate phase to mixed phase TiO_2 takes place in this temperature range. On calcinations at 450 ˚C for one hour the TiO_2 peaks become sharper indicating the more crystallinity and increased particle size. Also no peaks corresponding to titanium oxalate complex was present in the XRD spectrum. Synthesis of anatase phase or rutile phase TiO_2 alone from titanium oxalate complex has been reported by many groups. There are only few report on the synthesis of mixed phase anatase rutile mixed phase TiO_2 from titanium oxalate complex.[68] However, they used hydrothermal method for the synthesis of TiO_2, which require

relatively higher temperature and longer reaction time (120 ˚C, 12 hours). The amount of TiO_2 formed is also limited by the volume of the autoclave. In this method, TiO_2 synthesis can be done in open big glass vessels and hence is highly useful for the bulk synthesis of TiO_2.

The characteristic peaks in the XRD pattern of TiO_2 calcined at 450 ˚C such as 25.42˚, 37.19˚, 48.03˚, 54.26˚, 62.8˚ indicated the various planes (101), (004), (200), (112), (204) of anatase phase (JCPDS Card No.21-1272) and the peaks observed at 27.61˚, 36.32˚ and 54.31˚ corresponds to (110), (101) and (211) planes of rutile phase (JCPDS Card No.21-1276). The percentage of anatase to rutile was calculated using the Spurr equation.[25]

$$\chi = \frac{1}{[1+0.8\left(\frac{I_A}{I_R}\right)]} \qquad (9)$$

Where I_A and I_R are the integrated intensities of anatase (101) and rutile (110) peak respectively. The anatase/rutile composition was found to be 70:30. The crystallite size of anatase and rutile was calculated using Scherrer equation

$$D = {}^{0.9\lambda}/_{\beta cos\theta} \qquad (10)$$

It was found to be 8.3 nm for anatase and 35 nm for rutile. The presence of sulphuric acid in the aqueous precursor salt solution of TiO_2, induced a strongly acidic medium with a pH value of ~1. On refluxing this precursor solution for 2 hours titanium oxalate hydrate complex got precipitated.

Previous studies of the TiO_2 preparation in strongly acidic medium (H_2SO_4) under reflux condition at 90 ˚C for 4 hours, resulted in the preferential formation of anatase phase of TiO_2.[28] However when they added oxalate ions to the precursor solution only hydrated titanium oxalate was precipitated, which then was converted to mixed phase TiO_2 on calcination at 450 ˚C. Comparing these results with the XRD and TG-DTG the results of TiO_2 sample obtained in the present work, it may be concluded that oxalate ions play major role in the formation of anatase-rutile mixed phase TiO_2 in present method. During the calcination, titanium oxalate break down to form TiO_6 octahedra and finally it was converted to TiO_2.[69] The formation of rutile phase along with anatase phase may be due to the complexing ability of oxalate ions

to the Ti^{4+} ions and this effect helps in the creation and growth of rutile phase nuclei also during crystallisation.[70]

We also prepared 1 mol% Co, Mn, Cu, Ni and C-doped TiO_2 by precipitation of titanium oxalate complex in the presence of cobalt nitrate, manganese chloride, copper sulfate, nickel nitrate and ethylene glycol respectively. The sample was calcined at 450 ˚C for one hour. The XRD pattern of the pure and 1 mol% doped TiO_2 samples after calcinations, are given in the Figure 3.6.

After the introduction of cobalt ion, the intensity of all peaks increased compared to that of undoped TiO_2 indicating the higher crystalline nature of TiO_2. The anatase phase was found to be the dominant phase in the calcined sample. No diffraction line corresponding to cobalt oxide was seen in the XRD spectrum. This indicates the uniform dispersion of cobalt on TiO_2 lattice. The summary of the XRD results are presented in Table 3.1.

The crystallite size slightly decreased from 8.3 nm to 8.1 nm for anatase phase after of Co-doping. But in the case of rutile phase, the crystallite size increased from 35 nm to 41 nm as a result of doping. The Co^{2+} ions present at the surface of the TiO_2 crystallite prevent the mutual contact between the grains which reduces the crystallite size of anatase.[68] The effect of cobalt ion doping on d-spacing of the TiO_2 lattice, as measured from anatase (101) and rutile (110) diffraction lines, are given in the Table 3.1.

The XRD pattern of Co-doped TiO_2 showed a small shift in *d*-spacing of both anatase and rutile crystal phases. This shift indicates the incorporation of cobalt ions in the TiO_2 lattice. Since Co^{2+} has a larger ionic radius (0.79 A˚) than that of Ti^{4+} (0.745 A˚), a slight expansion of the unit cell occurs and leads to an increase of lattice parameters. The difference in oxidation state of Ti^{4+} and Co^{2+} ions creates oxygen vacancies to maintain electrical neutrality. The present method provides a simple route to prepare mixed phase TiO_2 and Co-doped TiO_2 without using hydrothermal conditions.[67]

Figure 3.6.(c) shows the XRD diffraction patterns of 1 mol% Ni-doped titanium dioxide powder sample, after calcination at 450 ˚C. The Ni-doped TiO_2 showed sharp and high intense XRD peaks, indicating high crystallinity of TiO_2. The XRD pattern

shows peaks corresponding to both anatase and rutile; the peaks at 25.24˚, 47.95˚ and 62.51˚ correspond to the (101), (200) and (204) planes, respectively, of anatase phase (JCPDS Card No.21-1272). The sample had a dominant anatase phase. The peaks at 27.45˚ and 54.12˚ confirmed the presence of rutile phase (JCPDS Card No.21-1276). The Spurr equation was used to calculate the phase composition ratio between anatase and rutile in 1 mol% Ni-doped TiO_2. The average crystallite sizes of 1 mol% Ni-doped TiO_2 sample was calculated by Scherrer's formula. 1 mol%-Ni doped TiO_2 sample exhibited a composition of 60% anatase and 40% rutile phase with a crystallite size of 11.3 nm and 25.6 nm, respectively. The crystallite size increased from 8.3 nm to 11.3 nm for anatase phase after doping. The average crystallite size of rutile phase reduced from 35 nm to 25.6 nm in 1mol% Ni-doped TiO_2. Table 3.1 contains an overview of 1 mol% Ni-doped TiO_2. At lower concentrations, nickel doping will stabilize the anatase phase.[71]

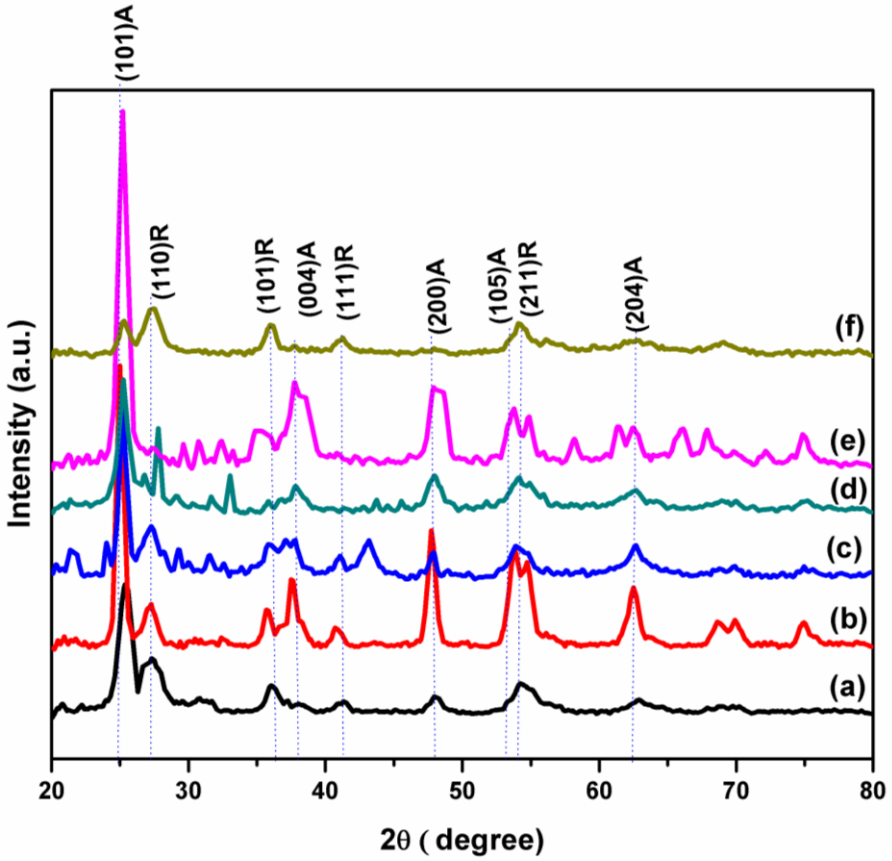

Fig. 3.6 The XRD pattern of a) TiO_2, b) 1 mol% Co-doped TiO_2, c) 1 mol% Ni-doped TiO_2, d) 1 mol% Mn-doped TiO_2, e) 1 mol% Cu-doped TiO_2 and f) 1 mol% C-doped TiO_2 calcined at 450 ˚C.

1 mol% Mn-doped TiO_2 was composed of anatase and rutile phases of TiO_2. Figure 3.6 (d) shows the diffraction patterns of the 1 mol % Mn-doped TiO_2 calcined at 450 ˚C. The sample exhibit anatase peaks at 25.1˚, 37.72˚, 47.89˚, 62.51˚, corresponding to the (101), (004), (200) and (204) planes, respectively. The characteristic peaks of rutile phase was observed at 27.49˚ and 54.12˚, corresponding to the (110) and (211) planes, respectively. The average crystallite size of anatase phase of 1 mol% Mn-doped TiO_2 nanoparticles was calculated from the anatase (101) peak at 25.10˚ by Debye-Scherrer's formula. The anatase phase had a particle size of 10.4 nm, whereas the rutile phase has a particle size of 99 nm. Anatase: rutile phase composition was found to be 71:29. No peaks corresponding to manganese oxide were observed in the XRD spectrum. Hence from the XRD results, it may be concluded that all three doped samples (Co, Ni, Mn) consist of mixed crystalline phases of anatase and rutile.

Table 3.1. Summary of d spacing and compositions of anatase and rutile.

Sample	d spacing (101)A˚	d spacing (110)A˚	Anatase (%)	Rutile (%)
TiO_2	3.5001	3.25	70	30
Co-doped TiO_2	3.5588	3.27	84	16
Ni-doped TiO_2	3.5359	3.26	60	40
Mn-doped TiO_2	3.5278	3.2092	71	29
Cu-doped TiO_2	3.5331	-	100	0
C-doped TiO_2	3.5078	3.2586	44	66

Figure.3.6 (e) display the X-ray diffraction pattern of 1 mol% Cu-doped TiO_2 sample after calcination at 450 ˚C. The peak at 25.10˚ corresponding to (101) plane confirms the presence of anatase phases. The other anatase peaks were located at 37.72˚, 47.89˚ and 62.51˚ and are indexed as (004), (200) and (204) planes,

respectively. In contrast to 1 mol% Co, 1 mol% Ni, 1 mol% Mn-doped samples, anatase phase was only present in 1 mol% Cu-doped TiO_2 with a crystallite size of 13.7 nm.

Figure.3.6 (f) presents the X-ray diffraction pattern of 1 mol% C-doped TiO_2 sample calcined at 450 ˚C. The sample exhibits peaks corresponding to both anatase and rutile phase of TiO_2. The rutile phase was identified by the peaks located at 27.30˚, 35.97˚, 41.20˚ and 54.1˚ corresponding to (110), (101), (111) and (211) planes, respectively. In addition to rutile phase, the anatase peaks were also observed at 25.29˚, 37.78˚, 47.89˚ and 62.51˚ and are indexed as (101), (004), (200) and (204) planes, respectively. The Scherrer's formula was used to calculate the average crystalline size of the sample by using the FWHM of the (110) peak for rutile phase and (101) peak for anatase phase. Crystallite size of anatase was found to be 10.5 nm and for the rutile phase, it was 15.47 nm. The mixed-phase 1 mol% C-doped nanocrystalline TiO_2 contain 66% rutile and 44% of anatase phase.

3.3.3 Raman spectral studies

Raman spectra was used to confirm the presence of anatase and rutile phases. The Raman spectra of TiO_2 calcined at 450 ˚C is given in Figure 3.7. The bands corresponding to both anatase and rutile phases of TiO_2 are present in the Raman spectra.

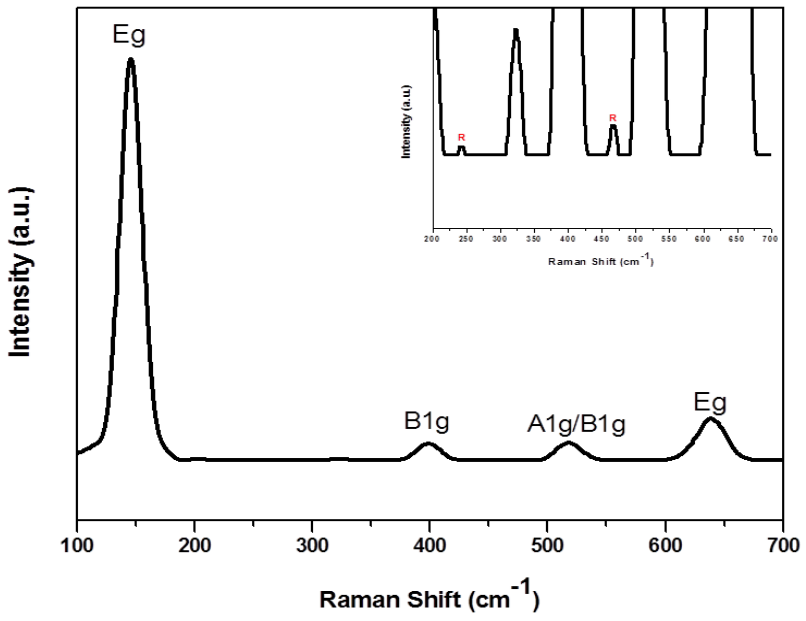

Fig. 3.7 Raman spectra of TiO_2 from potassium titanium oxide oxalate a) calcined at 450 ˚C inset shows the enlarged view of rutile peaks.

The bands at 146, 394, 517 and 642 cm^{-1} are assigned to the E_g, B_{1g}, A_{1g}/B_{1g}, and E_g fundamental Raman active modes of anatase. The Eg mode is due to the symmetric stretching vibration of the O-Ti-O bond of TiO_2 and the B_{1g} mode is due to the symmetric bending vibration of O-Ti-O. The A_{1g} mode is due to anti-symmetric bending vibration of O-Ti-O.[72] The sample also showed the characteristic bands at 610, 446 and 242 cm^{-1} corresponding to rutile. The enlarged view is shown in the inset. Raman active vibration modes of rutile are A_{1g} (610 cm^{-1}) and E_g (446 cm^{-1}). The E_g mode of rutile is due to the out of plane vibrational mode and A_{1g} mode is due to the Ti-O stretching vibration.

3.3.4 TEM analysis

The crystallographic structure, particle size and surface morphology of TiO_2 prepared from potassium titanium oxide oxalate were studied using TEM and the images are shown in Figure 3.8. The TEM images at different magnifications clearly show that the TiO_2 prepared from potassium titanium oxide oxalate is spherical in shape and that large number of primary particles are aggregated together to form a flower like morphology.

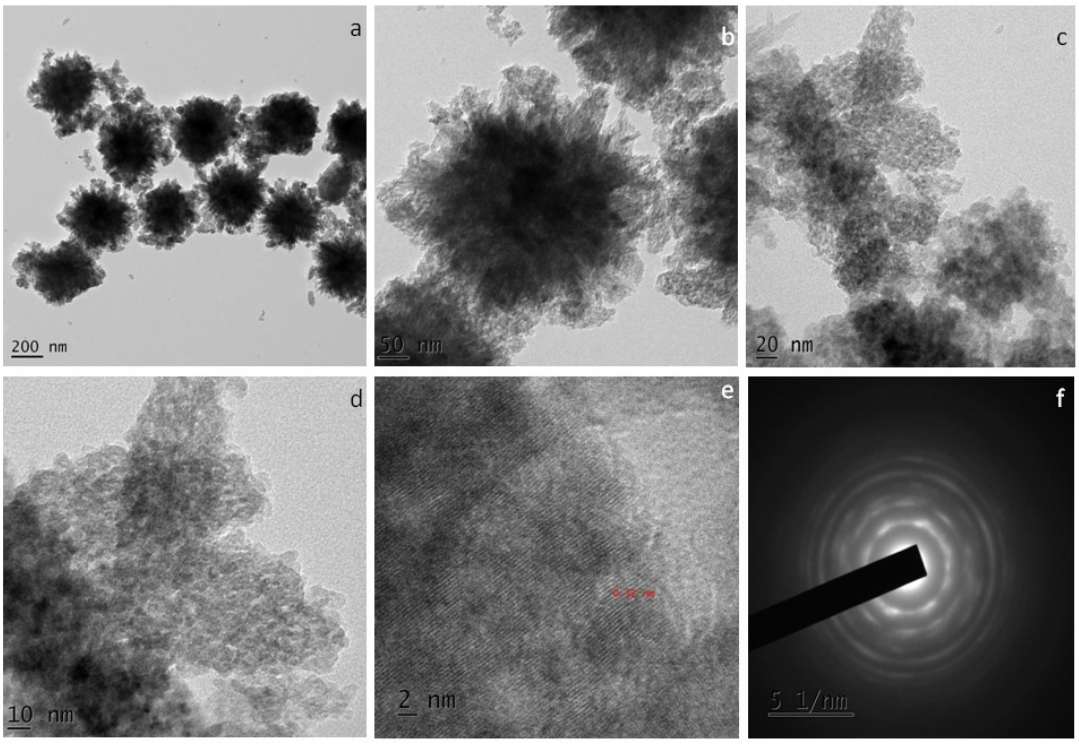

Fig. 3.8 The TEM images of TiO_2 from potassium titanium oxide oxalate calcined at 450 ˚C (a-d) are images at different magnifications, e) HRTEM and f) SAED pattern.

The nanoparticles obtained had an average primary particle size of 8 nm, which is in good agreement with the primary particle size obtained from the XRD (8.3 nm). Lattice fringes are very clear in the HRTEM image. From the image d-spacing of lattice fringes was calculated. The mixed phase of both anatase and rutile phases was observed, with d spacing 0.34 nm corresponding to (101) planes of anatase and 0.32 nm corresponding to (110) planes of rutile. By comparing with the XRD results, the *d*-spacings were indexed to interplanar distances of (101) planes of anatase and (110) planes of rutile phases. The SAED pattern shows the crystalline nature of the samples and concentric Debye-Sherrer ring, which can be indexed to anatase phase. These results are consistent with the XRD results.

The morphology and average primary particle size of the 1 mol% Co-doped sample was similar to that of undoped TiO_2. The TEM image of 1 mol% Co-doped TiO_2 calcined at 450 ˚C is given in Figure 3.9. The 1 mol% Co-doped TiO_2 were also analysed by HRTEM. The particles are crystalline in nature. The d-spacing of 0.34 nm between lattice fringe matches with the (101) planes of anatase. The concentric rings in the SAED pattern indicate the crystalline nature and small size of nanocrystals.

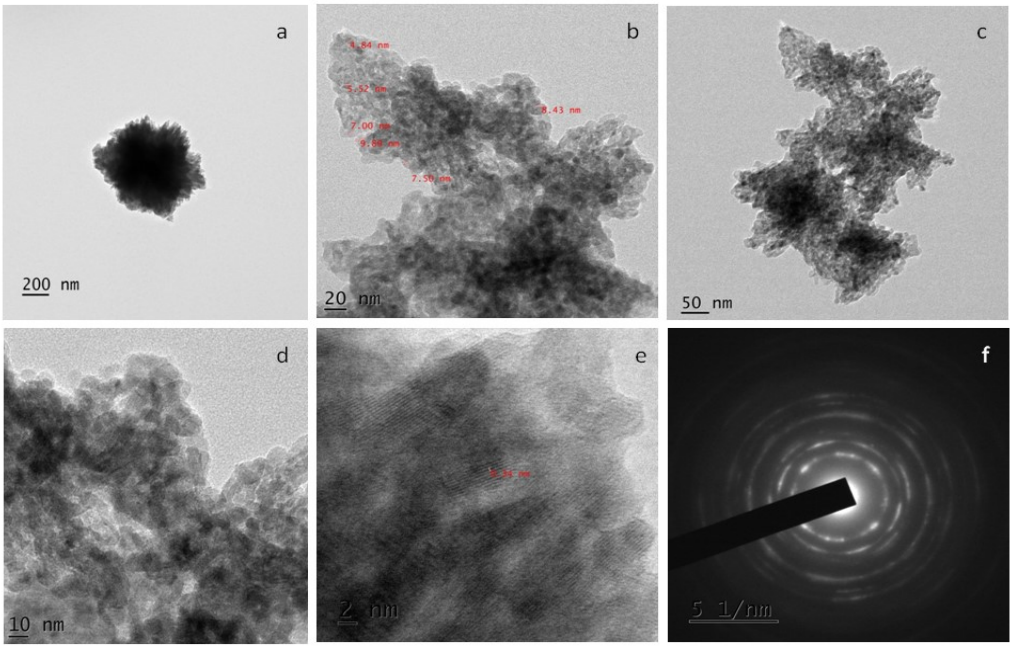

Fig. 3.9 TEM images of 1 mol% Co-doped TiO_2 calcined at 450 ˚C :(a-d) are images at different magnifications, e) HRTEM and f) SAED pattern.

The TEM images of 1 mol% Ni-doped TiO_2 calcined at 450 ˚C are presented in Figure 3.10. As seen in TEM images, the particles are aggregated spherical spheres and are having an average particle size of 11 nm. The separation between the lattice fringes are found to be 0.33 nm, which is equivalent to the interplanar distances of the characteristic (110) planes of rutile phase. The rutile phase formation was also confirmed from the d-value obtained from HRTEM. The selected area electron diffraction patterns indicate the features of anatase phase with the interplannar spacing (d) of 3.5 Å corresponding to (101) planes. The results are consistent with the XRD results.

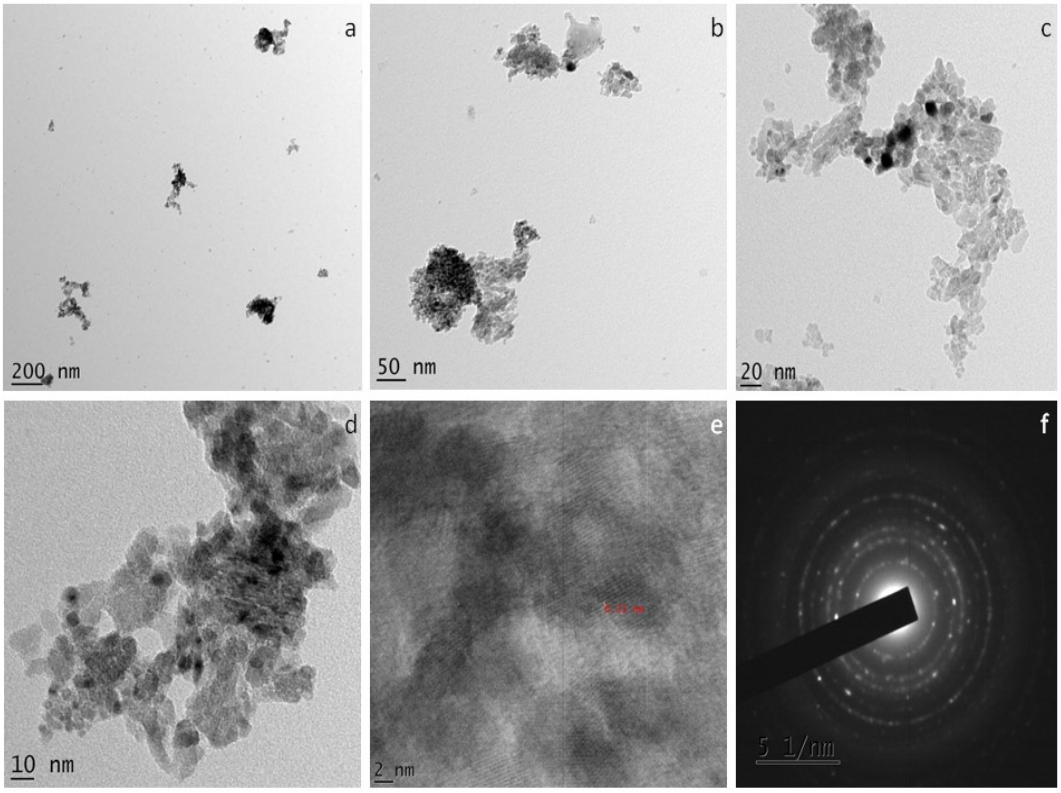

Fig. 3.10 TEM images of 1 mol% Ni-doped TiO_2 calcined at 450 ˚C :(a-d) are images at different magnifications, e) HRTEM and f) SAED pattern.

The TEM images of 1 mol% Mn-doped TiO_2 calcined at 450 ˚C are given in Figure 3.11. From the figure it can be seen that most of the particles in the samples appeared as spheres with non-uniform sizes. The average particle size in the sample was about 10 nm in diameter which is in agreement with the results obtained from the XRD analysis. The observed d-spacing in the HRTEM images of the sample is 0.31 nm, which corresponds to the (110) plane of rutile. The d-spacing values are in good agreement with the XRD data. Selected area electron diffraction patterns specify

the crystallographic features of (101) planes of anatase phase and the (110) plane of rutile.

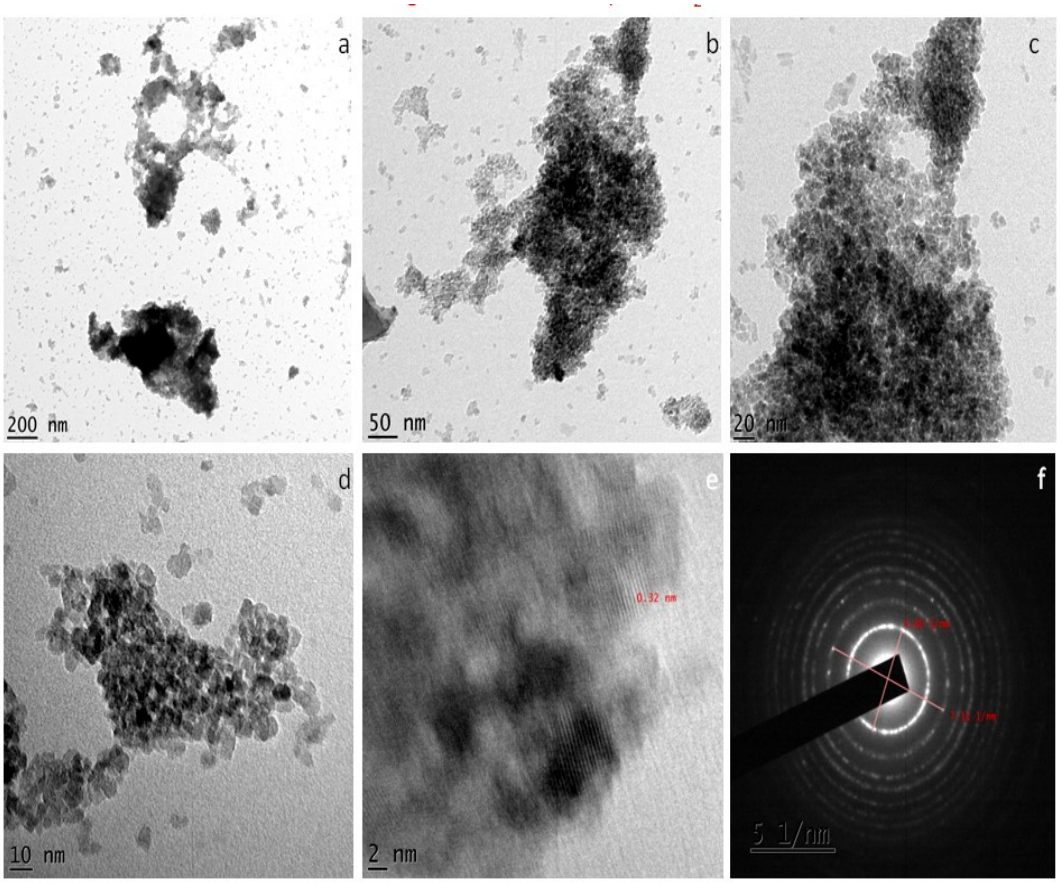

Fig. 3.11 TEM images of 1 mol% Mn-doped TiO_2 calcined at 450 ˚C :(a-d) are images at different magnification, e) HRTEM and f) SAED pattern.

The morphology of the 1 mol% Cu-doped TiO_2 sample, calcined at 450 ˚C was obtained from TEM and the images are given in Figure 3.12. The images showed that the sample was composed of uniform spherical nanoparticles. The average particle size was in the order of 13 nm. The lattice fringes are clearly observed in HRTEM images, indicating that the TiO_2 particles are crystalline and consists of only anatase. The results are consistent with the XRD data. The crystal lattice spacing of the nanoparticles were found to be 0.35 nm, which matches well with the (101) plane of anatase TiO_2. The SAED pattern of the sample shows rings corresponding to the anatase phase.

The morphology of 1 mol% C-doped TiO_2 was studied by TEM analysis and the images at different magnification are shown in the Figure 3.13. Particles are having uniform spherical shape and are highly crystalline with well resolved lattice structure.

The primary particle size of the sample was found to be 15 nm. The particle size obtained from TEM was in good agreement with that derived from XRD data. Particles were assembled in a common centre and appear to be petal shape and having the size of 112 nm. Sample exhibited flower like morphology and uniform particle size. Particles are highly agglomerated. The HRTEM images are presented in Figure 3.12(e). From the images, TiO_2 particles are polycrystalline in nature and observed d-spacing between the lattice fringes is 0.35 nm corresponding to (101) plane of the anatase phase. The corresponding SAED patterns are also displayed to show the sharp diffraction pattern of rutile and anatase mixed phase TiO_2.

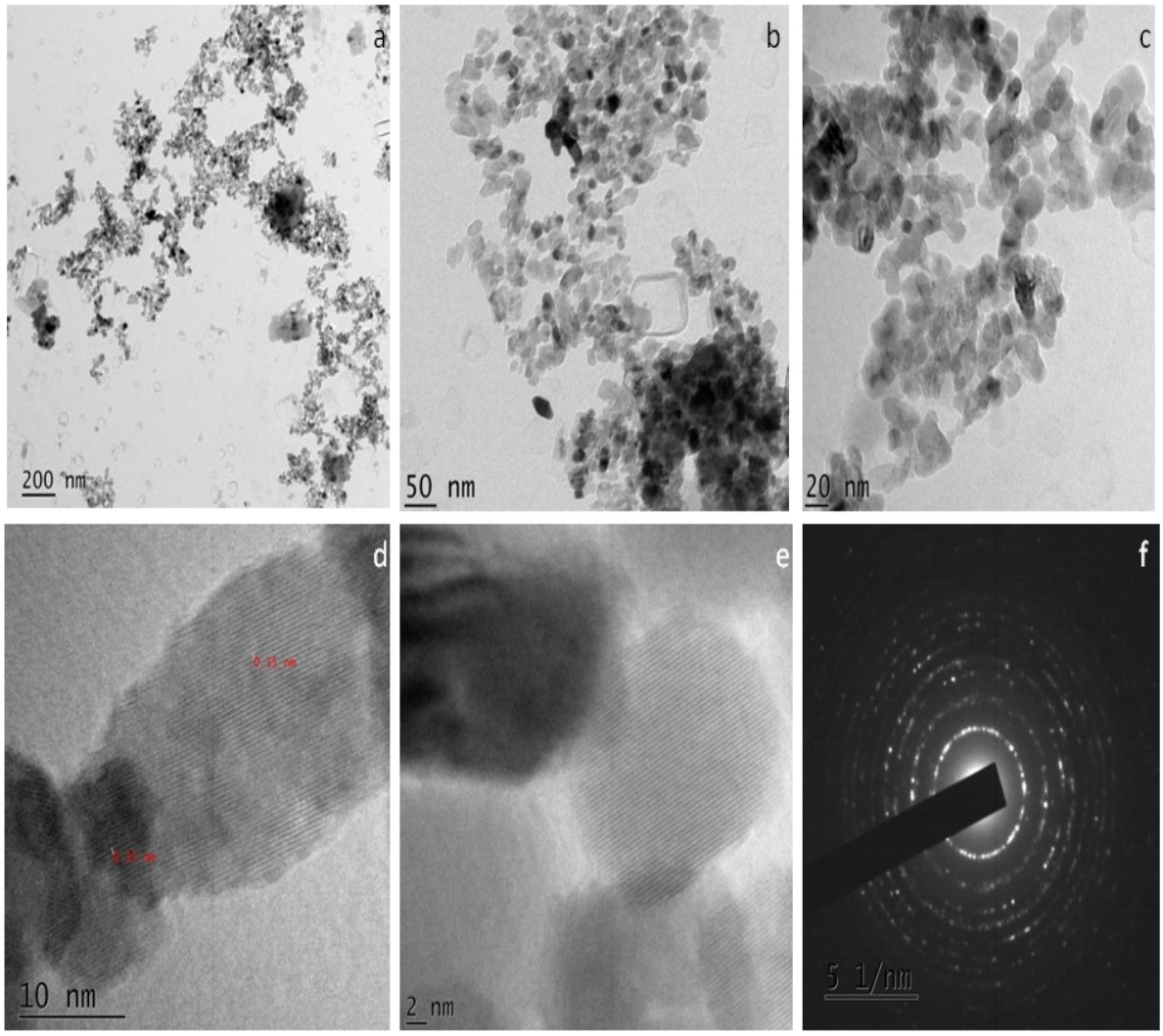

Fig. 3.12 TEM images of 1 mol% Cu-doped TiO_2 calcined at 450 ˚C :(a-d) are images at different magnification, e) HRTEM and f) SAED pattern.

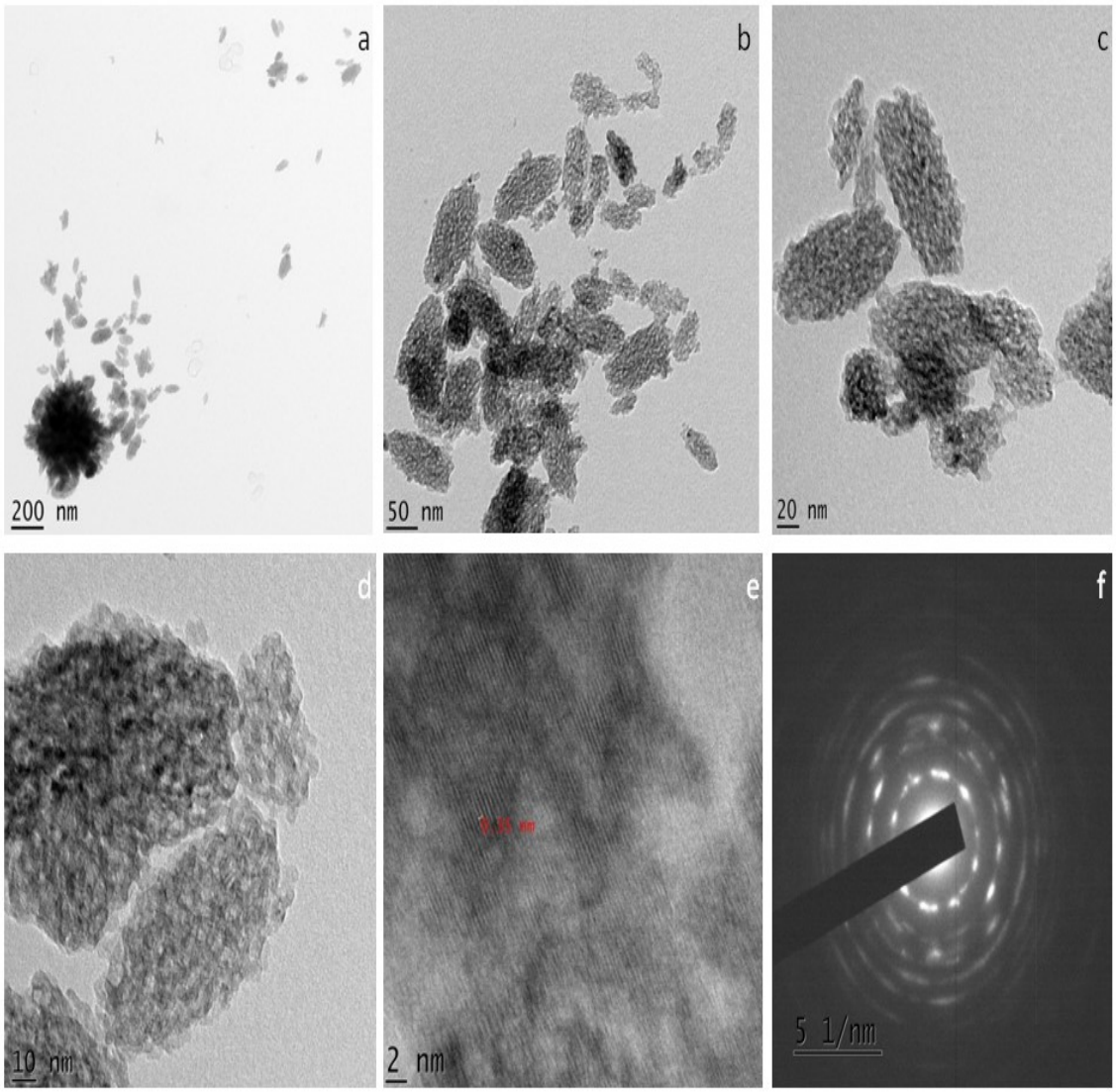

Fig. 3.13 TEM images of 1 mol% C-doped TiO_2 calcined at 450 ˚C :(a-d) are images at different magnification, e) HRTEM and f) SAED pattern.

3.3.5 Morphology and composition analysis by FESEM-EDS

The microstructure of TiO_2 prepared from potassium titanium oxide oxalate calcined at 450 ˚C were analysed by FESEM also and the results are shown in Figure 3.14. Images are in good agreement with the result of TEM images. The FESEM images of TiO_2 sample clearly show the self-assembled uniform flower like structures. The particles are agglomerated. The average size of the aggregated particles was found to be 200 nm. The FESEM image of 1 mol% Co-doped TiO_2 calcined at 450 ˚C was presented in Figure 3.15. The FESEM image of 1 mol% cobalt doped TiO_2 was similar to the FESEM images of the undoped TiO_2.

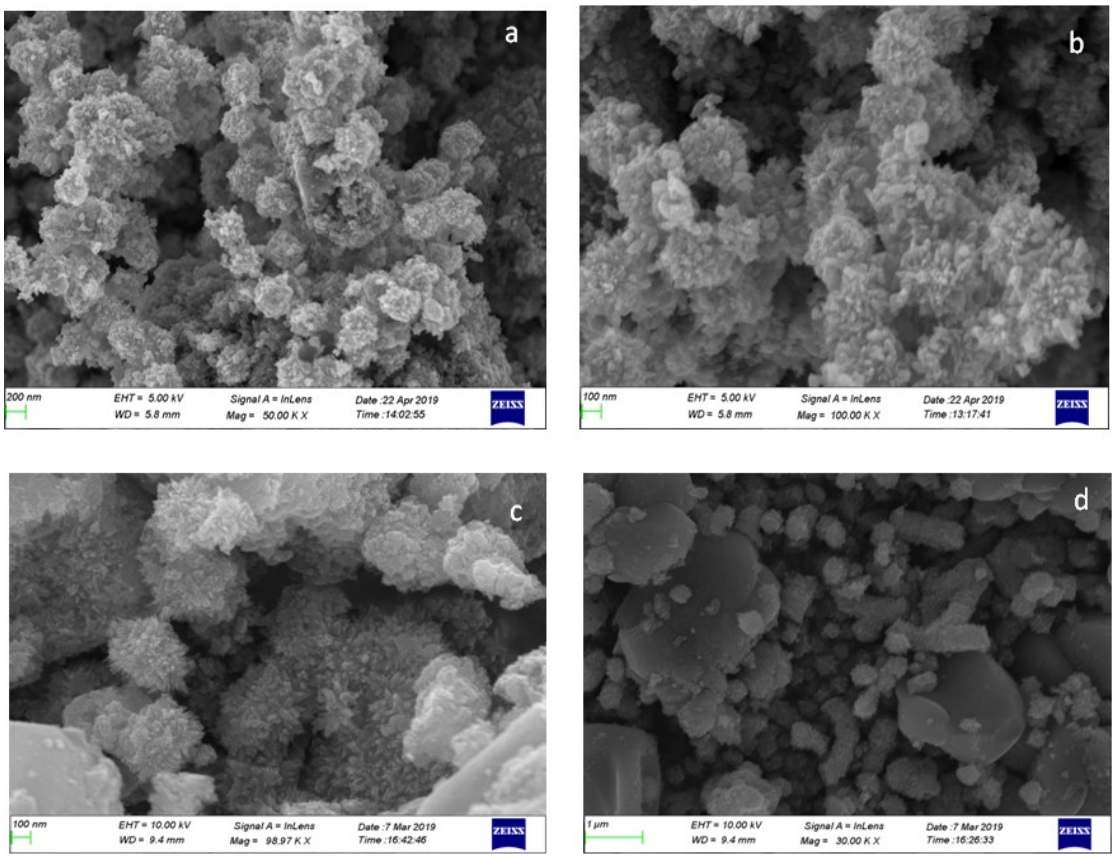

Fig.3.14 FESEM image of TiO_2 from potassium titanium oxide oxalate calcined at 450 ˚C: (a-d) are images at different magnifications.

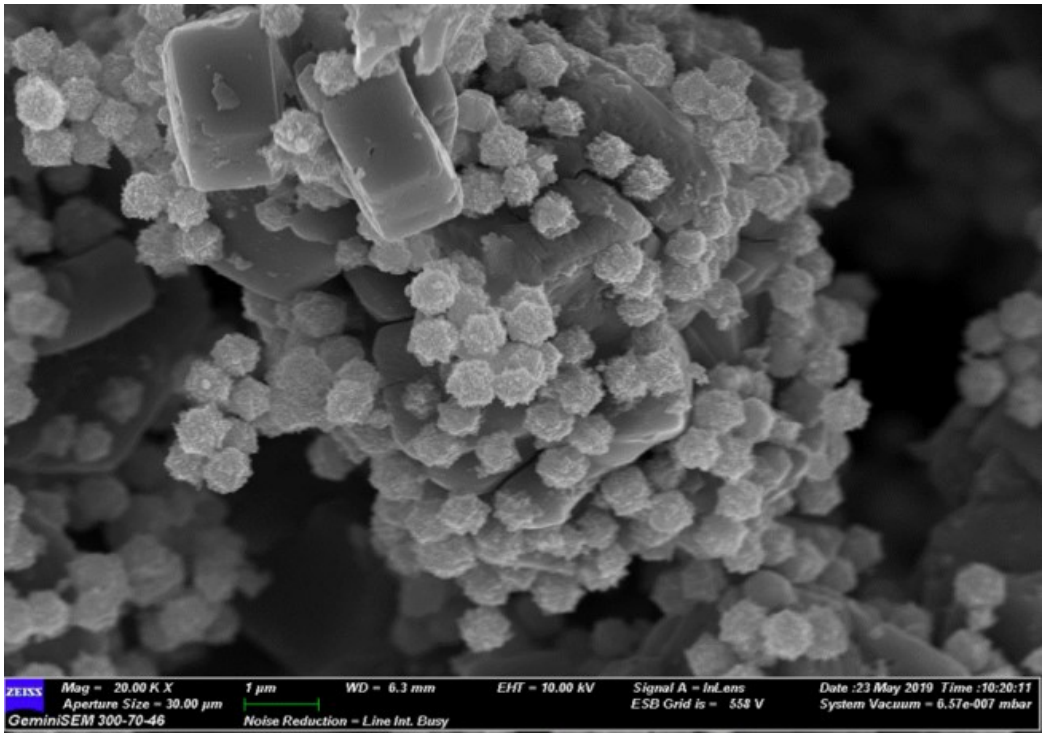

Fig. 3.15 FESEM image of 1mol% Co-doped TiO_2 calcined at 450 ˚C.

The elemental compositions of 1 mol% Co-doped TiO_2 was studied by EDS analysis. The EDS spectrum (Figure 3.16.) showed the presence of cobalt in addition to titanium and oxygen, indicating the successful Co-doping. The concentration of Co in the doped TiO_2, as measured from EDS, was close to the value of cobalt concentration, used in the preparation of Co-doped TiO_2.

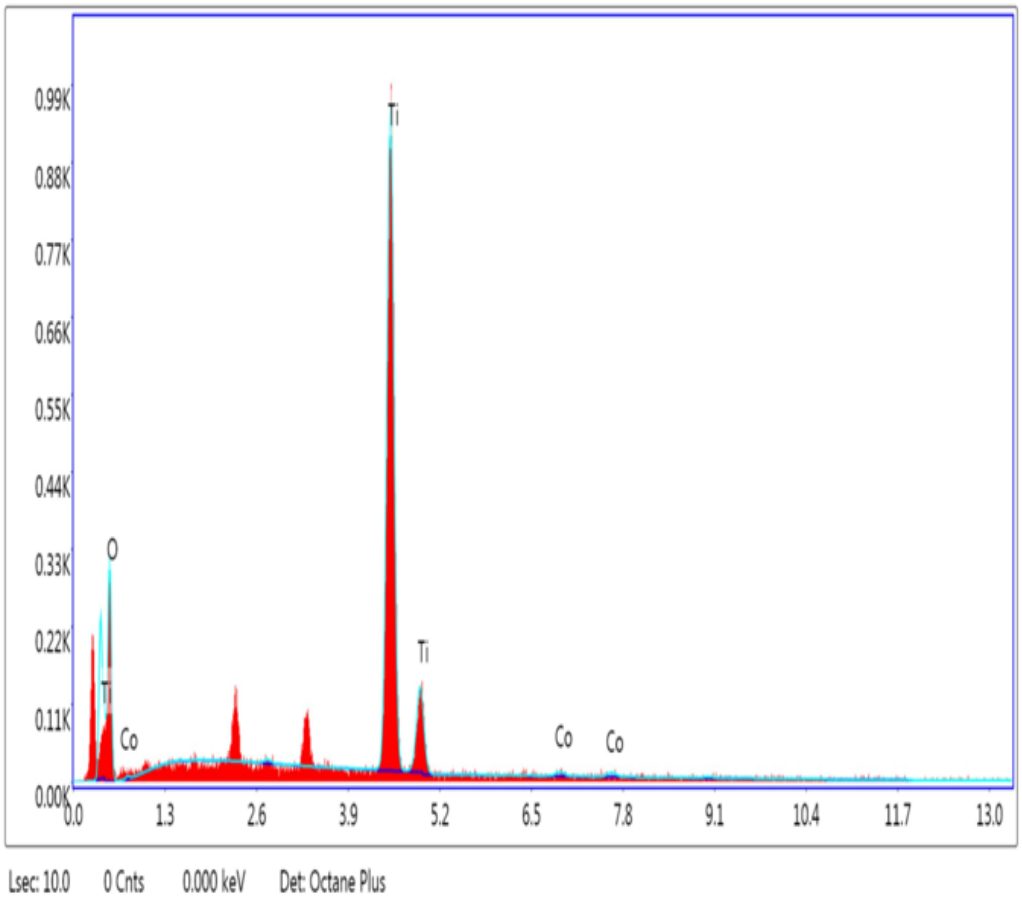

Fig. 3.16 EDS spectrum of 1 mol% Co-doped TiO_2.

FE-SEM images of 1 mol% Ni-doped TiO_2 shows agglomerated, spherical shaped nanoparticles as shown in Figure 3.17. Nanoparticles are seen as big clusters with different sizes and shapes in the sample. The aggregates are found to have diameter in the range from 10 nm to 1000 nm.

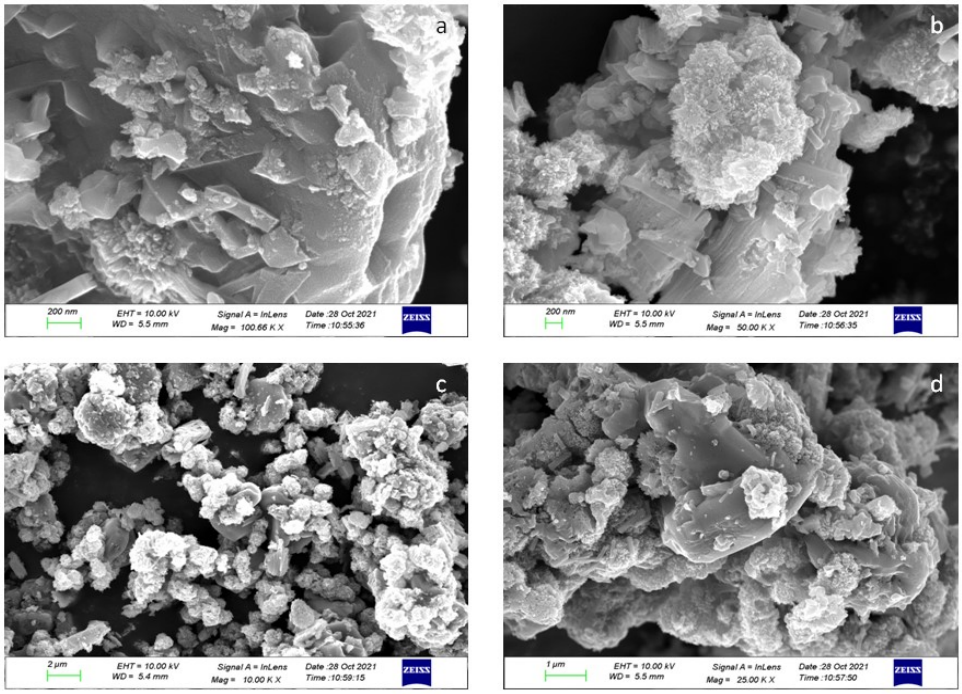

Fig. 3.17 FESEM images of 1mol% Ni-doped TiO_2 prepared from potassium titanium oxide oxalate and calcined at 450 ˚C: (a-d) are images at different magnifications.

Figure 3.18 shows the EDS spectrum of 1 mol% Ni-doped TiO_2. The spectrum confirmed the presence of nickel ions in TiO_2 crystal lattice.

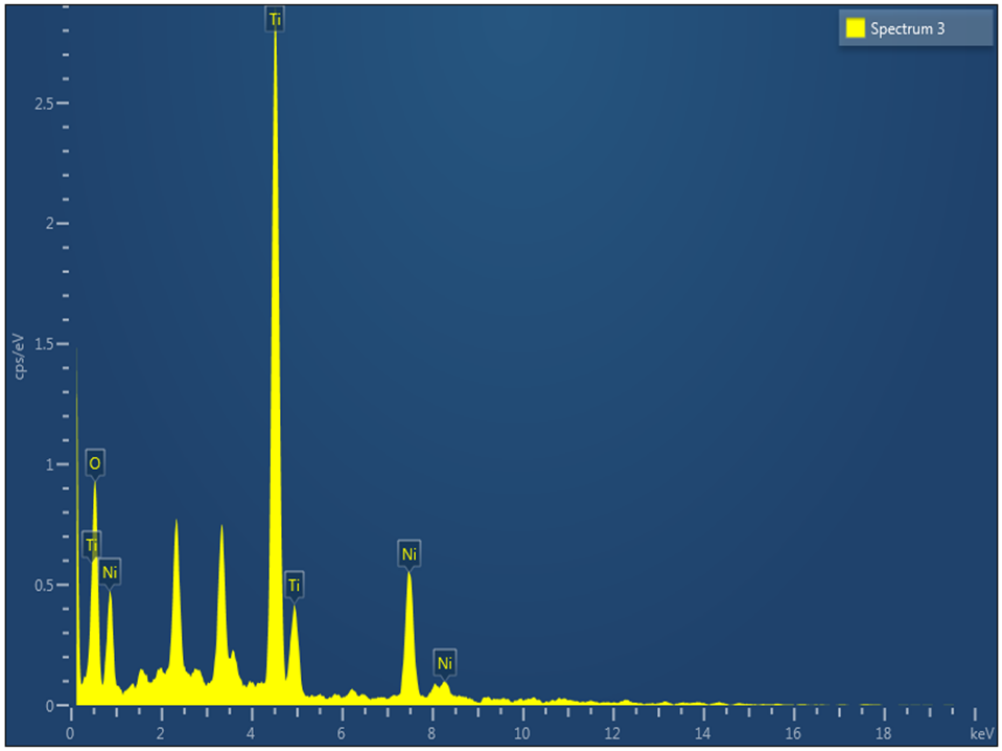

Fig. 3.18 EDS spectrum of 1 mol% Ni-doped TiO_2.

Morphological characteristic of 1 mol% Mn-doped TiO_2 was analysed by field emission scanning electron microscopy and are shown in Figure 3.19. Morphology of the sample consists of large size particles of irregular shape.

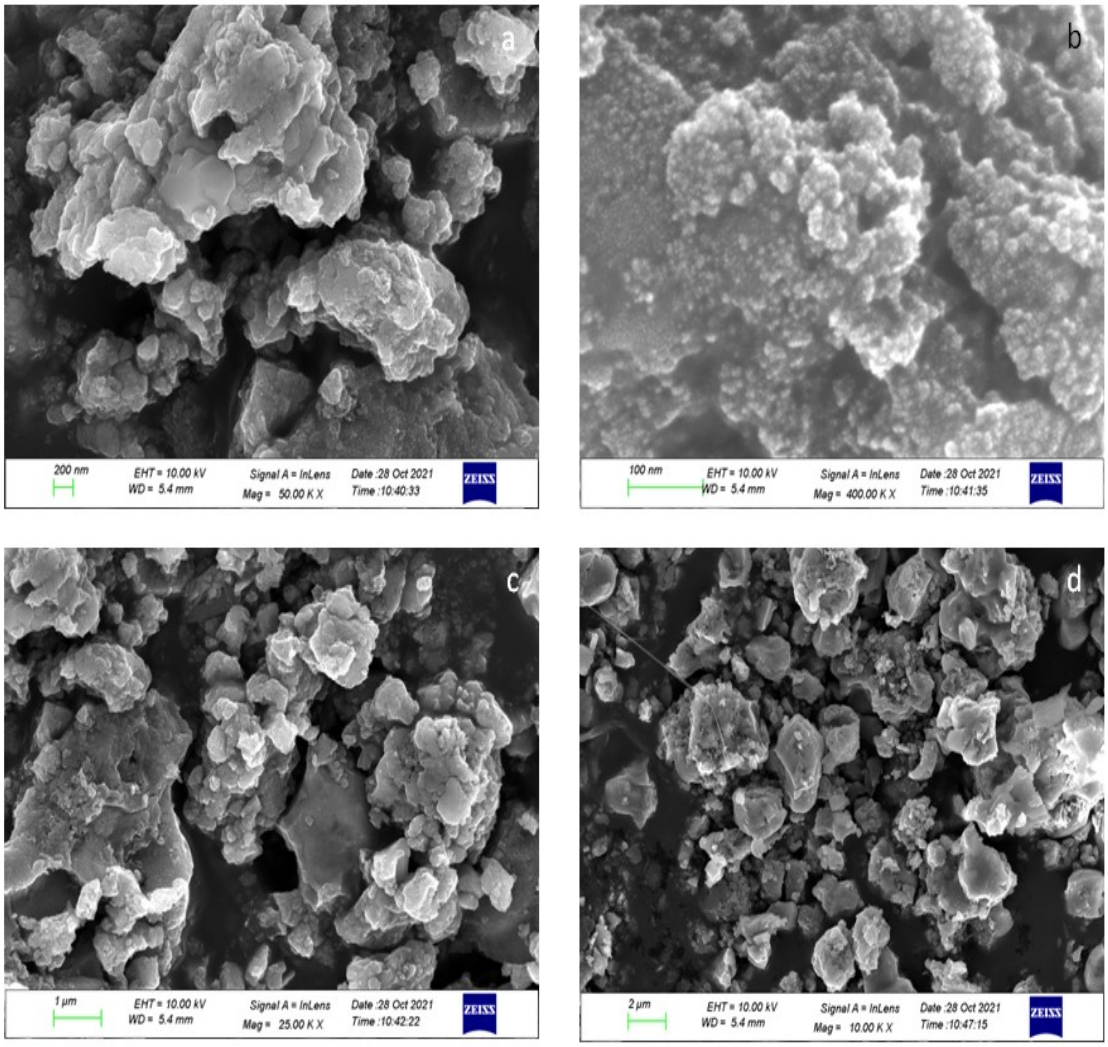

Fig.3.19 FESEM images of 1mol% Mn-doped TiO_2 prepared from potassium titanium oxide oxalate and calcined at 450 ˚C: (a-d) are images at different magnifications.

The EDS spectrum of 1 mol% Mn-doped TiO_2 is shown in Figure 3.20. The EDS spectrum shows that the manganese ions have been doped into the crystal lattice of TiO_2 and that the concentration of Mn^{2+} ion in the Mn doped TiO_2 sample is 0.09%, which is in good agreement with the concentration of Mn^{2+} used in the experiment.

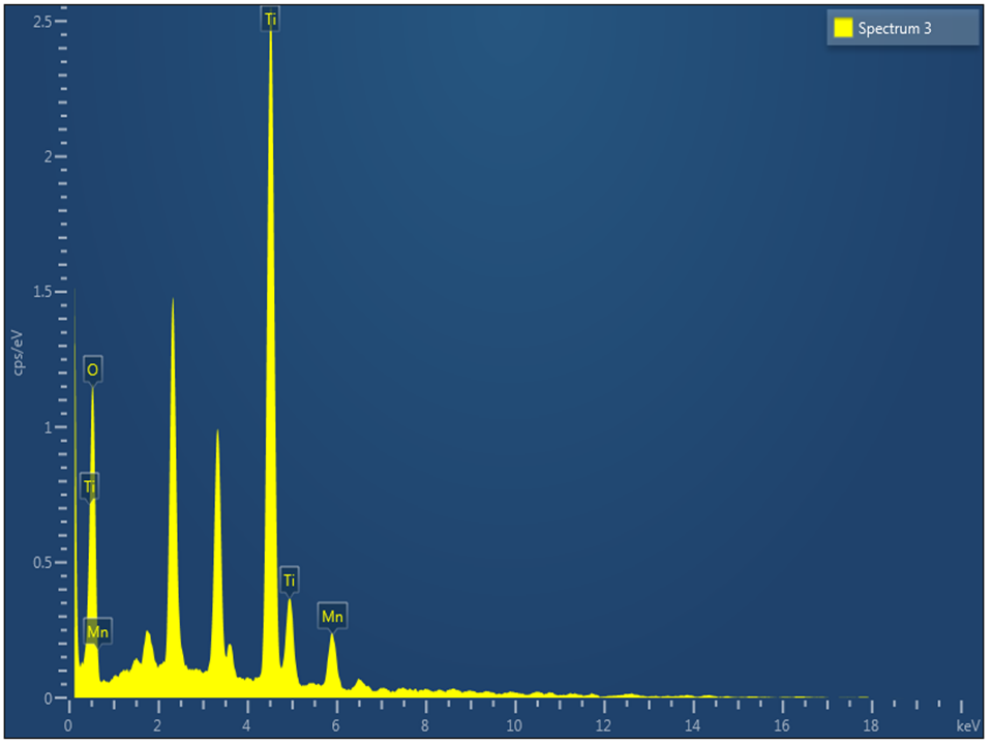

Fig. 3.20 EDS spectrum of 1 mol% Mn-doped TiO_2.

Figure 3.21 shows the surface morphologies of 1 mol% Cu-doped TiO_2 after calcination at 450 ˚C. Particles are agglomerated with nearly spherical shape and the average particle size was in the range of 10 nm.

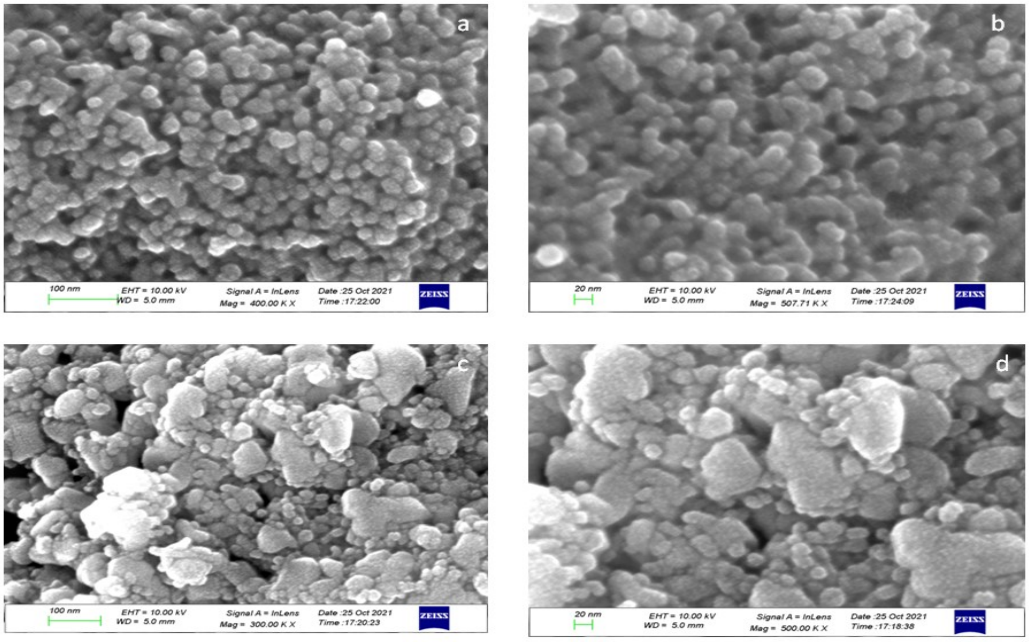

Fig.3.21 FESEM image of 1mol% Cu-doped TiO_2 prepared from potassium titanium oxide oxalate and calcined at 450 ˚C: (a-d) are images at different magnifications.

The EDS spectrum of 1 mol% Cu-doped TiO_2 is presented in Figure 3.22. The presence of copper ion in the doped TiO_2 sample was confirmed by the EDS spectrum.

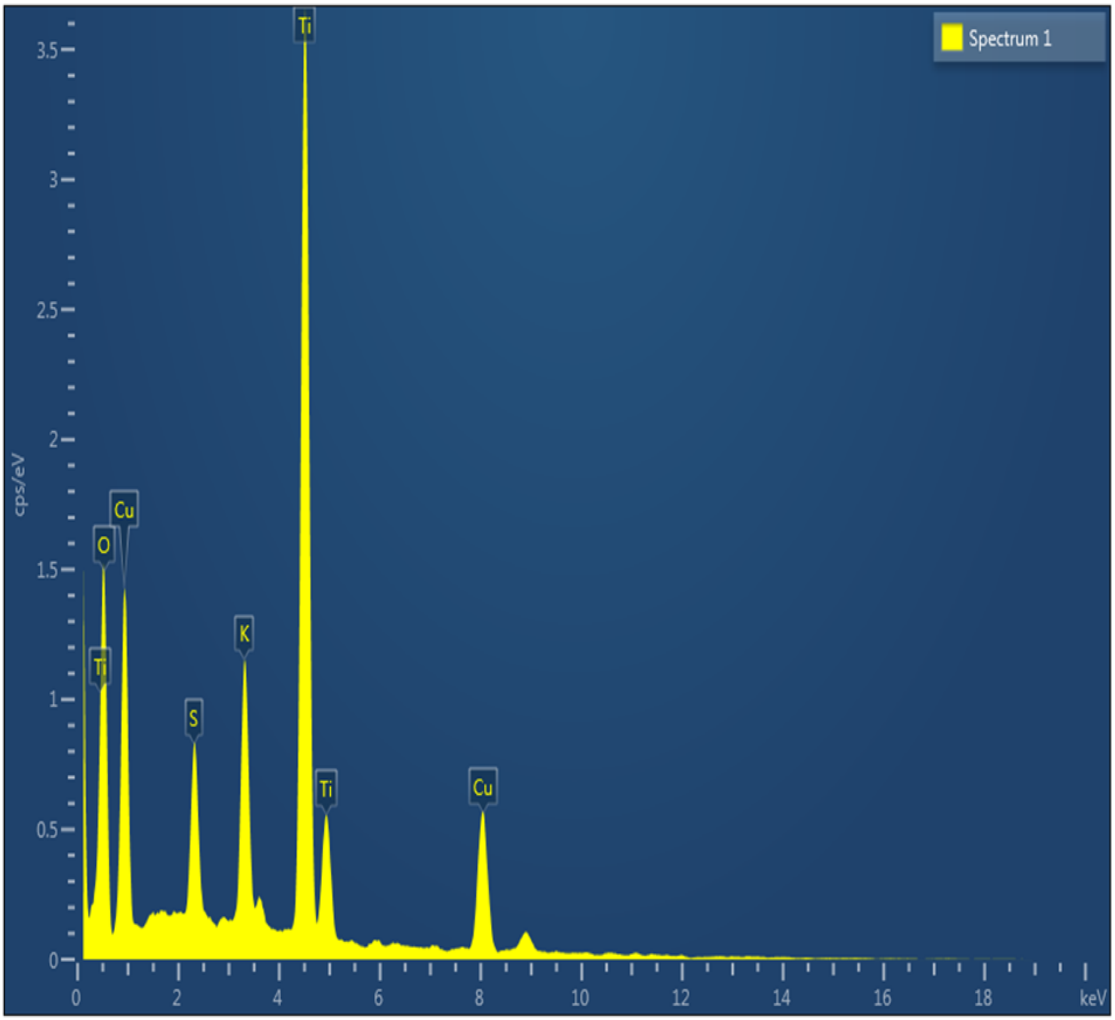

Fig. 3.22 EDS spectrum of 1 mol% Cu-doped TiO_2.

FESEM micrograph of 1 mol% C-doped TiO_2 at different magnification are presented in Figure 3.23. The particles are found to be nanospheres of irregular size, that are aggregated together and formed into nanoflowers, with a particle diameter of about 200 nanometers. From the FESEM images, we can conclude that morphology of the C-doped sample is different compared to undoped TiO_2.

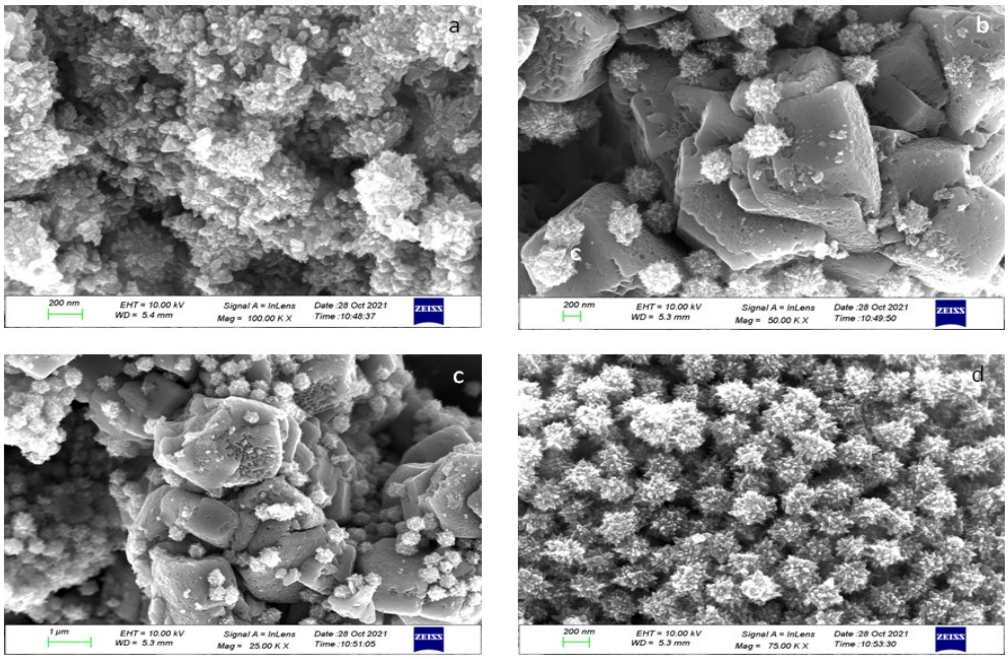

Fig.3.23 FESEM images of 1mol% C-doped TiO_2 prepared from potassium titanium oxide oxalate and calcined at 450 ˚C: (a-d) are images at different magnifications.

Figure 3.24 shows the EDS spectrum of 1 mol% C-doped TiO_2. The spectrum confirmed the presence of carbon in the doped sample.

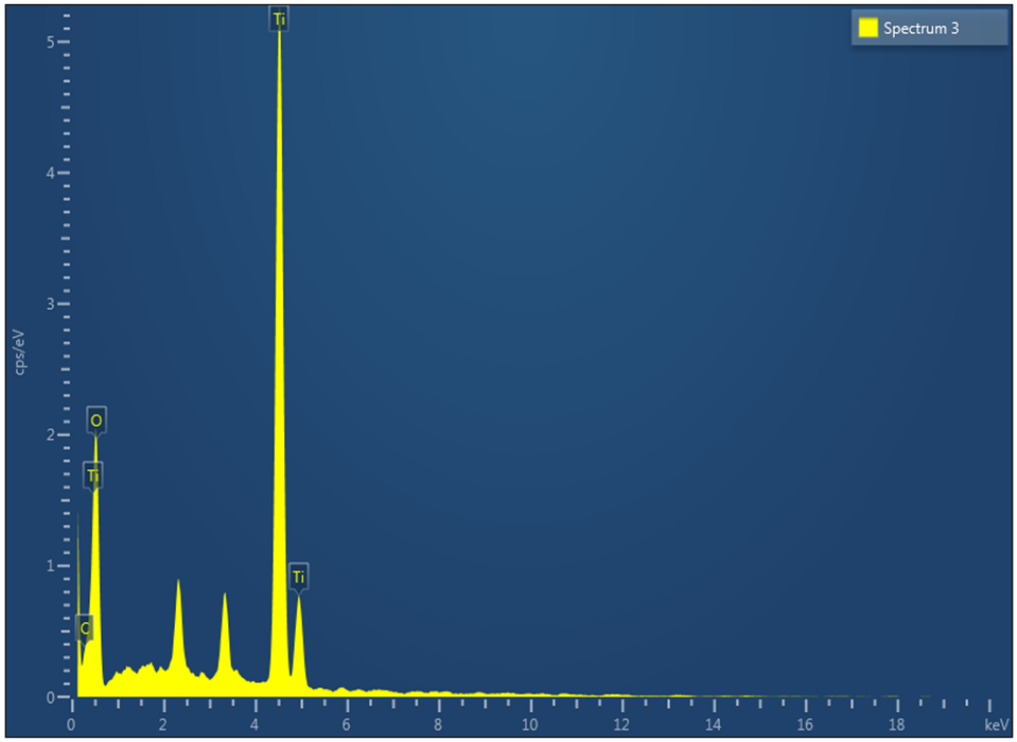

Fig. 3.24 EDS spectrum of 1 mol% C-doped TiO_2.

3.3.6 FT-IR spectral studies

The FT-IR spectra of the precipitate obtained after refluxing potassium titanium oxide oxalate and TiO_2 after calcination of the precipitate are given in Figure 3.25. The FT-IR spectra of oxalate complex show the absorption bands corresponding to different modes of the oxalate group at 1666 cm^{-1}, 1460 cm^{-1} and 1244 cm^{-1}. These peaks confirmed the formation of titanium oxalate complex [$Ti_2O_3(H_2O)_2(C_2O_4).3H_2O$], which are consistent with XRD data.[73] The broad band, at 3400 cm^{-1} is due to symmetric and antisymmetric stretching vibrational modes of adsorbed water molecules. In the FT-IR spectra of TiO_2 sample calcined at 450 ˚C, the peak corresponding to oxalate group was completely absent confirming the complete decomposition of titanium oxalate complex to TiO_2. These results are also consistent with the XRD data. The Ti-O-Ti stretching vibration band of TiO_2 was observed at 490 cm^{-1} and this band confirms the formation of TiO_2.[74]

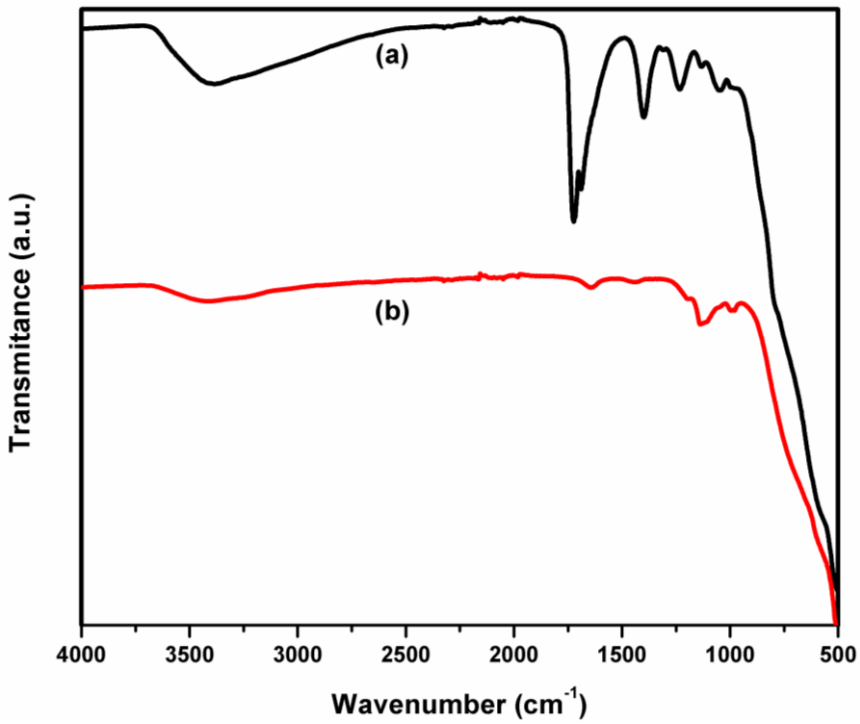

Fig. 3.25 FT-IR spectra of the precipitate obtained by refluxing a) potassium titanyl oxalate aqueous solution and b) sample after calcinations at 450 ˚C.

The FT-IR spectra of precipitate obtained by refluxing the aqueous solution of titania precursor along with the metal salts used for doping are presented in Figure 3.26. The FT-IR spectra of doped TiO_2 calcined at 450 ˚C were similar to pure TiO_2 and shown in Figure 3.27. In the doped TiO_2 samples calcined at 450 ˚C, the peak

corresponding to oxalate group was completely absent confirming the complete decomposition of titanium oxalate complex to TiO_2 in the doped TiO_2 samples also.

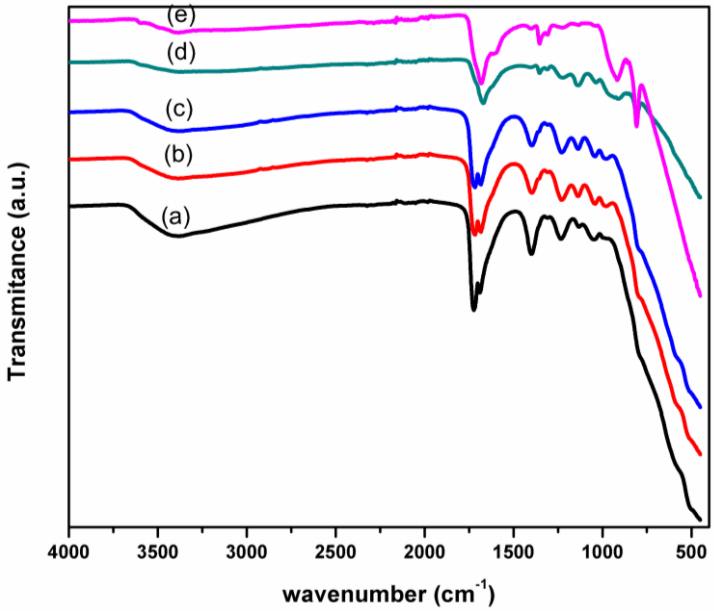

Fig. 3.26 FT-IR spectra of the precipitate obtained by refluxing pure potassium titanyl oxalate aqueous solution and that of the precipitates obtained by potassium titanyl oxalate with 1 mol% Co, 1 mol% Ni, 1 mol% Mn, and 1 mol% C are given in Figure 3.25 (a-e), respectively.

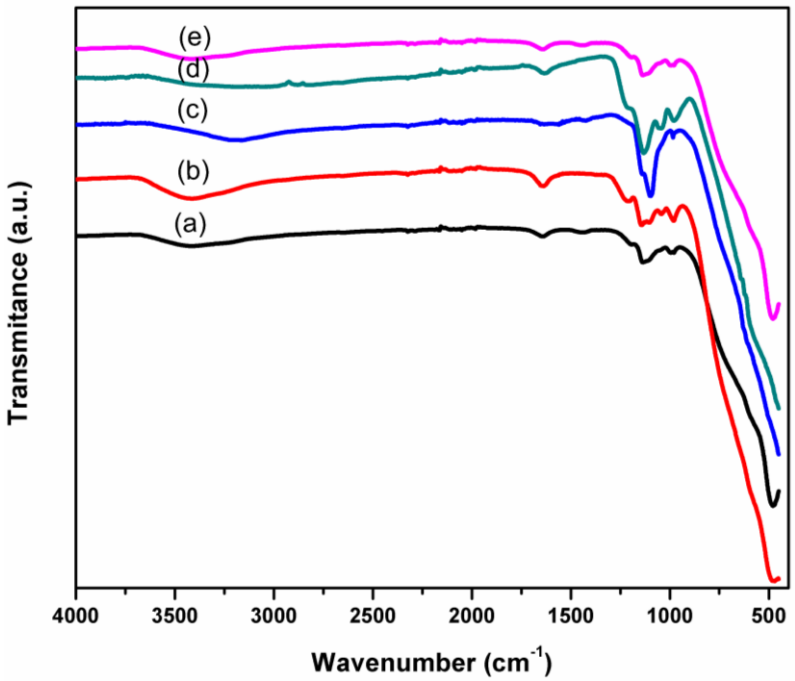

Fig. 3. 27 FT-IR spectra of a) TiO_2 and b) 1 mol% Co-doped TiO_2, c) 1 mol% Ni-doped TiO_2, d) 1 mol% Mn-doped TiO_2 and e) 1 mol% C-doped TiO_2 calcined at 450 ˚C.

3.3.7 UV-Visible diffuse reflectance spectra (DRS) and bandgap determination

UV-Visible diffuse reflectance spectrum was recorded to study the optical absorption property of the TiO_2 and 1 mol% doped TiO_2 samples, after calcination at 450 ˚C are presented in Figure 3.28. The DRS spectra show that the TiO_2 possess a near visible sharp absorption edge at 400 nm with λ_{max} peak at 365 nm. This supports the presence of rutile phase in the TiO_2. This band arises due to the charge-transfer from the valence band formed by 2p orbitals of the oxide ions to the conduction band formed by 3d t_{2g} orbitals of the Ti^{4+} cations.[75,76]

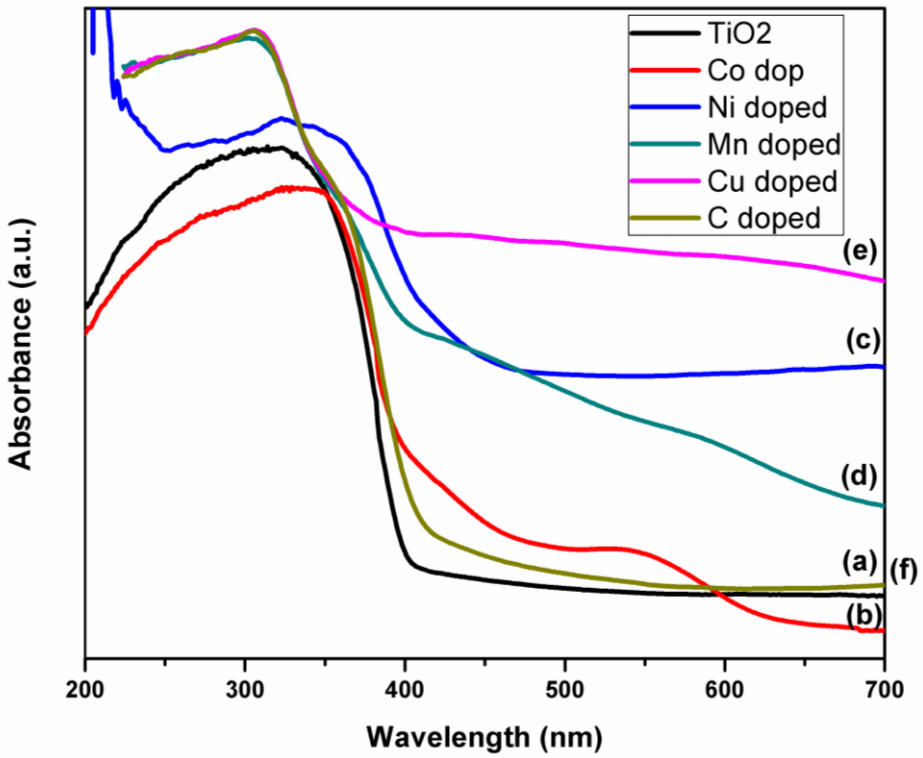

Fig. 3.28 i) Diffuse reflectance spectra of a) TiO_2, b)1 mol% Co-doped TiO_2, c)1 mol% Ni-doped TiO_2, d)1 mol% Mn-doped TiO_2, e)1 mol% Cu-doped TiO_2, f)1 mol% C-doped TiO_2 calcined at 450 ˚C.

Two absorption edges have been observed for 1 mol% Co-doped TiO_2, first peak is observed at 380 nm and second peak at 542 nm. The origin of absorption peak at 542 nm is attributed to Co^{2+} to Ti^{4+} charge transfer transition.[76,77] The high photoactivity of the 1 mol% Co-doped TiO_2 can be attributed to the presence of above charge transfer band.

Compared to pure TiO_2, 1 mol% Ni doped TiO_2 shows two absorption bands, one broad absorption band is in ultraviolet region and other one is in visible region.[78] Its

absorption maximum in UV region is at about 343 nm. Absorption in the visible region is due to crystal field splitting of $3d^8$ orbital.[79] The absorption edge of 1 mol% Ni doped TiO_2 sample is red shifted to visible region (490 nm) compared to pure TiO_2. These results are consistent with previous report on Ni-doped TiO_2 in literature.[80] The absorption maximum in the visible region is 695 nm. The absorption in the visible region is due to charge transfer from Ni^{2+} to Ti^{4+} ion.[79] Bashir et al. has also reported the appearance of the new absorption band in the visible region caused by Ni^{+2} doping and slight red shift in bandgap.[81]

The TiO_2 can absorb the visible light due to Mn^{2+} ion doping. The band gap energy and band structure of TiO_2 have been modified by Mn^{2+} ion doping. The intensive absorption band is present in the UV region ranging from 200-398 nm. The absorption band edge of TiO_2, which is situated at 400 nm, is red shifted to 465 nm after Mn^{2+} ion doping. It may be due to the presence of new electronic state formed after Mn^{2+} ion doping in the middle of the TiO_2 band gap.[82] As a result, the charge transfer gap between d electrons of Manganese ion and conduction band of TiO_2 is reduced.

The UV-Visible diffuse reflectance spectra, of 1 mol% Cu doped TiO_2 sample shows UV absorption as well as extended visible light absorption, up to 700 nm.[83] The change in colour from white to black in TiO_2 confirms the presence of Cu doping. The absorption spectra shows the band edge at 450 nm.[84] The absorption in UV region is caused by charge transfer from O2p to Cu d-state. The absorption in visible region is due to d-d electronic transition of Cu^{2+} ion.

UV-Visible diffuse reflectance spectra were recorded to confirm the presence of carbon in the doped TiO_2 sample. It is clear in the image that absorption edge of the 1mol% C-doped TiO_2 sample is extended to 426 nm with absorption maximum at 300 nm, indicating that carbon doping is effective for extending the absorption to visible light region.[85]

The bandgap energy of TiO_2 and 1 mol% doped TiO_2 samples are calculated by plotting absorption coefficient $(F(R)*E)^{0.5}$ vs energy of absorbed light using Kubelka-Munk function.[86] Figure 3.29 shows the graph of Kubelka-Munk function versus the energy of the absorbed light. From the graph, bandgap is calculated to be 3.0 eV for pure TiO_2 and 2.8 eV for 1 mol% Co-doped TiO_2[87-89]. Nguyen et al. has reported a

bandgap of 2.38 eV for TiO_2 doped with the same amount of cobalt (1%). [44] After Ni^{2+} ion doping, the band gap of Ni-doped TiO_2 has a significantly decreased and the Ni-doped TiO_2 has a lowest band gap of 2.5 eV.[90]

The bandgap energy of Mn-doped TiO_2 is found to be 2.6 eV. This result supports that the Mn^{2+} cations are incorporated into the TiO_2 host lattice. The Mn-doping is most effective to shift the absorption of TiO_2 to the visible region. The bandgap energy for 1 mol% Cu-doped TiO_2 is 2.7 eV.

The bandgap energy calculated from the Kubelka-Munk function for all the doped samples are listed in the Table 3.2. The reduction in bandgap energy with Cu doping is attributed to the intercalation of Cu^{2+} ions in the TiO_2 lattice and generation of oxygen vacancies due to charge compensation effect.[91] The lowering of bandgap ensures the visible light absorption. The optical bandgap calculated for 1 mol% C-doped TiO_2 is found to be 2.9 eV, which is smaller than that of pure TiO_2 indicating that the carbon is doped into TiO_2 crystal lattice.

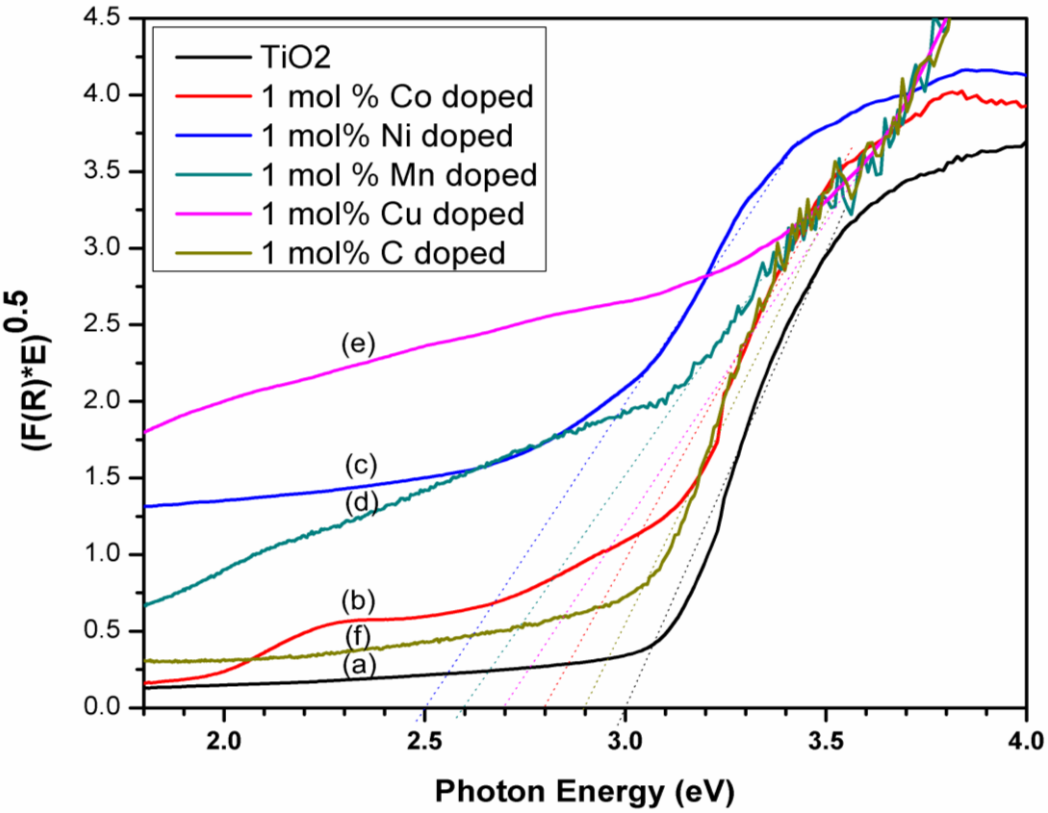

Fig. 3.29 Plot of the Kubelka-Munk function versus the energy of absorbed light. a) TiO_2, b)1 mol% Co-doped TiO_2, c)1 mol% Ni-doped TiO_2, d)1 mol% Mn-doped TiO_2, e)1 mol% Cu-doped TiO_2, f)1 mol% C-doped TiO_2calcined at 450 ˚C.

Table 3.2. Bandgap energy of doped sample.

Sample	bandgap (eV)	surface area ($m^2 g^{-1}$)
TiO_2	3	97.04
1 mol% Co-doped TiO_2	2.8	14.14
1 mol% Ni-doped TiO_2	2.5	88.48
1 mol% Mn-doped TiO_2	2.6	44.55
1 mol% Cu-doped TiO_2	2.7	36.19
1 mol% C-doped TiO_2	2.9	104.66

3.3.8 BET surface area analysis

BET adsorption desorption isotherms were plotted to calculate the specific surface area of TiO_2 and 1 mol% Co-doped TiO_2 calcined at 450 ˚C and are given in the Figure 3.30. At a relatively low pressure, monolayer of nitrogen was adsorbed on the material and this is shown by the initial part of the isotherm. As the pressure increases multilayer adsorption takes place as seen by a steep rise in the isotherm. A typical type-II isotherm is observed in both the samples. According to IUPAC classification this is a characteristic feature for macroporous (intra-particle pores) materials.[92] The isotherm indicates that the nanoparticles are aggregated to form macropores. The surface area of pure TiO_2 was found to be 97.04 $m^2 g^{-1}$ by BET method. For 1 mol% Co-doped TiO_2 it was only14.14 $m^2 g^{-1}$. Thus the surface area of TiO_2 has been significantly reduced by cobalt ion doping. The BET surface area, pore volume and pore diameter of the pure and 1 mol% Co-doped TiO_2 are presented in Table 3.3. The decrease in surface area may be due to increased crystallinity of Co-doped TiO_2. This observation is also consistent with XRD and HRTEM results.

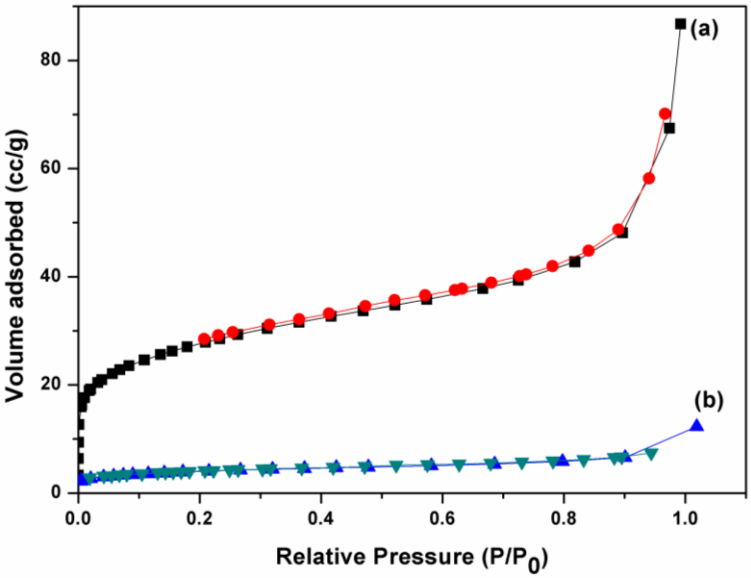

Fig. 3.30 Nitrogen physisorption isotherms of a) mixed phase TiO_2 and b) 1 mol% Co-doped TiO_2.

The nitrogen adsorption-desorption isotherms of 1 mol% Ni-doped TiO_2 is given in Figure 3.31. According to the IUPAC classification, 1 mol% Ni-doped TiO_2 exhibit type-IV isotherms and H1-type hysteresis loops. The surface area of 1 mol% Ni-doped TiO_2 powder is 88.48 $m^2 g^{-1}$. When TiO_2 was doped with 1 mol% Ni, crystallite size was increased and the BET surface area was reduced. The values of BET surface area, pore diameter and pore volume of 1 mol% Ni-doped TiO_2 are presented in Table 3.3.

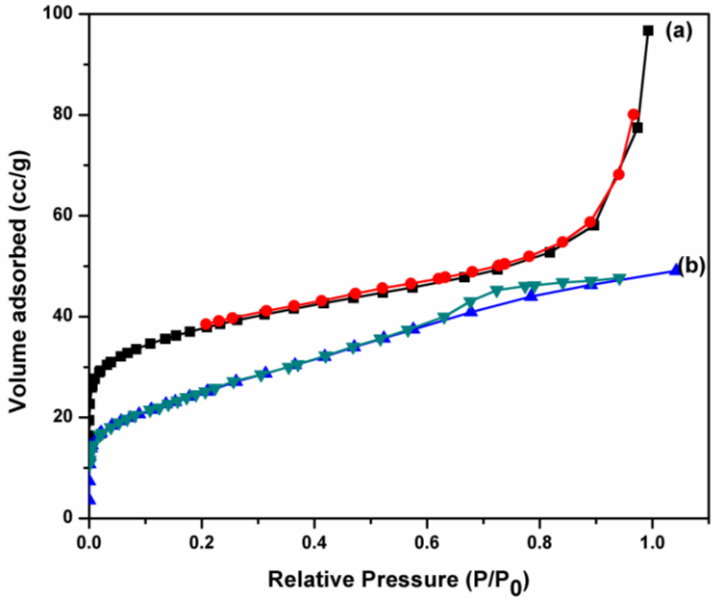

Fig. 3.31 Nitrogen physisorption isotherms of a) mixed phase TiO_2 and b) 1 mol% Ni-doped TiO_2.

The surface area of 1 mol% Mn doped TiO_2 was calculated using nitrogen adsorption-desorption measurements. Figure 3.32 displays the nitrogen adsorption-desorption isotherm. The isotherm has a typical type IV isotherm curve, indicating that the sample has mesoporous structure. The specific surface area is calculated to be 44.55 $m^2 g^{-1}$.

Table 3.3 Summary of BET surface area and pore size measurement

Sample	BET Surface area ($m^2 g^{-1}$)	Pore Volume ($cm^3 g^{-1}$)	BJH desorption pore size (nm)	Pore diameter (nm)
TiO_2	97.04	0.1028	1.26	5.3713
Co-doped TiO_2	14.14	0.0128	1.26	4.7776
Ni-doped TiO_2	88.485	0.0559	1.96	3.3648
Mn-doped TiO_2	44.554	0.0168	1.26	2.6445
Cu-doped TiO_2	36.196	0.0280	1.26	3.9441
C-doped TiO_2	104.66	0.0859	1.26	3.2857

The BET measurements were used to determine the surface area, pore size, and total pore volume of 1 mol% Cu-doped TiO_2. The N_2 adsorption-desorption isotherms of 1 mol% Cu-doped sample showed a typical type-II isotherm (Figure 3.33). This is a defining feature of macroporous (intra-particle pores) materials, according to IUPAC classification. The pore size was determined using the BJH method and are listed in Table 3.3.

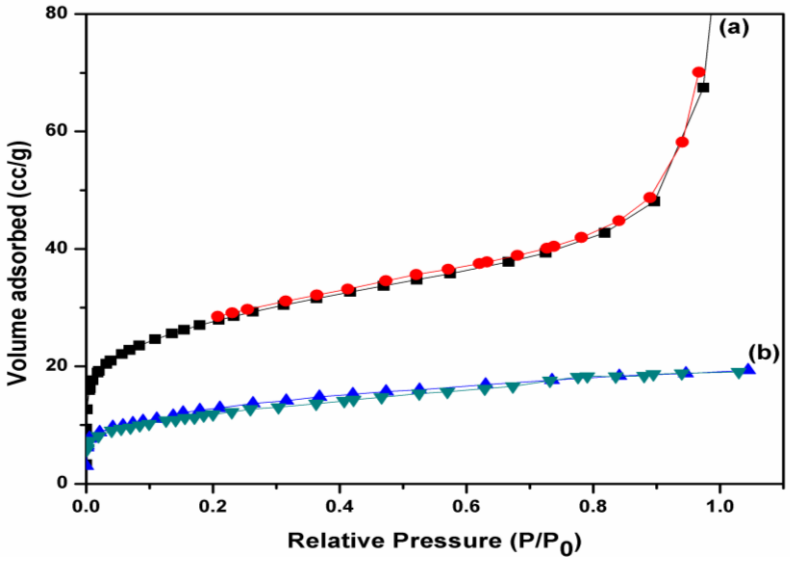

Fig. 3.32 Nitrogen physisorption isotherms of a) mixed phase TiO_2 and b) 1 mol% Mn-doped TiO_2.

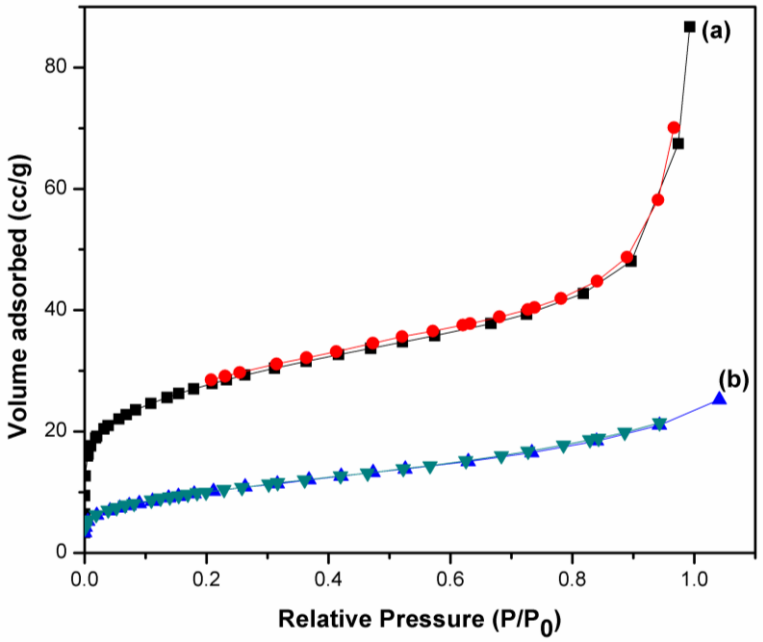

Fig. 3.33 Nitrogen physisorption isotherms of a) mixed phase TiO_2 and b) 1 mol% Cu-doped TiO_2.

The N_2 adsorption-desorption isotherms of pure TiO_2 and 1 mol% C-doped TiO_2 are shown in Figure 3.34. The 1 mol% C-doped sample is constituted of mesopores and micropores, as shown by the type IV adsorption isotherm with a hysteresis loop.[93] The 1 mol% C-doped TiO_2 sample has a surface area of 104.66 m^2 g^{-1} and an average pore diameter of 3.2857 nm, as shown in Table 3.3.

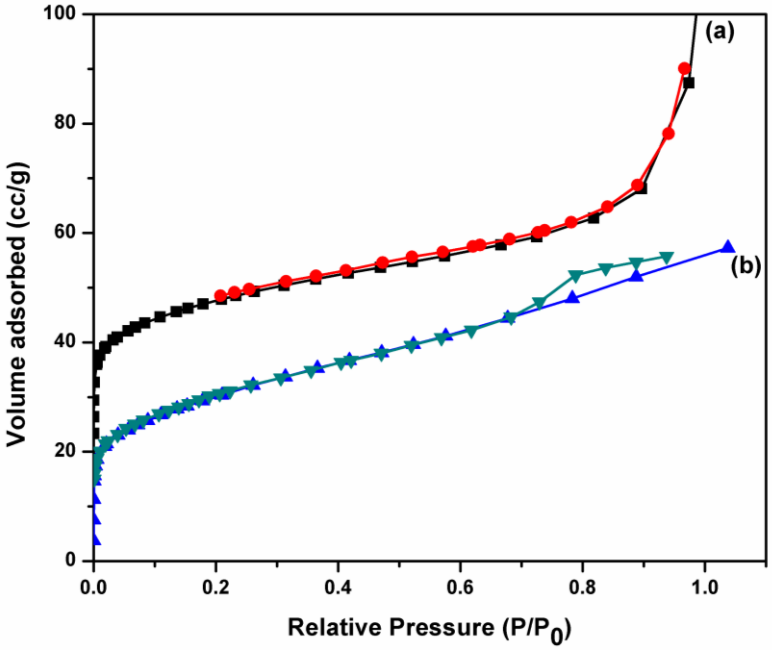

Fig. 3.34 Nitrogen physisorption isotherms of a) mixed phase TiO_2 and b) 1 mol% C-doped TiO_2.

3.3.9 Photocatalytic activity

The photocatalytic activity of mixed phase TiO_2 and 1 mol% doped TiO_2 (Co, Ni, Mn, Cu and C) for methylene blue dye degradation under LED visible light were studied and the results are shown in the Figure 3.35. The intensity of the absorption peak at 664 nm in the UV visible spectra of methylene blue was used to study the rate of its degradation. The percentage of photocatalytic degradation of methylene blue was determined by the following equation

$$\eta = (1 - A/A0) = (1 - C/C0)\ X\ 100 \qquad (11)$$

A_0 is the initial absorbance and A is the absorbance at time t and C_0 and C are the corresponding concentrations.

The percentage of degradation for 1 mol% Co-doped TiO_2, 1 mol% Ni-doped TiO_2, 1 mol% Mn-doped TiO_2, 1 mol% Cu-doped TiO_2, 1 mol% C-doped TiO_2 and pure TiO_2 after 5 hours of visible light irradiation were 17%, 21%, 15%, 12%, 11% and 9%, respectively, whereas these values were 74%, 79%, 70%, 65%, 62% and 60%, respectively, after 15 hours of irradiation. Photograph of the samples after photodegradation are given in Figure 3.36. These results show that the photocatalytic activity of the doped TiO_2 samples were generally higher than that of the pure TiO_2. Furthermore, the photocatalytic activity of doped TiO_2 varied from sample to sample. The lower bandgap of titania (2.5 eV), caused by the incorporation of Ni^{2+} ions into the titania lattice, makes 1 mol% Ni-doped TiO_2 more effective for methylene blue degradation. From the BET surface area measurement, the surface area of 1 mol% Ni-doped TiO_2 was found to be very high. This also explains its higher photocatalytic activity. Moreover, doping with Ni^{2+} ions may introduce trapping sites which may reduce the recombination of charge carriers.

These results indicate that the doping of Co^{2+} ions expands the photo response of TiO_2 to visible region. Dorraj et al. reported improved visible-light photocatalytic activity for TiO_2, co-doped with copper and iodine. The improved activity was attributed to strong visible light absorption and synergistic effects of Cu and I dopants causing effective charge separation.[94] Cao et al. reported improved visible light photocatalytic activity for C, N and Ce co-doped TiO_2 and they attributed it to a

lowered band gap of 2.14 eV.[95] The higher activity of Co-doped TiO_2 can be attributed to low bandgap energy (2.8 eV) leading to higher absorption of visible light.

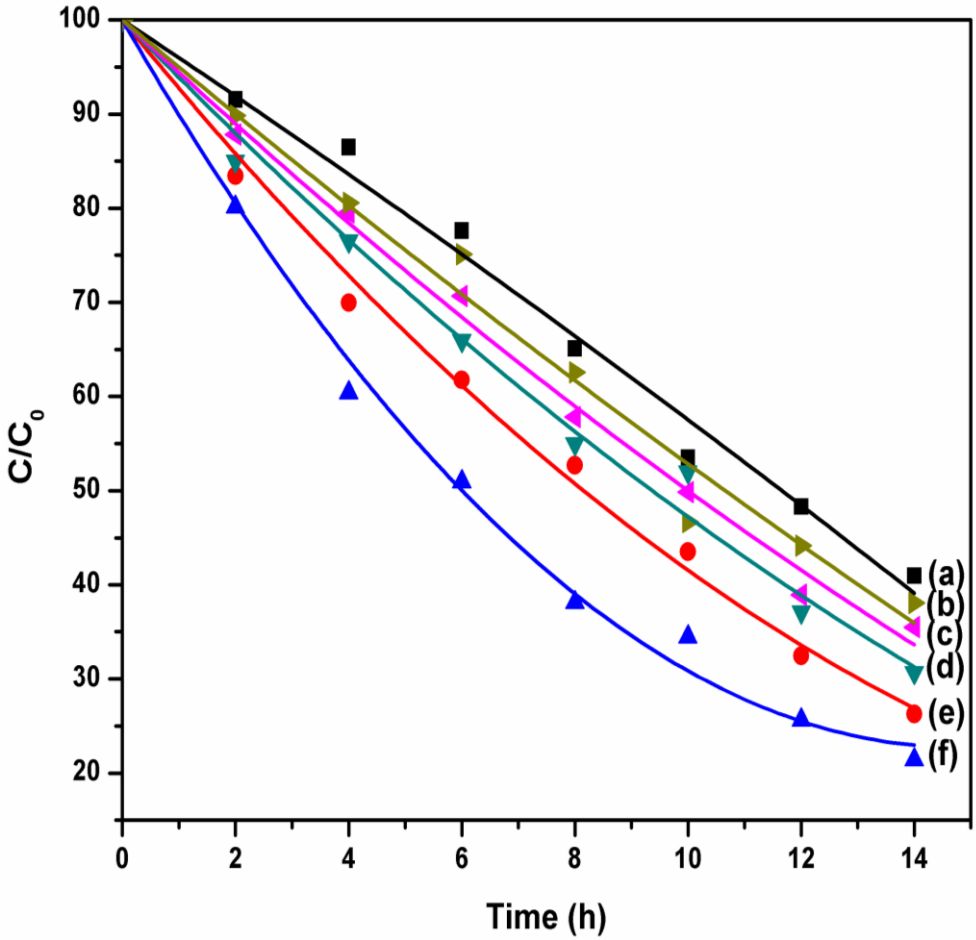

Fig. 3. 35 Plot of relative concentration as a function of time for the degradation of dye under LED visible light (a) TiO_2, b) 1 mol% C-doped TiO_2 c) 1 mol% Cu-doped TiO_2, d) 1 mol% Mn-doped TiO_2, e) 1 mol% Co-doped TiO_2 and f) 1 mol% Ni-doped TiO_2.

1 mol% Mn-doped TiO_2 has a greater photocatalytic activity than pure TiO_2. The increased defect sites generated by Mn^{2+} doping, resulting in increased optical absorption in the visible range, is responsible for the quicker degradation rate of MB under visible light irradiation in 1 mol% Mn-doped TiO_2.[96] The Mn^{2+} ion doping increases the life time of excited charge carriers resulting in the enhanced photocatalytic activity.

Doping with Cu also can create new electronic states in the band gap of TiO_2 and enriches the visible absorption spectrum by the Cu3d→Ti3d optical transition, lowering band gap energy which enhances the methylene blue degradation.[91] Doping inhibits recombination rate. The methylene blue degradation was also enhanced by carbon-doping, which reduces the band gap of TiO_2 to 2.9 eV.

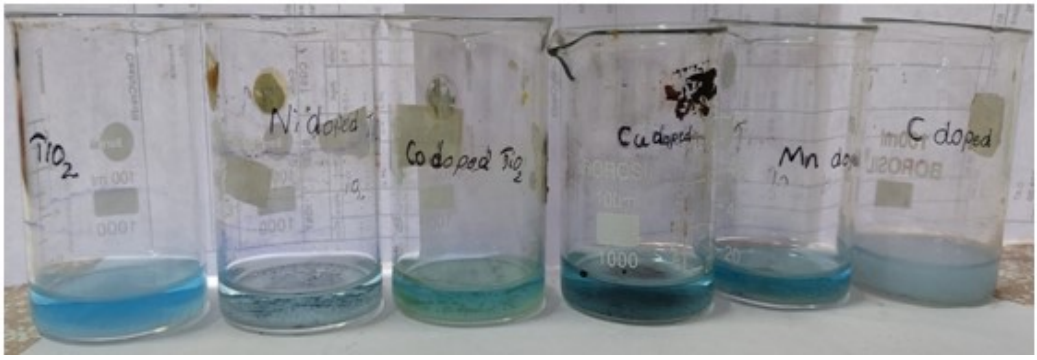

Fig. 3.36 Photograph of dye degradation test of doped and undoped TiO_2.

Many oxygen defects are produced during calcination at 450 ˚C due to desorption of surface oxygen and this improves photocatalytic activity of TiO_2.[97] In general, the photocatalytic activity depends on several parameters, such as phase structure, surface area and crystalline size etc. The mechanism of the photocatalytic activity of undoped TiO_2 may be explained as follows; when TiO_2 catalyst is exposed to light, electrons in the valence band are excited to the conduction band leaving holes in the valence band. The lower part of the conduction band is formed by overlapping the 3d-orbitals of Ti^{4+}. Valence band is formed by overlapping 2p-orbitals of oxygen. Figure 3.37 shows the energy band structure of mixed phases of anatase and rutile TiO_2.[98] The photogenerated electrons are captured by oxygen vacancies and facilitate the reduction of electron acceptors adsorbed on the active site of the photocatalyst surface. The electrons can be scavenged by O_2 and produces superoxide radicals $O_2^{\cdot -}$. The holes promote oxidation of electron donors. Positive holes can accept electrons from H_2O or OH^- ions and undergo oxidation to produce $HO^{\cdot}$ radicals. These radicals accelerate the decomposition of dye. The above properties of TiO_2 may be used for the practical application of wastewater treatment under sunlight. Charge carrier plays the vital role in the photocatalytic activity. These radicals decompose the dye to form CO_2 and H_2O. The high surface area creates more active sites.

$$TiO_2 + hv \longrightarrow e + h^+ \quad (1)$$

$$h^+ + H_2O \longrightarrow H^+ + OH^\bullet \quad (2)$$

$$e + O_2 \longrightarrow O_2^{-\bullet} \quad (3)$$

$$O_2^{-\bullet} + H^+ \longrightarrow HOO^\bullet \quad (4)$$

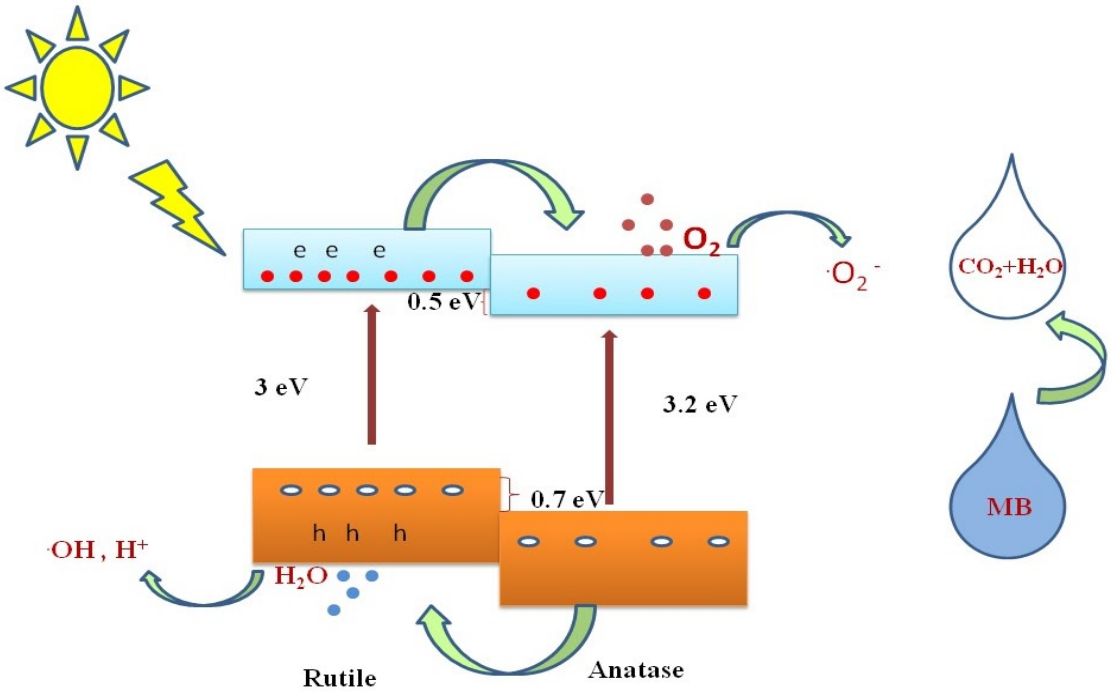

Fig. 3. 37 Schematic representation of the energy band structure of mixed phase of anatase and rutile TiO_2.

Introducing doping ions into the pure oxides did not show any change in the crystal structure but caused change in anatase rutile phase composition, a slight changes in their particle size and an increase in their photocatalytic activities. The photodegradation results show that the metal–doped TiO_2 exhibited a significant increase in the MB photodegradation rate comparable with that of pure TiO_2, This may be explained on the basis that the introduction of doping ions into the TiO_2 lattice can act as electron–hole separation centers and reduces the charge recombination rate. The carbon-doping into the TiO_2 lattice modifies the valence band level of TiO_2 and reduces the effective band gap energy and shift the light absorption into the visible light region. The UV Visible spectra of all doped samples showed that the doping ions

leads to an increase in the absorption in the visible region, and doped samples in general have higher photocatalytic activity than pure TiO_2.

3.4 Conclusion

In summary, nanocrystalline TiO_2 was synthesised from aqueous potassium titanium oxide oxalate by reflux method. The mixed phase anatase rutile nanocrystalline 1 mol% doped TiO_2 (Co, Ni, Mn, Cu and C) with varying rutile content were also synthesized. The complex $[Ti_2O_3(H_2O)_2(C_2O_4).\ 3H_2O]$ was formed during the reaction. The complex was decomposed to form anatase and rutile mixed phase TiO_2 on calcinations at 450 ˚C for one hour. The XRD, Raman spectra and TEM images confirm the formation of mixed phase TiO_2. The XRD spectra and TEM images of TiO_2 prepared from potassium titanyl oxide oxalate indicates the coexistence of anatase and rutile phases. The XRD results of TiO_2 obtained from potassium titanium oxide oxalate show that the primary particle size of anatase crystals is 8.3 nm and that of rutile crystals is 35 nm. Morphology and properties of TiO_2 depend upon the precursor and reaction conditions. Self-assembled uniform flower like structures were also found in the FESEM images of the mixed phase TiO_2. Agglomerated spherical particles were observed in single phase anatase TiO_2. On doping, the anatase-rutile phase composition was changed from 70:30 to 84:16, 60: 40, 71:29 and 33:67 on Co, Mn, Cu, Ni and C doping. The doped TiO_2 possessed visible light absorption and a reduction of bandgap. The surface area of TiO_2 was decreased during doping. The photocatalytic activity of TiO_2 and doped samples were tested by the degradation of methylene blue under white light LED irradiation. The doped TiO_2 exhibited higher photoactivity under white light LED irradiation than undoped TiO_2 and it can be attributed to lower bandgaps. Since solar light consists mainly of visible light (~49.4%), the better visible phtoactivity of doped TiO_2 indicate that these doped samples will be very useful for the fabrication of solar cells.

References

1. Alheety, M. A., Al-Jibori, S. A., Karadağ, A., Akbaş, H., & Ahmed, M. H. (2019). A novel synthesis of MnO_2, nanoflowers as an efficient heterogeneous catalyst for oxidative desulfurization of thiophenes. *Nano-Struct. Nano-Objects*, *20*, 100392.
2. Ferdous, Z., & Nemmar, A. (2020). Health impact of silver nanoparticles: a review of the biodistribution and toxicity following various routes of exposure. *International Journal of Molecular Sciences*, *21*(7), 2375.

3. Mahmood, A. R., Abdallah, I. Q., Alheety, M. A., Akbaş, H., & Karadağ, A. (2019). N, O-rich graphene oxide based eggshell membrane polymer: Preparation, characterization and its utility as nano sorbent for solid phase extraction of Pb (II) in various water samples. *In AIP Conference Proceedings*, 2144(1), 020003.

4. Alheety, N. F., Majeed, A. H., & Alheety, M. A. (2019). Silver nanoparticles anchored 5-methoxy benzimidazol thiomethanol (MBITM): Modulate, characterization and comparative studies on MBITM and Ag-MBITM antibacterial activities. *Journal of Physics: Conference Series,* 1294(5), 052026.

5. Alheety, M. A., & Hameed, A. A. (2018). Synthesis, characterization and antifungal activity of coated silver nanoparticles-nystatin and coated silver nanoparticles-clotrimazol. *Tikrit Journal of Pure Science*, *23*(7), 63-70.

6. Majeed, A. H., Hussain, D. H., Al-Tikrity, E. T. B., & Alheety, M. A. (2020). Poly (o-Phenylenediamine-GO-TiO_2) nanocomposite: modulation, characterization and thermodynamic calculations on its H_2 storage capacity. *Chemical Data Collections*, *28*, 100450.

7. Jasem, L. A., Hameed, A. A., Al-Heety, M. A., Mahmood, A. R., Karadağ, A., & Akbaş, H. (2019). The mixture of silver nanosquare and silver nanohexagon: green synthesis, characterization and kinetic evolution. *Materials Research Express*, *6*(8), 0850f9.

8. Alheety, M. A., Al-Jibori, S. A., Ali, A. H., Mahmood, A. R., Akbaş, H., Karadağ, A., Uzun, O., & Ahmed, M. H. (2019). Ag (I)-benzisothiazolinone complex: synthesis, characterization, H_2 storage ability, nano transformation to different Ag nanostructures and Ag nanoflakes antimicrobial activity. *Materials Research Express, 6*(12), 125071.

9. Adnan, L. A., Alheety, N. F., Majeed, A. H., Alheety, M. A., & Akbaş, H. (2021). Novel organic-inorganic nanohybrids (MnO_2 and Ag nanoparticles functionalized 5-methoxy-2-mercaptobenzimidazole): One step synthesis and characterization. *Materials Today: Proceedings*, *42*, 2700-2705.

10. Alheety, N. F., Hamad, M. A., Kalif, A. Z., Alheety, M. A., Mohammed, M. Y., & Akbaş, H. (2021). Biogenic silver nanowires for hybrid silver functionalized benzothiazolilthiomethanol as a novel organic–inorganic nanohybrid. *Mater. Today: Proc. Materials Today: Proceedings*, *43*, 2076-2082.

11. Wang, C., Zhan, Y., & Wang, Z. (2018). TiO_2, MoS_2, and TiO_2/MoS_2 heterostructures for use in organic dyes degradation. *Chemistry Select*, *3*(6), 1713-1718.

12. Zhu, T., & Gao, S. P. (2014). The stability, electronic structure, and optical property of TiO_2 polymorphs. *The Journal of Physical Chemistry C*, *118*(21), 11385-11396.

13. Kuvarega, A. T., Krause, R. W., & Mamba, B. B. (2011). Nitrogen/palladium-codoped TiO_2 for efficient visible light photocatalytic dye degradation. *The Journal of Physical Chemistry C*, *115*(45), 22110-22120.

14. Lacerda, A. M., Larrosa, I., & Dunn, S. (2015). Plasmon enhanced visible light photocatalysis for TiO_2 supported Pd nanoparticles. *Nanoscale*, *7*(29), 12331-12335.

15. Kumar, S. G., & Devi, L. G. (2011). Review on modified TiO_2 photocatalysis under UV/visible light: selected results and related mechanisms on interfacial charge carrier transfer dynamics. *The Journal of physical chemistry A*, *115*(46), 13211-13241.

16. Haider, A. J., Jameel, Z. N., & Al-Hussaini, I. H. (2019). Review on: titanium dioxide applications. *Energy Procedia*, *157*, 17-29.

17. Truong, Q. D., Le, T. H., Liu, J. Y., Chung, C. C., & Ling, Y. C. (2012). Synthesis of TiO_2 nanoparticles using novel titanium oxalate complex towards visible light-driven photocatalytic reduction of CO_2 to CH_3OH. *Applied Catalysis A: General*, *437*, 28-35.

18. Stephen, L. (2020). Titanium dioxide versatile solid crystalline: An overview. *Assorted Dimensional Reconfigurable Materials*.

19. Nakata, K., & Fujishima, A. (2012). TiO_2 photocatalysis: Design and applications. *Journal of photochemistry and photobiology C: Photochemistry Reviews*, *13*(3), 169-189.

20. Wang, X., Zhang, D., Xiang, Q., Zhong, Z., & Liao, Y. (2018). Review of water-assisted crystallization for TiO_2 nanotubes. *Nano-micro letters*, *10*(4), 1-28.

21. Hanaor, D. A., & Sorrell, C. C. (2011). Review of the anatase to rutile phase transformation. *Journal of Materials science*, *46*(4), 855-874.

22. Periyat, P., Baiju, K. V., Mukundan, P., Pillai, P. K., & Warrier, K. G. K. (2007). Aqueous colloidal sol–gel route to synthesize nanosized ceria-doped titania having high surface area and increased anatase phase stability. *Journal of sol-gel science and technology*, *43*(3), 299-304.

23. Zachariah, A., Baiju, K. V., Shukla, S., Deepa, K. S., James, J., & Warrier, K. G. K. (2008). Synergistic effect in photocatalysis as observed for mixed-phase nanocrystalline titania processed via sol-gel solvent mixing and calcination. *The Journal of Physical Chemistry C*, *112*(30), 11345-11356.

24. Yin, S., Zhang, Q., Saito, F., & Sato, T. (2003). Preparation of visible light-activated titania photocatalyst by mechanochemical method. *Chemistry Letters*, *32*(4), 358-359.

25. Zhang, H., & Banfield, J. F. (2000). Phase transformation of nanocrystalline anatase-to-rutile via combined interface and surface nucleation. *Journal of Materials Research*, *15*(2), 437-448.

26. Ohno, T., Sarukawa, K., Tokieda, K., & Matsumura, M. (2001). Morphology of a TiO_2 photocatalyst (Degussa, P-25) consisting of anatase and rutile crystalline phases. *Journal of Catalysis*, *203*(1), 82-86.

27. Barakat, M. A., Hayes, G., & Shah, S. I. (2005). Effect of cobalt doping on the phase transformation of TiO_2 nanoparticles. *Journal of nanoscience and nanotechnology*, *5*(5), 759-765.

28. Yamabi, S., & Imai, H. (2002). Crystal phase control for titanium dioxide films by direct deposition in aqueous solutions. *Chemistry of materials*, *14*(2), 609-614.

29. Xing, M., Li, X., & Zhang, J. (2014). Synergistic effect on the visible light activity of Ti^{3+} doped TiO_2 nanorods/boron doped graphene composite. *Scientific reports*, *4*(1), 1-7.

30. Yu, Y., Wen, W., Qian, X. Y., Liu, J. B., & Wu, J. M. (2017). UV and visible light photocatalytic activity of Au/TiO_2 nanoforests with Anatase/Rutile phase junctions and controlled Au locations. *Scientific reports*, *7*(1), 1-13.

31. Yu, J., Qi, L., & Jaroniec, M. (2010). Hydrogen production by photocatalytic water splitting over Pt/TiO_2 nanosheets with exposed (001) facets. *The Journal of Physical Chemistry C*, *114*(30), 13118-13125.

32. Singh, R., & Dutta, S. (2018). A review on H_2 production through photocatalytic reactions using TiO_2/TiO_2-assisted catalysts. *Fuel*, *220*, 607-620.

33. Luo, Z., Poyraz, A. S., Kuo, C. H., Miao, R., Meng, Y., Chen, S. Y., Jiang, T., Wenos, C., & Suib, S. L. (2015). Crystalline mixed phase (anatase/rutile) mesoporous titanium dioxides for visible light photocatalytic activity. *Chemistry of Materials*, *27*(1), 6-17.

34. Lomoth, R., & Ott, S. (2009). Introducing a dark reaction to photochemistry: photocatalytic hydrogen from [FeFe] hydrogenase active site model complexes. *Dalton Transactions*, (45), 9952-9959.

35 Hurum, D. C., Agrios, A. G., Gray, K. A., Rajh, T., & Thurnauer, M. C. (2003). Explaining the enhanced photocatalytic activity of Degussa P25 mixed-phase TiO_2 using EPR. *The Journal of Physical Chemistry B*, *107*(19), 4545-4549.

36. Hurum, D. C., Gray, K. A., Rajh, T., & Thurnauer, M. C. (2005). Recombination pathways in the Degussa P25 formulation of TiO_2: surface versus lattice mechanisms. *The Journal of Physical Chemistry B*, *109*(2), 977-980.

37. Baiju, K. V., Zachariah, A., Shukla, S., Biju, S., Reddy, M. L. P., & Warrier, K. G. K. (2009). Correlating photoluminescence and photocatalytic activity of mixed-phase nanocrystalline titania. *Catalysis letters*, *130*(1), 130-136.

38. Lee, J. S., You, K. H., & Park, C. B. (2012). Highly photoactive, low bandgap TiO_2 nanoparticles wrapped by graphene. *Advanced Materials*, *24*(8), 1084-1088.

39. Ullattil, S. G., Thelappurath, A. V., Tadka, S. N., Kavil, J., Vijayan, B. K., & Periyat, P. (2017). A sol-solvothermal processed 'Black TiO_2'as photoanode material in dye sensitized solar cells. *Solar Energy*, *155*, 490-495.

40. Peiris, S., de Silva, H. B., Ranasinghe, K. N., Bandara, S. V., & Perera, I. R. (2021). Recent development and future prospects of TiO_2 photocatalysis. *Journal of the Chinese Chemical Society*, *68*(5), 738-769.

41.Monazzam, P., & Kisomi, B. F. (2017). Co/TiO_2 nanoparticles: preparation, characterization and its application for photocatalytic degradation of methylene blue. Desalination and Water Treatment, 63 (2017) 283–292.

42. Daghrir, R., Drogui, P., & Robert, D. (2013). Modified TiO_2 for environmental photocatalytic applications: a review. *Industrial & Engineering Chemistry Research*, *52*(10), 3581-3599.

43. Kerrami, A., Mahtout, L., Bensouici, F., Bououdina, M., Rabhi, S., Sakher, E., & Belkacemi, H. (2019). Synergistic effect of Rutile-Anatase Fe-doped TiO_2 as efficient nanocatalyst for the degradation of Azucryl Red. *Materials Research Express*, *6*(8), 0850f5.

44. Nguyen, T. M. H., & Bark, C. W. (2020). Synthesis of cobalt-doped TiO_2 based on metal–organic frameworks as an effective electron transport material in perovskite solar cells. *ACS omega*, *5*(5), 2280-2286.

45. Fu, F., Zhang, Y., Zhang, Y., & Chen, Y. (2021). Synthesis of Mn-doped and anatase/rutile mixed-phase TiO_2 nanofibers for high photoactivity performance. *Catalysis Science & Technology*, *11*(12), 4181-4195.

46. Chanda, A., Rout, K., Vasundhara, M., Joshi, S. R., & Singh, J. (2018). Structural and magnetic study of undoped and cobalt doped TiO_2 nanoparticles. *RSC advances*, *8*(20), 10939-10947.

47. Barakat, M. A., Hayes, G., & Shah, S. I. (2005). Effect of cobalt doping on the phase transformation of TiO_2 nanoparticles. *Journal of nanoscience and nanotechnology*, *5*(5), 759-765.

48. Zhu, X., Pei, L., Zhu, R., Jiao, Y., Tang, R., & Feng, W. (2018). Preparation and characterization of Sn/La co-doped TiO_2 nanomaterials and their phase transformation and photocatalytic activity. *Scientific Reports*, *8*(1), 1-14.

49. Tian, J., Gao, H., Kong, H., Yang, P., Zhang, W., & Chu, J. (2013). Influence of transition metal doping on the structural, optical, and magnetic properties of TiO_2 films deposited on Si substrates by a sol–gel process. *Nanoscale research letters*, *8*(1), 1-11.

50. Ali, M., Hussain, R., Tariq, F., Noreen, Z., Toufiq, A. M., Bokhari, H., & Akhtar, N. (2020). Highly effective visible light-activated cobalt-doped TiO_2 nanoparticles for antibacterial coatings against Campylobacter jejuni. *Applied Nanoscience*, *10*(3), 1005-1012.

51. Khurana, C., Pandey, O. P., & Chudasama, B. (2015). Synthesis of visible light-responsive cobalt-doped TiO_2 nanoparticles with tunable optical band gap. *Journal of Sol-Gel Science and Technology*, *75*(2), 424-435.

52. Sá, J., Garlisi, C., Palmisano, G., Czapla-Masztafiak, J., Kayser, Y., & Szlachetko, J. (2018). Differences between bulk and surface electronic structure of doped TiO_2 with soft-elements (C, N and S). *Materials Chemistry and Physics*, *208*, 281-288.

53. Dong, F., Guo, S., Wang, H., Li, X., & Wu, Z. (2011). Enhancement of the visible light photocatalytic activity of C-doped TiO_2 nanomaterials prepared by a green synthetic approach. *The Journal of Physical Chemistry C*, *115*(27), 13285-13292.

54. He, J., Du, Y. E., Bai, Y., An, J., Cai, X., Chen, Y., Wang, P., Yang, X., & Feng, Q. (2019). Facile formation of anatase/rutile TiO_2 nanocomposites with enhanced photocatalytic activity. *Molecules*, *24*(16), 2996.

55. Xiong, Z., Wu, H., Zhang, L., Gu, Y., & Zhao, X. S. (2014). Synthesis of TiO_2 with controllable ratio of anatase to rutile. *Journal of Materials Chemistry A*, *2*(24), 9291-9297.

56. Almashhori, K., Ali, T. T., Saeed, A., Alwafi, R., Aly, M., & Al-Hazmi, F. E. (2020). Antibacterial and photocatalytic activities of controllable (anatase/rutile) mixed phase TiO_2 nanophotocatalysts synthesized via a microwave-assisted sol–gel method. *New Journal of Chemistry*, *44*(2), 562-570.

57. Ishigaki, T., Nakada, Y., Tarutani, N., Uchikoshi, T., Tsujimoto, Y., Isobe, M., Ogata, H., Zhang, C. & Hao, D. (2020). Enhanced visible-light photocatalytic activity of anatase-rutile mixed-phase nano-size powder given by high-temperature heat treatment. *Royal Society open science*, *7*(1), 191539.

58. Deshmukh, S. M., Tamboli, M. S., Shaikh, H., Babar, S. B., Hiwarale, D. P., Thate, A. G., sheikh, A.F., Alam M.A., Khetre, S. M., & Bamane, S. R. (2021). A facile urea-assisted thermal decomposition process of TiO_2 nanoparticles and their photocatalytic activity. *Coatings*, *11*(2), 165.

59. Hu, K., Lei, E., Zhao, D., Hu, C., Cui, J., Lai, L., Xiong, Q., & Liu, Z. (2018). Hydrothermal synthesis of a rutile/anatase TiO_2 mixed crystal from potassium titanyl oxalate: crystal structure and formation mechanism. *CrystEngComm*, *20*(24), 3363-3369.

60. Khlyustova, A., Sirotkin, N., Kusova, T., Kraev, A., Titov, V., & Agafonov, A. (2020). Doped TiO_2: the effect of doping elements on photocatalytic activity. *Materials Advances*, *1*(5), 1193-1201.

61. Zhang, Z., Wu, Q., Johnson, G., Ye, Y., Li, X., Li, N., Cui, M., Lee, J., D., Liu, C., Zhao, S., Li, S., Orlov, A., Murray, C., B., Zhang, X., Gunnoe, T., B., Su, D., & Zhang, S. (2019). Generalized synthetic strategy for transition-metal-doped brookite-phase TiO_2 nanorods. *Journal of the American Chemical Society*, *141*(42), 16548-16552.

62. Fu, F., Zhang, Y., Zhang, Y., & Chen, Y. (2021). Synthesis of Mn-doped and anatase/rutile mixed-phase TiO_2 nanofibers for high photoactivity performance. *Catal. Sci. Technol.*, *(12)*.

63. Kessler, V. G. (2013). Aqueous route to TiO_2-based nanomaterials using pH-neutral carboxylate precursors. *Journal of sol-gel science and technology*, *68*(3), 464-470.

64. Jo, W. K., & Tayade, R. J. (2014). New generation energy-efficient light source for photocatalysis: LEDs for environmental applications. *Industrial & Engineering Chemistry Research*, *53*(6), 2073-2084.

65. Boudaren, C., Bataille, T., Auffrédic, J. P., & Louër, D. (2003). Synthesis, structure determination from powder diffraction data and thermal behaviour of titanium (IV) oxalate $[Ti_2O_3 (H_2O)_2](C_2O_4)\cdot H_2O$. *Solid state sciences*, *5*(1), 175-182.

66. Hu, K., Lei, E., Zhao, D., Li, Y., Zhao, W., & Rong, H. (2020). Characteristics and performance of rutile/anatase/brookite TiO_2 and TiO_2–Ti_2O_3 $(H_2O)_2$ $(C_2O_4)\cdot H_2O$ multiphase mixed crystal for the catalytic degradation of emerging contaminants. *CrystEngComm*, *22*(6), 1086-1095.

67. Hu, K., E, L., Zhao, D., Li, Y., & Zhao, W. (2020). Direct Z-Scheme Janus-Shaped Heterojunction of TiO_2-Ti_2O_3 $(H_2O)_2$ $(C_2O_4)\cdot H_2O$: A Novel Photocatalyst or Photoanode. *ChemistrySelect*, *5*(13), 3892-3896.

68. Khade, G. V., Suwarnkar, M. B., Gavade, N. L., & Garadkar, K. M. (2016). Sol–gel microwave assisted synthesis of Sm-doped TiO_2 nanoparticles and their photocatalytic activity for the degradation of Methyl Orange under sunlight. *Journal of Materials Science: Materials in Electronics*, *27*(6), 6425-6432.

69. Hanaor, D. A., & Sorrell, C., C., (2011). Review of the anatase to rutile phase transformation. *Journal of Materials science*, *46*(4), 855-874.

70. Dambournet, D., Belharouak, I., & Amine, K. (2010). Tailored preparation methods of TiO_2 anatase, rutile, brookite: mechanism of formation and electrochemical properties. *Chemistry of materials*, *22*(3), 1173-1179.

71. Ganesh, I., Gupta, A., K., Kumar, P., P., Sekhar, P., S., C., Radha, K., Padmanabham, G., & Sundararajan, G. (2012). Preparation and Characterization of Ni-Doped TiO_2 Materials for Photocurrent and Photocatalytic Applications. *The Scientific World Journal*, *2012*.

72. Yan, J., Wu, G., Guan, N., Li, L., Li, Z., & Cao, X. (2013). Understanding the effect of surface/bulk defects on the photocatalytic activity of TiO_2: anatase versus rutile. *Physical Chemistry Chemical Physics*, *15*(26), 10978-10988.

73. Potdar, H. S., Deshpande, S. B., Deshpande, A. S., Khollam, Y. B., Patil, A. J., Pradhan, S. D., & Date, S. K. (2001). Simplified chemical route for the synthesis of barium titanyl oxalate (BTO). *International Journal of Inorganic Materials*, *3*(7), 613-623.

74. Parayil, S. K., Baltrusaitis, J., Wu, C. M., & Koodali, R. T. (2013). Synthesis and characterization of ligand stabilized CdS-Trititanate composite materials for visible light-induced photocatalytic water splitting. *International journal of hydrogen energy*, *38*(6), 2656-2669.

75. Parayil, S. K., Kibombo, H. S., Wu, C. M., Peng, R., Kindle, T., Mishra, S., Ahrenkiel, S. P., Baltrusaitis, J., Dimitrijevic, N. M., Rajh, T., & Koodali, R. T. (2013). Synthesis-dependent oxidation state of platinum on TiO_2 and their influences on the solar simulated photocatalytic hydrogen production from water. *The Journal of Physical Chemistry C*, *117*(33), 16850-16862.

76. Sadanandam, G., Lalitha, K., Kumari, V. D., Shankar, M. V., & Subrahmanyam, M. (2013). Cobalt doped TiO_2: A stable and efficient photocatalyst for continuous hydrogen production from glycerol: Water mixtures under solar light irradiation. international journal of hydrogen energy, 38(23), 9655-9664.

77. Stella, C., Prabhakar, D., Prabhu, M., Soundararajan, N., & Ramachandran, K. (2016). Oxygen vacancies induced room temperature ferromagnetism and gas sensing properties

of Co-doped TiO_2 nanoparticles. *Journal of Materials Science: Materials in Electronics*, *27*(2), 1636-1644.

78. Guan, B., Yu, J., Guo, S., Yu, S., & Han, S. (2020). Porous nickel doped titanium dioxide nanoparticles with improved visible light photocatalytic activity. *Nanoscale Advances*, *2*(3), 1352-1357.

79. Ganesh, I., Gupta, A. K., Kumar, P. P., Sekhar, P. S. C., Radha, K., Padmanabham, G., & Sundararajan, G. (2012). Preparation and Characterization of Ni-Doped TiO_2 Materials for Photocurrent and Photocatalytic Applications. *The Scientific World Journal*, *2012*.

80. Bashir, A., Rafique, U., Bashir, R., Jamil, S., Bashir, F., Sultan, M., Mubeen, M., Mehmood, Z., Iqbal, A., & Akhter, Z. (2021). Synthesis and comparative evaluation of optical and electrochemical properties of Ni^{+2} and Pr^{+3} ions co-doped mesoporous TiO_2 nanoparticles with undoped Titania. *Applied Nanoscience*, 11(1),1-17.

81. Bashir, A., Bashir, F., Mehmood, Z., Satti, M. S., & Akhter, Z. (2019). Synthesis, characterisation and investigation of enhanced photocatalytic activity of Sm^{+3}, Ni^{+2} co-doped TiO_2 nanoparticles on the degradation of azo dyes in visible region. *International Journal of Nanoparticles*, *11*(1), 37-61.

82. Chauhan, R., Kumar, A., & Chaudhary, R. P. (2012). Structural and photocatalytic studies of Mn doped TiO_2 nanoparticles. *Spectrochimica Acta Part A: Molecular and Biomolecular Spectroscopy*, *98*, 256-264.

83. Mathew, S., Ganguly, P., Rhatigan, S., Kumaravel, V., Byrne, C., Hinder, S. J., & Pillai, S.C.(2018).Cu-doped TiO_2: visible light assisted photocatalytic antimicrobial activity. *Applied Sciences*, *8*(11), 2067.

84. Kamble, R., Mahajan, S., Puri, V., Shinde, H., & Garadkar, K. (2018). Visible light-driven high photocatalytic activity of Cu-doped TiO_2 nanoparticles synthesized by hydrothermal method. *Material Science Research India*, *15*(3), 197-208.

85. Park, S. K., Jeong, J. S., Yun, T. K., & Bae, J. Y. (2015). Preparation of carbon-doped TiO_2 and its application as a photoelectrodes in dye-sensitized solar cells. *Journal of nanoscience and nanotechnology*, *15*(2), 1529-1532.

86. Smitha, V. S., Manjumol, K. A., Baiju, K. V., Ghosh, S., Perumal, P., & Warrier, K. G. K. (2010). Sol–gel route to synthesize titania-silica nano precursors for photoactive particulates and coatings. *Journal of sol-gel science and technology*, *54*(2), 203-211.

87. Zhao, H., Pan, F., & Li, Y. (2017). A review on the effects of TiO_2 surface point defects on CO_2 photoreduction with H_2O. *Journal of Materiomics*, *3*(1), 17-32.

88. Smitha, V. S., Saju, P., Hareesh, U. S., Swapankumar, G., & Warrier, K. G. K. (2016). Optical Properties of Rare-Earth Doped TiO_2 Nanocomposites and Coatings; A Sol-Gel Strategy towards Multi–functionality. *ChemistrySelect*, *1*(10), 2140-2147.

89. De Luna, M. D. G., Garcia-Segura, S., Mercado, C. H., Lin, Y. T., & Lu, M. C. (2020). Doping TiO_2 with $CuSO_4$ enhances visible light photocatalytic activity for organic pollutant degradation. *Environmental Science and Pollution Research*, *27*(20), 24604-24613.

90. Begum, N. S., Farveez Ahmed, H. M., & Gunashekar, K. R. (2008). Effects of Ni doping on photocatalytic activity of TiO_2 thin films prepared by liquid phase deposition technique. *Bulletin of Materials Science*, *31*(5), 747-751.

91. Ikram, M., Umar, E., Raza, A., Haider, A., Naz, S., Ul-Hamid, D. A., & Ali, S. (2020). Dye degradation performance, bactericidal behavior and molecular docking analysis of Cu-doped TiO_2 nanoparticles. *RSC Advances*, *10*(41), 24215-24233.

92. Sing, K. S. (1985). Reporting physisorption data for gas/solid systems with special reference to the determination of surface area and porosity. *Pure and applied chemistry*, *57*(4), 603-619.

93. Matos, J., Ocares-Riquelme, J., Poon, P. S., Montaña, R., García, X., Campos, K., Hernandez-Garrido, J., C., & Titirici, M. M. (2019). C-doped anatase TiO_2: Adsorption kinetics and photocatalytic degradation of methylene blue and phenol, and correlations with DFT estimations. *Journal of colloid and interface science*, *547*, 14-29.

94. Dorraj, M., Goh, B. T., Sairi, N. A., Woi, P. M., & Basirun, W. J. (2018). Improved visible-light photocatalytic activity of TiO_2 co-doped with copper and iodine. *Applied Surface Science*, *439*, 999-1009.

95. Cao, X. P., Li, D., Jing, W. H., Xing, W. H., & Fan, Y. Q. (2012). Synthesis of visible-light responsive C, N and Ce co-doped TiO_2 mesoporous membranes via weak alkaline sol–gel process. *Journal of Materials Chemistry*, *22*(30), 15309-15315.

96. Chauhan, R., Kumar, A., & Chaudhary, R. P. (2012). Structural and photocatalytic studies of Mn doped TiO_2 nanoparticles. *Spectrochimica Acta Part A: Molecular and Biomolecular Spectroscopy*, *98*, 256-264.

97. Tian, S., Yang, H., Cui, M., Shi, R., Zhao, H., Wang, X., Wang, X ., & Zhang, L. (2011). Monodisperse rutile TiO_2 nanorod-based microspheres with various diameters: hydrothermal synthesis, formation mechanism and diameter-and crystallinity-dependent photocatalytic properties. *Applied Physics A*, *104*(1), 149-158.

98. Pfeifer, V., Erhart, P., Li, S., Rachut, K., Morasch, J., Brötz, J., Reckers, P., Mayer, T., Ruhle, S., Zaban, A., Sero, I. M., Bisquert, J., Jaegermann, W., & Klein, A. (2013). Energy band alignment between anatase and rutile TiO_2. *The Journal of Physical Chemistry Letters*, *4*(23), 4182-4187.

Chapter 4

A simple method for the synthesis of anatase TiO_2 using a convenient precursor and comparative study of photocatalytic activities of Co-doped TiO_2 with pure TiO_2

Contents

Abstract

In this work, TiO_2 was prepared using a novel and simple method, using titanium tetraisopropoxide (TTIP) as a precursor. The TTIP underwent direct hydrolysis to anatase TiO_2 on refluxing its aqueous solutions and calcination at 450 ˚C for 1hour. The synthesized samples were characterized by TGA-DTG, X-ray diffraction (XRD), Fourier transform infrared spectroscopy (FT-IR), FESEM-EDX, XPS, UV-Visible spectroscopy, TEM and BET techniques. The XRD results of the uncalcined and calcined samples reveal that the both samples consist of only nanocrystalline anatase TiO_2. The crystallite size of TiO_2 was found to increase from 3 nm to 5 nm on calcination. 1 mol% Co-doped TiO_2 nonmaterial was also synthesized by the above method. The degradation of methylene blue was used to study the photocatalytic activities of the undoped TiO_2 and 1 mol% Co-doped TiO_2 under natural sunlight irradiation. The results show that the photocatalytic activity of doped TiO_2 is higher than that of undoped TiO_2.

4.1 Introduction

Photocatalysis has been widely used in a variety of fields, including solar cells, pollutant degradation and water splitting. Among the various photocatalysts, titanium dioxide has been widely employed for many environmental and energy applications. In the recent decade, numerous surface science methodologies have been used to study the mechanisms of photocatalysis, particularly that of TiO_2.[1] In 1972, Fujishima and Honda reported that photoelectrochemical water splitting could create O_2 on a TiO_2 electrode and H_2 on a platinum black electrode by irradiating the TiO_2 electrode

with UV light. Since then, researchers have been interested in TiO_2 semiconductor photocatalysis because of its potential application in energy production. The Fujishima et al. also reported photocatalytic reduction of CO_2 with different types of semiconductors like TiO_2, CdS, GaP, ZnO and SiC as photocatalysts in 1979.[2]

Titanium dioxide remains the most studied material for heterogeneous photocatalysis due to its chemical stability, low cost, non-toxicity and accessible bandgap.[3-5] However, TiO_2 has several drawbacks, such as poor absorption of visible light due to its large band gap (3.2 eV) and high recombination of photogenerated charge carriers.[6,7] Current research works mainly focuses on increasing the lifetime of excited charge carriers. To overcome these limitations, appropriate modifications has been applied, including doping, making heterojunctions and structural changes.[8]

Three crystalline phases of TiO_2 are anatase, rutile and brookite. Among them rutile phase is more stable. The anatase phase has been found to have the higher photocatalytic activity than rutile and brookite phases.[9] Anatase nanocrystalline has considerably greater surface area than rutile nanocrystalline, resulting in more active sites. Furthermore, anatase nanoparticles have more oxygen vacancies than rutile nanoparticles.[10] These three phases are made up of TiO_6 octahedra with different distortions. Photocatalytic activity of TiO_2 are also influenced by the phase composition and the phase composition mainly depends on the chemical procedure used to produce these crystals.

There are several methods for the preparation of TiO_2 including sol-gel, chemical vapour deposition (CVD) and hydrothermal methods, reverse micelles, wet-chemical synthesis by precipitation of hydroxide, electrochemical synthesis, solvothermal, sonochemical and microwave-assisted methods. Among these sol-gel, thermal decomposition and hydrothermal methods are the most commonly used methods.

The sol-gel method has been commonly used for preparing nanoparticle TiO_2 and involves following steps; hydrolysis and polycondensation of the titanium precursors (usually titanium alkoxide and titanium metal salt) and formation of sols, sol–gel transition (gelation), aging, drying and crystallization.[11] An acid-catalyzed hydrolysis of titanium precursor is usually used in this approach. The growth of Ti-O-Ti chains results in three-dimensional polymeric skeletons developed by gel with tight close packing. Nateq et. al. reported a method for the synthesis of titania nanocrystalline

particle with enhanced surface area via sol-gel method in water- oil micellar solution.[10] Prepared TiO_2 nanoparticles had a primary crystallite size of 10-15 nm with BET surface area over 100 $m^2 g^{-1}$. However, optimising the temperature and pH of the solution is essential to obtain homogeneous nanoscale TiO_2 particles. Moreover, the long processing time is required.

The hydrothermal method has also been used widely for the synthesis of TiO_2 nanoparticles. In hydrothermal method, the temperature of the solvent is increased above its boiling point at elevated pressure. The advantages of this technique include a restricted particle size distribution, controlled morphology, less particle agglomeration and higher phase homogeneity. Luo et. al. have synthesised TiO_2 nanomaterials with controlled morphologies using hydrothermal method and nanobelt, nanourchin and nanotube were obtained depending up on the temperature, time, and additives.[12] Most of the previously reported hydrothermal methods have yielded anatase phase. Beyer et al. has been used hydrothermal approach to prepare phase pure rutile TiO_2 nanoparticles with a rod-like morphology.[13] Safety issues throughout the reaction process and the need of expensive autoclave are the drawbacks of the hydrothermal method.

Thermal decomposition of inorganic titanium salts during heating is one of the simplest method for the preparing TiO_2 particles. Nevertheless, the salt characteristics and decomposition conditions may have significant impact on the synthesis of particles, particularly in their dimensions and agglomeration. Sofronov et. al. has been reported preparation of TiO_2 by thermal decomposition of titania precursors especially titanium nitrate, titanium oxyfluoride and titanium oxysulphate at various temperatures, with and without organic additive.[14] Titanium nitrate was thermally decomposed at 700 ˚C to produce anatase and rutile phases, while titanium oxyfluoride and oxysulfate produced only anatase. Deshmukh et al. reported preparation of titania nanoparticles by urea-assisted thermal decomposition of titanium oxysulphate with various weight ratios of urea. The anatase phase, spherical nanoparticles of TiO_2 with crystalline size of 14–19 nm were obtained.[15]

Most of the traditional methods involved corrosive precursors or complicated and expensive equipments and experimental conditions. The water assisted crystallisation of TiO_2 has been considered to be most efficient and convenient approach at low

temperature.[16] The synthesis of nanostructured titania in the aqueous phase has been described using a variety of synthetic techniques. The reflux method is comparatively easy, for scale up and has the potential to fabricate TiO_2 with controlled morphology.[17] It needs simple equipment, environmentally friendly process conditions.

Traditional titanium precursors may be used in the most of the aqueous phase synthesis. Titanium isopropoxide, titanium butoxide, titanium ethoxide, titanium acetylacetonate, titanium chloride, potassium titanium oxalate are the different precursors used for the synthesis of TiO_2 in the laboratory scale.[18] Commonly used precursors of titania are tanium isopropoxide and titanium chloride. These precursors are moisture-sensitive. Among them titanium isopropoxide is one of the most popular precursor for TiO_2 nanoparticles. Titanium isopropoxide itself react with water to give TiO_2 and hence it is very difficult to control the size and morphology. The effect of different alkoxides on the size of TiO_2 nanoparticles was studied by Vorkapic and Matsoukas.[19] They found that as the length of alkoxy groups increases, the size of TiO_2 nanoparticles decreases. The pyrolysis of titanium tetraisopropoxide in helium/oxygen atmosphere produced TiO_2 nanoparticles with sizes less than 10 nm.[20] Another commonly used precursor is titanium chloride. However, it quickly undergo hydrolysis in air producing HCl gas and titanium hydroxides. The titanium hydroxides may get precipitated in the lungs on inhalation. Rab et al. reported a precipitation method for the synthesis of anatase, spherical TiO_2 from titanium chloride precursor in water and glycerol reaction medium.[21] Single phase TiO_2 nanocrystals were synthesized by Cao T. et al. from a $TiCl_4$/butanol mixture and reported that the molar ratio of $TiCl_4$ to butanol determines the crystal phase and morphology.[22] Li et.al. reported that the hydrolysis of titanium chloride in aqueous H_2SO_4 solution at very low temperature 0-90 ˚C produced anatase TiO_2 nanocrystals in the size range of 10 nm to 50 nm.[23] The effects of the reaction parameters such as reaction temperature, sulfuric acid concentration, and the calcination temperature on the particle size and crystal phase were also reported.

This chapter aims to report the synthesis of titanium dioxide via refluxing aqueous solution of TTIP for the photocatalytic applications. Nanocrystalline anatase phase TiO_2 was obtained by refluxing the aqueous titanium tetraisopropoxide solution. The calcination at 450 ˚C of the same sample increased the crystallite size. The structural,

optical and crystallinity of the prepared TiO_2 and 1 mol% Co-doped TiO_2 samples were also investigated using characterization techniques like TGA-DTA, X-ray diffraction (XRD), Fourier transform infrared spectroscopy (FT-IR), FESEM-EDX, XPS, UV-Visible spectroscopy, TEM and BET surface area. The photocatalytic activities of TiO_2 and 1 mol% Co-doped TiO_2 for the degradation of organic dye under sunlight irradiation were also studied.

4. 2 Materials and method

4. 2.1 Materials

Titanium (IV) isopropoxide (Sigma- Aldrich, 97%), sulphuric acid (Merck, 98%) and cobalt nitrate hexahydrate (Merck, 99%) were used as starting materials. All solutions were prepared by using deionised water. Chemicals were used without any pre-treatment.

4.2.2 Preparation of TiO_2 and Co-doped TiO_2 from titanium isopropoxide

Titanium (IV) isopropoxide was used as titanium source for the synthesis. Con. Sulphuric acid (31.28 g) was added to 200 mL of distilled water in RB flask kept in a ice cold water then 25 mL of titanium (IV) isopropoxide was added drop wise to the above solution under vigorous stirring. Stirring was continued for 30 minutes. A clear solution of Ti(IV) sulphate solution was obtained. Then 25 mL of the above solution was diluted with 175 mL of water and refluxed at 100 ˚C for two hours. The resulting suspension was filtered and washed with distilled water many times. Schematic representation for the preparation of anatase phase TiO_2 is given in the Figure 4.1. The samples were dried in a hot air oven at 100 ˚C. The prepared sample was calcined at 450 ˚C for two hours. The 1 mol% Co-doped TiO_2 was synthesized by same method by adding cobalt nitrate.

4.2.3 Photocatalytic activity of undoped and 1 mol% Co-doped TiO_2 for methylene blue dye degradation

The degradation of methylene blue dyes under the sunlight was used to assess the photocatalytic activity of titanium dioxide and 1 mol% Co-doped TiO_2 photocatalysts. The experiment was carried out with 0.01 g of TiO_2 or Co-doped TiO_2 dispersed in 100 mL of 10^{-4} M solution of the dye under the sunlight irradiation. Prior to photocatalytic experiment, the suspension was stirred in the dark for 30 minutes for

equilibrium adsorption. It was then exposed to sunlight under constant magnetic stirring. Then 5 mL of the suspensions were withdrawn at 10 minutes intervals and the solutions were centrifuged and the absorption of the samples were measured using UV-Visible spectrophotometer in the wavelength range of 200 to 800 nm. The degradation of the dye was monitored by measuring the absorbance at λ_{max} of 615 nm.

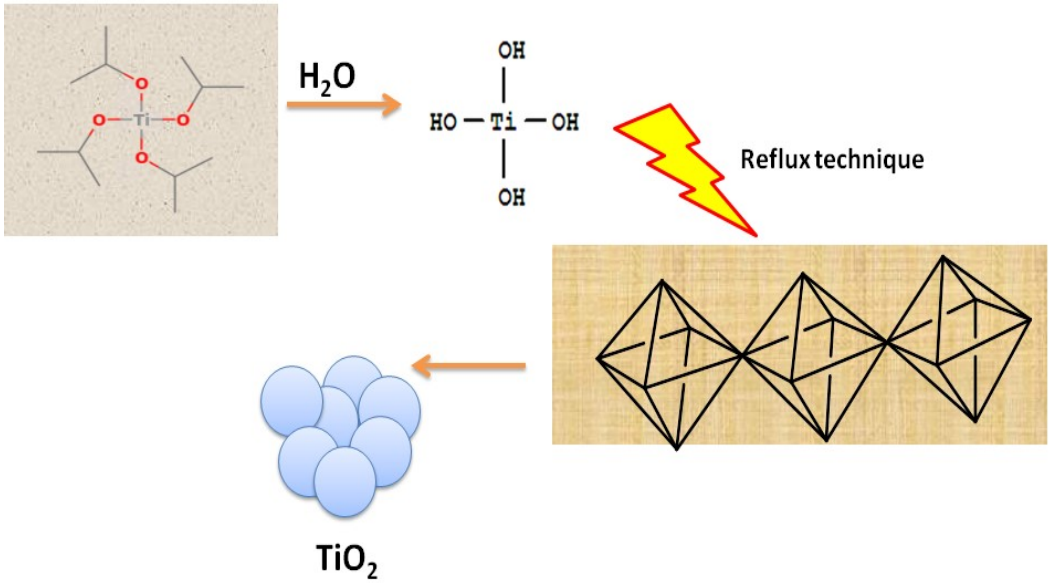

Fig. 4.1 Schematic representation of anatase phase TiO_2 formation mechanism.

4. 3 Results and discussion

4.3.1 Thermogravimetric analysis

The thermal decomposition of the TiO_2 synthesized by reflux method was analyzed by thermogravimetric and derivative thermogravimetric analysis. Figure 4.2 shows the TGA-DTG curve of TiO_2. It can be clearly seen that TG curve descends until it becomes horizontal around 414 ˚C. Figure shows two main stages of mass loss in TGA and two main exothermic peaks in DTG. Dehydration of water is the first weight loss below 100 ˚C which account 18% of total weight loss. The second and main stage, which occurred between 182 to 414 ˚C was corresponding to removal of chemically bounded water molecules making TiO_2 surface free of hydroxyl groups.[24] This corresponds to 35% of total weight loss. The DTG curve had exothermic peaks in the same temperature ranges as the TGA curve, indicating the mass loss.[25] After

414 ˚C, no mass loss were recorded in the thermogram until 700 ˚C. The mass of the material remains constant confirming the formation of TiO_2.

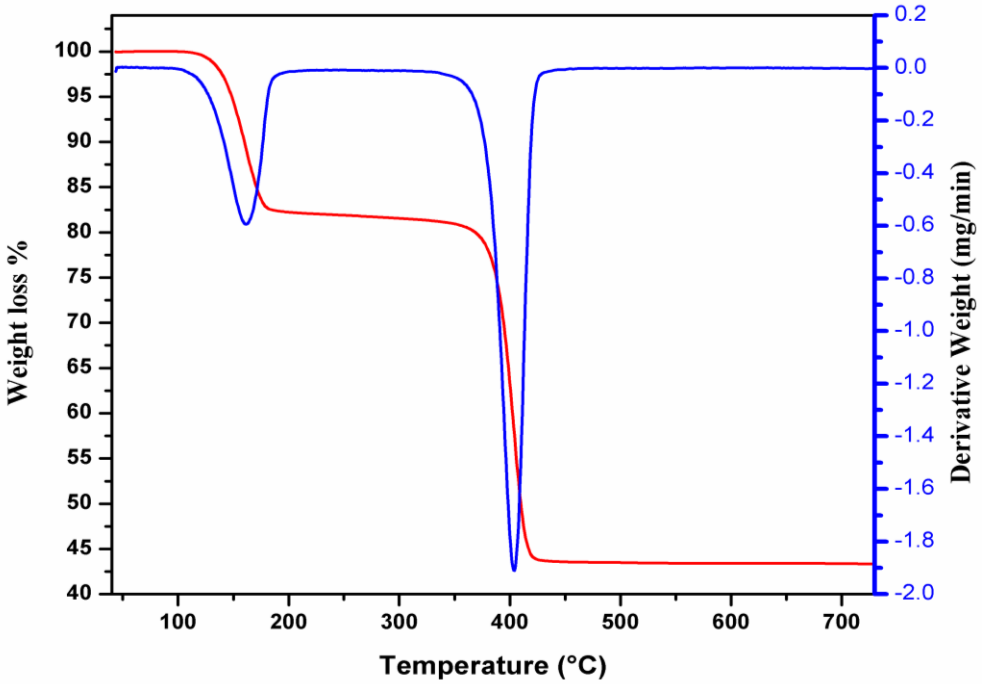

Fig. 4.2 TG-DTG curve of prepared TiO_2 sample.

4.3.2 XRD analysis

The crystal structure and phase purity were analysed using powder X-ray diffraction spectrum. The XRD pattern of the as prepared precipitate obtained by refluxing titanium isopropoxide solution and after calcination at 450 ˚C are shown in the Figure 4.3. The anatase phase was the only crystalline phase in both the samples.

The XRD result indicates that pure crystalline anatase TiO_2 was directly formed after refluxing the aqueous titanium isopropoxide. The presence of only peaks corresponding to anatase phase indicates that the present method is very effective in obtaining single phase anatase TiO_2 nanoparticles at low temperature. The characteristic lattice planes corresponding to the anatase phase, (101), (004), (200), (112) and (105), at 25.62˚, 38.12˚, 48.12˚, 54.81˚, 62.91˚and 69.61˚were observed in both the samples. All the diffraction peaks are indexed to the pure anatase phase (JCPDS Card No.21-1272).[26,27] The calcination enhances the intensity of the peaks indicating the increased crystallinity of the sample.

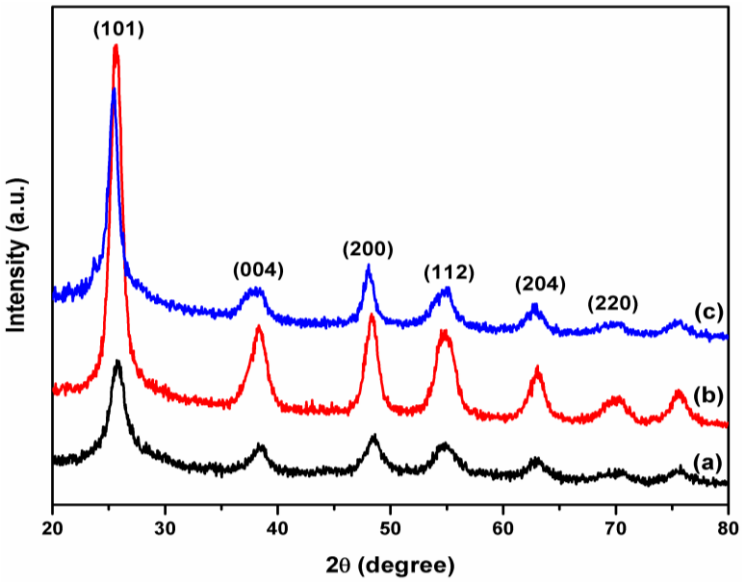

Fig. 4.3 XRD pattern of TiO_2 a) prepared TiO_2 b) TiO_2 calcined at 450 ˚C c) 1 mol% Co-doped TiO_2 calcined at 450 ˚C.

The crystallite size of the anatase phase was calculated using FWHM of the most intense diffraction peak at (101) 25.62˚, using Scherrer equation given in chapter 3. The crystallite size was found to be 3 nm for uncalcined sample and 6.5 nm for calcined sample at 450 ˚C. Hence the diffraction peaks are broad due to the small crystallite size of TiO_2.

Figure 4.3 (C) displays the XRD patterns of 1 mol% Co-doped TiO_2 synthesized by the same method using cobalt nitrate as the cobalt source and titanium tetraisopropoxide as the titanium source. The XRD result shows the presence of only anatase phase of TiO_2. There was no peak observed corresponding to metal oxide of doping element in the XRD spectrum, which is consistent with previous reports on Co-doped TiO_2.[28] Thus, the XRD patterns clearly show that the current method produces only single phase TiO_2. The crystallite size of the 1 mol % Co-doped TiO_2 sample was also calculated using Scherrer's equation and was found to be 6.4 nm.

4.3.3 TEM analysis

The crystallographic structure, particle size and surface morphology of TiO_2 prepared from Titanium isopropoxide and 1 mol% Co-doped TiO_2 calcined at 450 ˚C were studied using TEM. The images are shown in Figure 4.4 and Figure 4.5, respectively.

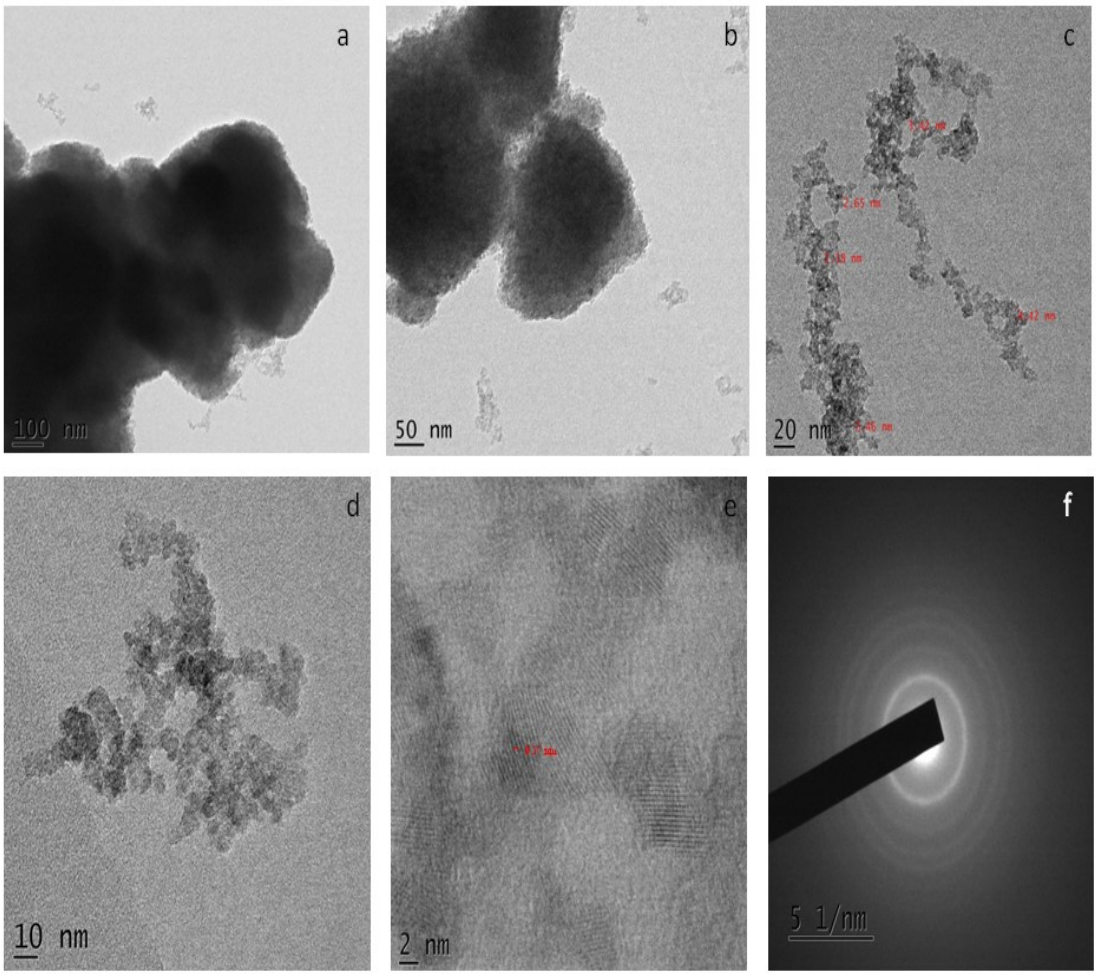

Fig. 4.4 TEM images of TiO_2 from titanium isopropoxide calcined at 450 ˚C: (a-d) are images at different magnification, e) HRTEM and f) SAED pattern.

Titania particles are agglomerated and having different particle size. The particles are appeared to be spherical in shape. The images indicate that the particles are agglomerated and average particle size was about 6 nm in diameter. The HRTEM image shows that the interplannar distance (d) is 0.35 nm corresponding to (101) plane of anatase, which is in good agreement with XRD data.[29] The lattice fringes of anatase TiO_2 are clearly visible at a certain area of the particle. Selected area electron diffraction (SAED) pattern of the sample shows continuous concentric Debye-Scherrer rings.[30] It shows that the sample is highly crystalline nature. The distinct rings are corresponding to different planes of tetragonal anatase TiO_2.[31]

The TEM images of 1 mol% Co-doped TiO_2 at different magnifications clearly show that the particles are agglomerated and having different particle size and shape. The nanoparticles obtained had an average primary particle size of 6 nm, which is in

good agreement with the primary particle size obtained from the XRD. Lattice fringes were very clear in the HRTEM images. From the HRTEM image, d spacing of lattice fringes was found to be 0.33 nm corresponding to (101) planes of anatase. By comparing with the XRD results, the *d* spacings were indexed to interplanar distance of (101) of anatase. The SAED pattern shows the crystalline nature of the samples and concentric Debye-Sherrer rings, which can be indexed to anatase phase. These results were consistent with the XRD results.

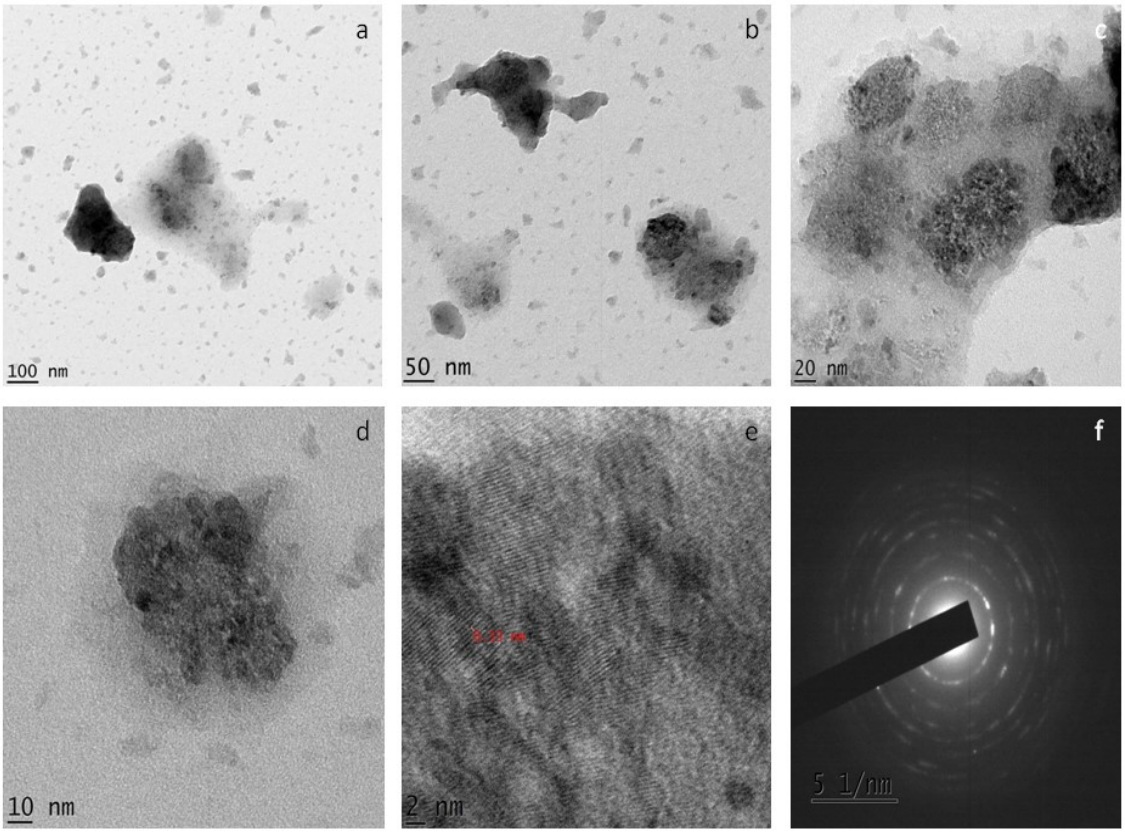

Fig. 4.5 TEM images of 1 mol% Co-doped TiO_2 calcined at 450 ˚C: (a-d) are images at different magnifications, e) HRTEM and f) SAED pattern.

4.3.4 Morphological studies by FESEM

The surface morphology was analyzed using FESEM images. The FESEM images of TiO_2 from titanium isopropoxide calcined at 450 ˚C at different magnifications are shown in the Figure 4.6. These images showed irregularly shaped structures with rough surface due to the agglomeration of spherical particles during calcinations. Images are in good agreement with the result of TEM images. The individual sphere size of 300-400 nm made up of granular 6 nm sized anatase TiO_2 nanoparticles.

Interconnected small granular TiO_2 nanoparticles of the spherical structures exhibit the roughness.

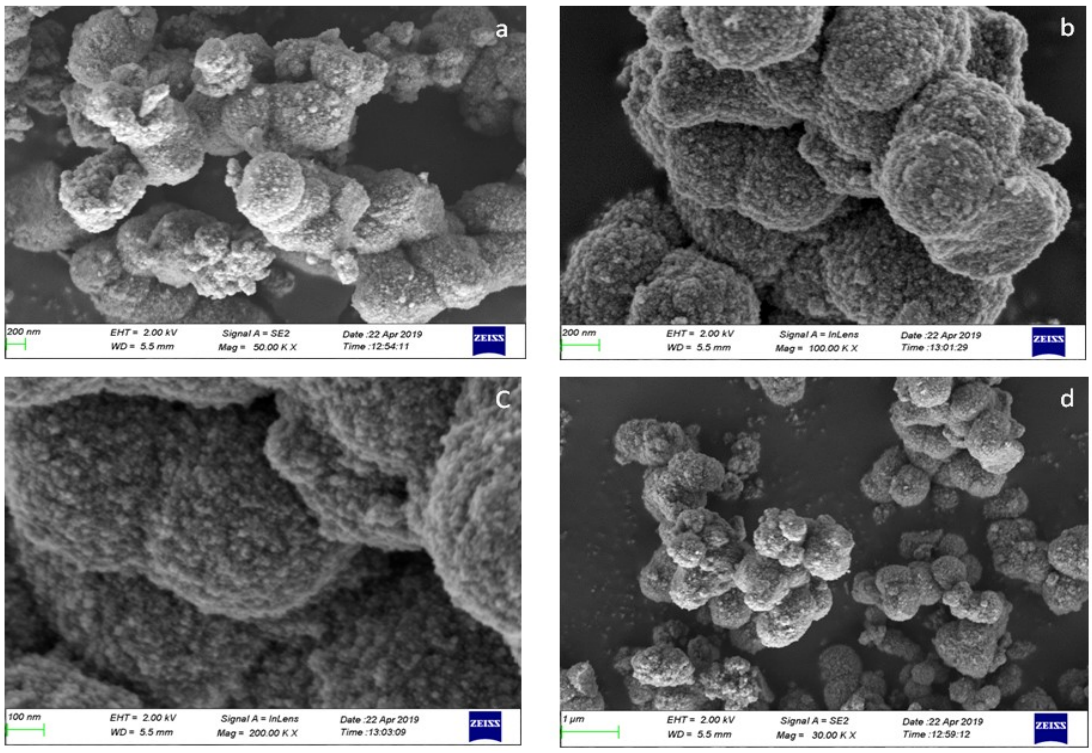

Fig.4.6 FESEM image of TiO_2 from titanium isopropoxide calcined at 450 ˚C: (a-d) are images at different magnifications.

The microstructure of 1 mol% Co-doped TiO_2 calcined at 450 ˚C were further analysed by FESEM and are shown in Figure 4.7. The FESEM images show spherical shaped nanoparticles agglomerated together to form big clusters. The average size of the aggregated particles was found to be 200 nm.[32] Fomekong et al. have reported synthesis of 1 mol% Co-doped TiO_2 by co-precipitation route and the particles were spherical and agglomerated with sizes of around 70 nm.

The EDS spectral analysis was carried out to find out the % of Co ion present in TiO_2 lattice. The EDS spectrum of Co-doped TiO_2 is shown in the Figure 4.8. Spectrum indicates the presence of Co element in addition to Ti and O element in the 1 mol% Co doped TiO_2 sample. The weight ratio of cobalt in the 1 mol% Co-doped sample is close to 1, which is the same ratio of metal precursors used for the preparation of Co-doped TiO_2. The spectrum shows two peaks at 0.2 and 4.5 keV. The bulk TiO_2 has the most intense peak, whereas the surface TiO_2 has the least intense peak.[33] In the EDS, there are peaks at 0.6, 6.9 and 7.5 keV corresponding to

cobalt. The less intense peak of Co-doped TiO_2 is assigned to cobalt in the TiO_2 lattices. The presence of cobalt ions in the TiO_2 lattice was confirmed by EDS spectrum. Therefore it may be concluded that the cobalt ions are uniformly distributed throughout the anatase crystallites.[34]

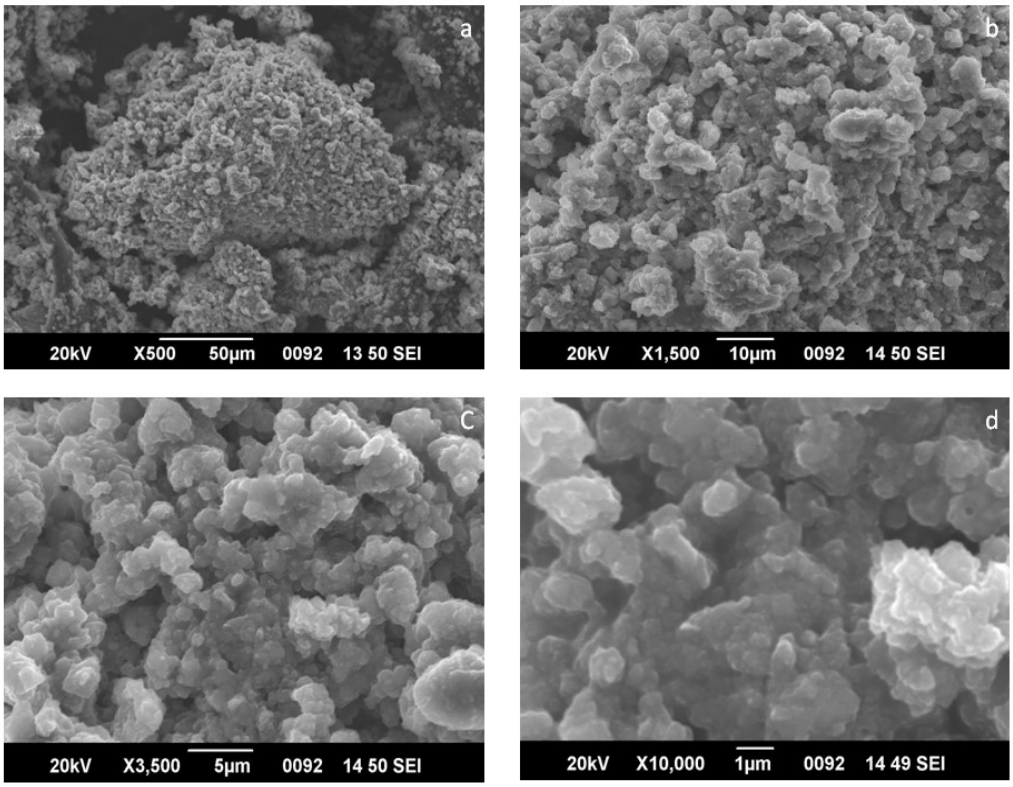

Fig.4.7 FESEM image of 1 mol% Co-doped TiO_2 calcined at 450 ˚C: (a-d) are images at different magnifications.

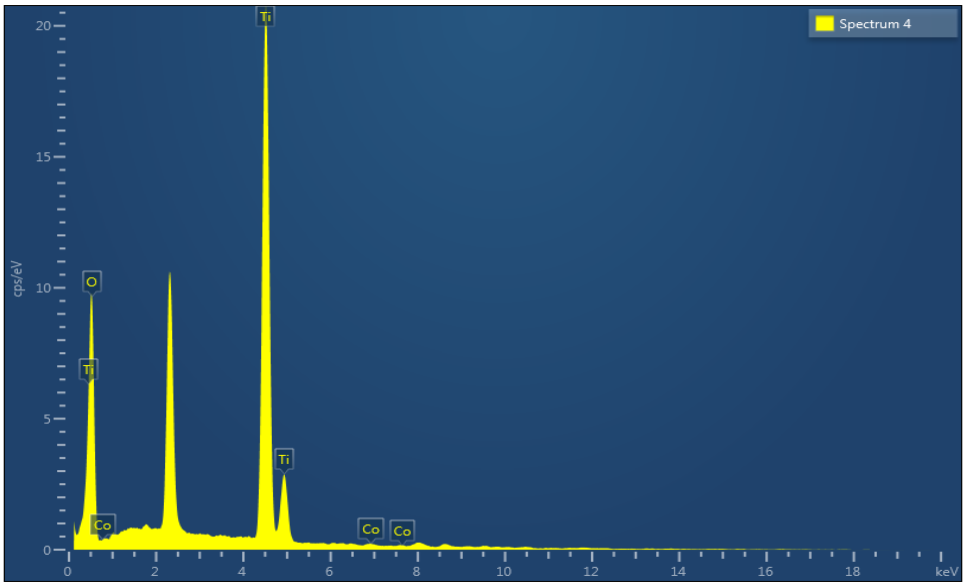

Fig.4.8 EDS spectrum of 1 mol% Co-doped TiO_2 nanoparticles calcined at 450 ˚C.

4.3.5 Surface analysis using XPS

XPS data of 1 mol% Co-doped TiO_2 is shown in the Figure 4.9. In the wide XPS spectrum binding energy peaks are observed at 458.6 eV, 529.8 eV and 782.6 eV indicating the presence of Ti, O and Co elements.

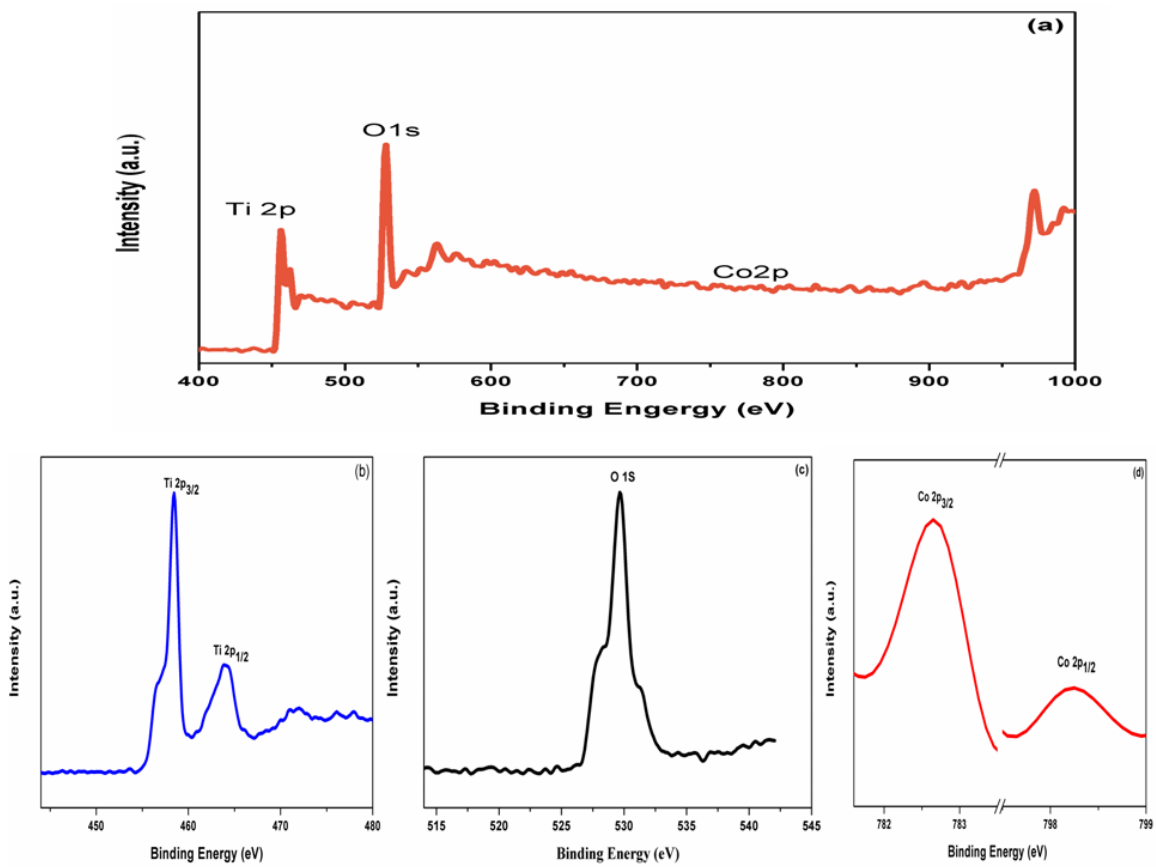

Fig. 4.9 XPS spectrum of 1mol% Co-doped TiO_2 a) wide spectrum, b) deconvoluted Ti 2p, c) O 1s and d) Co 2p.

The peaks observed at 458.5 eV and 464.24 eV corresponds to the spin orbital splitting of Ti $2p_{3/2}$ and Ti $2p_{1/2}$ and indicates the presence of Ti^{4+} in the TiO_2 lattice.[35] The difference between the two peaks is 5.67 eV again confirming the existence of Ti^{4+}.

A peak at 529.8 eV in the deconvoluted spectrum of oxygen is due to the existence of O^{2-} ions in the Ti-O-Ti bond.[36] Co 2p spectrum could be deconvoluted into two peaks, one at 782.6 eV corresponding to Co $2p_{3/2}$ and other at 798.2 eV corresponding to Co $2p_{1/2}$. The spin orbit splitting of two peaks was 15.6 eV indicating the existence of cobalt in the +2 oxidation state.

4.3.6 FT-IR spectral studies

The FT-IR spectra were recorded to study the nature of functional groups and bonding. The FT-IR spectra of the precipitate obtained by refluxing the aqueous solution of titanim isopropoxide and of the sample after calcinations at 450 ˚C for two hours are shown in the Figure 4.10(a-b). In Figure 4.10 (a), the band at 3355 cm^{-1} corresponds to the OH stretching vibrations and the peak at 1615 cm^{-1} is due to bending vitiation. The appearance of these two peaks indicate the presence of chemically bounded water molecules and hydroxyl groups on the surface of the titania. These bands are completely absent in the calcined sample indicating the removal of chemically bound water molecules and hydroxyl groups from the surface. These results are consistent with TG/DTG data. The band at 750-500 cm^{-1} corresponds to the characteristics stretching vibration of O-Ti-O bond.[37,38]

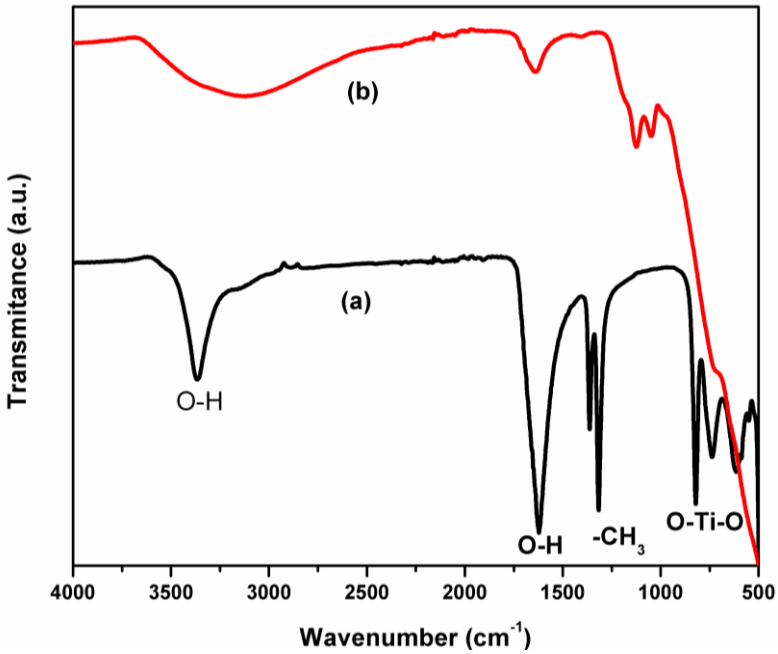

Fig. 4.10 FT-IR spectra of TiO_2 obtained from titanium isopropoxide a) as prepared and b) calcined at 450 ˚C.

The FT-IR spectra of 1 mol% Co-doped TiO_2, obtained by refluxing the aqueous solution of titanim isopropoxide in the presence of 1 mol% Co ions and sample after calcinations at 450 ˚C for two hours are shown in the Figure 4.11. The broad band, at 3400 cm^{-1} is due to symmetric and antisymmetric stretching vibrational modes of

adsorbed water molecules. The FT-IR spectra of calcined and uncalcined Co-doped TiO_2 were similar to the corresponding FT-IR spectra of the undoped TiO_2.

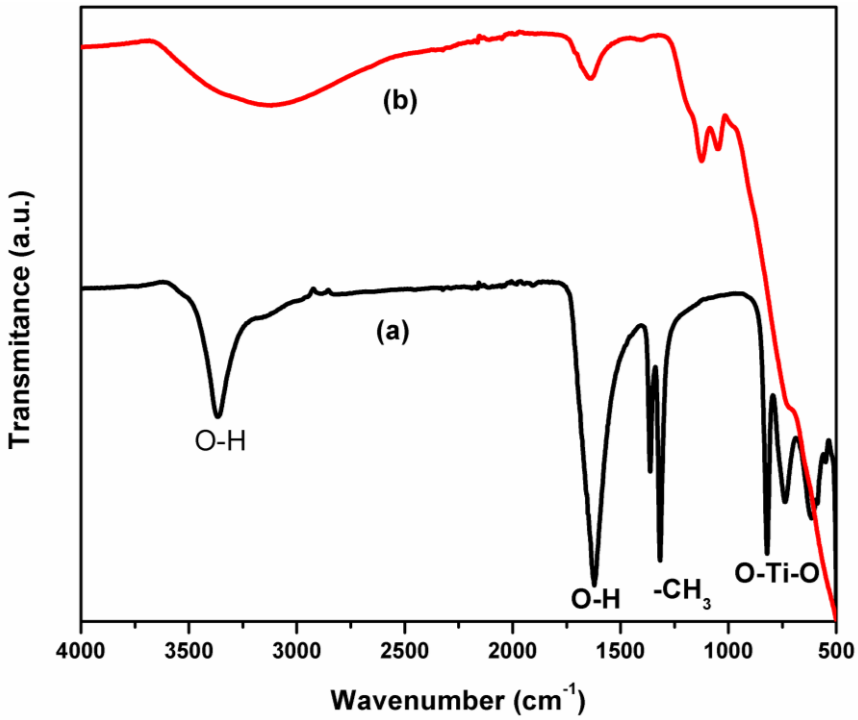

Fig. 4.11 FT-IR spectra of 1 mol % Co-doped TiO_2 obtained from titanium isopropoxide a) as prepared and b) calcined at 450 ˚C.

4.3.7 Optical absorption studies

UV-Visible diffuse reflectance spectroscopy was used to study the optical property of pure TiO_2 and cobalt doped TiO_2 nanoparticles. The absorption spectra are shown in Figure 4.12. The optical transition due to the energy band gap causes a strong absorption band in the UV range and showed almost constant value over visible region. For a 1 mol% Co doped TiO_2 sample, strong absorption band in the UV region and small absorption band in visible light were clearly visible. Both the samples showed strong absorption band at around 345 nm and can be attributed to the optical transition caused by the energy band gap. Adsorption edges were red shifted to visible region in 1 mol% Co-doped TiO_2 nanoparticles. The calculated optical band gap value for pure TiO_2 is 3.0 eV. As shown in Figure 4.13, the band gap energies of both samples were determined using the absorption coefficient $(F(R)*E)^{0.5}$ vs. the energy of absorbed light from the Kubelka-Munk function. The bandgap for Co-doped TiO_2 is red shifted to 2.8 eV. The cobalt doping reduced the distance between the conduction band and valence band and this could be the reason for higher

photocatalytic activity. The lower bandgap energy of 1 mol% Co-doped TiO_2 compared with pure TiO_2, leads to higher photocatalytic behavior under visible light irradiation.

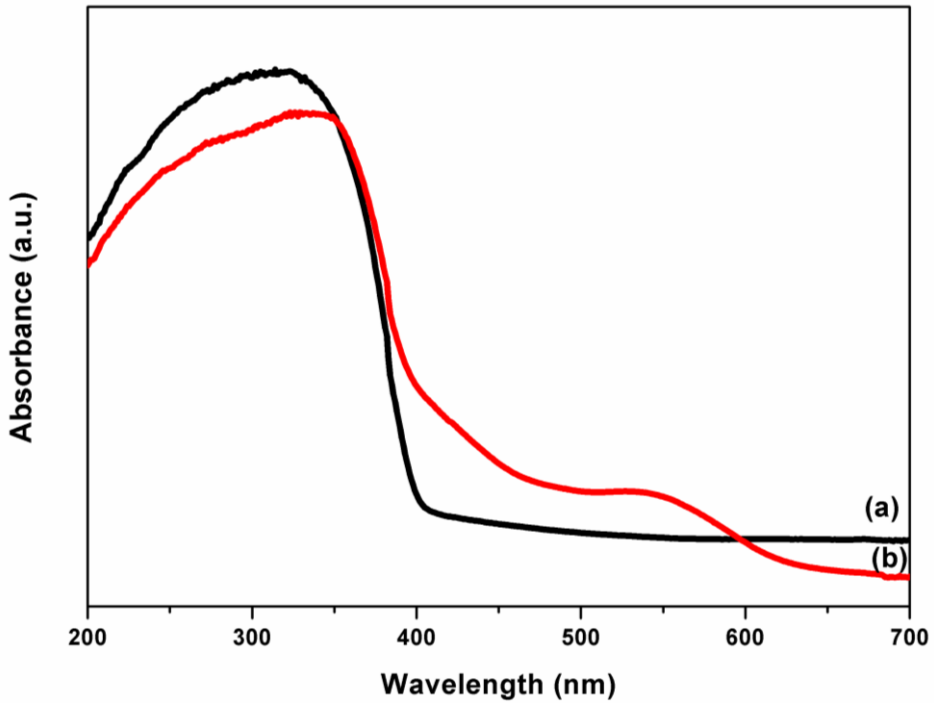

Fig. 4.12 Diffuse reflectance spectra of a) TiO_2, b) 1 mol% Co-doped TiO_2 calcined at 450 ˚C.

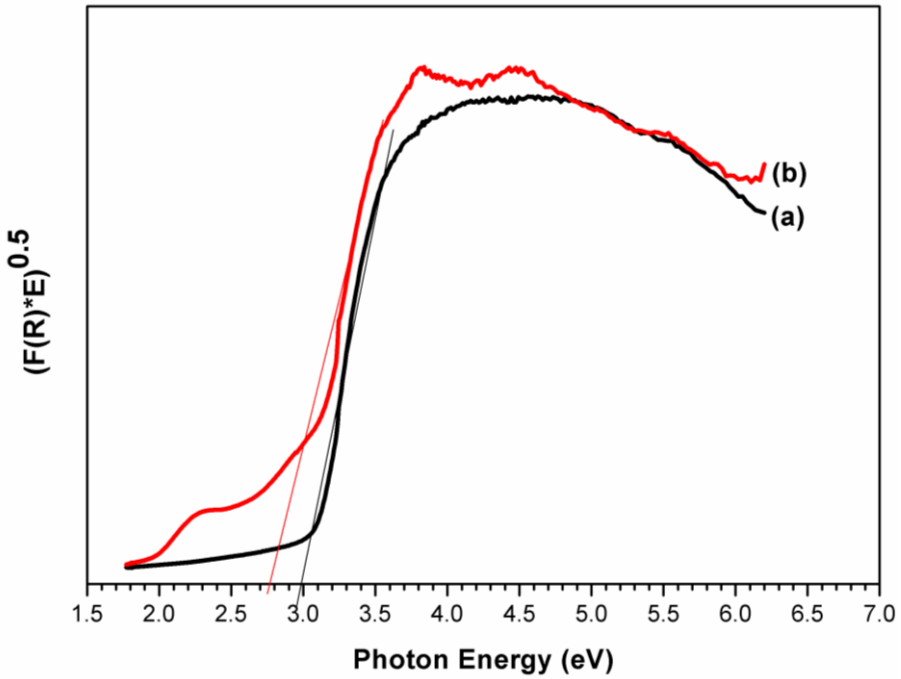

Fig. 4.13 Plot of the Kubelka–Munk function versus the energy of absorbed light. a) TiO_2, b) 1 mol% Co-doped TiO_2.

4.3.8 Photocatalytic activity

The photocatalytic activity of anatase phase TiO_2 and 1 mol% Co-doped anatase TiO_2 were studied by following methylene blue dye degradation under sunlight. The rate of dye degradation was determined by measuring the intensity of absorption peak at 664 nm in the UV visible spectra. The percentage photocatalytic degradation of methylene blue was determined by the equation mentioned in chapter 3. The results are shown in the Figure 4.14.

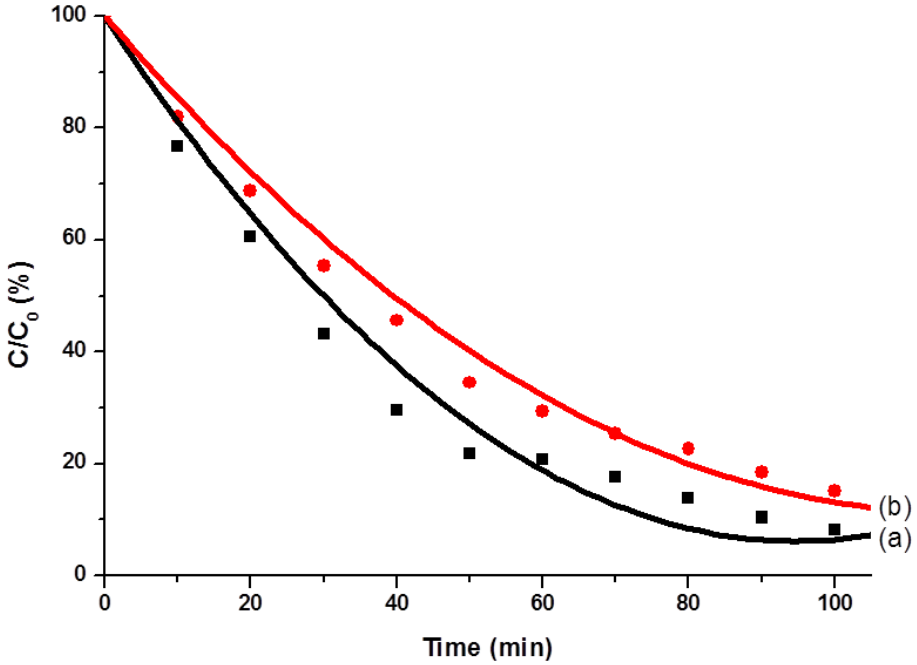

Fig. 4.14 Plot of relative concentration as a function of time for the degradation of dye under sunlight (a) 1 mol% Co-doped anatase TiO_2 and b) Anatase TiO_2.

1 mol% Co-doped anatase TiO_2 exhibited higher photocatalytic activity under natural sunlight irradiation. The percentage of degradation for 1 mol% Co-doped anatase TiO_2 and pure anatase TiO_2 after 10 minutes of sunlight irradiation were 24% and 18%, respectively, whereas these values were 93% and 85% after 100 minutes of irradiation.

The higher activity of 1 mol% Co-doped TiO_2 can be attributed to low bandgap energy (2.8 eV) which lead to higher absorption of visible light. The higher photocatalytic activity of 1 mol% Co-doped TiO_2 may also be due to crystal defects

induced by doping, which prevents the recombination of charge carriers. The pure TiO_2 cannot absorb the visible light theoretically.

The rate constants for the photodegradation of methylene blue were obtained from a plot of $\ln(C_0/C)$ vs time. The reaction rate constant was calculated by the following equation

$$ln(C_0/C) = kt \qquad (12)$$

where t is the reaction time, C is the concentration of dye at time t and C_o is the initial concentration.

Kinetics of photocatalytic activity were studied from the linear relationship between $\ln(C_0/C)$ and time. The reaction rate constant is calculated from the slope of the straight line in the Figure 4.15. The order of the reaction is pseudo-first-order. For sunlight irradiation, the rate constant for pure 1 mol% Co-doped anatase TiO_2 was 0.02484 min^{-1} whereas for TiO_2 a lower value of 0.01792 min^{-1} was obtained.

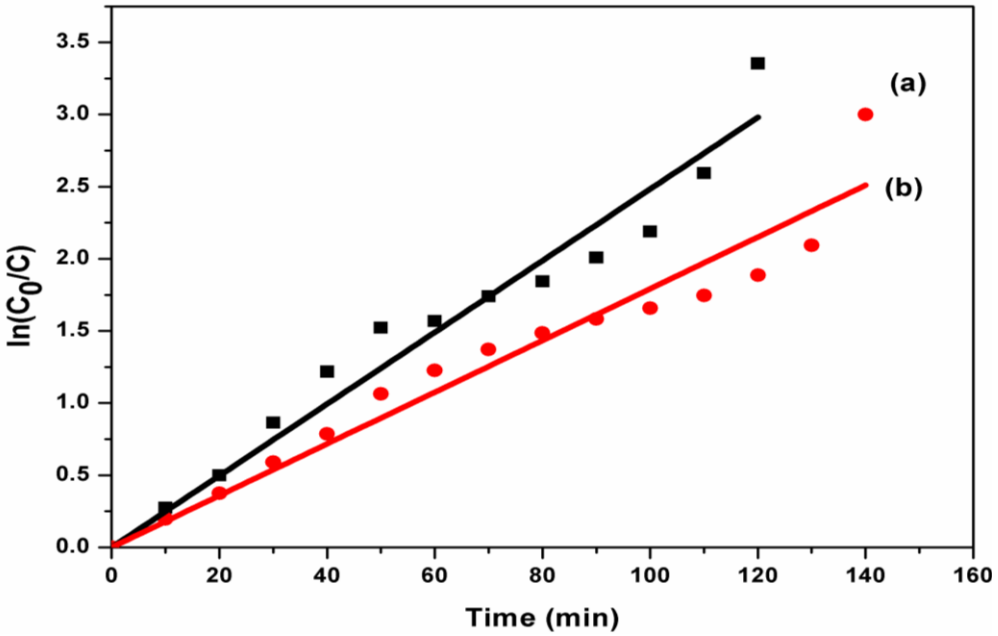

Fig.4.15 Pseudo first order kinetics plot for the degradation of methylene blue under sunlight a) 1 mol% Co-doped anatase TiO_2 and b) anatase TiO_2.

4.3.9 Dye-sensitized solar cells (DSSCs)

Solar cells made up of semiconductor metal oxides are an alternative to silicon solar cells. The dye-sensitized solar cell (DSSC) is made up of four basic components:

transparent conducting metal oxide coated substrate, counter electrode, dye and electrolyte. TiO_2 is the best semiconductor metal oxide for DSSC. Anatase phase titania is commonly used as a photo-anode material in DSSC. The dye is very important since it absorbs sunlight directly. Ruthenizer 535-bis TBA and Ruthenizer 535 have been found to be most effective sensitizers for titanium dioxide. However, these dyes are very costly since sophisticated methods and purification steps are required for synthesis. Moreover, limited abundance and availability of noble metals have forced the scientific community to search for natural dyes. The use of natural dyes in the fabrication of DSSC offers more cost-effective manufacturing alternative.

Fabrication of solar cell

The doctor blade method was used to make TiO_2 nanoparticle coating on the top of fluorine doped tin oxide (FTO) transparent glass plate. The TiO_2 film on FTO is immersed in dye solution for the adsorption of dye molecules on the surface of TiO_2. Iodide/triodide (I^-/I^{3-}) were used as liquid electrolyte. Carbon coated FTO glass plate was used as counter electrode. Two electrodes and an electrolyte in between were sandwiched together to form the cell assembly. Schematic representation of cell assembly is shown in Figure 4.16. In our studies, fruit juices from pomegranate and beetroot was used as dyes in the fabrication of DSSCs. The voltage and current of cells under natural sunlight irradiation were measured using a digital voltmeter ammeter and the values are shown in Table 4.4.

Table 4.4. Summary of current and voltage measurement of DSSC for various natural dyes.

Natural Dye	Voltage (V)	Current (μA)
Beetroot	0.19	100
Pomegranate	0.6	180

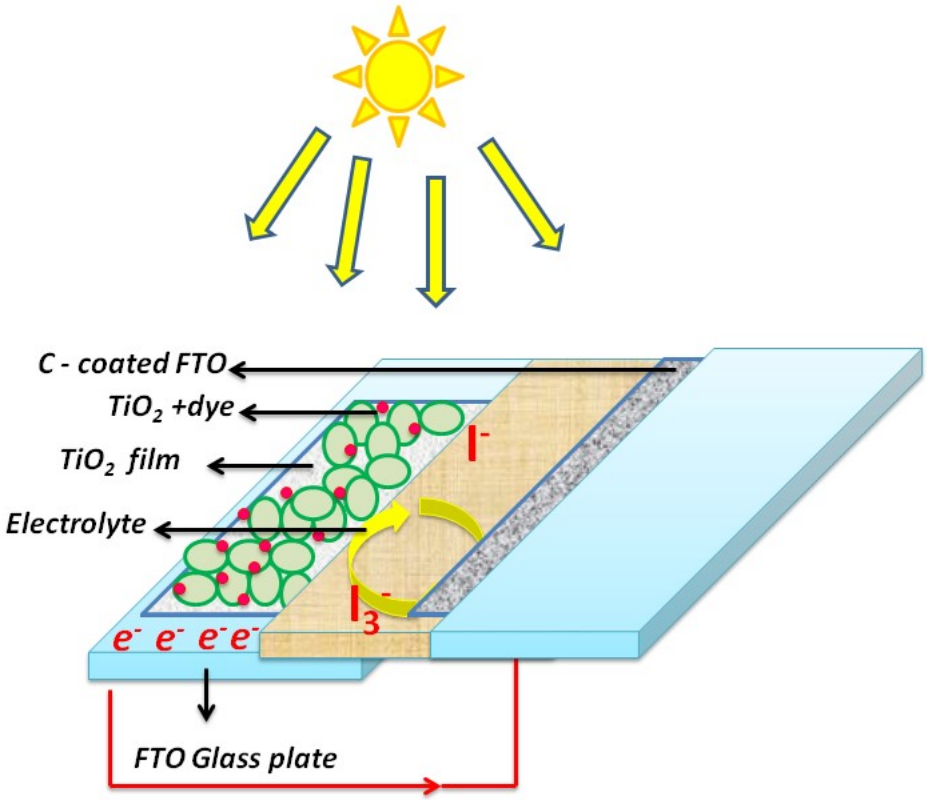

Fig. 4.16 Schematic representation of cell assembly.

DSSC have been constructed and photograph is given in Figure 4.17. However, the magnitude of the current was very low. The results suggest that the natural dyes can be used in the place of costly synthetic dyes for the fabrication of low cost solar cell.

Fig. 4.17 Photograph of Dye sensitised solar cell assembly.

4.4 Conclusion

In summary, nanocrystalline anatase TiO_2 was synthesised from titanium isopropoxide through an aqueous reflux route. 1 mol% Co-doped anatase phase TiO_2 has been successfully prepared using this method. Properties of both doped and undoped titania were analysed. The XRD and TEM images confirmed the formation of anatase TiO_2. The XRD result of TiO_2 shows that the primary particle size of the as prepared anatase crystals is 3 nm and that of calcined sample is 6.5 nm. The crystalline nature of the calcined sample was also confirmed by HRTEM images. From the FESEM images, the particles were found to be spherical and agglomerated. The XPS and EDS were used to determine the presence of cobalt ion in the TiO_2 lattice. The UV-Visible diffuse reflectance spectrum shows that 1 mol% Co-doped TiO_2 has also an absorption in the visible region. Degradation of methylene blue in presence of sunlight was used to study the photocatalytic activity of the Co-doped and undoped TiO_2 samples. TiO_2 is excellent photocatalyst under UV light irradiation. Cobalt doping extends the optical absorption of TiO_2 to the visible region and allows efficient use of sunlight for photocatalysis. The result of the present study shows that cobalt-ion doping enhances the photocatalytic activity of TiO_2. Finally, prepared anatase TiO_2 was also used to fabricate DSSC using natural dyes pomegranate and beetroot as photosensitizers.

References

1. Guo, Q., Zhou, C., Ma, Z., & Yang, X. (2019). Fundamentals of TiO_2 photocatalysis: concept, mechanisms, and challenges. *Advanced Materials*, *31*(50), 1901997.
2. Su, T. M., Qin, Z. Z., Ji, H. B., Jiang, Y. X., & Huang, G. (2016). Recent advances in the photocatalytic reduction of carbon dioxide. *Environmental Chemistry Letters*, *14*(1), 99-112.
3. Kennedy, J., Hayward, J., Davies, P. R., & Bowker, M. (2021). Hydrogen production by the photoreforming of methanol and the photocatalytic water–gas shift reaction. *Journal of Physics: Energy*, *3*(2), 024007.
4. .Kang, X., Liu, S., Dai, Z., He, Y., Song, X., & Tan, Z. (2019). Titanium dioxide: from engineering to applications. *Catalysts*, *9*(2), 191.
5. Li, R., Li, T., & Zhou, Q. (2020). Impact of titanium dioxide (TiO_2) modification on its application to pollution treatment—a review. *Catalysts*, *10*(7), 804.
6. Bui, V. K. H., Tran, V. V., Moon, J. Y., Park, D., & Lee, Y. C. (2020). Titanium dioxide microscale and macroscale structures: A mini- review. *Nanomaterials*, *10*(6), 1190.

7. Nyamukamba, P., Okoh, O., Mungondori, H., Taziwa, R., & Zinya, S. (2018). Synthetic methods for titanium dioxide nanoparticles: a review. *Titanium Dioxide—Material for a Sustainable Environment; Yang, D., Ed*, 151-175.

8. Pan, Y., Yuan, X., Jiang, L., Yu, H., Zhang, J., Wang, H., Guan, R., & Zeng, G. (2018). Recent advances in synthesis, modification and photocatalytic applications of micro/nano-structured zinc indium sulfide. *Chemical Engineering Journal*, *354*, 407-431.

9. Odling, G., & Robertson, N. (2015). Why is anatase a better photocatalyst than rutile? The importance of free hydroxyl radicals. *ChemSusChem*, *8*(11), 1838-1840.

10. Nateq, M. H., & Ceccato, R. (2019). Sol-gel synthesis of TiO_2 nanocrystalline particles with enhanced surface area through the reverse micelle approach. *Advances in Materials Science and Engineering*, *2019*.

11. Periyat, P., Baiju, K. V., Mukundan, P., Pillai, P. K., & Warrier, K. G. K. (2007). Aqueous colloidal sol–gel route to synthesize nanosized ceria-doped titania having high surface area and increased anatase phase stability. *Journal of sol-gel science and technology*, *43*(3), 299-304.

12. Luo, W., & Taleb, A. (2021). Large-scale synthesis route of TiO_2 nanomaterials with controlled morphologies using hydrothermal method and TiO_2 aggregates as precursor. *Nanomaterials*, *11*(2), 365.

13. Beyer, J., Mamakhel, A., Søndergaard-Pedersen, F., Yu, J., & Iversen, B. B. (2020). Continuous flow hydrothermal synthesis of phase pure rutile TiO_2 nanoparticles with a rod-like morphology. *Nanoscale*, *12*(4), 2695-2702.

14. Sofronov, D., Rucki, M., Demidov, O., Doroshenko, A., Sofronova, E., Shaposhnyk, A., Kapustnik, O., Mateychenko, P.,& Kucharczyk, W. (2020). Formation of TiO_2 particles during thermal decomposition of $Ti(NO_3)_4$, $TiOF_2$ and $TiOSO_4$. *Journal of Materials Research and Technology*, *9*(6), 12201-12212.

15. Deshmukh, S. M., Tamboli, M. S., Shaikh, H., Babar, S. B., Hiwarale, D. P., Thate, A. G., sheikh, A.F., Alam M.A., Khetre, S. M., & Bamane, S. R. (2021). A facile urea-assisted thermal decomposition process of TiO_2 nanoparticles and their photocatalytic activity. *Coatings*, *11*(2), 165.

16. Wang, X., Zhang, D., Xiang, Q., Zhong, Z., & Liao, Y. (2018). Review of water-assisted crystallization for TiO_2 nanotubes. *Nano-micro letters*, *10*(4), 1-28.

17. Ramos-Delgado, N. A., Gracia-Pinilla, M. Á., Mangalaraja, R. V., O'Shea, K., & Dionysiou, D.D.(2016).Industrial synthesis and characterization of nanophotocatalysts materials: titania. *Nanotechnology reviews*, *5*(5), 467-479.

18. Kong, L., Karatchevtseva, I., Blackford, M., Chironi, I., & Triani, G. (2012). Synthesis and characterization of rutile nanocrystals prepared in aqueous media at low temperature. *Journal of the American Ceramic Society*, *95*(2), 816-822.

19. Vorkapic, D., & Matsoukas, T. (1998). Effect of temperature and alcohols in the preparation of titania nanoparticles from alkoxides. *Journal of the American Ceramic Society*, *81*(11), 2815-2820.

20. Seifried, S., Winterer, M., & Hahn, H. (2000). Nanocrystalline titania films and particles by chemical vapor synthesis. *Chemical Vapor Deposition*, *6*(5), 239-244.

21. Rab, N., Chong, F. K., Mohamed, H. I., & Lim, W. H. (2018). Preparation of TiO_2 nanoparticles by hydrolysis of $TiCl_4$ using water and glycerol solvent system. In *Journal of Physics: Conference Series* (Vol. 1123, No. 1, p. 012065). IOP Publishing.

22. Cao, T., Li, Y., Wang, C., Shao, C., & Liu, Y. (2011). One-step nonaqueous synthesis of pure phase TiO_2 nanocrystals from $TiCl_4$ in butanol and their photocatalytic properties. *Journal of Nanomaterials*, *2011*.

23. Li, W., & Zeng, T. (2011). Preparation of TiO_2 anatase nanocrystals by $TiCl_4$ hydrolysis with additive H_2SO_4. *PloS one*, *6*(6), e21082.

24. Wu, C. Y., Tu, K. J., Deng, J. P., Lo, Y. S., & Wu, C. H. (2017). Markedly enhanced surface hydroxyl groups of TiO_2 nanoparticles with superior water-dispersibility for photocatalysis. *Materials*, *10*(5), 566.

25. Zoccal, J. V. M., Arouca, F. O., & Gonçalves, J. A. S. (2010). Synthesis and characterization of TiO_2 nanoparticles by the method pechini. In *Mater. Sci. Forum* 660, 385-390.

26. He, J., Du, Y. E., Bai, Y., An, J., Cai, X., Chen, Y., Wang, P., Yang, X., & Feng, Q. (2019). Facile formation of anatase/rutile TiO_2 nanocomposites with enhanced photocatalytic activity. *Molecules*, *24*(16), 2996.

27. Duarte, C. A., Goulart, L. R., Filice, L. D. S. C., Lima, I. L. D., Campos-Fernández, E., Dantas, N. O., Silva, A. C. A., Soares, M. B. P., Santos, R. R. D., Cardoso, C. M. A., Franca L. S. D. A., Rocha, V. P. C., Ribeiro, Perez, G., Carvalho L. N., & Alonso-Goulart, V. (2020). Characterization of crystalline phase of TiO_2 nanocrystals, cytotoxicity and cell internalization analysis on human adipose tissue-derived mesenchymal stem cells. *Materials*, *13*(18), 4071.

28. El Mragui, A., Logvina, Y., Pinto da Silva, L., Zegaoui, O., & Esteves da Silva, J. C. (2019). Synthesis of Fe-and Co-doped TiO_2 with improved photocatalytic activity under visible irradiation toward carbamazepine degradation. *Materials*, *12*(23), 3874.

29. Luo, Z., Poyraz, A. S., Kuo, C. H., Miao, R., Meng, Y., Chen, S. Y., Jiang, T., Wenos, C., & Suib, S. L. (2015). Crystalline mixed phase (anatase/rutile) mesoporous titanium dioxides for visible light photocatalytic activity. *Chemistry of Materials*, *27*(1), 6-17.

30. Chanda, A., Rout, K., Vasundhara, M., Joshi, S. R., & Singh, J. (2018). Structural and magnetic study of undoped and cobalt doped TiO_2 nanoparticles. *RSC advances*, *8*(20), 10939-10947.

31. Lin-Vien, D., Colthup, N. B., Fateley, W. G., & Grasselli, J. G. (1991). *The handbook of infrared and Raman characteristic frequencies of organic molecules*. Elsevier.

32. Lontio Fomekong, R., & Saruhan, B. (2019). Synthesis of Co^{3+} doped TiO_2 by co-precipitation route and its gas sensing properties. *Frontiers in Materials*, *6*, 252.

33. Monazzam, P., & Kisomi, B. F. (2017). Co/TiO_2 nanoparticles: preparation, characterization and its application for photocatalytic degradation of methylene blue. *Desalination Water Treat.,63,283.*

34. Jalali, J., & Mozammel, M. (2017). Degradation of water-soluble methyl orange in visible light with the use of silver and copper co-doped TiO_2 nanoparticles. *J. Mater. Sci.: Mater. Electron.*, *28*(7), 5336-5343.

35. Liu, Y., Feng, H., Yan, X., Wang, J., Yang, H., Du, Y., & Hao, W. (2017). The origin of enhanced photocatalytic activities of hydrogenated TiO_2 nanoparticles. *Dalton Transactions*, *46*(32), 10694-10699.

36. Parayil, S. K., Razzaq, A., & In, S. I. (2015). Formation of titania-silica mixed oxides in solvent mixtures and their influences for the photocatalytic CO_2 conversion to hydrocarbon. *Journal of nanoscience and nanotechnology*, *15*(9), 7285-7292.

37. Liu, Z., Jian, Z., Fang, J., Xu, X., Zhu, X., & Wu, S. (2012). Low-temperature reverse microemulsion synthesis, characterization, and photocatalytic performance of nanocrystalline titanium dioxide. *International Journal of Photoenergy*, *2012*.

38. Peng, G. W., Chen, S. K., & Liu, H. S. (1995). Infrared absorption spectra and their correlation with the Ti-O bond length variations for TiO_2 (rutile), Na-titanates, and Na-titanosilicate (natisite, $Na_2TiOSiO_4$). *Applied spectroscopy*, *49*(11), 1646-1651.

Chapter 5

Wet chemical synthesis of ZnO nanoparticles and its photocatalytic activity studies under visible light irradiation

Contents

Abstract

In this work, wet chemical process such as simple precipitation, reflux technique and sol-gel based Pechini's method were used to synthesize nanostructured zinc oxide (ZnO) crystals from zinc nitrate hexahydrate as starting materials and ammonia/hexamethylene tetraamine as a precipitating agent or carboxylic acid such as oxalic acid/citric acid as chelating agents. The precipitates were calcined at 550 ˚C resulting in the formation of different shapes of zinc oxide crystals. The samples were characterized by X-ray diffraction, UV-Visible spectroscopy, FT-IR spectroscopy, TG-DTG, BET surface area, SEM and TEM techniques. The XRD pattern confirmed the formation of hexagonal wurtzite structure of ZnO nanoparticles having an average size of 16.29 nm and 12.31nm, for oxalic acid and citric acid methods, respectively. The crystallite size was found to be 27.8 nm for 2 hour refluxed sample and 33.8 nm for 4 hours refluxed sample. UV- Visible diffused reflectance spectra were used to determine the optical properties of the samples. The bandgap energy of ZnO was found to be 3.1 eV, 3.04 eV and 3.1 eV oxalic acid method, citric acid methods, reflux route, respectively. Finally, Methylene blue dye degradation was used to study the photocatalytic activity of ZnO under visible LED light irradiation and was found to have remarkable activity.

5.1 Introduction

Zinc oxide is a member of wide-bandgap semiconductors having the band gap energy of 3.37 eV. The ZnO has recently emerged as a promising building component in piezoelectric transducers, photovoltaic devices, UV detectors, photocatalysts, gas and biosensors, and light-emitting diodes.[1-3] It is also used in paints, animal feed, cosmetics, pharmaceuticals, ceramics and rubber industries.[4] The ZnO is a highly photosensitive material with good chemical stability, high electron mobility, large

piezoelectric response and exciton binding energy (60 meV).[5-7] It is used as transparent conducting oxide in smart windows and solar cells.[8] Because of its high crystalline and low-dimensional feature enhance electron transportation. In addition it posses two emission bands, first of which is in the UV region and second of which is a deep level band that cover whole visible spectrum.[9] Hence it is suitable for photocatalytic reaction. The novel properties of ZnO nanomaterials are depend upon its size, shape, crystallinity, morphology and crystallographic orientation. In recent years, great attention has been given to the preparation of ZnO nanopowder due to the various attractive properties and applications.

The ZnO occurs naturally as the mineral zincite. Thermodynamically stable crystallographic phase of ZnO is wurtzite. It has a hexagonal tight packing of oxygen and zinc atoms, with zinc atoms in tetrahedral sites in its ionic structure. Zinc oxide has been prepared using a variety of techniques, including magnetron sputtering, spray pyrolysis, chemical vapour deposition, sol–gel process, hydrothermal synthesis, thermal decomposition precipitation method, flame spray pyrolysis and pulsed laser deposition. It is more desirable to synthesise ZnO using low-cost technologies based on solution phase growth. Many wet chemical methods have been reported for the synthesis of ZnO, such as thermal decomposition, sol-gel technique and precipitation. Wet chemical processes are carried out at low temperature and are cost effective and scalable. In wet chemical process, reactant, reaction time, concentration etc. have significant role on the morphology of ZnO nanoparticles.

Compared to other traditional methods, homogeneous precipitation techniques are simple and it is easy to produce ZnO in various sizes and shapes on large scale and in repeatable manner.[10] Nevertheless, intermediate compounds are precipitated depending upon the types of precursor and subsequently converted into zinc oxide by thermal decomposition processes. Precipitation from inorganic or organic solution is a bottom up process. This method can be used to easily control nucleation, growth and ageing of particles in solution. The precipitation method can be controlled by different factors such as concentration and pH.[4] Kumar et.al reported the synthesis of ZnO nanoparticles from zinc sulfate heptahydrate and sodium hydroxide using simple precipitation method. Morphology of the ZnO samples was found to change and the bandgap was found to decrease, by increase in calcination temperature. The absorption maximum was also found to be shifted to higher wavelength region, by

increase in calcination temperature.[11] Srivastava et.al reported the pyrolysis of oxalate produced by conventioanal precipitation method followed by calcinations at 450℃ to synthesis ZnO nanomaterials.[12] They obtained nano-rods having diameter 75-300 nm.

The sol–gel method using zinc nitrate and citric acid has proved to be a relatively simple, low cost and low temperature method for synthesizing uniformly distributed zinc oxide nanoparticles.[13] Alpha-hydroxycarboxilic acid such as citric acid can be used as a precipitating agent and it is also act as capping agent. Akbar et.al has been synthesized ZnO using simple precipitation technique with the addition of citric acid.[14] They obtained ZnO nanorods and they attributed reason for anisotropic growth as being due to citric acid molecules adsorbed on the surface of ZnO nuclei.

The citric acid serves two important functions: 1) it plays as fuel for the combustion reaction 2) it chelates with metal cations and forms complexes, thus preventing the precipitation of hydroxylated compounds.[15] Nitrate anion works as oxidizer.

In particular, the reflux technique has attracted attention because of its simple experimental setup and high potential for scaling-up. The ZnO is relatively uniform in size and shape. The solution phase growth methods for nanostructures have received lot of attention because they do not require high temperatures or vacuum systems.[16]

A long series of papers has been published for the synthesis of ZnO using hexamethylenetetramine.[17] It is a non-ionic, heterocyclic organic compound with molecular formula $(CH_2)_6N_4$. It functions as a nonpolar chelating agent that preferentially adheres to the ZnO crystal's nonpolar facets, exposing just the (001) plane for epitaxial growth.[18,19] The following are the most important equations for the growth of ZnO from $Zn(NO_3)_2$ and HMTA precursors at 90 ºC.[20]

$$(CH_2)_6N_4 + 6\,H_2O \longrightarrow 6HCHO + 4\,NH_3 \quad (1)$$

$$NH_3 + H_2O \rightleftharpoons NH_4^+ + OH^- \quad (2)$$

$$2OH^- + Zn^{2+} \rightleftharpoons Zn(HO)_2 + H_2O \quad (3)$$

$$Zn(OH)_2 \rightleftharpoons ZnO + H_2O \quad (4)$$

HMTA buffer the pH of the reaction and act as continuous source of hydroxide ions through thermal decomposition.[21,22] It ensures crystalline and morphological

properties better than other reducing agents. The growth takes place at temperature ranging from 55 to 95 ˚C. It was recently reported that the growth rate and morphology of the produced nano-rods/wires can be controlled to some extent by changing the experimental parameters, such as temperature and precursor concentration. Vayssieres et.al synthesised single crystalline hexagonal rods array of ZnO on transparent conducting tin oxide glass substrate from aqueous solution of zinc nitrate and HMTA at 95 ˚C.[23] They also reported that the material was readily crystalline and additional heat treatment was not required.

In present work, we synthesised nanosized ZnO materials through three wet chemical methods; (i) simple precipitation using ammonia (ii) sol-gel method (Pechini's method) using carboxylic acids, oxalic acid and citric acid and (iii) reflux technique using as HMTA in aqueous medium.

In a neutral solution, zinc oxide is insoluble, but it is soluble in an highly acid or alkali solution.[24] So we selected weak acid and base for the study. Furthermore, the structural and optical properties and photocatalytic activity of ZnO were also studied. The particle size, crystallinity and morphology were characterized using X-ray diffraction, TEM and SEM techniques. The photoactivity of prepared ZnO samples were analyzed by the photodegradation of methylene blue under visible light irradiation.

5. 2 Materials and method

5. 2.1 Materials

Zinc nitrate hexahydrate (Merk, 99%), Ammonium hydroxide min. 25% (Merck, 99%), Oxalic acid (Merck, 99%), Citric acid (Merck, 99%) and hexamethylene tetramine-HMTA (Merck, 99%) were used as starting materials for the synthesis of ZnO samples. All solutions were prepared by using deionised water. Chemicals were used without any pre-treatment.

5.2.2 Synthesis of ZnO nanoparticles

5.2.2.1 Precipitation method

The precipitation method was used to make ZnO nanoparticles using zinc nitrate hexahydrate and ammonium hydroxide as precursors. The 0.04 M zinc nitrate solution was prepared and a dilute ammonium hydroxide solution was slowly added drop wise

into the above solution until pH of the solution reaches 10. The solution was stirred. White coloured precipitates were filtered, washed with water and dried at 120 ˚C for 2 hours. Then the precipitate was calcined at 550 ˚C by heating from room temperature at a heating rate of 15 degrees per minute. Figure 5.1 shows a schematic representation of the preparation of the above method.

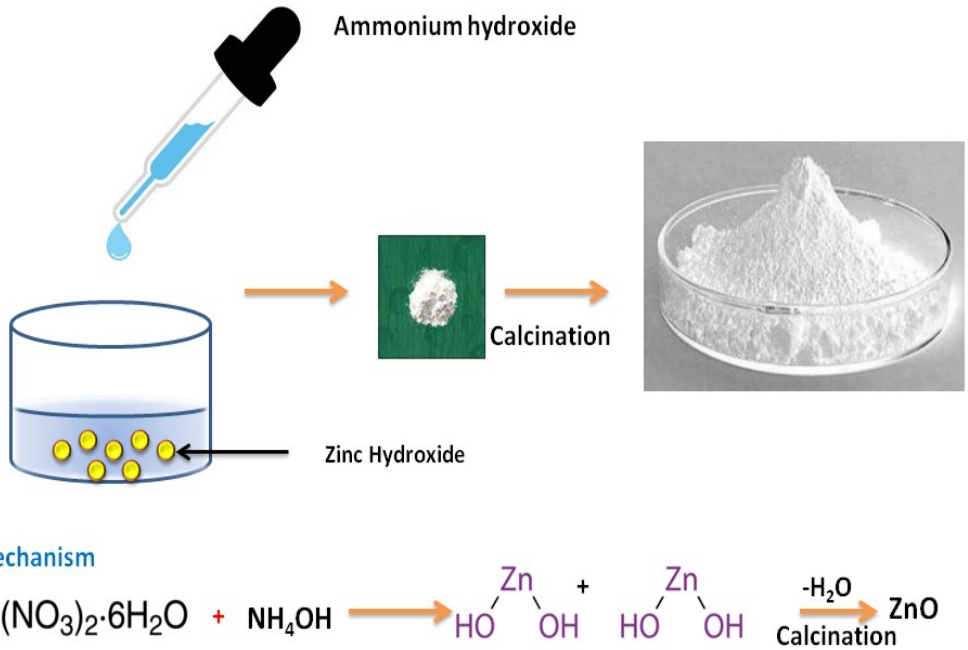

Fig. 5.1 Schematic representation of precipitation method

5.2.2.2 Sol-Gel method

(i) Preparation using oxalic acid

Zinc nitrate and carboxylic acid such as oxalic acid solution were prepared separately. The oxalic acid was added slowly into the zinc nitrate solution under magnetic stirring. Solution was refluxed at 100 ˚C for one hour. The precipitate were collected, rinsed with distilled water, dried in a muffle furnace at 550 ˚C for 1 hour and ground to fine powder. Figure 5.2 shows a schematic representation of the preparation method.

(ii) Preparation using citric acid

Zinc nitrate and citric acid solution were prepared separately. Zinc nitrate solution was added to citric acid and a colloidal solution was obtained. Then concentrated ammonium hydroxide was added until the pH reached 7. The solution became more and more viscous during heating at 100 ˚C and finally become xerogel.

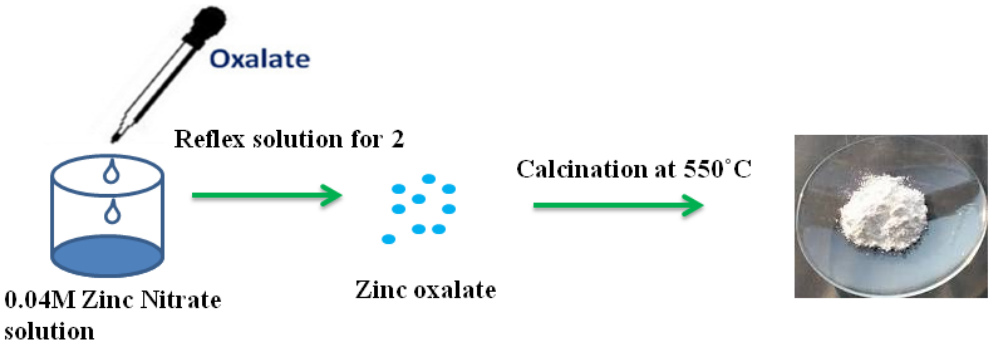

Fig. 5.2 Experimental method for the preparation of ZnO from zinc nitrate and oxalic acid.

5.2.2.3 Reflux route

An aqueous solution of 0.04 M zinc nitrate solution was prepared and a solution of 0.04 M HMTA solution was added to above solution under magnetic stirring. The solution was transferred to a round bottom flask and heated at 100 ˚C for 2 hours. White coloured precipitate was gradually obtained. The precipitate was collected, washed with distilled water, dried and then calcined in a muffle furnace at 550 ˚C for 1 hour. The above procedure was repeated by changing the refluxing time to 4 hours. The powders were characterized by various analytical techniques. The above procedures were also repeated by changing the HMTA concentration to 0.02 M.

The photocatalytic activities of these samples were analysed under visible LED light irradiation by studying methylene blue dye degradation. A suspension of the ZnO in the MB solution was stirred in the dark for half an hour to complete the adsorption desorption equilibrium of the dye on the nanoparticles. The suspension was exposed to visible LED light radiation under stirring. The dye concentration in the suspension was measured and monitored using a UV-Visible spectrophotometer, every 15 minutes. Degussa TiO_2 was used for comparison of the photoactivity.

5. 3 Results and discussion

(1) Characterization of ZnO prepared by precipitation method

5.3.1.1 XRD analysis

X-ray diffraction pattern of ZnO prepared by precipitation method and calcined at 550 ˚C is shown in the Figure 5.3. The diffraction peaks are indexed to the wurtzite

structure of ZnO (JCPDS 036-1451), which is predominantly c-axis oriented.[25] The peaks at 2θ = 31.8˚, 34.6˚, 36.5˚, 47.7˚, 56.6˚ and 63.5˚ corresponds to the hexagonal crystal planes (100), (002), (101), (102), (110) and (103) of ZnO. No characteristic peaks corresponding to other phases of ZnO or $Zn(OH)_2$ were observed in XRD spectra, indicating the presence of single phase wurtzite structure. The presence of strong and sharp peaks indicates that the ZnO are highly crystalline in nature. The average primary crystallite size of ZnO was estimated from (101) XRD peak using Debye-Scherrer's equation and was found to be 46.87 nm. The nucleation and growth of ZnO crystal from the aqueous solution are affected by the precursor concentration, pH etc. Fast nucleation and growth of the crystal occurs at high concentration of ammonium hydroxide and at high pH.

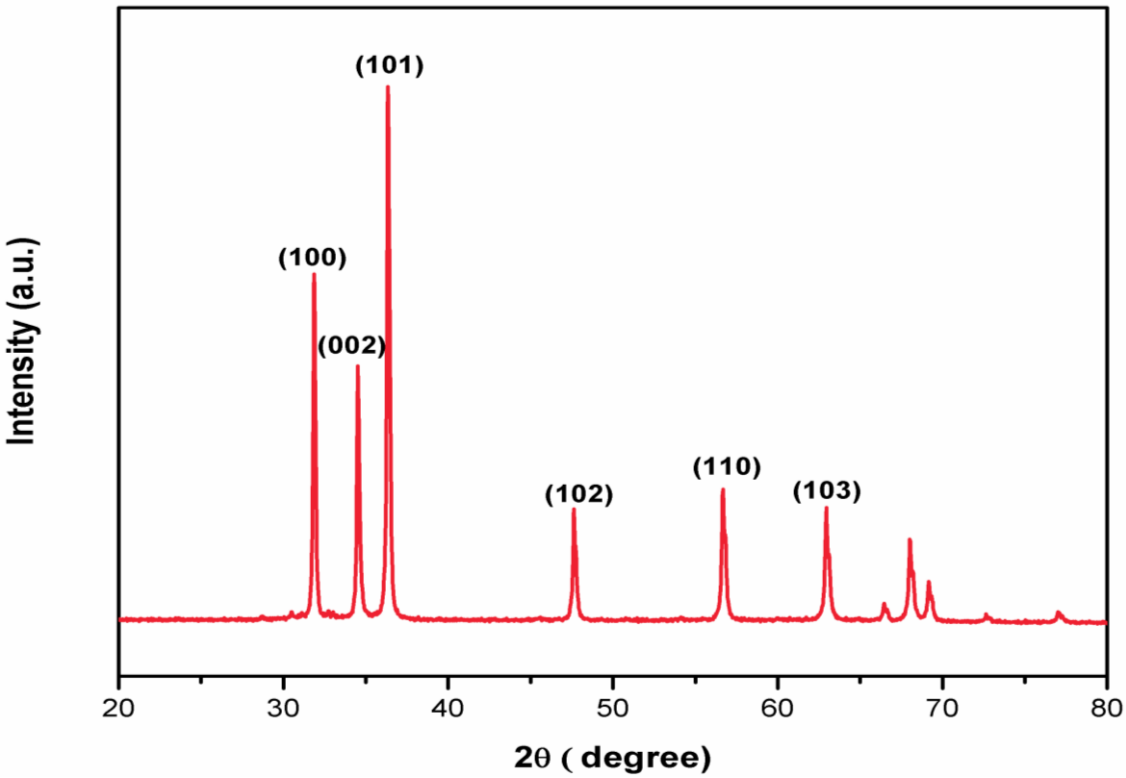

Fig. 5.3 XRD pattern of ZnO prepared using zinc nitrate and ammonia solution after calcination at 550 ˚C.

5.3.1.2 Morphological studies by FESEM

Morphology of the ZnO prepared by precipitation method using zinc nitrate and ammonia solution was studied by FESEM. The FESEM images of ZnO nanoparticles prepared by precipitation method (calcined at 550 ˚C) at different magnification are shown in Figure 5.4. From the images, it was observed that the particles are spherical

shape and agglomerated to form bigger clumps of diameter around 200 nm. At higher concentration of ammonia, the Zn^{2+} forms stable complexes with ammonia. As a result, the heterogeneous nucleation of ZnO occurs and particle size increases slowly.[13] Ammonia solution plays a vital role in the formation of ZnO nanostructure. Hydroxide ion causes the formation of primary nanocrystallite in the solution and rapidly assembles together to form larger aggregates.

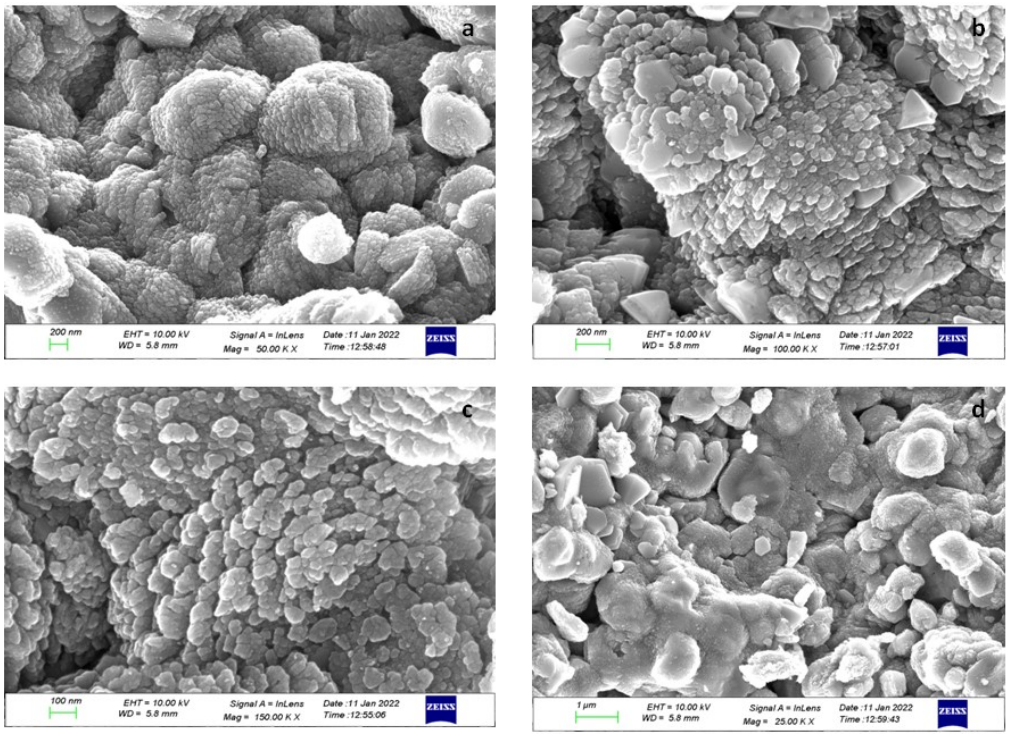

Fig.5.4 FESEM image of ZnO prepared by precipitation method using zinc nitrate and ammonium hydroxide and after calcination at 550 ˚C: (a-d) are images at different magnifications.

5.3.1.3 FT-IR spectral studies

The results from the previous analysis were further supported by the FT-IR analysis. The FT-IR spectra of precipitate obtained by the addition of zinc nitrate and ammonium hydroxide and calcined sample (at 550 ˚C) are given in the Figure 5.5. Broad bands around 3600-3000 cm^{-1} are observed in the sample obtained by precipitation. These bands correspond to stretching vibration of –OH groups. The band at 1645 cm^{-1} is attributed to bending vibration of O-H groups. A sharp band at 1363 cm^{-1} corresponding to symmetric stretching vibration of N-O bond. After calcinations, the broad band corresponding to O-H and N-O vibrations disappeared due to the decomposition of nitrate groups and elimination of water. The IR spectra supports the formation of zinc hydroxynitrates ($Zn(OH)(NO_3)\cdot H_2O$) during the

precipitation method.[26] However, these bands are completely absent in the calcined sample. Only a band at 500-400 cm^{-1} corresponding to stretching vibration of Zn-O bond was observed in the calcined sample indicating the formation of ZnO on calcination.[27]

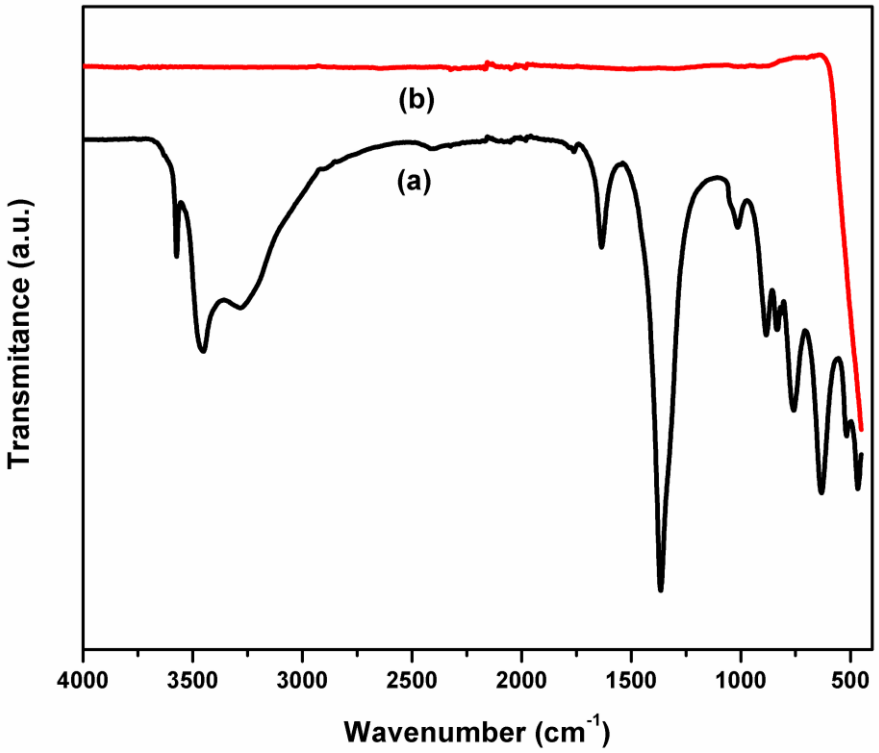

Fig.5.5 FT-IR spectra of ZnO a) before calcination and b) after calcination at 550 ˚C.

(II) Characterization of ZnO prepared by sol-gel method

5.3.2.1 XRD analysis

XRD patterns of ZnO obtained by sol-gel method using oxalic acid, after calcination at 550˚C is presented in Figure 5.6. From the figure it is clear that the XRD indexed with the typical wurtzite structure. The major peaks are observed at 31.81˚, 34.46˚, 36.28˚, 47.57˚, 56.63˚ and 62.87˚ corresponding to (100), (002), (101), (102), (110) and (103) planes, respectively. These data are in good agreement with JCPDS 36-1451 of pure wurtzite ZnO.[28] The average primary crystallite size was calculated using Sherrer equation. The primary crystallite size of the particles obtained by the sol gel method (16.29 nm) was found to be less than that obtained by the precipitation method (46.87 nm).

We obtained the similar XRD pattern for ZnO prepared by sol-gel method using citric acid and is shown in Figure 5.7. The major peaks in the XRD spectrum were observed at 31.66˚, 34.30˚, 36.13˚, 47.42˚, 56.46 ˚ and 62.71˚ and were indexed to the lattice planes (100), (002), (101), (102), (110), (103). The XRD patterns are in good agreement with standard wurtzite ZnO (JCPDS 36-1451). No characteristics peaks for other phase were observed in the XRD spectrum revealing the formation of pure wurtzite structure of ZnO. Sharp peaks in the XRD pattern indicate the highly crystalline nature of ZnO. The average primary crystallite size of the nanoparticles were calculated by Scherrer equation and was found to be 12.31 nm. It is clear that full width at half maximum value is higher compared to that of ZnO obtained by oxalic route, indicating the lower crystallite size of nanoparticles. The crystallite size of ZnO prepared by the sol gel methods (16.29 nm and 12.31 nm, for oxalic acid and citric acid methods, respectively) are lower than that obtained by precipitation method (46.87 nm).

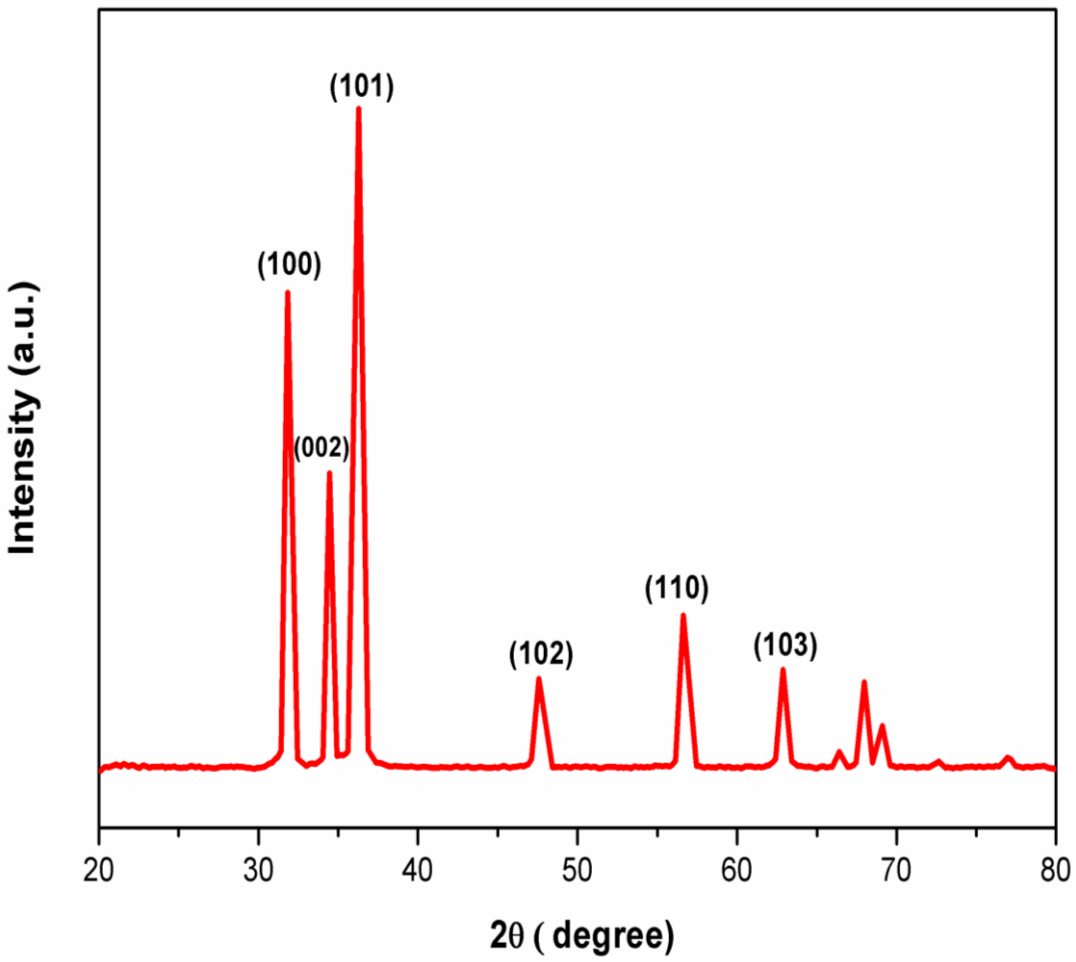

Fig. 5.6 XRD pattern of ZnO prepared by sol gel method using zinc nitrate and oxalic acid solution calcined at 550 ˚C.

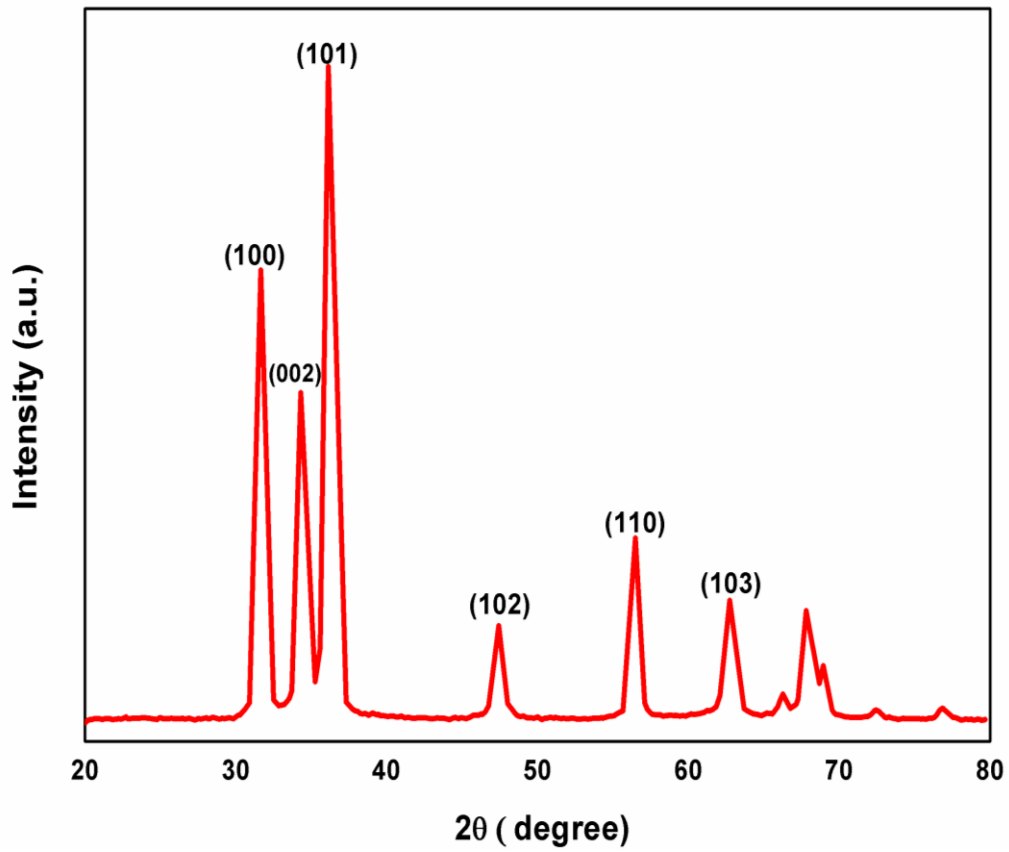

Fig. 5.7 XRD pattern of ZnO prepared by sol gel method using zinc nitrate and citric acid solution after calcination at 550 ˚C.

Citric acid is an effective complexing agent in the prevention of precipitation of $Zn(OH)_2$.[13] Two carboxylate groups of citric acid form coordinate bonds with the Zn^{2+} ion resulting in the formation of asymmetric and symmetric structure. Zinc citrate complex prevents the formation of $Zn(OH)_2$. Citric acid also increases viscosity during evaporation of sol, which in turn allowed for a faster sol-gel transition and prevents aggregation. It was observed that the grain sizes of the ZnO particles were minimum at pH 1.

5.3.2.2 Morphological studies by SEM

This SEM analysis was used to understand the surface morphology of the sample. Figure 5.8 shows the SEM images of ZnO prepared by sol-gel method using zinc nitrate and oxalic acid. It is very clear from the SEM images that the particles are highly agglomerated with irregular shape. Average particle size is in the range 1μm.

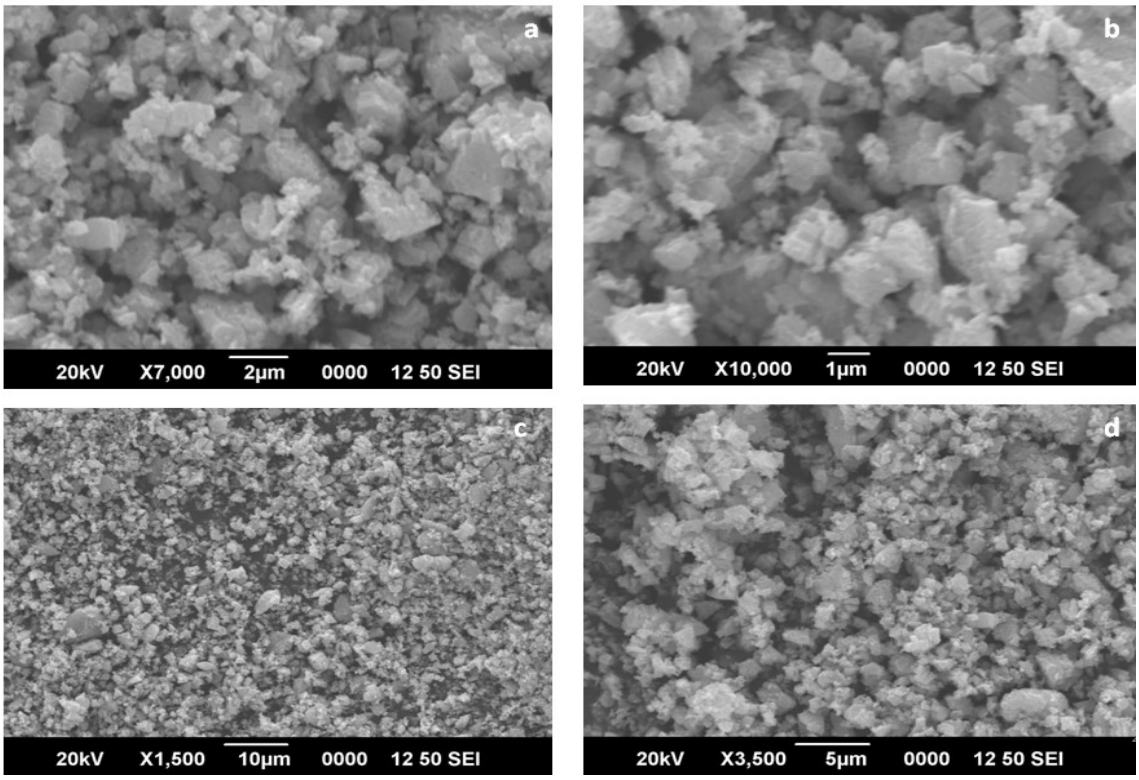

Fig.5.8 FESEM images of ZnO prepared by sol gel method using zinc nitrate and oxalic acid after calcination at 550 ˚C: (a-d) are images at different magnifications.

5.3.2.3 Morphological studies by TEM

The morphologies of ZnO synthesised by the sol-gel method using oxalic acid and citric acid were also analysed by TEM and images are shown in Figure 5.9 and Figure 5.10, respectively. The TEM images clearly show that the particles are spherical and having different particle sizes. The diameter of the spherical nanoparticles was in the range of 30-60 nm in oxalic acid route. In the citric acid route, size was in the range of 10-30 nm. The crystalline nature of the ZnO was studied using HR-TEM and SEAD. The HR-TEM images indicated that the particles were highly crystalline in nature. The interplanar distance of nano particles is 0.23 nm in oxalic acid route and 0.22 nm in citric acid route. This corresponds to (101) plane of ZnO. The SAED patterns also confirm the crystalline structure and hexagonal wurtzite structure of ZnO. In oxalic acid route the concentric rings are very clear with distinguishable spots. These spots corresponding to crystal planes are consistent with the XRD pattern. From SAED pattern of ZnO prepared by citric acid route, the rings are more spread out without sharp spots (faded edges) compared to oxalic acid route indicating the lower size of the particle. Zhang et.al reported the formation of spherical ZnO nanoparticles of size 20-30 nm by citric acid method.[13,29] Poonguzhali et al. has reported the formation of

ZnO spherical nanoparticle by a green combustion method using natural citric acid from lemon juice.[30]

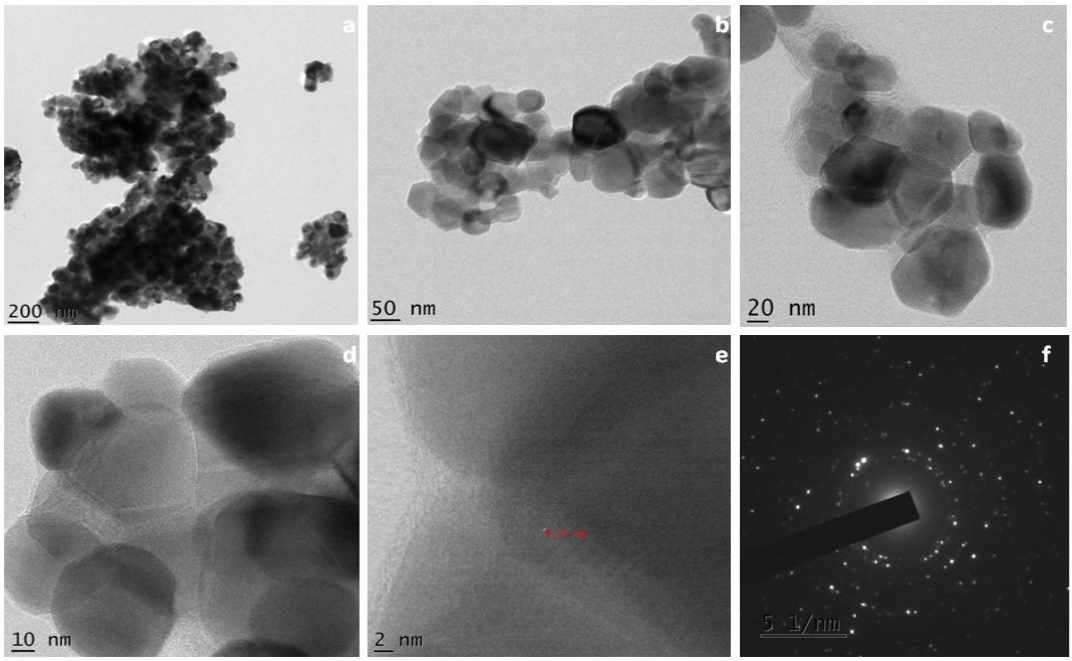

Fig. 5.9 TEM images of ZnO prepared by sol-gel method using oxalic acid and after calcination at 550 ˚C; (a-d) are images at different magnifications, e) HRTEM and f) SAED pattern.

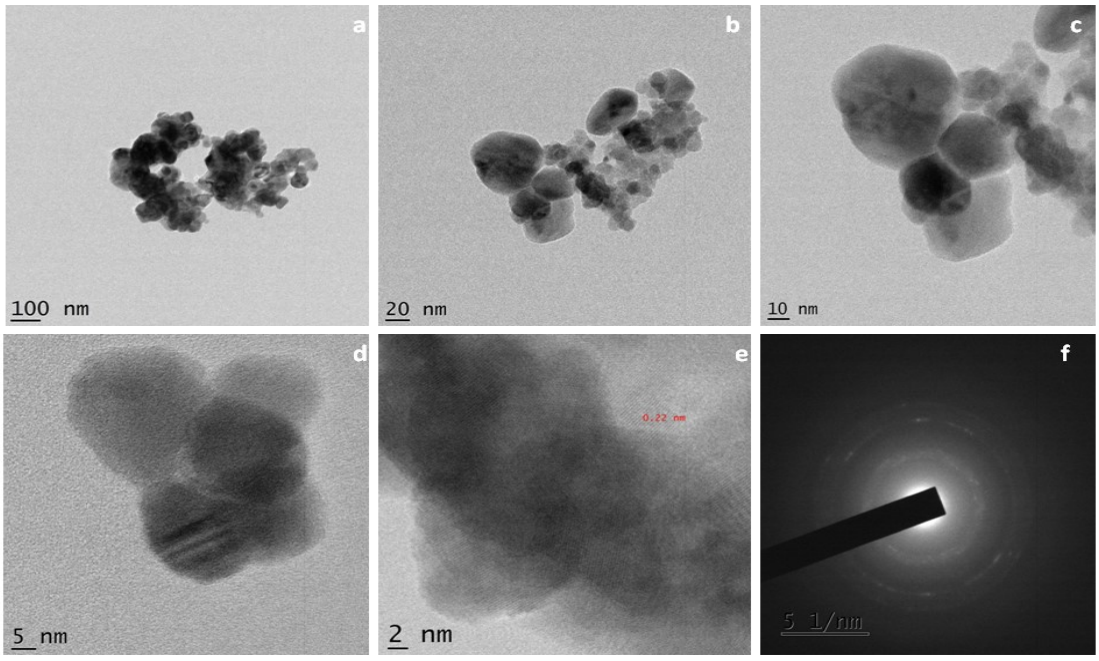

Fig. 5.10 TEM images of ZnO prepared by sol-gel method using citric acid and after calcination at 550 ˚C :(a-d) are images at different magnifications, e) HRTEM and f) SAED pattern.

5.3.2.4 UV-Visible diffuse reflectance spectra (DRS) and bandgap determination

Diffuse reflectance spectroscopy is widely used to study the optical property and bandgap energy of the solid materials. Diffuse reflectance spectra of ZnO prepared by sol-gel method using oxalic acid after calcination at 550 ˚C is shown in Figure 5.11. The sample exhibited its characteristic absorption in UV region and sharp cut off in the visible region. The band is corresponding to the excitation of electrons from the valence band to the conduction band. The curve has two absorption maxima λmax at 220 nm and 305 nm.

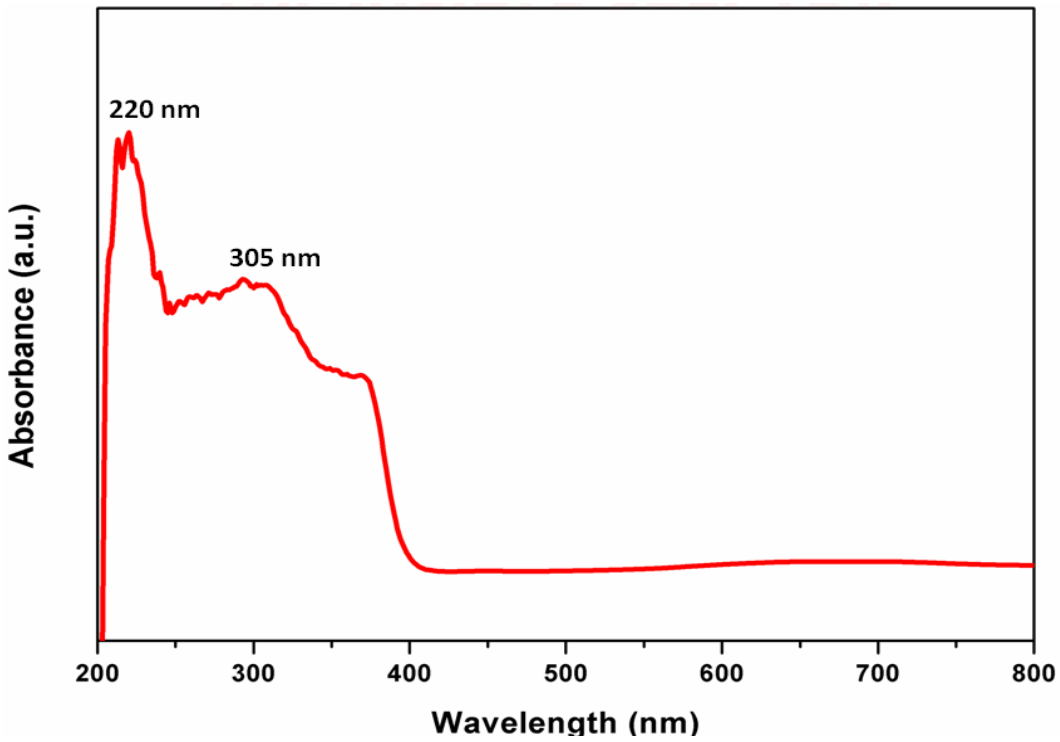

Fig. 5.11 Diffuse reflectance spectra of ZnO prepared by sol-gel method using oxalic acid and after calcination at 550 ˚C.

Band gap energy of ZnO was calculated using the absorption coefficient $(F(R)*E)^{0.5}$ vs. the energy of absorbed light using the Kubelka-Munk function. Figure 5.12 represent the graph of Kubelka-Munk function versus the absorbed light energy. Extrapolating the linear portion of the curve to the x-axis gives the band energy of the sample. The bandgap energy of ZnO prepared using oxalic acid is found to be 3.1 eV, using the above method.

UV-DRS spectrum of ZnO prepared by sol-gel method using citric acid followed the same trend as observed in the ZnO prepared by oxalic acid method. Diffuse

reflectance spectra of ZnO prepared by sol-gel method using citric acid showed characteristic absorption band in UV region with two absorption maxima at 224 nm and 311 nm. Figure 5.13 shows the UV-DRS spectra of ZnO prepared using citric acid. Bandgap energy was calculated as explained previously. Figure 5.13 represent the graph of Kubelka-Munk function versus the absorbed light energy for ZnO prepared using citric acid. The bandgap was found to be 3.04 eV.

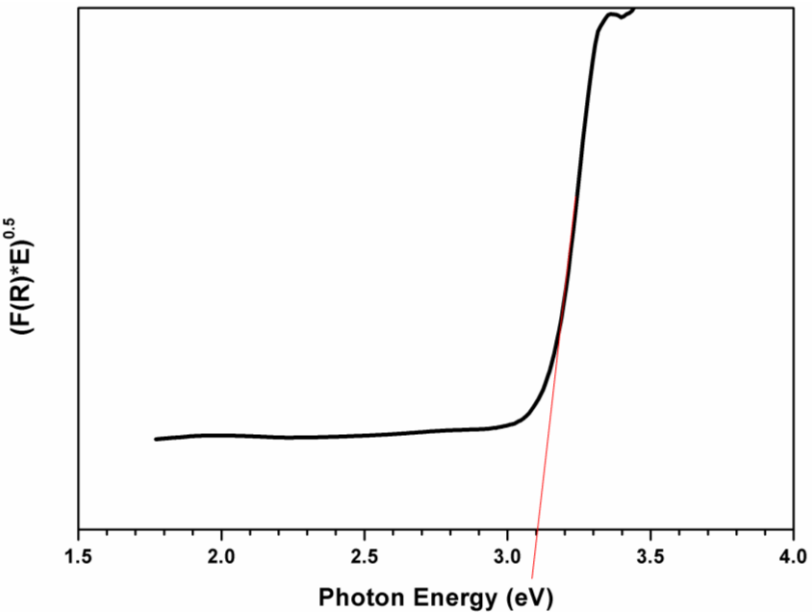

Fig. 5.12 Plot of the Kubelka-Munk function versus the energy of absorbed light for ZnO prepared by sol-gel method using oxalic acid and after calcination at 550 ˚C.

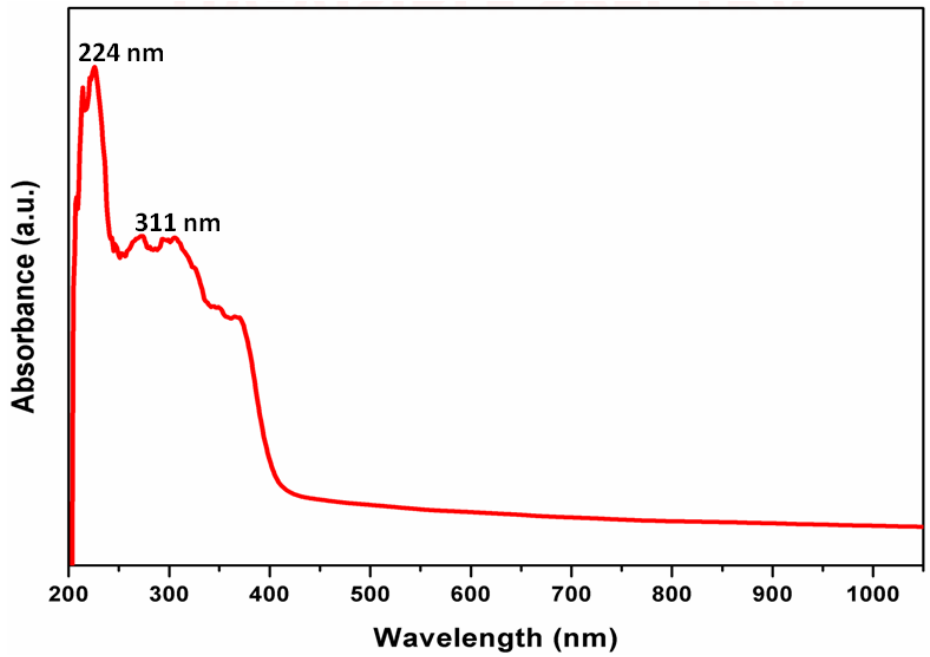

Fig. 5.13 Diffuse reflectance spectra of ZnO prepared by sol-gel method using citric acid and after calcination at 550 ˚C.

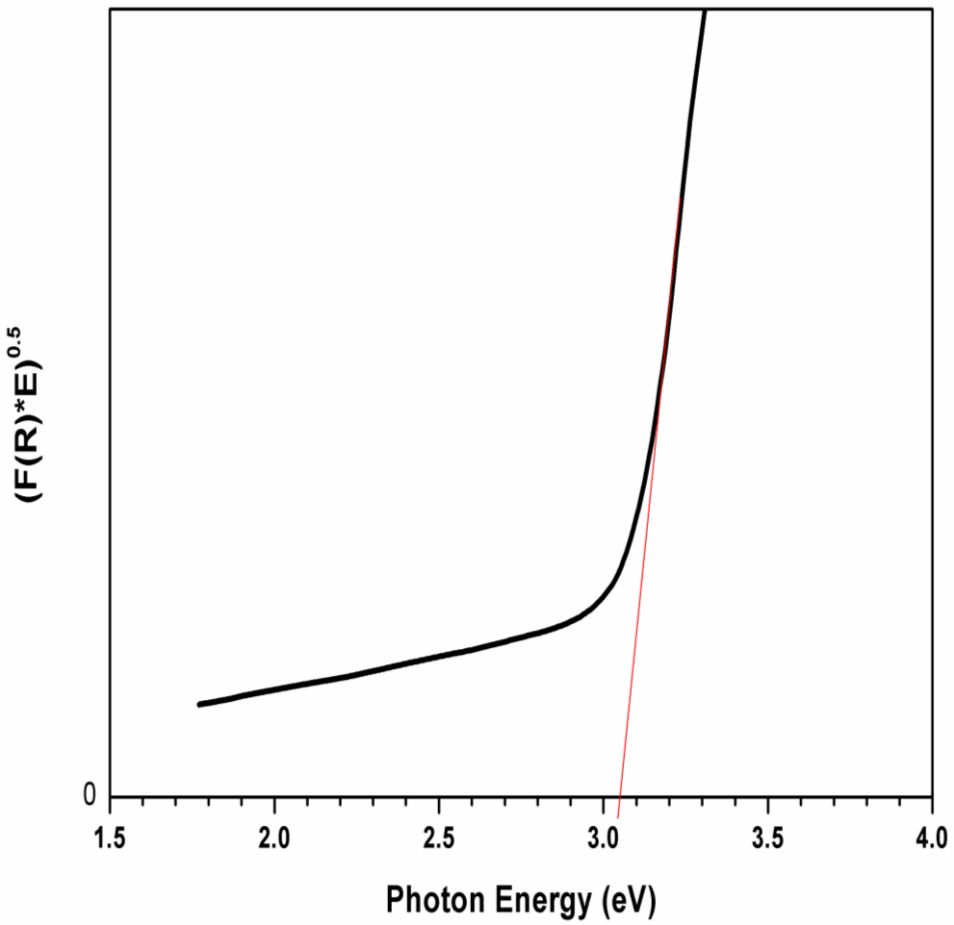

Fig. 5.14 Plot of the Kubelka-Munk function versus the energy of absorbed light for ZnO prepared by sol-gel method using citric acid and after calcination at 550 ˚C.

5.3.2.5 FT-IR spectral studies

Above result was further supported by FT-IR spectra. FT-IR spectra of as prepared and calcined ZnO prepared using oxalic acid are represented by Figure 5.15. For the as prepared sample, broad band at 3441 cm^{-1} corresponds to the stretching vibration of hydroxyl group. A sharp band at 1660 cm^{-1} represents the stretching vibration of carbonyl group. Band at 1315 cm^{-1} is the characteristic stretching band of nitro group. The formation of zinc oxalate was further supported by FT-IR spectra. During calcination, these bands are disappeared. For the calcined sample a characteristic band at 550-400 cm^{-1} corresponding to Zn-O bond was only obtained. The FT-IR spectra of as prepared and calcined ZnO prepared using citric acid are shown in Figure 5.16. Similar result was obtained for ZnO prepared by citric acid route.

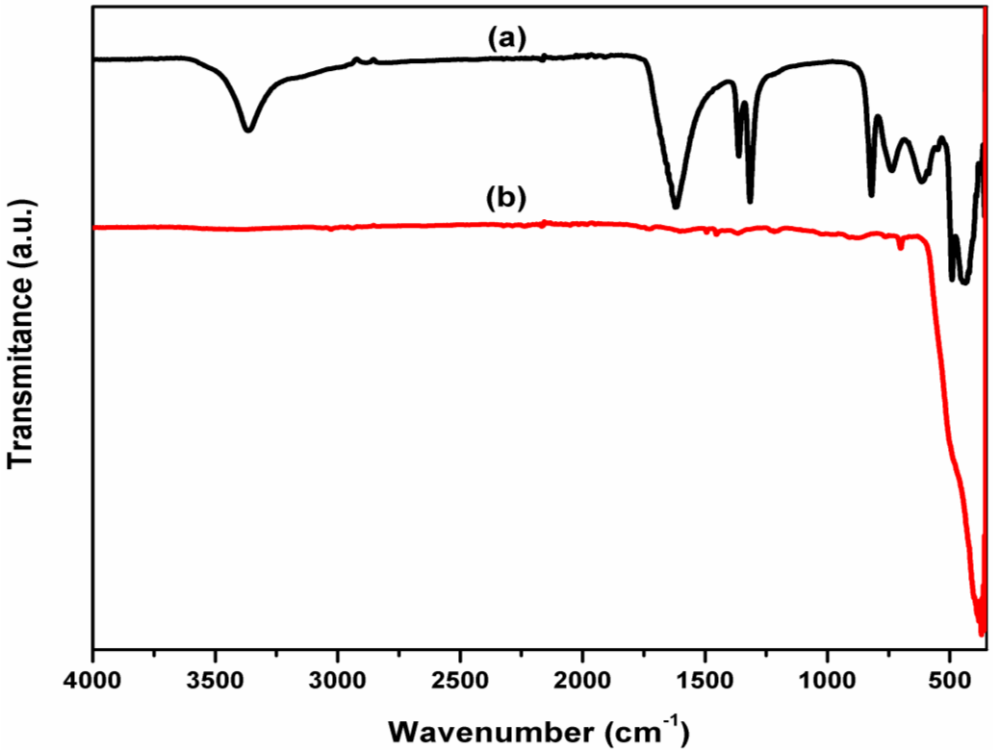

Fig. 5.15 FT-IR spectra of ZnO prepared using oxalic acid a) before and b) after calcination at 550 ˚C.

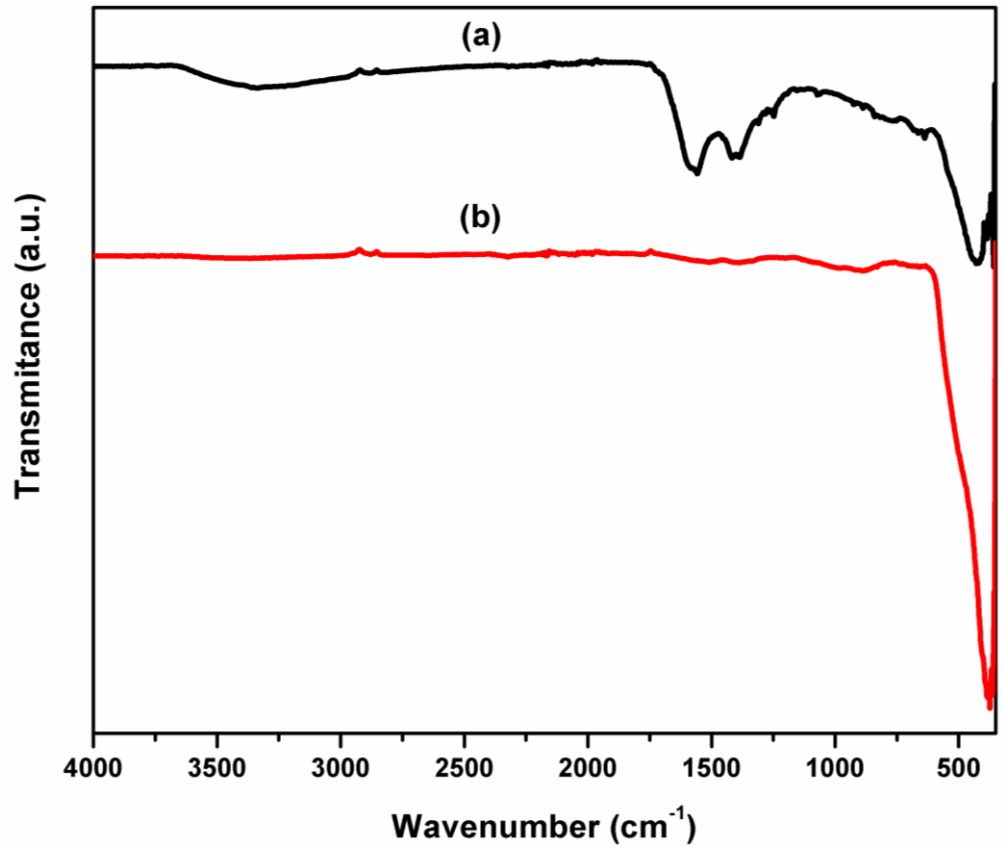

Fig. 5.16 FT-IR spectra of ZnO prepared using citric acid a) before and b) after calcination at 550 ˚C.

(III) Characterization of ZnO prepared by reflux route

5.3.3.1 Thermogravimetric analysis

Thermogravimetric analysis was conducted for the precipitate obtained from refluxing zinc nitrate and HMTA after 2 hours. Figure 5.17 shows the TGA and DTG curves of ZnO prepared by reflux route. The thermogram represents three stages of decomposition of ZnO precursor between 40-400 ºC. The first stage with peak centred at 130 ºC with a mass loss of 4.93% is due to dehydration of physisorbed water. The second stage of decomposition occurred with peak centred at 166.8 ºC with a mass loss of 7.34%. Second stage was due to the dehydration of intercalated water.[31] Third stage of decomposition is from 200-315 ºC, which accounts for only 3.3% weight loss. Decomposition of nitro group occurred within the temperature range. Liang, Mei-Keat, et al. investigated the influence of reflux time on ZnO formation using zinc nitrate hexahydrate and HMTA.[31] They have clearly observed the decomposition of precipitate after refluxing the precursors for half an hour, 24 hours and 48 hours. Our result is similar to similar to that of half an hour refluxed sample. They reported that the total weight loss decreased with the progress of refluxing time. Gerbreders et al. reported the equimolar amount of zinc nitrate and HMTA precursors are commonly used for the synthesis of ZnO nanostructures.[21]

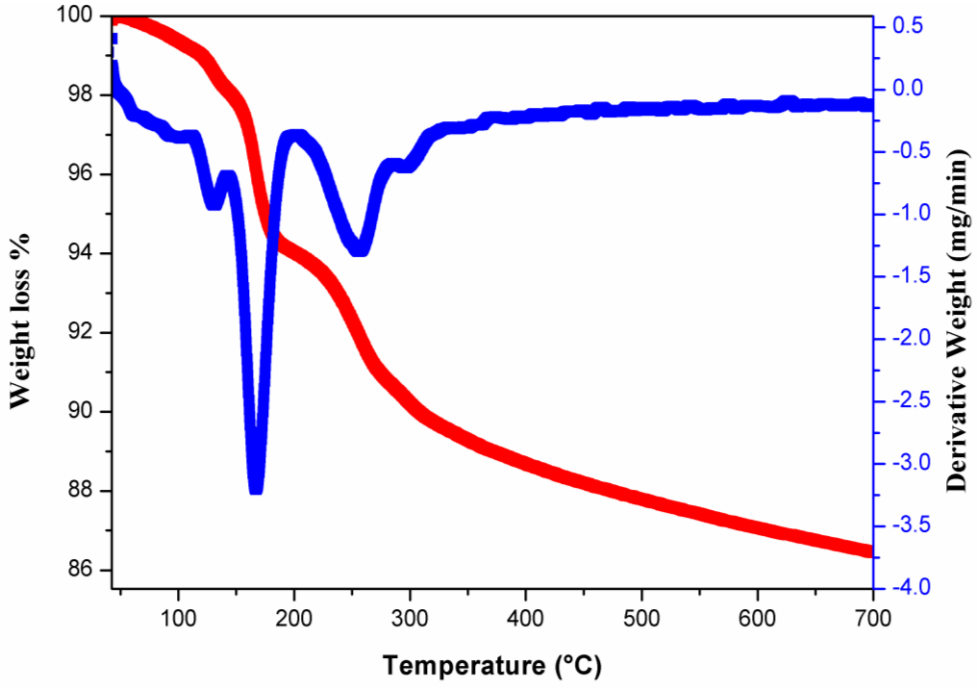

Fig. 5.17 TG-DTG curve of prepared ZnO by reflux route (2 hours) using HMTA.

5.3.3.2 XRD analysis

Crystalline structure of ZnO powder prepared by reflux route is analysed by X-ray diffraction spectrum. The XRD patterns of ZnO prepared by reflux method using zinc nitrate and HMTA (2 hours refluxed) are shown in Figure 5.18. For the 2 hours refluxed sample, extra peaks were appeared in addition to wurtzite ZnO. These additional peaks are indexed to JCPDS 47-965 and indicates the formation of zinc hydroxynitrate. However, these phase is completely absent in 4 hours refluxed sample. The XRD spectrum of ZnO refluxed for 4 hours is shown in the Figure 5.19 and the peaks are seen at 31.4 º, 34.2 º, 36.1 º, 47.3º, 56.5º, 62.7º, corresponding to the (100), (002), (101), (102), (110) and (103) planes, respectively. Peaks were indexed to JCPDS 75-0576. It confirmed the completely transformation to fully crystalline wurtzite ZnO. The peaks are very sharp and intense, indicating the high crystalline nature of the prepared sample. The crystallite size was calculated using Debye-Scherrer's equation. The crystallite size was found to be 27.8 nm for 2 hour refluxed sample and 33.8 nm for 4 hours refluxed sample.

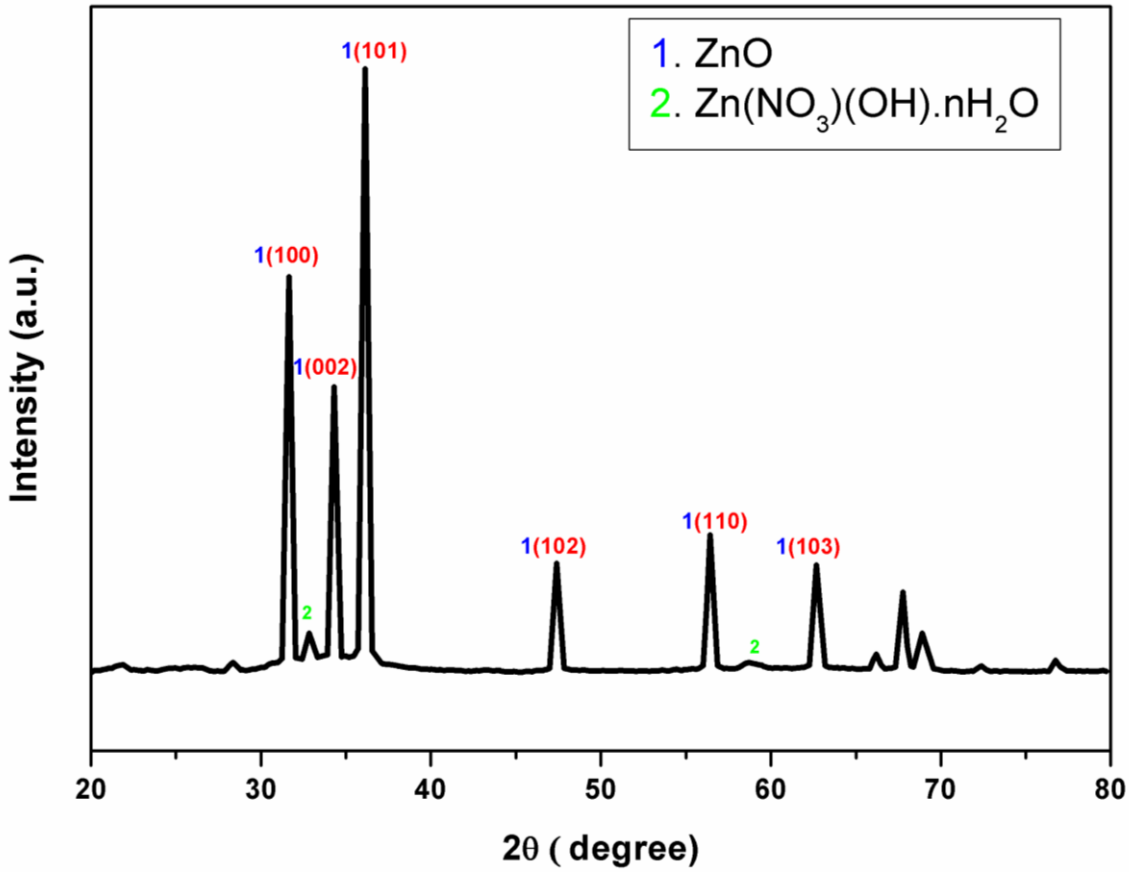

Fig. 5.18 XRD pattern of ZnO prepared by reflux route using zinc nitrate and HMTA solutions refluxed for 2 hours.

Many of the other precursors for the preparation of ZnO and methods reported earlier require calcinations at or above 550 ˚C. The present work have the advantage that phase pure crystalline nano ZnO can be prepared even at reflux temperature 100 ˚C.

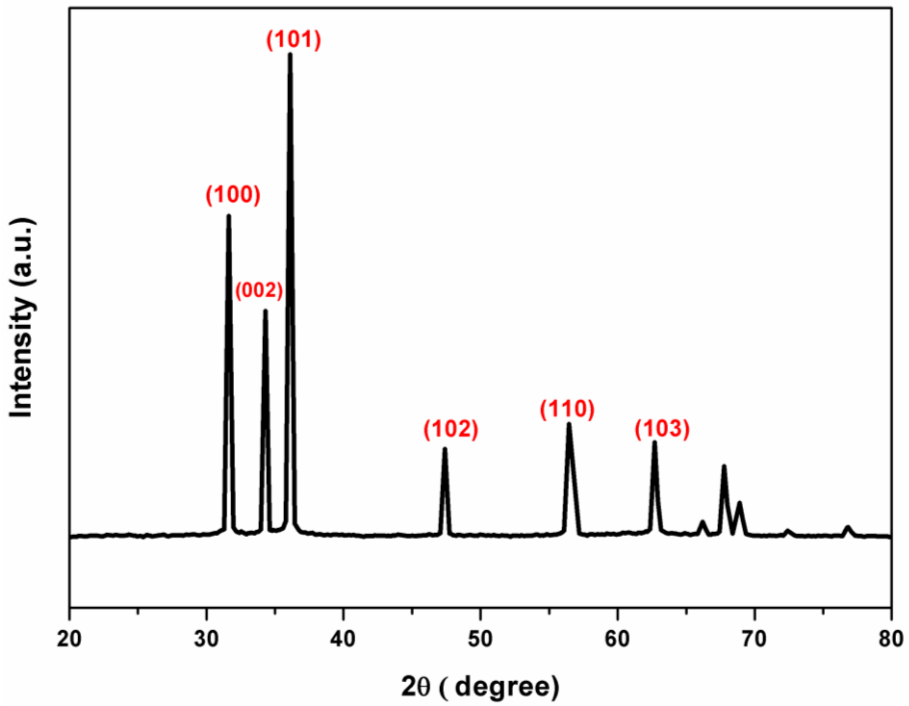

Fig. 5.19 XRD pattern of ZnO prepared by reflux route using zinc nitrate and HMTA solutions refluxed for 4 hours.

5.3.3.3 Morphological studies by TEM

TEM technique was used to understand the effect of HMTA on the morphology of the sample. Figure 5.20 shows the TEM images of ZnO obtained by refluxing Zinc nitrate and HMTA (4 hours). Images clearly indicate the nanorod structure. The average length of the nanorod is < 50 nm. The HRTEM images support the crystalline nature of the ZnO nanorods. The interplanar spacing between the lattice was found to be 0.26 nm corresponding to the (002) planes. The SAED pattern also shows the unidirectional growth of nanorods. The SAED pattern and lattice fringe width are in good agreement with the XRD results. The HMTA has a significant impact on the morphology of zinc oxide due to slow generation of OH^- ions. The growth of zinc oxide occurs only in one direction to form nanorods. Sahlevani et al. reported the influence of HMTA during thermo-hydrolysis. They proposed that HMTA acts as virtual shell around ZnO nanostructure and hence leads to enhanced axial growth.[32] In

the presence of HMTA, rapid hydrolysis occurs and generated $Zn(OH)_2$ nuclei aggregates to form rod like morphology.

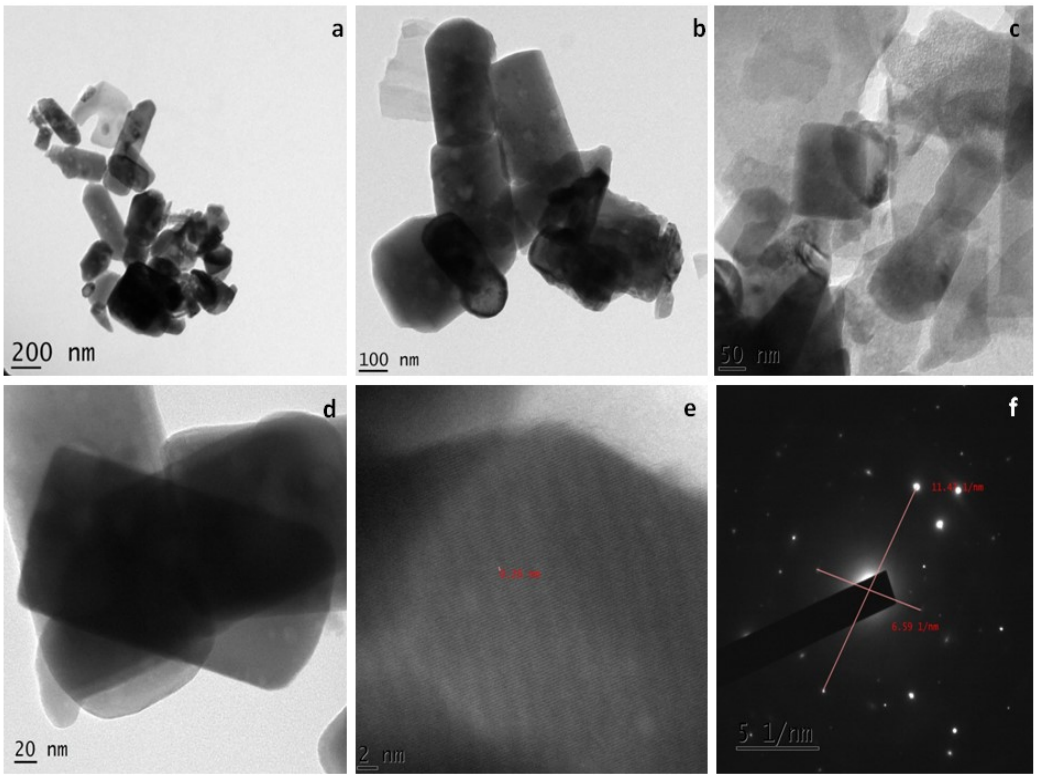

Fig. 5.20 TEM images of ZnO prepared by reflux route using zinc nitrate and HMTA :(a-d) are images at different magnifications, e) HRTEM and f) SAED pattern.

5.3.3.4 FT-IR analysis

The formation of ZnO were further confirmed by FT-IR spectra. The FT-IR spectra of ZnO prepared using zinc nitrate and HMTA refluxed for 2 and 4 hours are shown in the Figure 5.21. For sample refluxed for 2 hours, there are two absorption bands at 1335 cm^{-1} and 3481 cm^{-1}. Since XRD results have indicated the formation of $Zn(OH)(NO_3).H_2O$ along with ZnO, these two bands can be attributed to stretching vibrations of hydroxyl ion and nitrate ion.[33] For sample refluxed for 4 hours, the intense band at 433 cm^{-1} is due to the stretching vibration of Zn-O bond and the peaks corresponding to hydroxyl group and nitro group are completely absent. This shows that the reaction time controls the decomposition of $Zn(OH)(NO_3).H_2O$ to zinc oxide.

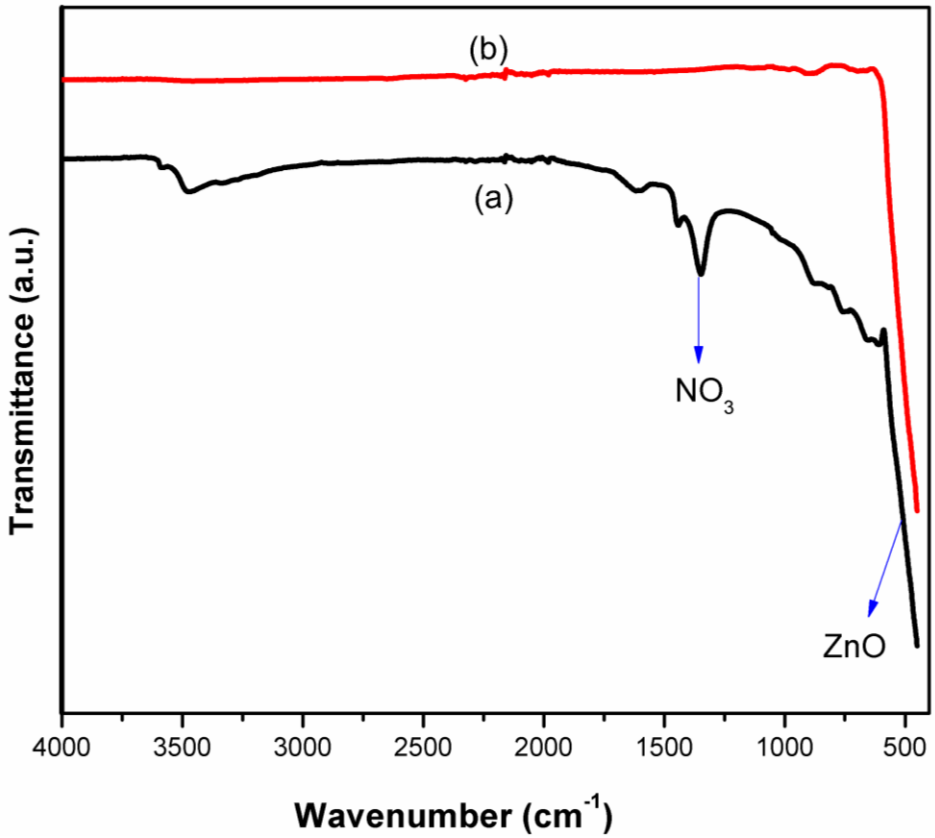

Fig. 5.21 FT-IR spectra of ZnO prepared using HMTA a) precipitate obtained after refluxing 2 hours and b) precipitate obtained after refluxing 4 hours.

5.3.3.5 UV-Visible diffuse reflectance spectrum and bandgap calculation

UV-Visible spectroscopy was used to study the optical properties of ZnO prepared using precursors zinc nitrate and HMTA and refluxing for 4 hours. Figure 5.22 shows the diffused reflectance spectra of ZnO. The spectrum has two absorption maxima at λ_{max} = 308 nm and 366 nm. The ZnO absorb entire UV region of the spectrum. For the electronic excitation, the energy of the incident photons should be higher than or equal to bandgap energy. The percentage reflectance of the ZnO was measured using UV-Visible diffuse reflectance spectra. The bandgap energy of ZnO was calculated by plotting Kubelka-Munk function versus the absorbed light energy and extrapolating the linear portion of the graph and are given in Figure 5.23. The bandgap energy of ZnO powder is found to be 3.1 eV. Compared to earlier reports the value is smaller and this may be due to the structural defects that arises during the preparation.[34]

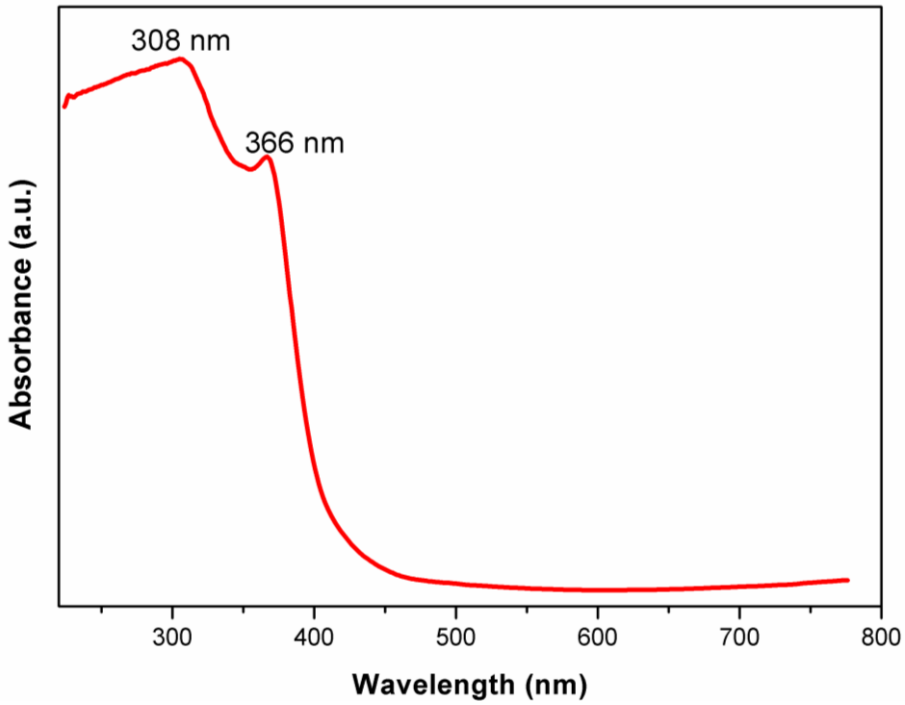

Fig. 5.22 Diffuse reflectance spectra of ZnO prepared using zinc nitrate and HMTA, refluxed for 4 hours.

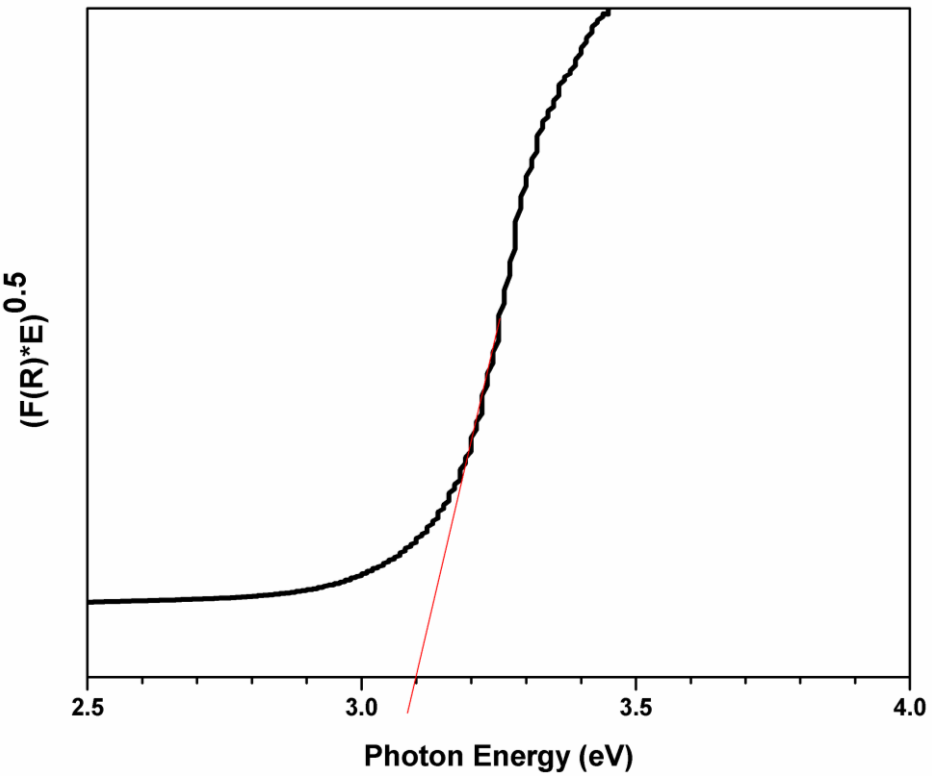

Fig. 5.23 Plot of the Kubelka-Munk function versus the energy of absorbed light for ZnO prepared using zinc nitrate and HMTA, refluxed for 4 hours.

5.3.3.6 Photoluminescence spectra

Photoluminescence spectrum is a most effective technique to study the emission properties of zinc oxide. The photoluminescence spectra of ZnO prepared using zinc nitrate and HMTA refluxed for 4 hours is shown in Figure 5.24. The spectra shows three emission peaks, one band at 380 nm near UV region, second and third emission bands at 603 nm and 662 nm in the visible region. The emission band at UV region is the characteristic emission of zinc oxide, mainly due to the near band edge emission (NBE) or recombination of exciton between valence band and conduction band.[35,36] The visible emission band at 603 nm and 662 nm is caused by photo-generated electron transition from conduction band to deeply trapped hole may be due to structural defects.[35,37] The position and intensities of the emission bands may vary depending upon the preparation conditions. The high intensity peak represents fast electron hole recombination and wider peak represent better electron-hole separation.[3]

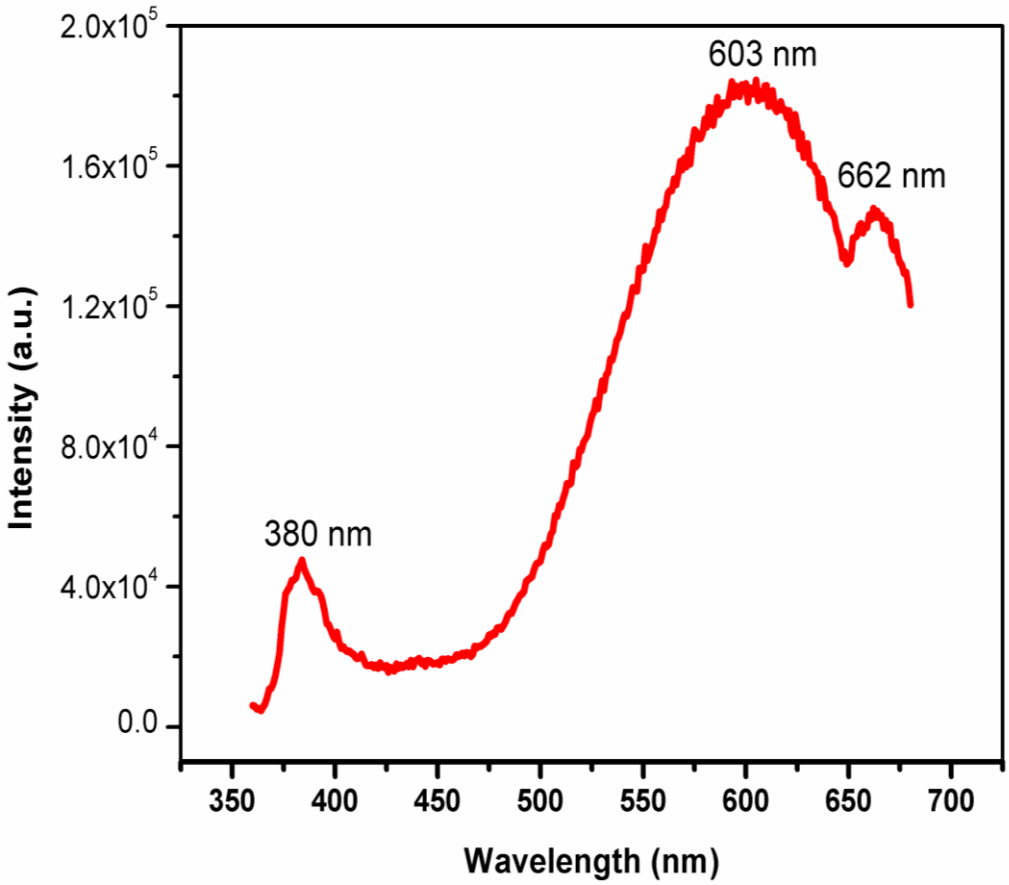

Fig. 5.24 Photoluminescence spectra of ZnO prepared from zinc nitrate and HMTA, after refluxing for 4 hours.

5.3.3.7 Photocatalytic activity of ZnO

ZnO has been employed as photocatalyst in variety of applications. Photocatalytic property of ZnO prepared using zinc nitrtate-citric acid and zinc nitrtate-HMTA were evaluated using methylene blue dye degradation under visible LED light irradiation. Degussa TiO_2 was used as reference for comparison. The photocatalytic ativity was calculated by measuring the decrease in concentration of dye against time and are shown in Figure 5.25. After 20 hours of visible light irradiation, only 35% of dye was degraded with ZnO sample prepared using zinc nitrtate and HMTA. The photograph of degradation of methylene blue is provided in Figure 5.26. The ZnO prepared using citric acid exhibited better catalytic activity than other. Sample showed 65% removal of MB under visible light irradiation. The surface area of the ZnO may also affect the photocatalytic activity. The BET surface area measurements were performed on zinc oxide samples and surface area was found to be 10.1 m^2/g for ZnO obtained by citric acid route and 0.81 m^2/g for ZnO obtained by HMTA. The smaller crystallite size and porous nature of ZnO sample obtained by the thermal decomposition of zinc–citric acid complex might be the reason for its higher photocatalytic activity.

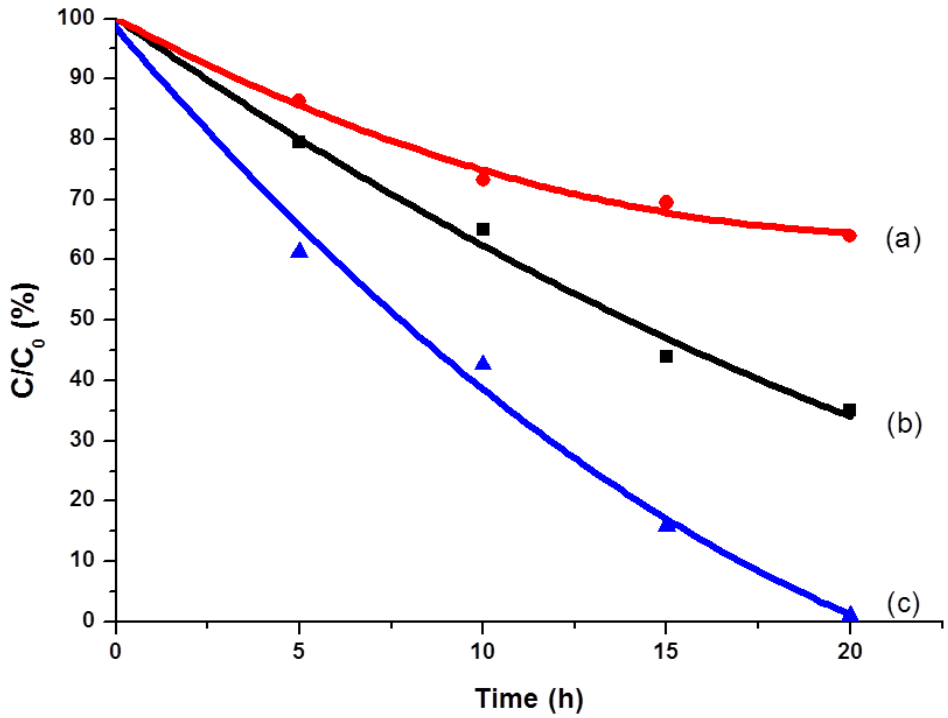

Fig. 5. 25 Plot of relative concentration as a function of time for the degradation of dye under LED visible light (a) ZnO prepared using HMTA b) ZnO prepared using citric acid and c) TiO_2.

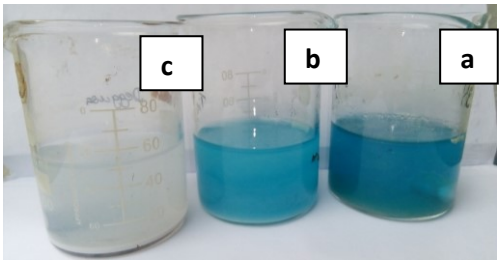

Fig. 5. 26 Photograph of dye degradation test of a) ZnO obtained using HMTA, b) ZnO obtained using citric acid route, c) Degussa TiO_2.

Bandgap energy of material plays an important role in the photocatalytic property. According to photochemisty, a radiation of energy equal to or greater than bandgap energy can excite electrons from valence band to conduction band and generate electron and hole pair. These charge carriers diffuse to the ZnO catalytic surface and electrons combine with molecular oxygen and forms superoxide radical anions for the dye degradation. Holes react with water to form hydroxyl radicals. Oxygen vacancies trap the electron and reduces the recombination of photogenerated charge carriers. Hence oxygen defects present in the catalyst act as active sites for higher catalytic degradation of dye.

5.4 Conclusion

In summary, ZnO nanopowder were prepared by various wet chemical processing methods and characterised by XRD, TEM, FT-IR, BET surface area and UV-DRS techniques. Agglomerated and spherical nano zinc oxide powder was obtained by simple precipitation method. The zinc oxide prepared through sol-gel method using oxalic acid and citric acid resulted in spherical nanopowder, having particle size < 18 nm. The ZnO nanorods were also prepared via thermal hydrolysis of zinc nitrate using HMTA at low temperature. The change in morphology in this case may be due to slow and controlled release of hydroxide ion. The XRD spectrum of ZnO samples confirmed the wurtzite crystalline structure. The bandgap of ZnO are 3.1 eV, 3.04 eV and 3.1 eV, respectively, for samples prepared via oxalic acid route, citric acid route and HMTA route. The bandgap energy of ZnO nanocrystals is lower than theoretical value (3.37 eV) probably due to oxygen vacancy. According to the present study morphology, bandgap and particle size of the final product depend upon the precursors and experimental conditions. Photocatalytic degradation studies of ZnO samples were carried out and compared with pure TiO_2 under visible LED light.

Among the prepared zinc oxide samples, ZnO prepared by sol-gel method using citric acid shows highest photocatalytic activity. The results indicates that the surface area, crystallite size and oxygen vacancies have significant role in the photocatalysis. This study strongly suggests that the ZnO can be successfully applied for photocatalysis for environmental application, under visible light irradiation.

Reference

1. Wang, H. C., Hong, Y., Chen, Z., Lao, C., Lu, Y., Yang, Z., Zhu, Y., & Liu, X. (2020). ZnO UV photodetectors modified by Ag nanoparticles using all-inkjet-printing. *Nanoscale Research Letters*, *15*(1), 1-8.
2. Abd-Alghafour, N. M., Kadhim, I. H., & Naeem, G. A. (2021). UV detector characteristics of ZnO thin film deposited on corning glass substrates using low-cost fabrication method. *Journal of Materials Science: Materials in Electronics*, 1-12.
3. Mirzaeifard, Z., Shariatinia, Z., Jourshabani, M., & Rezaei Darvishi, S. M. (2020). ZnO photocatalyst revisited: Effective photocatalytic degradation of emerging contaminants using S-doped ZnO nanoparticles under visible light radiation. *Industrial & Engineering Chemistry Research*, *59*(36), 15894-15911.
4. Suntako, R. (2015). Effect of zinc oxide nanoparticles synthesized by a precipitation method on mechanical and morphological properties of the CR foam. *Bulletin of Materials Science*, *38*(4), 1033-1038.
5. Schneider, S. L., & Lim, H. W. (2019). A review of inorganic UV filters zinc oxide and titanium dioxide. *Photodermatology, photoimmunology & photomedicine*, *35*(6), 442-446.
6. Prasad, A. R., Basheer, S. M., Gupta, I. R., Elyas, K. K., & Joseph, A. (2020). Investigation on bovine serum albumin (BSA) binding efficiency and antibacterial activity of ZnO nanoparticles. *Materials Chemistry and Physics*, *240*, 122115.
7. Prasad, A. R., Ammal, P. R., & Joseph, A. (2018). Effective photocatalytic removal of different dye stuffs using green synthesized zinc oxide nanogranules. *Materials Research Bulletin*, *102*, 116-121.
8. Bairy, R., Shankaragouda Patil, P., Maidur, S. R., Vijeth, H., Murari, M. S., & Bhat, U. (2019). The role of cobalt doping in tuning the band gap, surface morphology and third-order optical nonlinearities of ZnO nanostructures for NLO device applications. *RSC advances*, *9*(39), 22302-22312.
9. Adam, R. E., Pozina, G., Willander, M., & Nur, O. (2018). Synthesis of ZnO nanoparticles by co-precipitation method for solar driven photodegradation of congo red dye at different pH. *Photonics and Nanostructures-Fundamentals and Applications*, *32*, 11-18.

10. Raj, C. J., Joshi, R. K., & Varma, K. B. R. (2011). Synthesis from zinc oxalate, growth mechanism and optical properties of ZnO nano/micro structures. *Crystal Research and Technology*, *46*(11), 1181-1188.

11. Kumar, S. S., Venkateswarlu, P., Rao, V. R., & Rao, G. N. (2013). Synthesis, characterization and optical properties of zinc oxide nanoparticles. *International Nano Letters*, *3*(1), 1-6.

12. Richa, S. (2012). Investigation on temperature sensing of nanostructured zinc oxide synthesized via oxalate route. *Journal of Sensor Technology*, *2012*.

13. Zhang, Y. L., Yang, Y., Zhao, J. H., Tan, R. Q., Cui, P., & Song, W. J. (2009). Preparation of ZnO nanoparticles by a surfactant-assisted complex sol–gel method using zinc nitrate. *Journal of sol-gel science and technology*, *51*(2), 198-203.

14. Akbar, I., Yuwono, A. H., Sofyan, N., Ramahdita, G., & Sholehah, A. (2015). Effect of citric acid addition upon the precipitation process on the nanostructural characteristics of ZnO nanoparticles. *International Journal of Technology*, *6*(7), 1205-1210.

15. Anedda, R., Cannas, C., Musinu, A., Pinna, G., Piccaluga, G., & Casu, M. (2008). A two-stage citric acid–sol/gel synthesis of ZnO/SiO_2 nanocomposites: study of precursors and final products. *Journal of Nanoparticle Research*, *10*(1), 107-120.

16. Ghassan, A. A., Mijan, N. A., & Taufiq-Yap, Y. H. (2019). Nanomaterials: an overview of nanorods synthesis and optimization. *Nanorods and Nanocomposites*, *11*(11), 8-33.

17. Strano, V., Urso, R. G., Scuderi, M., Iwu, K. O., Simone, F., Ciliberto, E., Spinella, C. & Mirabella, S. (2014). Double role of HMTA in ZnO nanorods grown by chemical bath deposition. *The Journal of Physical Chemistry C*, *118*(48), 28189-28195.

18. Baruah, S., & Dutta, J. (2009). Effect of seeded substrates on hydrothermally grown ZnO nanorods. *Journal of sol-gel science and technology*, *50*(3), 456-464.

19. McPeak, K. M., Le, T. P., Britton, N. G., Nickolov, Z. S., Elabd, Y. A., & Baxter, J. B. (2011). Chemical bath deposition of ZnO nanowires at near-neutral pH conditions without hexamethylenetetramine (HMTA): understanding the role of HMTA in ZnO nanowire growth. *Langmuir*, *27*(7), 3672-3677.

20. Gerbreders, V., Krasovska, M., Sledevskis, E., Gerbreders, A., Mihailova, I., Tamanis, E., & Ogurcovs, A. (2020). Hydrothermal synthesis of ZnO nanostructures with controllable morphology change. *CrystEngComm*, *22*(8), 1346-1358.

21. Murillo, G., Leon-Salguero, E., Martínez-Alanis, P. R., Esteve, J., Alvarado-Rivera, J., & Güell, F. (2019). Role of aluminum and HMTA in the hydrothermal synthesis of two-dimensional n-doped ZnO nanosheets. *Nano Energy*, *60*, 817-826.

22. Sugunan, A., Warad, H. C., Boman, M., & Dutta, J. (2006). Zinc oxide nanowires in chemical bath on seeded substrates: role of hexamine. *Journal of Sol-Gel Science and Technology*, *39*(1), 49-56.

23. Vayssieres, L., Keis, K., Lindquist, S. E., & Hagfeldt, A. (2001). Purpose-built anisotropic metal oxide material: 3D highly oriented microrod array of ZnO. *The Journal of Physical Chemistry B*, *105*(17), 3350-3352.

24. Romadhan, M. F., Suyatma, N. E., & Taqi, F. M. (2016). Synthesis of ZnO nanoparticles by precipitation method with their antibacterial effect. *Indonesian Journal of Chemistry*, *16*(2), 117-123.

25. Basnet, P., Samanta, D., Inakhunbi Chanu, T., Mukherjee, J., & Chatterjee, S. (2019). Assessment of synthesis approaches for tuning the photocatalytic property of ZnO nanoparticles. *SN Applied Sciences*, *1*(6), 1-13.

26. Chouillet, C., Krafft, J. M., Louis, C., & Lauron-Pernot, H. (2004). Characterization of zinc hydroxynitrates by diffuse reflectance infrared spectroscopy—structural modifications during thermal treatment. *Spectrochimica Acta Part A: Molecular and Biomolecular Spectroscopy*, *60*(3), 505-511.

27. Darroudi, M., Sabouri, Z., Oskuee, R. K., Zak, A. K., Kargar, H., & Abd Hamid, M. H. N. (2014). Green chemistry approach for the synthesis of ZnO nanopowders and their cytotoxic effects. *Ceramics International*, *40*(3), 4827-4831.

28. Chauhan, J., Shrivastav, N., Dugaya, A., & Pandey, D. (2017). Synthesis and characterization of Ni and Cu doped ZnO. *MOJ Poly Sci*, *1*(1), 26-34.

29. Nehru, L. C., & Sanjeeviraja, C. (2014). Microwave-assisted combustion synthesis of nanocrystalline ZnO powders using zinc nitrate and various amount of organic fuels as reactants: influence of reactant parameters-A status review. *Nano Hybrids*, *6*, 75-110.

30. Poonguzhali, R. V., Kumar, E. R., Sumithra, M. G., Arunadevi, N., Rahale, C. S., Munshi, A. M., Mersal, G. A. M. & El-Metwaly, N. M. (2021). Natural citric acid (lemon juice) assisted synthesis of ZnO nanostructures: Evaluation of phase composition, morphology, optical and thermal properties. *Ceramics International*, *47*(16), 23110-23115.

31. Liang, M. K., Limo, M. J., Sola-Rabada, A., Roe, M. J., & Perry, C. C. (2014). New insights into the mechanism of ZnO formation from aqueous solutions of zinc acetate and zinc nitrate. *Chemistry of Materials*, *26*(14), 4119-4129.

32. Farhang Sahlevani, S., Udayabhaskar, R., Pandiyarajan, T., Sanhueza, F., Contreras, D., Gracia-Pinilla, M. A., & Mangalaraja, R. V. (2019). Influence of refluxing time and HMTA on structural and optical properties of rod, prism like ZnO nanostructures. *Journal of Materials Science: Materials in Electronics*, *30*(6), 5670-5680.

33. Mihaiu, S., Madarasz, J., Pokol, G., Szilagyi, I. M., Kaszas, T., Mocioiu, O. C., Atkinson, I., Toader, A., Munteanu, C., Marinescu, V. E., & Zaharescu, M. (2013). Thermal behavior of ZnO precursor powders obtained from aqueous solutions. *Rev Roum Chim*, *58*(4–5), 335-345.

34. Adam, R. E., Pozina, G., Willander, M., & Nur, O. (2018). Synthesis of ZnO nanoparticles by co-precipitation method for solar driven photodegradation of Congo red dye at different pH. *Photonics and Nanostructures-Fundamentals and Applications*, *32*, 11-18.

35. Nandi, A., Majumder, R., Nag, P., Datta, S. K., Saha, H., & Majumdar, S. (2017). Precursor dependent tailoring of morphology and bandgap of zinc oxide nanostructures. *Journal of Materials Science: Materials in Electronics*, *28*(15), 10885-10892.

36. Koyano, M., QuocBao, P., ThanhBinh, L. T., HongHa, L., NgocLong, N., & Katayama, S. I. (2002). Photoluminescence and Raman spectra of ZnO thin films by charged liquid cluster beam technique. *physica status solidi (a)*, *193*(1), 125-131.

37. Raoufi, D. (2013). Synthesis and microstructural properties of ZnO nanoparticles prepared by precipitation method. *Renewable Energy*, *50*, 932-937.

Chapter 6

Summary and conclusion

In summary, the present research work represents the synthesis and characterization of nanoscale semiconducting metal oxides, TiO_2 and ZnO, and study of their photocatalytic activity. The TiO_2 were synthesised using various precursors such as potassium titanium oxide oxalate and titanium isopropoxide. The TiO_2 was also prepared by doping with different transition metal ions and carbon for enhancing the visible light absorption. The photocatalytic properties of the samples were evaluated under LED light as well as natural sunlight irradiation. The ZnO was also prepared via different methods and its photocatalytic activities were studied under visible LED light exposure.

Introduction, characterization techniques and its principles are given in Chapter 1 and 2, respectively.

In Chapter 3, synthesis of anatase rutile mixed phase TiO_2 from potassium titanyl oxide oxalate via reflux route are given. The complex $[Ti_2O_3(H_2O)_2(C_2O_4).\ 3H_2O]$, formed by the hydrolysis of potassium titanium oxide oxalate, was decomposed to anatase and rutile mixed phase TiO_2, by calcination at 450 ºC. The TG-DTG, XRD, Raman, electron microscopy, FT-IR, UV-DRS, N_2 physisorption and UV-Visible techniques were used to characterize the nanomaterials. Doping of TiO_2 with 1 mol% Ni, Co, Mn, Cu and C were also done for enhancing the visible light absorption. The results are included in chapter 3. The structural properties of pure as well as doped TiO_2 were evaluated. The percentage composition of anatase and rutile phase was found to change on doping. For 1 mol% Cu-doped sample, only anatase phase TiO_2 was obtained. Finally, photocatalytic activity of the samples were studied by following the degradation of methylene blue dye under visible LED light irradiation. 1 mol % Ni doped TiO_2 shows the highest photocatalytic activity among doped TiO_2 samples.

Chapter 6

Chapter 4 of the thesis describes the preparation of anatase TiO_2 from titanium isopropoxide via reflux route. 1 mol% Co-doping was used to reduce the bandgap to visible region. Visible light absorption properties of the sample were studied by UV-Visible Diffuse reflectance spectra. Various characterization techniques, including TG, XRD, TEM, FESEM-EDS, XPS, FT-IR and UV-DRS were used to characterize the samples. The anatase phase was only observed in both pure and 1 mol% Co-doped sample, as shown by the XRD patterns. The TEM images indicated that the TiO_2 nanoparticles were highly agglomerated and SAED pattern further confirmed the existence of anatase phase. The XPS and EDS analyses indicated the presence of cobalt ion in TiO_2 crystal lattice. The samples were used for the photocatalytic degradation study of dye under sunlight. The kinetics of dye degradation using TiO_2 and 1mol% Co-doped TiO_2 photocatalysts under sunlight were studied, and the results are included in this chapter.

Chapter 5 includes the synthesis of ZnO through different wet chemical processing techniques like simple precipitation method, sol-gel method and reflux techniques using slow decomposition of HMTA. Zinc nitrate hexahydrate was used as the zinc source. ZnO samples prepared by various methods were characterized using a variety of instrumental techniques including XRD, FESEM, TEM, FT-IR and UV-DRS. X-ray diffraction patterns confirmed the wurtzite structure of ZnO. Spherical shape of the ZnO, prepared by simple precipitation and sol-gel method, was confirmed by FESEM. The nanorods morphology of ZnO was obtained by the thermal hydrolysis of zinc nitrate using HMTA. The crystalline nature of the ZnO nanoparticles was further confirmed by HRTEM and SAED pattern. Finally the photocatalysis properties of ZnO samples were studied by following the methylene blue dye degradation under visible LED light illumination.

Photocatalysis offer environmentally friendly process for decomposing toxic organic materials. Both TiO_2 and ZnO were found to be highly active for the degradation of dye. In future, ZnO may be used for self cleaning coatings in tiles and ceramics.

.....ꕥ.....

Chapter 7

Recommendations

In this thesis work nano mixed phase anatase rutile TiO_2 and doped TiO_2 were prepared from potassium titanium oxide oxalate as precursor. Anatase phase of TiO_2 was also synthesised by the hydrolysis of titanium isopropoxide. ZnO nanopowders were prepared by various wet chemical processing methods. In future work, influence of variation of experimental parameters such as pH, concentration of precursor, calcination temperature on the phase composition of TiO_2 and ZnO may be systematically studied. Influence of varying metal and non-metal dopant concentration on the phase composition of TiO_2 and ZnO may also be studied.

In future the doped and undoped TiO_2 and ZnO, prepared in this study, can be tested for further applications such as antibacterial activity, as a photoanode material in DSSC and in supercapacitors etc.

In this thesis work, the methylene blue was selected as a dye to evaluate the photocatalytic activity. In the future, the photocatalytic activity can be further extended by measuring the degradation of other organic dyes, such as methyl orange, textile dyes etc.

In future, the techniques like LC/MS/MS, GC/MS, HPLC, Organic Carbon (TOC) can be use to study the intermediate products formed during the photocatalytic degradation of methylene blue.

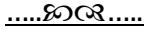

List of Publications

1. Ambily, K. J., Moly, P. P., Elsa, P. J., Jeena, C. B & Joy, V. T. (2021). A simple method for the synthesis of anatase-rutile mixed phase TiO_2 using a convenient precursor and higher visible-light photocatalytic activity of Co-doped TiO_2. *Materials Today: Proceedings*, *49*, 1408-1417.
2. Jeena, C. B., Elsa, P. J., Moly, P. P., Ambily, K. J., & Joy, V. T. (2022). A dendrite free Zn-Fe hybrid redox flow battery for renewable energy storage. *Energy Storage*, *4*(1), e275.
3. Elsa, P. J., Jeena, C. B., Moly, P. P., & Ambily, K. J. A novel synthetic route for cerium nickel mixed oxide ($CeNi_{O.5}O_y$) nanoparticles and study of its hydrogen storage property. *International Journal of Scientific &Technology Research*, 8(8), 1563-1568.
4. Moly, P. P., Jeena, C. B., Elsa, P. J., Ambily, K. J., & Joy, V. T. (2018). High performance polyvinyl alcohol/calcium titanate nanocomposite anion-exchange membranes as separators in redox flow batteries. *Polymer Bulletin*, *75*(10), 4409-4428.

Paper Presentation in Conferences

1. K. Ambily Jacob, P. Moly Peter, P. Elsa Jose, C. Jeena Balakrishnan, V. Joy Thomas presented **paper** entitled "A simple method for the synthesis of anatase-rutile mixed phase TiO_2 using a convenient precursor and higher visible-light photocatalytic activity of Co-doped TiO_2" in the 2021 Global Conference on Recent Advances in Sustainable Materials, held on 29-30, July **2021** held at A.J. Institute of Engineering &Technology, Karnataka, India

2. K. Ambily Jacob, P. Moly Peter, P. Elsa Jose, C. Jeena Balakrishnan, V. Joy Thomas presented **paper** entitled "Synthesis and characterization of ZnO by wet chemistry rout: Evaluation of photocatalytic activity" in the International Conference on Sustainable Technology Applications for Green Engineering Solutions Stage 2020, held on 17,18 July 2020 held at NSS Engineering college , Palakkad, Kerala, India.

3. K. Ambily Jacob, P. Moly Peter, P. Elsa Jose, C. Jeena Balakrishnan, V. Joy Thomas presented **paper** entitled "Natural Dyes as Sensitizers for Dye Sensitized Solar Cells" in the National Seminar on Recent trends in materials Science (NSRTMS-2019), held on 5&6 December 2019 held at Govt. College Chittur, Palakkad, Kerala, India.

4. K. Ambily Jacob, P. Moly Peter, P. Elsa Jose, C. Jeena Balakrishnan, V. Joy Thomas presented **paper** entitled "Natural fruit juice as sensitizers for efficient solar energy conversion" in the International Conference on Energy and Environment (iCEE 2k19), held on 12-14 December 2019 held at TKM College of Ars and Science, Kollam, Kerala, India.

5. K. Ambily Jacob, P. Moly Peter, P. Elsa Jose, C. Jeena Balakrishnan, V. Joy Thomas presented **paper** entitled "Synthesis and characterization of ZnO and metal doped ZnO for solar cell application" in the International Conference on Chemistry and Physics of Materials, held on 19-21 December 2018 held at St.Thomas College, Thrissur, Kerala, India.

6. K. Ambily Jacob, P. Moly Peter, P. Elsa Jose, C. Jeena Balakrishnan, V. Joy Thomas presented **paper** entitled "Synthesis and Characterization of TiO2 for solar cell Application" in the National Seminar on Emerging Trends in Nanomaterials Science and Technology, held on 19-20 December 2017 held at SNGS College, pattambi, Palakkad, Kerala, India.

7. K. Ambily Jacob, P. Moly Peter, P. Elsa Jose, C. Jeena Balakrishnan, V. Joy Thomas presented **paper** entitled "Synthesis and characterization of co doped tio_2 for trapping solar energy " in the International Seminar on Advances in PhotoResponsive Materials (APRM -2017), held on 14-15 November 2017 held at Maharaja's College, Ernakulam, Kerala, India.

8. K. Ambily Jacob, P. Moly Peter, P. Elsa Jose, C. Jeena Balakrishnan, V. Joy Thomas presented **paper** entitled "Synthesis of dye sensitized solar cells using natural dyes for effective solar energy harvesting" in the Science academies lecture workshop on Advances in Supramolecular Chemistry and Nanoscience, held on 3-4 March 2017 held at St.Joseph's College, Irinalakuda, Kerala, India.

9. K. Ambily Jacob, P. Moly Peter, P. Elsa Jose, C. Jeena Balakrishnan, V. Joy Thomas presented **paper** entitled "Synthesis and characterization of chalcogenides for effective solar energy harvesting" in the National seminar on Emerging Trends in Chemical Research, held on 28th February and 1st March 2017 held Christ College, Irinalakuda, Kerala, India.

<u>.....ꕥ.....</u>